Experimental Investigation on Flux Activated TIG Welding of Different Steels

A Dissertation submitted
in partial fulfillment of the requirements
for the Degree of

Master of Engineering
in
Production Engineering

by

Surinder K. Tathgir

Regd. No. 851282001

Under the Supervision of

Dr. Anirban Bhattacharya
Assistant Professor
MED, TU, Patiala

MECHANICAL ENGINEERING DEPARTMENT

THAPAR UNIVERSITY, PATIALA

July, 2015

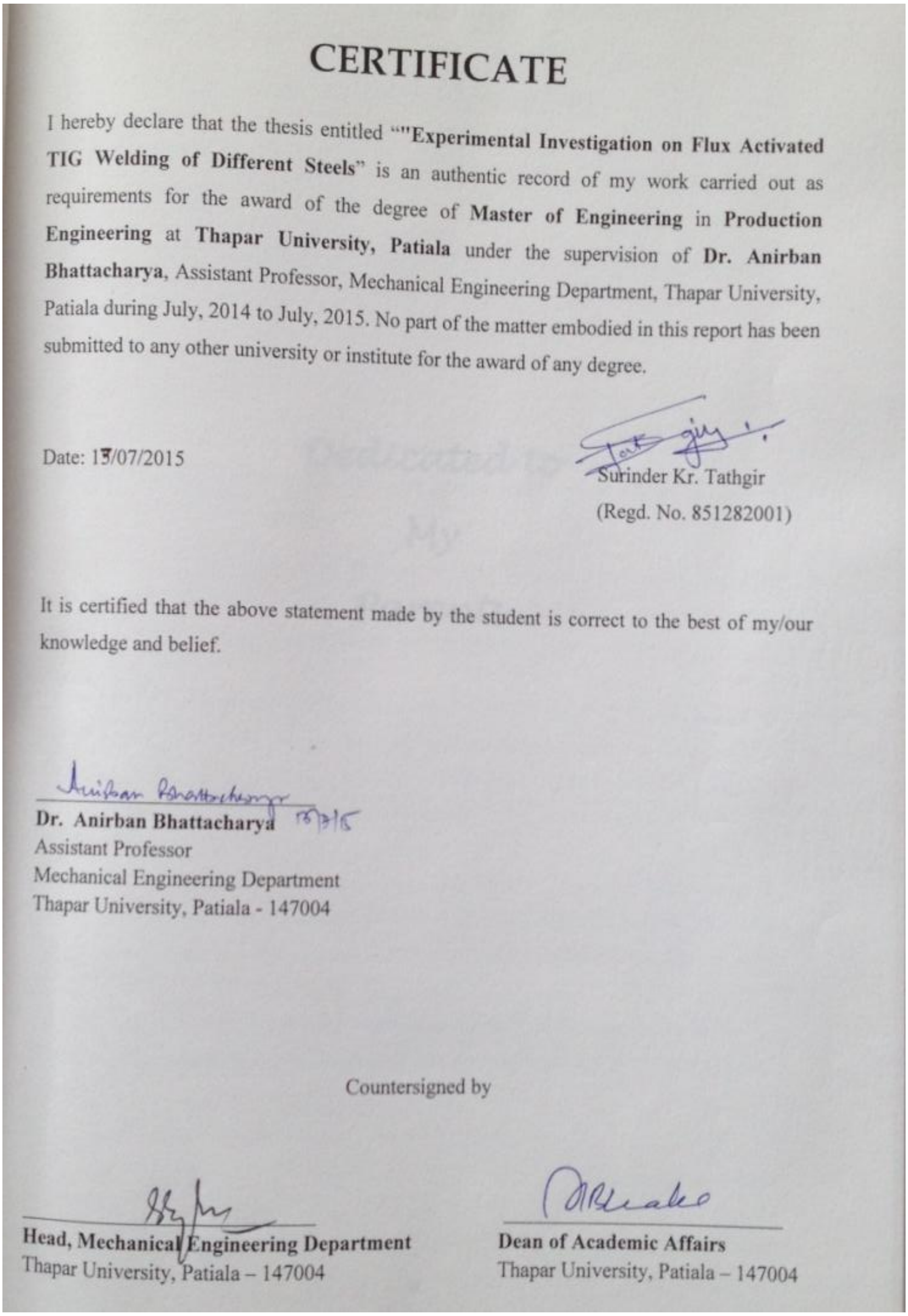

CERTIFICATE

I hereby declare that the thesis entitled “"**Experimental Investigation on Flux Activated TIG Welding of Different Steels**” is an authentic record of my work carried out as requirements for the award of the degree of **Master of Engineering** in **Production Engineering** at **Thapar University, Patiala** under the supervision of **Dr. Anirban Bhattacharya**, Assistant Professor, Mechanical Engineering Department, Thapar University, Patiala during July, 2014 to July, 2015. No part of the matter embodied in this report has been submitted to any other university or institute for the award of any degree.

Date: 13/07/2015

Surinder Kr. Tathgir
(Regd. No. 851282001)

It is certified that the above statement made by the student is correct to the best of my/our knowledge and belief.

Dr. Anirban Bhattacharya 13/7/15
Assistant Professor
Mechanical Engineering Department
Thapar University, Patiala - 147004

Countersigned by

Head, Mechanical Engineering Department
Thapar University, Patiala – 147004

Dean of Academic Affairs
Thapar University, Patiala – 147004

Dedicated to

My

Parents

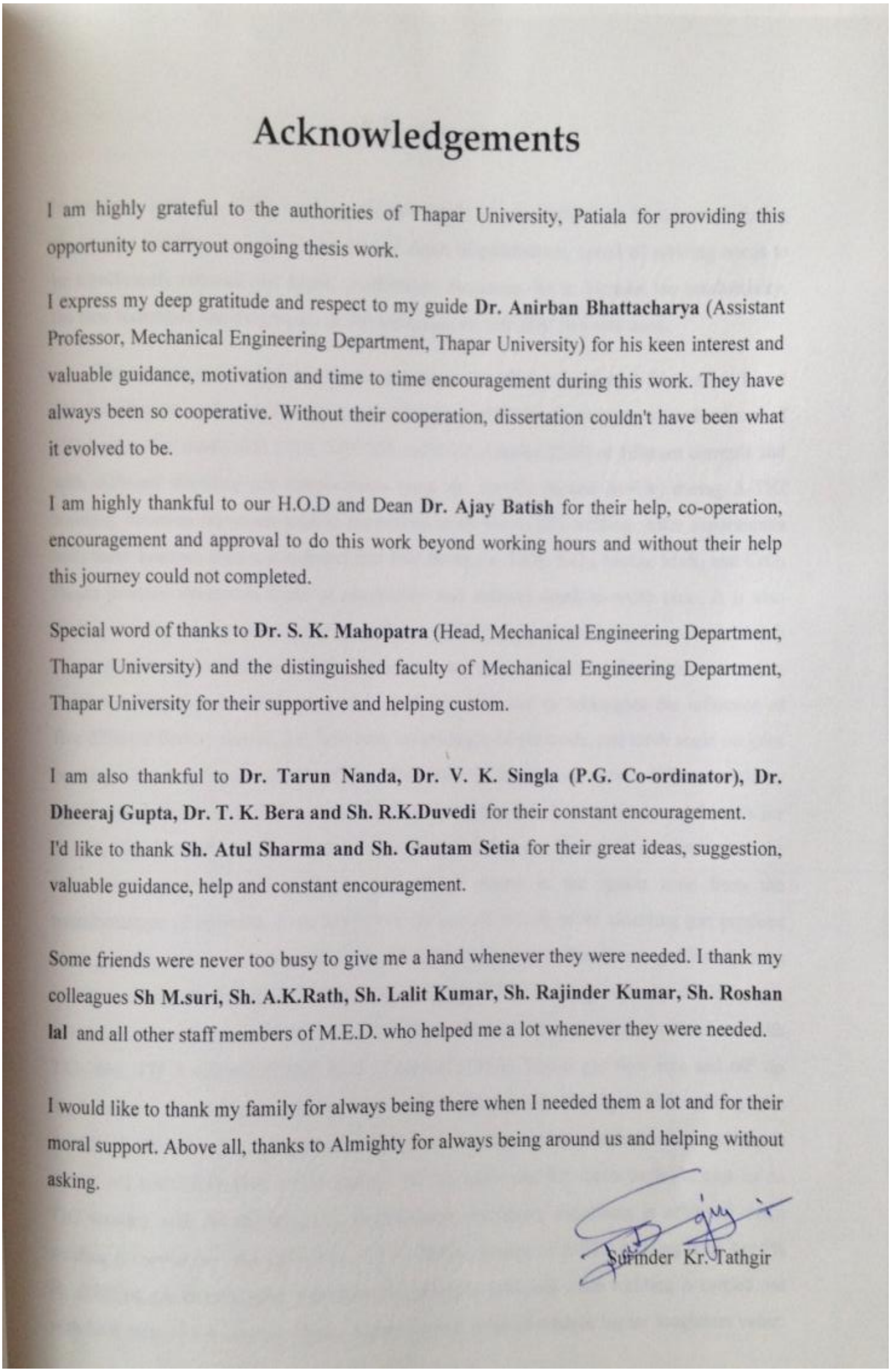

Acknowledgements

I am highly grateful to the authorities of Thapar University, Patiala for providing this opportunity to carryout ongoing thesis work.

I express my deep gratitude and respect to my guide **Dr. Anirban Bhattacharya** (Assistant Professor, Mechanical Engineering Department, Thapar University) for his keen interest and valuable guidance, motivation and time to time encouragement during this work. They have always been so cooperative. Without their cooperation, dissertation couldn't have been what it evolved to be.

I am highly thankful to our H.O.D and Dean **Dr. Ajay Batish** for their help, co-operation, encouragement and approval to do this work beyond working hours and without their help this journey could not completed.

Special word of thanks to **Dr. S. K. Mahopatra** (Head, Mechanical Engineering Department, Thapar University) and the distinguished faculty of Mechanical Engineering Department, Thapar University for their supportive and helping custom.

I am also thankful to **Dr. Tarun Nanda, Dr. V. K. Singla (P.G. Co-ordinator), Dr. Dheeraj Gupta, Dr. T. K. Bera and Sh. R.K.Duvedi** for their constant encouragement.
I'd like to thank **Sh. Atul Sharma and Sh. Gautam Setia** for their great ideas, suggestion, valuable guidance, help and constant encouragement.

Some friends were never too busy to give me a hand whenever they were needed. I thank my colleagues **Sh M.suri, Sh. A.K.Rath, Sh. Lalit Kumar, Sh. Rajinder Kumar, Sh. Roshan lal** and all other staff members of M.E.D. who helped me a lot whenever they were needed.

I would like to thank my family for always being there when I needed them a lot and for their moral support. Above all, thanks to Almighty for always being around us and helping without asking.

Surinder Kr. Tathgir

Abstract

In tungsten inert gas (TIG) welding, limited depth of penetration can be achieved during single pass welding. To achieve the desired depth of penetration, speed of welding needs to be significantly reduced and hence, productivity decreases. So to increase the productivity, the new technique was developed. In this technique an activated flux was used.

The present work is an attempt to investigate the effect of activated flux and different gas shielding on weld morphology, mechanical properties, microstructure, microhardness of different graded steel (AISI 1020, AISI 304, AISI 316, Duplex 2205) at different currents and with different shielding gas compositions (pure Ar, Ar+5% H_2 and Ar+He) during A-TIG welding. Fourteen fluxes are used in the present study for A-TIG welding. After experiments with these fourteen fluxes, it is found that five fluxes i.e. TiO_2, SiO_2, MoO_3, MoS_2 and CrO_3 fluxes produce maximum depth of penetration and reduces depth-to-width ratio. It is also finding that the small percentage of H_2 in the Ar shielding gas dramatically increase the depth of penetration up to 200% to 300%. So, based upon these results five fluxes are selected to carry out further study. Then parametric study is conducted to investigate the influence of five different fluxes, current, gas flow rate, vertex angle of electrode, and torch angle on joint bending load, toughness, microhardness. This study is carried out at two different welding speeds and under the two different shielding environments (i.e. 2 mm/s for Ar and 3 mm/s for Ar+5% H_2). From the result of microstructure it is found that fluxes do not deteriorate the mechanical properties and sufficient austenite is found in the fusion zone from the transformation of austenite from ferrite but the use of 5% H_2 in Ar shielding gas produce some porosity in the weld zone. It is also found that penetration increases significantly with increase of current during A-TIG welding. During ATIG welding with Ar shielding gas environment, maximum bending load (22.6 kN) is obtained when welding is carried out with TiO_2 flux, 175 A current. Higher level of current (175A), higher gas flow rate and 60° tip angle helps to obtain higher bending load of the welded joints. During A-TIG welding with Ar+5% H_2 shielding gas environment, maximum bending load is obtained when welding is carried out with MoO_3 flux, 150 A current, 60° tip angle and 85° torch angle. In case of A-TIG welding with Ar shielding gas environment, maximum toughness is achieved when welding is carried out with CrO_3 flux, 175 A current. In case of A-TIG welding with Ar+5% H_2 shielding gas environment, maximum toughness is achieved when welding is carried out with SiO_2 flux, 175 A current. Hence, higher current helps to achieve higher toughness value.

Lathy and skeletal type δ-ferrite is also finds in some A-TIG welded samples. Maximum value of microhardness (446.147 HVN) in the FZ is obtained in case of Ar shielding, with SiO2 flux at 125 A (low current) and in case of Ar+5% H2 shielding the maximum microhardness (444.77 HVN) is found with CrO3 flux at 125 A current.

Key words: TIG; A-TIG; Marangoni convection; Austenitic Stainless Steel; Compounds; AISI; Depth-of-Penetration; Fluxes; SEM; Microhardness; Face bend; Toughness.

Contents

Chapter 4 Parametric Study During ATIG for Mechanical and Metallurgical Study 79-154

List of Figures

List of Tables

Acronyms

TIG	Tungsten Inert Gas Welding
A-TIG	Activated TIG Welding
ANOVA	Analysis of Variance
ARR	Array
DF	Degree of Freedom
SEM	Scanning Electron Microscope
OA	Orthogonal Array
FZ	Fusion Zone
HAZ	Heat Affected Zone
W/D	Width-to-Depth
AISI	American Iron and Steel Institute

Chapter 1

Introduction

1.1 Introduction

Welding is a joining process of different materials, generally metals or thermoplast by causing local coalescence. It means when two or more than two droplets come together to form a single droplet. This is done by melting the base metal by applying heat (from any source) or bringing the two metals at the plastic stage, in which filler metal (same composition) may or may not be applied, that together form a molten pool (the weld puddle) which on cooling produce a strong joint. Pressure is used, where the metals bring to plastic stage. Another variant of this process are soldering and brazing, in which low lower melting point material is used to join two similar or dissimilar metals. In both soldering and brazing, the work pieces do not bring to melting point. Soldering and brazing are temporary joints and can be reopened by applying heat. Welding is also said to be bond which is permanent in between two materials. Components of different material for assembly are easily welded by different welding techniques. The use of different welding techniques for different application of fabrications is extensive. Welding is used now a day in every sector of engineering. Welding is widely used in aerospace industries, railways, shipping industries, automobile sector and electronics sector. Actually all welding processes are not applicable at every place so it is the work of an experience welder to decide so many factors like size, shape, material and the most important factor is economical price for fabrication. Welding generally effects the metallurgy of the materials, which could be accomplished by post welding heat treatment to the welded material by seeing the properties of the material used.

Classification of welding processes

Welding can be classified on the basis of two things:

1. Source of heat: e.g. electric arc, gas flame, chemical reaction, radiant energy, electric resistance etc.
2. Type of interaction: If solid to solid interaction is there then it is called solid state welding or pressure welding and if liquid to liquid interaction is there then is called fusion welding.

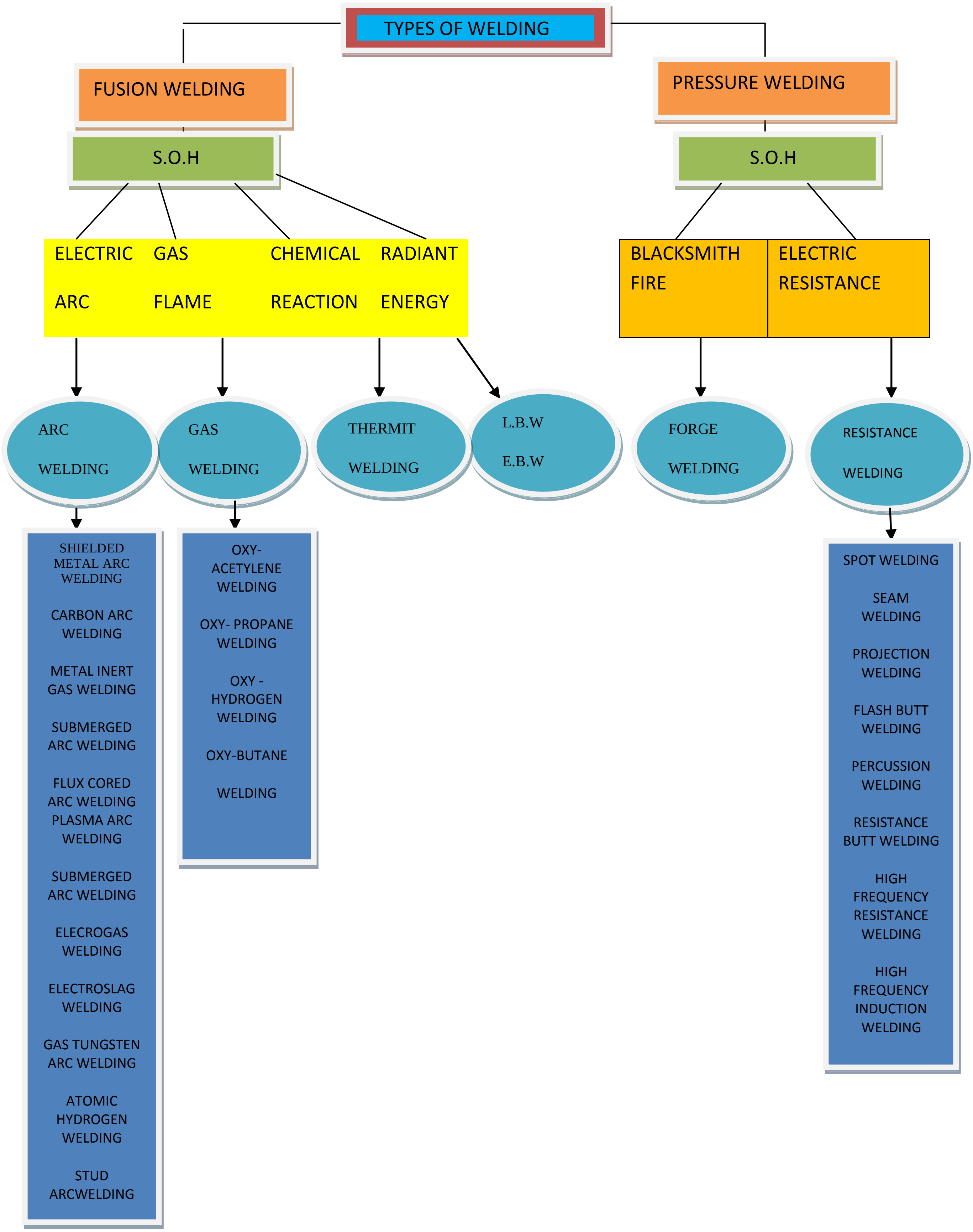

Figure 1.1: Flowchart of types of welding

1.2 Arc Welding

Arc welding is a type of fusion welding process, in which necessary heat is produced by an electric arc (source of heat) between an electrode and work piece. In an arc welding the bonding interaction is takes place in liquid state. Through electrode the essential amount of heat is produced to make the two objects to be welded fuse together and make a healthy joint. Arc welding is mostly done without the application of pressure. This type of welding is done with both AC or DC power supply according to the application, availability and also the electrode used may be consumable or non-consumable. Arc welding is mostly done without the application of pressure. Arc welding can be manual, semi automatic and fully automatic.

1.3 Tungsten Inert Gas Welding

1.3.1 Overview of TIG

Tungsten inert gas welding (TIG) is a fusion welding process which comes under an arc welding. Some of the researchers give another name, known as gas tungsten arc welding (GTAW). In Europe it is known as TIG welding, wolfram inert gas (WIG) in Germany, and still referred to by the original trade names Argon arc or Helium arc welding in some countries. These names are called so because of the use of Argon and Helium gas. TIG welding was introduced in early 1940’s. In most of the countries only Ar is used for shielding, due to its availability.

As the name suggest TIG welding use an electric arc which is produced between a non consumable electrode and the workpiece. In other methods of arc welding generally an arc is produced by scratching or by hitting method, but in this method to avoid tungsten inclusion and to protect the electrode tip an arc is produced from a gap of 5-6 mm with the help of high frequency high voltage unit (HFHV). To avoid overheating of electrode negative terminal is given to the electrode, but straight polarity is generally not suitable for non-ferrous materials.

For thicker jobs and to avoid over heating of welding torch water-cooled torches are developed. TIG welding is one of the most suitable processes, which is used all over the world to produce quality welds. TIG welding process is applied for joining a wide range of metals, including stainless steel, aluminium alloys, magnesium and reactive metals such as titanium.

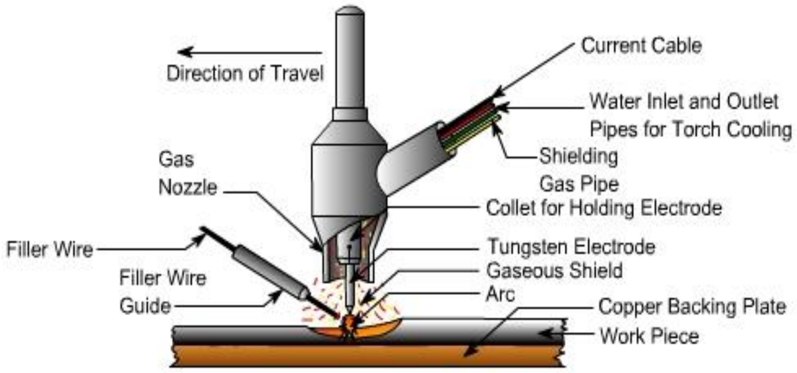

Figure 1.2: Schematic diagram of TIG welding operation [www. Nptel.ac.in]

In the recent developments in TIG welding process different types of mixture of inert gases with double shielding methods are also tried by many researchers to enhance the productivity of TIG welding. To achieve higher deposition rate, hot wire method is also used to improve the production rate and it is done by resistance heating method. As the filler metal is heated prior to the weld zone, it helps to remove the surface contamination of the filler wire, thus produce high quality weld. To weld lower thick metals and to achieve good control over the heat input, pulse TIG welding is developed. With this variant of TIG welding the welding torch can be manipulated easily for the exact location. Tungsten is a strong emitter of electrons and it has a high melting point, so it is widely used in this process. The main limiting factor is the speed of TIG welding. Fig. 1.2 shows the TIG welding operation.

1.3.2 Principle of Operation

After making proper electrode tip by grinding the welding current and Inert gas supply are adjusted at selected parameter. First an arc is formed between a Cu metal plate and the tungsten electrode by using a high frequency high voltage unit and then brings it on the workpiece. With the help of high frequency high voltage unit an arc jumps across the air gap of 3 to 5 mm. As the air gets ionized due to flow of electron, hence an arc is produced between two terminals. This method avoids damaging of electrode tip, tungsten inclusion and its loss.

Once an arc produced, it is allowed to stay on the job to form a molten weld pool. The welding is started by moving the torch along the joint as in oxy acetylene welding. If it is doing manually, then care should be taken of constant gap between the electrode and the workpiece. Cu plates should be placed on both ends of the job for easy arc initiation and an arc is shut by increasing the arc length at the far end. The post flow of shielding gas is necessary to impose on the solidifying weld pool and on the electrode for a little moment even after the process stop. Hence, weld metal and electrode can be protected from atmospheric contamination. The welding torch and filler metal are generally kept at an angles of 45-80^{o} and 10-20^{o} respectively in down hand position or for a flat job. A leftward welding technique like in gas welding is used. Filler metal, if required, may be impopse by dipping method or by keeping the filler in the groove joint. While doing this, the tungsten electrode should be kept little away from weld pool. While doing manipulation and altering of filler rod into the molten weld pool, the end of filler may get contaminated and thus contaminate the weld pool. So to avoid contamination, it should to keep the heated end of the filler rod always within the inert atmosphere while welding and even withdrawing the same from weld pool during welding.

1.3.3 TIG Set-up

Basic Equipments of TIG

The basic equipments of TIG consist of:

- Welding Torch
- Electrode
- Power Supply
- Shielding gas

Welding Torch

Welding torch is one of the basic and most important equipment for TIG welding. Torch in TIG welding may be automatic or manually operated. There is no hard and fast difference in the operation of manually operated and automatically operated torch in construction but the difference comes just in the motion or the position of the torch. Air cooled torch is designed for low heat input operations (up to about 200 A), while water cooled torch is recommended for high heat input (up to about 600 A). The torch is connected with cables to the power source and it also has gas hoses for shielding, which are connected with gas cylinder.

The main parts of the manually operated torch are the collet, tungsten electrode (Non consumable), end rubber cap, ceramic cap and torch handle. The material used in ceramic cap is ceramic because of its temperature withstand property. Different sizes of caps are used according to the required shielding gas flow. The material of the collet is generally of brass or copper in order to transmit high current and heat effectively. Electrode used is of tungsten, the size of the electrode depend upon the thickness of the material to be welded. The collet is adjustable to some extent. The torch body is made of heat-resistant material, insulating plastics or fibres, covering the cables and gas hose, providing prtection from heat and electricity to protect the operator.

Shielding Gas

The primary functions of the shielding gas in the arc welding processes are to provide a blanket of inert atmosphere or suitable medium for the stable operation of a sustained low voltage arc and to provide shielding from atmospheric contamination. Secondary, important, functions include the control of weld bead geometry and mechanical properties.

I. Arc Support and Stability

The electric arc is a sustained flow of current in an ionized atmosphere. It includes equal number of electrons and ions which flow between two terminals. Due to ionization of the gas an arc is initiate and maintained. The ease of ionization is indicated by the ionization potential of the gas and values for the common gases are given in Table 1.1. Argon, in particular, has a low ionization potential and is commonly used in the TIG process. Argon is heavier than air and it has a density of 1.33 times than air and 10 times than helium. But argon produces a viscous arc that may result into poor arc manipulation, hence not suitable for deep grooves joint or thick metals. The thermal conductivity of the gas will also influence the arc stability; a high thermal conductivity may result in a reduction in the diameter of the conducting core of the arc and this can lead to an increase in voltage and a reduction in arc stability. Hydrogen, which has a lower ionization potential but a higher thermal conductivity than argon, increases the arc voltage when mixed with argon and may affect both arc stability and arc initiation if more than 8% is added.

Table 1.1: Basic properties of comman shielding gases supplies [Norish, 2006]

Element	First Ionization potential	Density (kg/m^3)
Argon	15.75	1.784
Helium	24.58	0.178
Hydrogen	13.59	0.083
Nitrogen	14.54	1.161
Oxygen	13.61	1.326
Carbon dioxide	14.0	1.977

II. Shielding From Atmospheric Contamination

The effectiveness of the gas in providing shielding from atmospheric contamination will depend on its chemical reactivity and its physical properties. In TIG welding, it is necessary to protect the tungsten electrode from oxidation and, for this reason; an inert gases argon or helium is normally used. It is also necessary to protect the weld metal from adverse gas–metal reactions such as the formation of porosity, inclusions, surface oxidation or embrittlement. Common active gases which may cause problems in this respect are oxygen, nitrogen and hydrogen. Most materials form oxides when heated in an oxidizing atmosphere, whereas nitrogen may form insoluble nitrides with reactive metals (Ti, Ta, V and Nb) and soluble compounds with other metals (Fe, Mn, Cr and W). Hydrogen is soluble in most metals, but can form compounds with the reactive metals.

III. Shielding According to Material

The choice of different shielding gases is shown in Table 1.2.

Table1.2: Shielding gas according to material [Parmar, 2011]

Sr. No.	Materials	Shielding gases
1.	Mild Steel	Argon , Carbon dioxide
2.	Stainless Steel	Argon, Argon + hydrogen (max 5%)
3.	Aluminum	Argon is preferable for lower thickness and Helium is preferable for higher thickness.
4.	Magnesium	Argon is preferable for lower thickness and Helium is preferable for higher thickness.
5.	Copper/Nickel	Argon is preferable for Lower thickness and Helium is preferable for higher thickness.
6.	Titanium	Argon

Electrodes

Electrode used in tungsten arc welding is non consumable and generally of tungsten material because tungsten is refractory metal and has the highest melting temperature among pure metals, at 3,410°C. Tungsten is also a strong emitter of electrons in the arc column. The tungsten electrodes used in GTAW are usually alloyed with a small amount of thoria or zirconia in order to improve arc starting, by reducing the work function of the tungsten and improving its emission characteristics. Pure tungsten electrodes are less expensive as compared to thoriated or zirconiated tungsten electrode.

- Pure tungsten electrodes (classified EWP) are used for general purpose at low level of current. They have poor heat resistance as compared to thoriated tungsten electrode. They are not used specifically for AC welding of e.g. magnesium and aluminium.
- Thorium oxide (thoria) is added in the range of 1-2% in tungsten, so name is called thoriated tungsten was designed for DC power source and can withstand higher temperatures than pure tungsten. It also helps to make tungsten more resistant to atmospheric contamination.
- Zirconium is also added in tungsten from 1-2% which helps it to increase the current carrying capacity while improving arc stability during welding operation. It may also help to increase electrode life. But the zirconium tungsten electrodes life is less than thorium tungsten electrode.
- In addition to this, some electrode manufacturers are producing an alternative tungsten alloys for electrodes with specified metal composition.

The stable arc operating time (continuous arc operation) may be extended by up to 100% when an electrode with a fine, homogeneous distribution of thorium particles (70 h stable arc operation at 125 A) is substituted for an electrode with a less regular composition (35 h stable operation), while the re-ignition delays can be reduced from 4% of the total number of arc starts to 1% with the better quality electrode Although thoria ($ThO_{2)}$ is effective in improving arc striking and tip shape retention, it is naturally radioactive. Concern about potential safety implications, for particular electrode manufacture, has led to the investigation of alternative alloying elements additions. Oxides of the rare earth elements lanthanum, yttrium and cerium appear to offer similar characteristics to thorium [Norish, 2006].

Power Source

TIG welding power sources have, from the basic transformer types of power sources which were used with add-on units to enable the power source to be used as a TIG unit, e.g. high frequency unit and/or DC rectifying units. The basics of TIG welding has almost remained the same, but the advent of technology TIG welding power sources have made the TIG processes more controllable and more portable in some cases. The TIG power source uses main power connected to a suitable power for the TIG process being used. This can be either AC or DC. The one thing that all TIGs have in common is that they are CC (Constant

Current) type power sources. This means only output adjustment will control the power source amps. The voltage will be up or down depending on the resistance of the welding arc.
A TIG power source can be of the AC or DC type.

The principle of electric circuits will apply to only DC power sources. This means 2/3rd (approximately70%) of the total heat is always on the positive terminal and 1/3rd (approximately 30%) at the negative terminal. So when a DC power source is used whatever is connected to the positive side will have 70% of the energy output (heat). When using an AC power source, which has an output of a wave form, the average on both terminals will be the same. This is because for one half of the wave form (cycle) the positive terminal will have 70% of the energy, but as the wave form moves to the other half of the cycle it will move to the negative terminal, which will then have the 70% of the energy.

Other things to check on TIG power sources are:

- Current (Amperage) to do the job.
- Does the amperage go low enough for light material and high enough for thick material?
- Power Supply - 400 Volt, 230 Volt - single or three phases.
- Will an engine driven power source be better to do the job? (Must have CC range). Might need suitable extra add-ons to do e.g., HF unit.
- Does the TIG welding need an AC power source or DC power source, as different material will need a different power type?

1.4 Welding of Stainless Steel

Stainless steels are the iron base alloys in which the 10% or more chromium is added to increase its properties like hardenability and corrosion resistance. Chromium and other elements are also found in it to increase the manufacturing ability of the steels for industrial applications. It responded well when heat treatment is done. A film of for chromium oxide is formed which retards further oxidation, rust or corrosion.

Properties of stainless steels:

- It provides higher corrosion resistance.
- Higher toughness at cryogenic temperature.
- Provide more work hardening as compared to other steels.
- Provide high temperature hot strength.

- Gives better ductility.
- Gives good strength and other mechanical properties.
- Gives good luster after buffing and better surface appearance.

Classification of stainless steels as per their structure matrix is as follows:

A. Austenitic Stainless steel
B. Ferritic Stainless steel
C. Martenistic stainless steel
D. Duplex Stainless steel (ferrite and austenite-50%)
E. Precipitation Hardening Stainless Steel (PH stainless steel)

During welding of the stainless steels the temperature of base metal adjacent to the weld /fusion zone reach at a level at which micro structural changes occurs. The degree at which these changes occurred and their effect on final weld metal, in term of resistance to corrosion and mechanical properties depends upon the constituent elements, thickness and filler metal, joint design, weld method, type of shielding, other welding parameters and welder skill. Weldability of different grades which are easily welded depends upon the nature of the family to which it belongs to.

Heat conductivity of Cr-Ni steels is about 50 percent less than that of mild steel, so less heat input is required for a given workpiece of Cr-Ni steel. As a general rule about 10 per cent less current is used with stainless steel electrodes as compared to mild steel.

Melting rate of stainless steel electrodes is higher than the melting rate of M.S. electrodes. So this may be another reason for slightly lower current (about 10%) being used in stainless steel welding. Thermal expansion of Cr-Ni steels is about 50 percent greater than for M.S. This will increase the chance of warping and buckling. Hence suitable fixture must be used while welding stainless steels. Electrical resistance is 6 to 12 times higher than M.S. and hence it may cause over heating in the electrodes. Hence shorter electrodes are generally recommended to reduce electrode heating.

A. Austenitic Stainless Steel

Austenitic stainless steels are the most widely used for welding purposes. They are used in many industrial applications such as chemical processing, pharmaceutical manufacturing, food processing and liquid gas storage. Weldability of these steels is usually very good. Austenitic stainless steel contains a minimum of 16% and maximum 26% chromium with 8-24% nickel. They range of grades of austenitic stainless steel is from AISI 304 to super austenitic such as 904L and with 6% Molybdenum. Machining of austenitic steel can be improved by adding elements like Molybdenum, Titanium or Copper. Nickel promotes austenite formation, increase higher temperature strength, ductility, and provides corrosion resistance. These additions can make the steel, which is suited to ambient temperature applications. Nickel in austenitic stainless steel provides ductility, which suited to low temperature or cryogenic applications; otherwise it may be brittle at lower temperature. Austenitic stainless steel is generally non-magnetic in nature and is not hardened by heat treatment. The principal alloying elements are sometimes reflected in the name of the steel. A common name for AISI 304 is 18/8, for 18% chromium and 8% nickel. A good formability characteristic gives it beautiful look. Manganese promotes the stability at room temperature.

AISI 304 and AISI 316 stainless steels have low carbon percentage and molybdenum in type 316 helps to improve corrosion resistance. So, with 2-3% molybdenum the 316 stainless steel gives high temperature properties. AISI 321 and AISI 327 stainless steel are stabilized against the problem of carbide precipitation. Except free machining grades, rest all the austenitic stainless steel grades are easily welded. The produced welded joint is characterized by a high degree of toughness. However, the main consideration during welding of austenite stainless steel welding is on heat of welding, contamination, porosity, carbide precipitation and cracking of weld. Too much extra heat input produced large thermal gradient across the joint which may affect corrosion resistance and its strength.

Carbide Precipitation

When the austenitic steel is heated or cooled in the range of 425-870°C, the carbon precipitate at the grain boundaries, where it combine with chromium to form chromium rich carbide [nadkarni, 1988]. This rich chromium carbide is known as carbide precipitation. Due to this carbide precipitation, inter granular corrosion can occur which reduced corrosion resistance.

It can be controlled by:

- Adding those elements in steel which have great affinity for carbon than does chromium (like columbium and titanium).
- Rapid quenching may be the solution of carbide precipitation.
- Post weld heat treatment may again distribute the carbide into the solution.
- Restricting the carbon content up to 0.03%.

Even in case of stabilised steels sensitisation occurs, not during welding but during reheating of welding specimen at around 650°C or when it subjected to service at this temperature.

Hot Cracking

Austenitic stainless steel weld metal is also suffer for inter dendritic cracking which is known as hot cracking or micro fissuring (generally not visible with naked eyes). The name hot crack is so called because the cracks occur at high temperature. This type of problem is visible when the stress imposed on the weld metal is high. Wholly austenitic structures are highly prone to this type of defect, while the weld metal with a duplex structure of delta ferrite is not support to hot cracking. Small increase of carbon and nitrogen can reduce the susceptibility to hot cracking. Penning is not suitable in this case because of the difficulty of doing at high temperature.

B. Ferritic Stainless Steel

The standard grades of ferritic stainless steel are: AISI 405, AISI 409, AISI 430 and AISI 430Ti. Ti and Al is a strong ferrite former. The ferritic grades do not gives good welding properties because of its inherent more carbon content, which made it brittle and relatively poor corrosion resistance. The major problems are due to large grain growth in the HAZ and it can be controlled to some extent by using minimum heat input. AISI 446 (FSS) contain 25% Cr, which is brittle. Sometime embrittlement in the weld zone is due to Cr-rich alpha prime particles, which result to inter granular corrosion. Hence, the joint has lower toughness value. Sigma phase forms in the range of 650 to 850°C, so to dissolve it need to heat treated above 900°C.

Filler metal used for welding should be of same composition or of an austenitic grade to help in improving impact strength. Excessive grain coarsening or grain growth in HAZ is a common problem and is difficult to overcome, so most of the ferritic stainless steel is welded in thin gauges. Preheat to 50^{o}C to 250^{o}C which anneals residual stresses. It is magnetic in nature and gives high ambient temperature strength. It is also subject to hydrogen embrittlement.

TIG and MIG are used to produce good welding joint. The plasma and electron beam welding is also used to weld ferritic stainless steel (FSS). Hydrogen is generally avoided in the shielding, because martensite is often formed during welding in the FZ and HAZ.

C. Martensitic Stainless Steel

Martensitic stainless steels (11-18% Cr with more than 1%C) were among the first stainless steels developed due to incapability to produce low carbon steel. AISI 403, 410, 414, 416 and 420etc are the common standard martenistic steel. These steels can be welded but caution needs to be taken during welding as they can produce a very hard and brittle zone in welding region. Modification of these steels involve the addition of V, Mo, Ni and tungsten, which leads the increment of carbon content, so the problem of cracking can’t avoided. Cracking is the common problem in the welding zone and it can be tackle/rectified with pre-heating and with post weld heat treatment.

These steels are generally welded with austenitic filler rods to increase the ductility of the weld joint. Preheating temperature for martenistic stainless steels is 200^{o}C-300^{o}C and post heat is 700^{o}C and slow cool to remove brittleness. These steel are generally magnetic and the metallurgical structure of these steels are martenistic.

D. Duplex Stainless Steel

Duplex stainless steels can achieve good weldability as compared to other types of stainless steel and has a narrow nickel range of about 4-7%. It contains both austenite and ferrite and having high mechanical strength. These are magnetic in nature. Generally TIG and SMAW processes can be used to weld duplex stainless steel. For the duplex grade of 2205 the standard filler is used of duplex 2209. The nickel content in duplex steel helps to maintain the ferrite/austenite structure (50/50) in the weld bead, thus maintaining strength, ductility and corrosion resistance.

During welding of this steel austenite is transformed into ferrite on heating. When the ferrite temperature increases then ferrite grain growth occurs. Sometimes Widmanstatten type structure has occurred during transformation from ferrite, which is poor in mechanical properties. The microstructure of the welding/fusion zone can be controlled by proper selection of filler metal, dilution, by the cooling of weld and base metal. Cooling rate is the primary factor in case of HAZ, which decide the percentage of ferrite and austenite in this zone. Processes like electron beam, laser beam welding and resistance welding have fast cooling rate as compared to other processes, so transformation of austenite from ferrite is retarded consequently.

Resistance to pitting corrosion is affected by the ferrite content in the weld metal, and resistance increases with an increase of ferrite content up to 50% of the ferrite content. If the ratio of $Cr_{eq}/Ni_{eq}=2.5$, then it give 50% ferrite content and the range of 40-50% gives good toughness value at lower temperature [Ref.: Welding Technology and Design, by Radhakrishnan]. TIG welding commonly used to weld duplex stainless steel, but it has low deposition rate. TIG welding also required large opening of root gap. Duplex stainless steels have lower thermal expansion as compare to austenitic steel.

E. Precipitation Hardening Stainless Steel

The latest in the development of special stainless steels are precipitation hardening steel (PH steel), which are combine good strength with high corrosion resistance. The key elements of this type of steel are Cu, Cb, Ti and Al. During aging they precipitate which render harder and stronger matrix. These steels are divided into three different categories depending upon their structural matrix. These are martensitic, semi austenitic and austenitic precipitation hardening steel.

In martensitic PH steel, if the variation of alloying elements varied then it can lead to excess delta ferrite. If large amount of stable austenite is present then it can be retained at room temperature after annealing. If carbon and nitrogen is increased then it may lead to contamination in the weld structure, which also deteriorates its mechanical properties.

The semi austenite PH steel are not subjected to cracking, because they are normally welded under annealed condition and they are precipitated hardened in 450-600ºC temperature range. Same composition of filler metal is used for groove and fillet joint.

The austenitic PH steel are generally non magnetic and it has austenitic structure. The hardness of this steel is also lower than other two types of PH steel.

1.5 Flux Activated TIG Welding

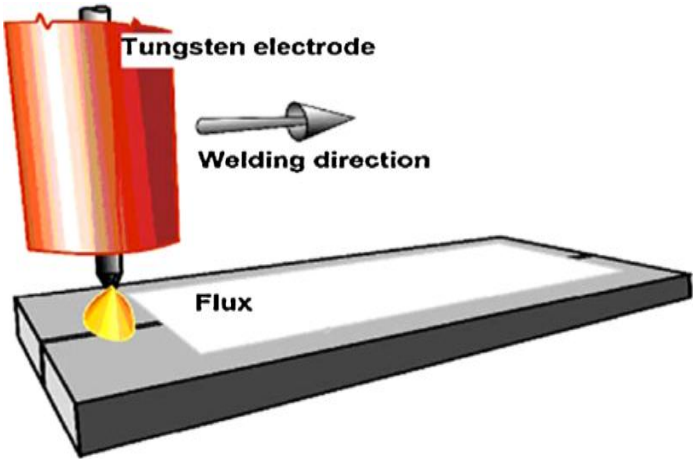

Figure 1.3: Schematic of A-TIG welding process [Dhandha and Badheka, 2015]

Flux activated TIG welding or A-TIG is same as ordinary TIG welding in operation except that the flux is used in the form of powders and applied on the surface of joint line. It is made into a paste by mixing with acetone or ethanol and this may applied by means of a brush, as shown in Fig. 1.3. A-TIG has been developed to overcome the limitation of TIG welding. It means to enhance the penetration performance of TIG welding. Significant increase in penetration (i.e. 300%) can be achieved in a single pass. In A-TIG process when flux or a single compound is applied on the job surface with the help of acetone then it dry in few seconds, due to evaporation of acetone and finally leaving a layer of flux on the surface. The A-TIG process is suitable for any position welding. In this process different types of inert gases or the mixture of gases in different proportion can be used. By using A-TIG process, overall welding costs can be reduced up to 50%. The factors to get the economics in overall costs can be achieved through:

- Less bevel angle requirements for thick jobs.
- Welding can be done in single pass so no need of multipass.
- Short of welding times as we can achieve significant penetration at higher speed.
- Reduced consumption of welding filler wire as there is no need of bevel edge preparation.
- Elimination of beveled edges and grinding.
- Produced minimum distortion at high heat input.

The main application of A-TIG is in industries to produce pipes and tubes for nuclear industry. Pressure vessels and heat exchangers are also fabricated for the chemical industries by A-TIG welding. Some shipbuilders are also using this technique of welding.

The key limitation of ordinary TIG welding of austenitic stainless steel like SS-304 is the minimum thickness of base metal which can be welded in a single pass, so to overcome this limitation and improvements in weld penetration have long been sought in the researchers mind. Hence, A-TIG welding can be the best solution for high quality welds.

1.5.1 AISI 4340 (High Tensile Low Alloy Carbon Steel)

Fusion and resistance welding methods are employed for AISI 4340 alloy steel. Preheat and post heat treatment is generally used while welding of this type of steel. AISI 4340 alloy steel are also known as low alloy steel containing chromium, nickel and molybdenum and it can be heat treated. High toughness and strength can be achieved in the heat treated condition. It produces cracks when it is not heat treated. Machining and grinding process can be performed either in the annealed or tempered conditions. Good ductility and formability is the main advantage of this type of steel in annealed condition. Cold working operation can also be employed in the annealed condition. AISI 4340 alloy steel can be annealed upto 844°C (1550 °F) followed by slow cooling. It has density = 7.85 g/cm^3, Melting Point-1427^{o}C, Tensile Strength -745 MPa and Yield strength-470 MPas. Poor bead appearance is a common problem in case of A-TIG. After some time rusting may appear on the weld surface which may deteriorate its mechanical properties.

1.5.2 Schaeffler Diagram

If the carbon content in the Cr-Ni steel is less than 0.12% then Schaefflar diagram can be helpful as a tool to determine the constituent of the main phases present in the weld zone like austenite with ferrite and austenite with martensite, but it does not tells the composition and the perfect volume of carbide phase. But if the carbon content is greater than above mentioned amount then it is impossible for it to determine the forecast of actual phases, due to the consumption of carbon by the process of carbide formation. The Fig. 1.4 represents the schaeffler diagram which shows the area of austenite, ferrite and martensite phase with relation to Ni equivalent on y-axis and Cr equivalent on x-axis.

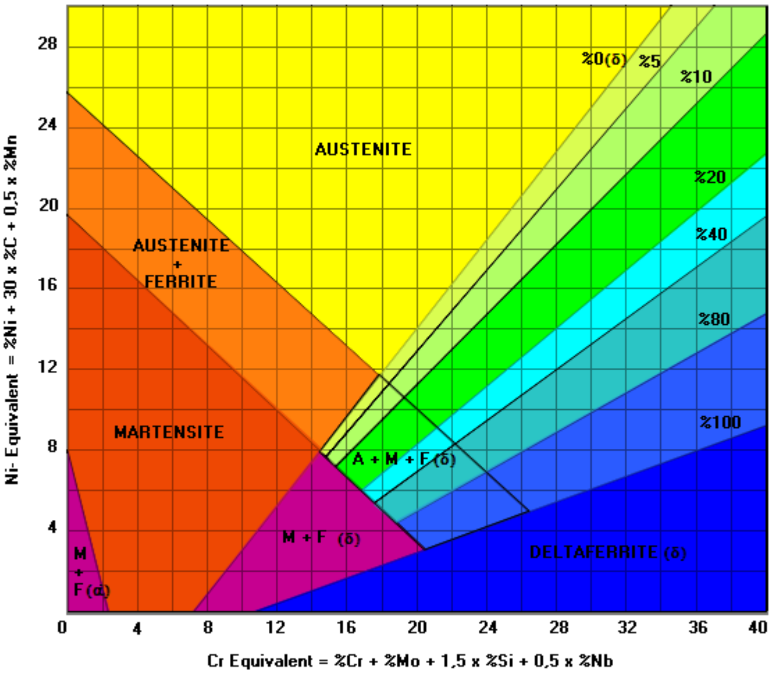

Figure 1.4: Schaeffler diagram [http://www.magmaweld.com]

Chapter - 2

Literature review

2.1 Introduction

Several research works have been carried out all over the world for predicting and enhancing the mechanical properties. Different kinds of steels and other metals had been welded by TIG and A-TIG process to find out the influence of different process parameters on mechanical properties and their microstructures. Weld penetration depth (weld morphology) and the factors responsible for this change have been reported by many researchers. Some of the researchers had carried out their study on the effect of different shielding gases and their mixtures on different types of steels. Brief reviews of literature on the studies related to A-TIG welding are presented here. The available literatures are categorized in the following broad categories:

- Influence of single compound activated flux on microstructure and mechanical properties.
- Effect of shielding gas on joint quality.
- Effect of process parameters and thermal stress analysis.

2.2 Literature review

2.2.1 Effect of Activated Flux on Microstructure and Mechanical Properties.

Modenesi et al. [2000] carried out a study on the use of A-TIG welding for the austenitic stainless steels with a single component flux. Specimens of size 125 mm×50 mm for the A-TIG welding were prepared of austenitic stainless steel (AISI 304) plates having thickness range of 5 to 8 mm. A-TIG welding was completed by constant movement of plate with the help of mechanized system under TIG welding torch. Weld geometry change were also compared to variations in the electrical signals from the arc and the arc shape. The influence of the flux on the micro structural changes was also analysed. Authors prove that, use of single component flux significantly increased the penetration of the weld bead. Use of fluxes, like SiO_2, TiO_2, Cr_2O_3 and AlF_3, significantly enhance penetration as compared with conventional TIG welding.

Ruckert et al. [2007] proposed optimization of the design of silica coating to increase productivity of TIG welding of 304L stainless steel. It was investigated by analysing coating geometry and thickness on weld penetrations. Two coating designs were investigated. One was a 20 mm wide coating on the weld zone and the second design investigated by two parallel coatings 1–7 mm apart around the weld line. The minimum thickness for continuous coatings was kept limited (50 µm) whereas for 2 mm apart coatings was extended from 70 to 200 µm. Tensile tests were executed to find the mechanical behaviour in different zones of the welded joint. The reduced tensile strength of the weld metal was recognised to silica particles. The welding was carried out on 6 mm thick sheet with 2.4 mm diameter of electrode at three level of current (100 A, 125 A and 150 A). Ar was used as shielding gas and an arc length of 2 mm was used. The minimum thickness in A-TIG was revealed to vary between 40 and 70 µm depending on the input current. The weld penetration firstly increased with coating up to 50–70 µm and subsequently decreased. This rapid fall in penetration was examined by higher energy consumption needed to break the flux coat. Authors found that the optimized coating thickness in A-TIG should in the range of 40 and 70 µm depending on the heat input and for FB-TIG welding it justified for large range of thickness coat.

Chern et al. [2010] carried out a study to find the influence of the single compound fluxes, in the TIG welding on surface appearance, weld morphology, distortion, mechanical properties, and microstructures on duplex stainless steel. In this study different powder based fluxes like TiO_2, MnO_2, SiO_2, MoO_3, and $Cr2O_3$, applied on the joint surface to perform A-TIG welding. Significant increase in weld penetration was found with SiO_2, MoO_3, and $Cr2O_3$ fluxes by the authors, as shown in Fig. 2.1. Hence, the A-TIG welding process increases weld bead penetration and the weld depth-to-width ratio, reduces the angular distortion and exhibited greater mechanical strength.

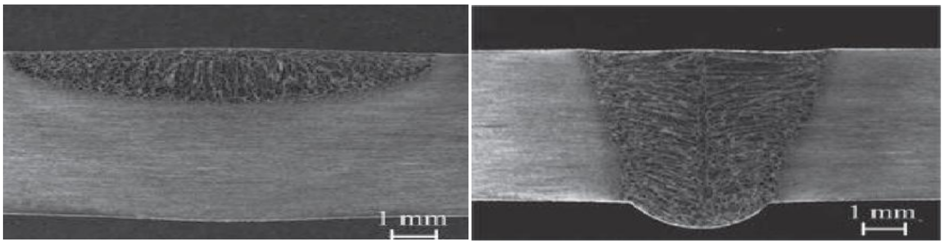

(a) No flux
(D:1.8mm; W:11.2mm; D/W:0.16)

(b) With TiO_2 flux
(D:4.8mm; W:6.9mm; D/W:0.69)

Figure 2.1: Effect of oxide flux on weld morphology [Chern et al., 2011]

Sakthivel et al. [2011] investigated the creep rupture strength of austenitic stainless steel (AISI 316) joints using single-pass A-TIG and multi-pass TIG (MP-TIG) welding process. Lean coating of a mixed component flux was applied on the weld line surface. Authors found that, weld zone in both type of welding joints possessed columnar and equiaxed dendrites with δ-ferrite at the border of fusion and HAZ. Their result revealed that, both the weld joints consisted lower creep rupture strength as compared to base metal, but A-TIG welding joint exhibited higher creep rupture strength than the MP-TIG joint. Reduced creep cavitations in the weld zone of A-TIG joint than the conventional MP-TIG joint were also observed.

Ruan et al. [2012] carried out a study by employing double wire metal inert gas welding (MIG) on 6082-T6 Al-alloy plate. SiO_2 activated flux was applied partially on the plate surface. Optical, scanning electron microscopy and energy dispersive spectroscopy were employed for microstrutural analysis. Mechanical properties were also investigated by using tensile and microhardness test. No significance difference was noticed in microhardness of the joints prepared with coated and uncoated surface. Wider heat affected zone (HAZ) with SiO_2 flux was observed as compared to without flux. The penetration with SiO_2 flux was found 26% deeper than without flux penetration. The tensile test result showed that SiO_2 flux could not produce significant impact on the tensile strength.

Lin & Wu [2012] had carried experimental studies to explore the influence of activated fluxes and process parameter to the weld penetration and depth-to-width ratio (DWR) of weld by the A-TIG welding process. The authors try two types of techniques which include A-TIG and face bound TIG (FB-TIG) as shown in Fig. 2.2. In the initial experiments they used single-component fluxes like SiO_2, NiO, MoO_3, Cr_2O_3, TiO_2, MnO_2, ZnO and MoS_2, based on the higher depth to width ratio of weld bead. Out of these fluxes four different fluxes were selected to make six new mixtures of 50% ratio of each for Inconel 718 alloy. For A-TIG weldment SiO_2 + MoO_3 (50% each) flux and with 75˚ tip angle of electrode was used for good welding results. The improvement of the DWR of Inconel 718 alloy welds from 60 to 75 degrees of electrode angle was 28%. They concluded that the weld bead geometry of Inconel alloy welds via FB-TIG with 1.2 mm gap are slender than that applying A-TIG process. Result revealed that, FB-TIG process produced full penetration in alloy in single pass weld for 6.35 mm thick job.

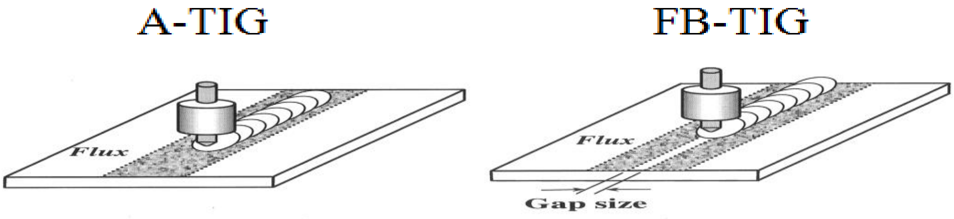

Figure 2.2: A-TIG and FB-TIG [Lin and Wu., 2012]

Arunkumar et al. [2012] carried out investigation using specific activated flux to increase the penetration in single pass by A-TIG welding. Joint with A-TIG welding was performed with single pass welding, while the multipass welding run was made with conventional TIG welding using 9Cr-1Mo filler wire. Authors concluded that the constriction behaviour of A-TIG welding helps to achieve higher depth of penetration. Higher strength of the joint was achieved by A-TIG welding as compared to multipass conventional TIG welding, but the multipass TIG welding possessed higher toughness than the A-TIG weld joint after post weld heat treatment (PWHT). They also concluded that, no degradation in the microstructure and mechanical properties of A-TIG welding joint as compared to joint produced by conventional TIG welding process.

Vasudevan and Vasantharaja [2012] studied the influence of flux activated TIG welding of low activated ferritic/martenistic (LAFM) steel. Using optimum flux combination, they perform A-TIG welding on square butt joint configuration. They did welding on both sides of the joint. The mechanical properties of the A_TIG welding joint was compared with the joint of electron beam welding joint. Authors found different types of martensite in the FZ and HAZ. Coarse and harder martensite (420–430 VHN) was found in the weld and HAZ, while PWHT condition possessed tempered martensite (256 VHN). Failure occurred always at the base metal, which exhibited the good tensile strength of A-TIG weld joint. It was also reported that, the mechanical properties of A-TIG welded joint were less as compared to elecdton beam welded joint and the base metal but can be improved by PWHT process.

Sambherao [2013] investigated the use of activated flux for increasing penetration depth with GTAW process in austenitic stainless steel. The effect of multi component fluxes of specific oxides on the surface appearance, weld morphology and retained delta-ferrite content with TIG process on 6mm thick AISI 316 steel was investigated. It was found that TiO_2 flux has significant effect on the depth of penetration for this steel. Author reported that marangoni convection and constriction of arc are the main factors behind this. With the addition of Fe_2O_3 with TiO_2 flux, the marangoni convection effect was found and it leads to increase in weld depth than that of with TiO_2 flux only.

Morisada et al. [2014] adopted a new technique using atmospheric oxygen in active flux tungsten inert gas welding (A-TIG) at varied gas flow rate to enhance the depth of penetration of 10 mm thick AISI 304 stainless steel plates having less sulphur content (20 ppm). The welding current, the welding speed, and the arc length were maintained at 180 A, 2 mm/s, and 3 mm, respectively. Argon with varying gas flow rate between 1 L/min and 20

L/min was used in the study. A special type of nozzle cap was also designed for drawing atmospheric oxygen. Result showed that the penetration depth was influenced by atmospheric oxygen and Marangoni convection also plays a significant role to achieve maximum penetration. Using helium as shielding gas with this technique produced three times penetration as compared to conventional TIG welding. Hence it was concluded that, the atmospheric oxygen by using special type cap does not deteriorate the joint strength of AISI 304 stainless steel.

Arivazhagan &Vasudevan [2015] studied A-TIG welding of 12 mm thick2.25Cr-1Mo (P22) steel with in-house developed activated fluxes. Effect of post weld heat treatment (PWHT) on the impact toughness was also studied by the researcher. Double layers were used to complete the joint at 250 A current. No crack was detected in the weld. There was no pro-eutectoid ferrite in the weld metal and the toughness was found of 133 J. After PWHT at 730 ◦C for 1 h, the toughness increased to 177 J. It was observed that A-TIG weld joint exhibited high hardness and good toughness, hence no requirement of post weld heat treatment.

Dhandha & Badheka [2015] explore the effect of activating fluxes on weld bead morphology of P91 steel (modified 9Cr–1Mo or P91 steel) using CaO, Fe_2O_3, TiO_2, ZnO, MnO_2 and CrO_3 fluxes. The author used Ar as shielding gas and the experiment was done on 6 mm thick plate at 200 A with a travel speed of 100 mm/min. The author concluded that the activating flux has a substantial effect on the penetration depth and the decreased bead width is major impact of the activated fluxes Fe_2O_3, ZnO, MnO2 and CrO_3 and these were also suitable to weld modified 9Cr–1Mo steel. They also reported that Marangoni effect, arc contriction, electromagnetic force and buoyancy force played a major role in increasing depth of penetration.

Shen et al. [2015] investigated the influence of nano-particles strengthening activating flux on the microstructural changes and mechanical properties of TIG welded joints of AZ31 magnesium alloy. The authors used mixed TiO_2 and nano-SiC particles (60:40) coated on the samples before welding tests. For each welding condition, at least five specimens were made. Two of these were used for metallographic examination and other three were tensile shear test specimens. It was found that the increased surface coating density of the flux damaged the macro-appearance of welding seam and increased the weld width and penetration due to the application of the TiO_2. Author reported that part of SiC particles decreased the precipitation of the β-$Mg_{17}Al_{12}$ and reacted with AZ31 magnesium alloy to produced Al_4C_3

and Mg_2Si phases. Micro hardness in HAZ decreased due to the coarsened α-Mg grains as flux have high surface coating density. Author also reported that the UTS of NSA-TIG welding joints increased firstly because of the refinement of α-Mg grains and distribution strengthening effects of particles including β-$Mg_{17}Al_{12}$, Mg_2Si and SiC, but then decreased rapidly due to the significant agglomerations of the nano-SiC particles.

2.2.2 Effect of Shielding Gas on Joint Quality

Tusek and Suban [2000] investigated the impact of hydrogen blended argon shielding gas in TIG and MIG welding of high-alloy stainless steel. This study was carried out with different volume percent additions of hydrogen to the argon i.e., 0.5, 1.0, 5.0, 10 and 20%. Five welds were produced with three levels of currents i.e. 150 A, 200 A and 250 A in different Ar and H_2 mixture. TIG welding was performed on 8 mm thick job and while MIG welding was performed on 10 mm thick workpiece. The addition of hydrogen in argon gas and their impact on welding parameters, depth of penetration, welding efficiency was also explored. Addition of hydrogen to argon increased melting of job by 10-30%. It was also proved that, the mixture of Ar + H_2 found a stable process and produce quality weld in case of TIG welding of high alloy austenitic stainless steel. Finally author recommend the 20% addition of hydrogen in argon but the same is not true case of MIG welding.

Durgutlu [2003] investigated the effect of hydrogen mixed argon as a shielding gas on TIG welding joint of AISI-316 stainless steel. The microstructure, depth of melted metal and its mechanical properties were examined by the author. The author used three different volume percentage of shielding gas for his experimental study i.e. pure argon, Ar+1.5% H_2 and Ar +5% H_2. Higher depth of melted metal and the bead width was achieved with maximum percentage of hydrogen content, but the highest tensile strength of the AISI 316 TIG was achieved with shielding gas of Ar+1.5% H_2. The main impact of higher content of hydrogen was found on the mean grain size of the weld metal and consequently increased with higher hydrogen content. After bend test, no surface cracks or tearing were found on the samples that were welded with three variant of gas mixtures. The result revealed low hardness of weld metal as compared to HAZ and base metal hardness. The author also reported that, the more hydrogen content present in the shielding gas affect the mean size and orientation of the weld metal which result into deviations of the grains.

Gulenc et al. [2005] studied the effect of hydrogen mixed argon as shielding gas in metal inert gas welding of 10 mm thick AISI 304L stainless steel. Authors used 1.2 mm diameter of filler wire for the MIG welding of austenitic stainless steel. Authors investigated the mechanical and micro structural changes of the welded samples. MIG welding was carried out with different mixtures of shielding environment which include pure argon, Ar+1.5% H_2 and Ar+5% H_2 at three level of current, 140, 180 and 240 A. Maximum tensile strength was found in case of the samples which were welded with the shielding of Ar+1.5% H_2 and with maximum current i.e. 240 A. Result revealed that the impact strength of the welding increases with Ar+5% shielding mixture (high H_2 content) and higher heat input. The base metal hardness was found greater than the hardness of HAZ and weld metal. The bending test and microscopic investigations was also done to characterise it. Authors also concluded that the toughness of welded joint is influenced with more hydrogen content, which produced large grains size and constitute a low hardness of the weld metal and HAZ as compare with the base metal hardness. They also reported that the specimen which were welded with pure Ar contribute less tensile strength as compare to the mixture of hydrogen and argon, as the maximum tensile strength given by the specimens which were welded with Ar+1.5% H_2.

Michler. [2007] studied the toughness and hydrogen compatibility of austenitic stainless steel weld at cryogenic temperature. The author used different types of austenitic steel with a suitable combination of filler wires for the multipass TIG welding of 12 mm thick steels. Toughness test (Charpy) were performed for each specimen and compared with -196°C and no significant difference was found. All the toughness value was greater than the standard values of toughness at -10 °C. To find the presence of martensite in the weld zone, samples were cut from all weld specimens and kept at -269°C. Cooling at such a low temperature and presence of δ-ferrite could not produce more martensite. No correlation was found between δ-ferrite and toughness.

Lu et al. [2007] had investigated the effect of reverse of Marangoni convection on the weld bead profile. The stationary TIG welding experiments were made on SUS 304 stainless steel having lower oxygen content 0.0038 w% and sulphur content 0.0005 w% by using direct current. Two variant of mixture of shielding gases including O_2 and Ar gas, Ar+0.1%O_2 and Ar+0.3%O_2 were applied in TIG welding. After completion of TIG welding, oxygen/nitrogen analyzer was used to find out the percentage of oxygen present in the weld metal. Authors found that, due to high percentage of oxygen content in the weld metal corresponding to the Ar+0.3%O and the surface active elements changes the surface tension gradient from negative to positive, which consequently changes the flow of molten metal from outward to inward, called reverse Marangoni convection. Hence, it helps to increase the weld penetration. The authors proved that the strength of the Marangoni convection determines the shape and strength of the joint and the factors such as the percentage of oxygen content also influence the bead morphology which can change the profile of penetration dramatically. Naumann and Michler [2009] carried out a study for hydrogen embrittlement of orbital TIG welding joint of 6 mm diameter and 0.85 mm thick tubes of different austenitic stainless steel (AISI 304, 316l, 316Ti, 316l mod.). The 5% δ-ferrite (app.) content was found in all TIG welded joint. Tensile test of AISI 304 welded joint was done under hydrogen atmosphere and others were performed under helium atmosphere. The specimens of hydrogen atmosphere were fractured in the base metal and the specimens of helium study were fractured from fusion/HAZ. They concluded that the δ-ferrite content did not influence to hydrogen embrittlement environment as compared to base metal.

Lu et al. [2010] investigated the weld morphology and the effect of oxygen on electrode under two shielding gases. Ar and Ar+CO_2 double shielded TIG welding of SUS 304 stainless steel was performed with a special torch to impinge two shielding gases on the weld pool. They studied weld shape and electrode morphology, oxygen absorption and marangoni convection, and the effect of double shielding on weld bead profile. They concluded that the flow rate of inner shielding gas had great impact on the weld shape and consequently produced oxidised and wide weld bead with less penetration. The outer layer shielding environment which has an active gas (CO_2) dissolved well in the molten metal and tends the outward flow of molten metal to inward direction. Hence the authors also prove that Marangoni convection occurs when weld metal oxygen content reached above 70×10^{-6}.

Lu et al. [2012] carried out a comparative study for conventional TIG welding using pure He as shielding with double-shielded TIG welding including 20% oxygen to improve weld penetration and its morphology by varying process parameters (i.e., speed, arc length and current) on a martensitic stainless steel having less than 5% Ni content. They found that the oxygen mixed helium gas produced narrow and deeper weld bead as compared to single shielded gas. Weld pool shape was also influence by the arc length. Results showed that deep penetration was achieved with minimum gap of 1.5 mm and vice versa. Authors also reported that the effect of arc length was significant in case of double shielding method as compare to pure helium or single shielding method. The increasing trend of depth to width curve was found pure helium gas while it was not true for the double shielding environment. They also found that the oxygen content present in the weld metal produce a great impact on Marangoni convection. The high oxygen content enhance inward flow but thick oxide layer on the weld pool crate reverse effect and deteriorate mechanical properties.

Niagaj [2011] carried out experimental investigation to study the effect of A-TIG welding on deformation of austenitic steel components. It was investigated that with the use of TIG and ATIG welding there is reduction in angular distortion in austenitic stainless steel with activated flux BC-31. It was found that welding pipe connectors with austenitic steel plates gives four times less distortion as compared to traditional TIG welding process.

Zou et al. [2014] investigated the effect of oxygen content, used in the outer layer of shielding with Ar as inner shielding gas on the weld shape with the AA-TIG (advance activated TIG) welding of duplex stainless steel. Thus effect of the oxygen content on the weld shape and crystallographic orientation relationship between two kind of austenitic phase and ferrite phase was investigated. It was found that the increased oxygen content helps to increase both the depth to width ratio and the density of oxide film. They found that the crystallographic orientation of the widmanstatten austenite phase and ferrite phase followed the K-S relationship. Oxide layer present on weld pool plays an important role in affecting the crystallographic orientation relationship between the intra granular phase and ferrite phase.

Vasudevan et al. [2014] carried out a study of welding processes on the residual stress and distortion in SS 316LN made by TIG and A-TIG welding processes which involved different joint configurations. Less current (135 A and 140 A) was used for conventional TIG welding and more current (250 A and 285 A) were used on 16 mm thick plate. Author concluded that different joint design exhibited different microstructures, peak tensile residual stress and angular distortion values. Double side joint of A-TIG welding creates coarser grain with lower ferrite content, and low tensile residual stress whereas double side joint of TIG weld produce small grain with higher ferrite content, and helps to form higher tensile residual stress values. The significant difference between these values, was due to lower (straight edge) and higher (v-groove) weld metal volume. Both A-TIG and TIG weld joints displayed lower angular distortion values while Y grooved joint displayed maximum angular distortion values due to non-uniform distribution of residual stresses. The author recommended A-TIG welding process to minimize residual stress and distortion in the weld joint.

2.2.3 Effect of Process Parameters and Thermal Stress Analysis

Diaz et al. [2010] investigated the comparative study in which thermal stress distribution or distortion with its magnitude in the tungsten inert gas (TIG) welding process of austenitic and duplex stainless steel specimens is compared by FEM. The finite element method which includes two techniques (birth and death) to analyze the vertical displacement evolution was used by the authors. Besides FEM, angular deformation and bending of specimen along length was also performed. Thermo graphic image was used, which helped to compare the results followed by numerical simulation at selected locations. It was concluded by the authors that the optimum value for the calculations for this parameter was about 75% of the fusion temperature, paricularly 1173 K (for duplex steel) and 1073 K (for austenitic steel). The overall deformation or distortion was found opposite for both types of steel. It was also concluded that the agreement was found good for both experimental as well as in numerical method.

Xiong et al. [2012] carried out a study to find the effect of effect of welding parameters on temperature distribution in case of twin-electrode (separated and insulated) coupled TIG welding arc. In his study the author used a special torch for his experiment as shown in Fig 2.3. The electrodes are separated from each other and tuned from 0.5 mm to 6 mm. The author used 3.2 mm diameter tungsten electrode with argon shielding. In experimental study, coupling arc images were captured by high speed camera and obtained using an imaging system. The arc temperatures were measured and the maximum temperature was found in the middle of both electrodes. Authors concluded that the arc length effect the peak temperature and found increased when the length decreased. When the distance increased then the temperature also decreased in the centre of the arc but temperature distribution at the anode area also spread, consequently decreased at the anode due to reduction of current and thermal density by large area of contact with an arc.

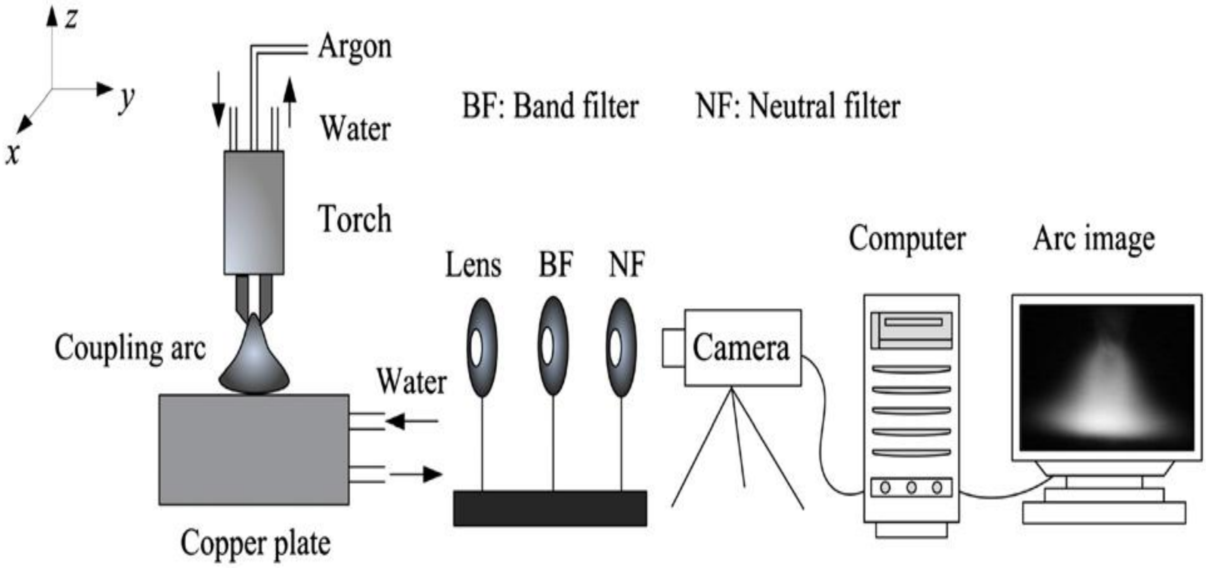

Figure 2.3: Schematic diagram of the experimental setup [Xiong et al., 2012]

2.3 Summary of Literature

The literature review presented in section 2.2 revealed that the flux used in the A-TIG process causes an inward flow of molten metal (Marangoni effect) along with electromagnetic forces, gravitational forces or bouncy forces, Lorentz force or drag forces caused by the passage of shielding gas over the weld pool and more constricted arc hence deeper penetration [Modenesi et al., 2000; Arunkumar et al., 2012; Dhandha & Badheka,2015]. Some author also presented another technique i.e. face bound technique to enhance the penetration depth and compared with single coating technique (single and mixed flux) and they found that the achieved penetration was slender than A-TIG welding [Lin & Wu., 2012; Ruckert et al., 2007]. Some studies also focussed on the optimum quantity of flux for the face bound technique to achieve maximum penetration depth in case of austenitic stainless steel [Ruckert et al., 2007; Shen et al., 2015]. Different types of fluxes was used in case of A-TIG welding to find out their effects on weld morphology, angular distortion, mechanical properties, microstructures and surface appearance of different types of steel and found that A-TIG process helps to increase depth of penetration and the weld depth-to-width ratio, and tends to reduce the angular distortion with greater mechanical strength [Chern et al., 2011; Sambherao, 2013; Dhandha and Badheka, 2015]. Some of the authors also developed activated fluxes to enhance the depth of penetration for different types of steels to improve the penetration depth without deteriorating the mechanical properties [Arunkumar et al., 2012; Vasudevan and Vasantharaja, 2012; Arivazhagan &Vasudevan, 2015]. Argon is widely available inert gas for TIG welding of stainless steels and nickel alloys. It produces a stable welding arc and is suitable for all grades of stainless steel. But as the thickness of the material increases, fusion and porosity problems can arise. To overcome these problems argon and hydrogen mixture is the preferred gas mixture for manual TIG welding of austenitic grades of stainless steels. Some authors intentionally studied the effect of H_2 in Ar as shielding gas in MIG and TIG welding processes of different steel and found that the toughness value increases with the increase of H_2 content in Ar but the tensile strength increases up to a maximum of 1.5% addition of H_2 in Ar [Gulenc et al., 2005]. Some of the authors also investigated the same study in both MIG & TIG welding processes and they reported an increased melting rate with an increase in current. Finally authors also suggested that hydrogen may be used up to 20% in case of conventional TIG welding of 8 mm thick plate [Tusek & Suban, 2000]. One of the authors suggests 1.5% H_2 +Ar mixture to get maximum tensile strength in case of SS 316 steel [Durgutlu, 2003]. Some of the authors also focus their study on the use of O_2 with Ar to investigate the role of reverse Marangoni convection on the weld morphology. They found that when dissolved oxygen content the in weld metal is over a critical value i.e. 0.01 w%, corresponding to the mixture of Ar+0.3% O_2 used as shielding gas, the Marangoni convection changes produce the reverse effect. Hence, the liquid metal flow from outward to inward direction and the weld shape considerably changes from wide shallow shape to narrow and deep shape. Few of the authors also investigated electrode oxidation behaviour Ar-(Ar-CO_2) double shielded TIG welding. They concluded that double shielded TIG welding using the pure inert Ar gas (for inner shielding) and the active CO_2 or Ar+CO_2 gas as the for outer layer shielding can protect well the tungsten electrode from oxidation and consequently enhance the penetration [Lu et al., 2010].

2.4 Scope and Objectives of the Present Work

Majority of stainless steel are iron based alloys containing more than 10% chromium and >5% nickel which provides the corrosion resistant properties for which stainless steel are widely used in industries. Many researchers tried various types and grade of stainless steels for their study on various types of welding. TIG welding is one of the fusion welding processes to achieve the good quality welding for stainless steel. Inconsistent weld penetration has been observed while welding of austenitic stainless steels by TIG or multiple pass TIG welds. Some of the researcher used various inert gases to achieve more penetration. However to over the limitation of penetration depth and to achieve productivity with good mechanical properties in a single run researcher used various types of compound as a flux. Thus there is ample scope to find the effect of different fluxes, shielding gases and process parameters that can affect the mechanical properties and metallurgical properties of austenitic stainless steel. Based on above mentioned scope the following objectives are identified for the present work.

- To study the influence of various types of activated fluxes on the weld morphology of different types of steels like AISI 304, AISI 316, Duplex 2205, AISI 4340 and AISI 1020.
- To investigate the effect of current and shielding gases (Ar, Ar+He, Ar+5% H_2) in single compound A-TIG welding with TiO_2 flux on different graded steels.
- To investigate the constriction of arc under A-TIG welding process and its impact on the welding.
- Study the influence of activated flux and parameters on weld fusion zone and HAZ microhardness variation.
- Metallurgical studies of fusion zone and HAZ by optical micrograph and SEM observation.
- To study the effect of flux composition, shielding gas and current on weld bead morphology for AISI 304, AISI 316, Duplex 2205 and AISI 4340. The change in arc column behavior is also studied.
- Investigate the effect of welding current, types of fluxes, shielding gas, flow rate, vertex angle and torch angle on weld joint bending strength, toughness and microhardness during A-TIG at different welding speed.

Chapter 3

Influence of Activated Flux and Shielding Gases on Welding Bead

3.1 Introduction

In the present work first it is decided to find the effect of fine grained single flux (TiO_2) on the penetration behavior for different graded steels like low carbon steel, austenitic stainless steels and duplex stainless steel to compare the influence of activated flux. Further, the effect of shielding gas composition (Ar and Ar + 5% H2) and current on depth of penetration in TIG and ATIG is studied experimentally and compared. Variations in depth of penetration, width-to-penetration (WP) ratio, and microhardness are also studied for AISI 1020, AISI 304, AISI 316 and Duplex 2205 steels using WTh-2 (2% thoriated tungsten electrode). Arc behavior during TIG and ATIG welding of four different materials at different current settings are also observed to study the process behavior. Metallurgical studies are carried out to understand the solidification behavior and its significance on the weld fusion and heat affected zone.

3.2 Materials and Methods

3.2.1 Chemical Composition of Workpiece

Atomic absorption spectrometry (AAS) is a technique to measure the concentrations of elements present in an alloy. The workpiece materials used in the present work, low carbon steel (AISI 1020), austenitic stainless steel (AISI 304, AISI 316) and duplex stainless steel (Duplex 2205) plates are cut to sizes 100 mm×50 mm×5 mm for TIG and A-TIG welding. The compositions of four different steel workpieces are obtained by atomic absorption spectrometer (Spectroscopy Foundry Master, Make: IS, Germany, shown in Fig. 3.1) and their compositions are given in Table 3.1.

Figure 3.1: Atomic absorption spectrometer

Table 3.1- Compositions of different workpieces/ materials

Material	% Composition										
	C	Mn	Si	Cr	Ni	S	P	Mo	Cu	N	Fe
AISI 1020	0.18	0.66	-	-	-	0.05	0.035	-	-	-	Balance
AISI 304	0.05	0.978	0.33	20.2	8.26	0.008	0.049	0.169	0.382	-	Balance
AISI 316	0.072	1.781	0.582	17.4	11.729	0.021	0.041	1.214	-	-	Balance
Duplex 2205	0.1	1.46	0.327	23.1	4.92	0.005	0.020	3.26	0.198	0.16	Balance
AISI 4340	0.35	1.55	0.918	0.199	0.277	0.150	0.182	0.500	0.152	-	Balance

3.2.2 Cleaning of Workpieces and Flux Coating

Before A-TIG welding the workpieces are cleaned with acetone to remove surface contaminants. For flux coated ATIG, the fine grained TiO_2 compound is mixed in appropriate proportion with acetone to make a suitable paste and is applied on the plate top surface with the help of brush for about 12 mm width and thickness could vary between 20–25 μm. Flux coating is allowed to completely dry and it is ensured that acetone completely evaporates. Fig. 3.2 shows the method mixing and pasting of flux on workpiece.

Figure 3.2: Activated flux applied with a paintbrush

Figure 3.3 shows sample representation of flux coat after evaporation of acetone and are used for A-TIG welding.

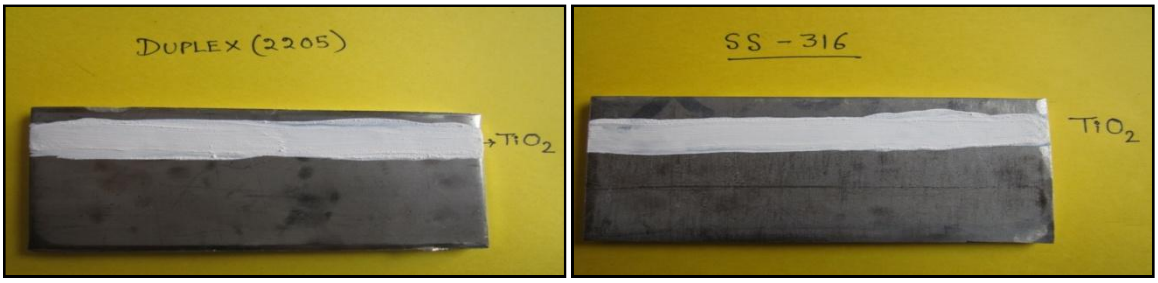

(a) (b)

Figure 3.3: (a) Duplex 2205 with TiO_2 flux coating, (b) AISI 316 plate with TiO_2 flux coating

3.2.3 Welding Setup

TIG as well as A-TIG welding are performed on tungsten inert gas welding machine (Make: TECHNOWELD MDX – 300, INDIA) available at Central Workshop and shown in the Fig. 3.4. DC power source is used with static volt-ampere (V-I) characteristics of the drooping type, that is, of the constant current type.

Figure 3.4: TIG Welding Set-up

The basic equipments of TIG welding consist of:

- Welding torch
- Shielding gas supply
- Electrode
- Power supply

Process parameters selected for the study are

- Current (2 level) – 140 A and 170 A
- Gas used: Ar and Ar+5%H_2
- Gas flow rate-10 L/m
- Material - AISI 1020, AISI 304, AISI 316 and Duplex 2205 steels,
- Electrode thoriated Tungsten (EWTh-2) diameter (*d*) 3.2 mm,
- Vertex angle of electrode = 60°
- Conical length of electrode tip: 3.8 mm, welding speed 3.3 mm/s.

3.2.4 A-TIG welding Technique

Welding are completed for creating beads on plates at different process parameters and shielding gas compositions. All welding are carried out maintaining tip angle of 40° from the vertical. Schematic arrangement of the welding setup and sample representation of flux coat and welding process are shown in Fig. 3.6. Welding are carried out at 140 A and 170 A current with and without using activated flux to compare the influence of current and flux on depth of penetration. Two different shielding gases *i.e.*, pure Ar and Ar+5% H_2 are used as shielding gas. Figure 3.5 shows the set up before welding and in this setup Cu-plates are used for easy arc initiation.

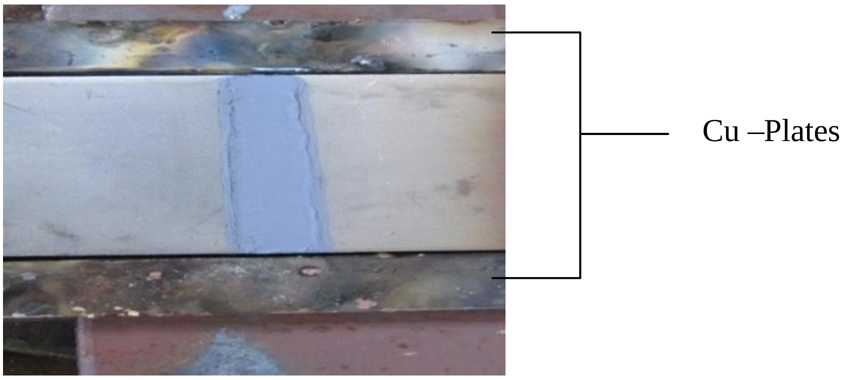

Figure 3.5: Set up before A-TIG welding

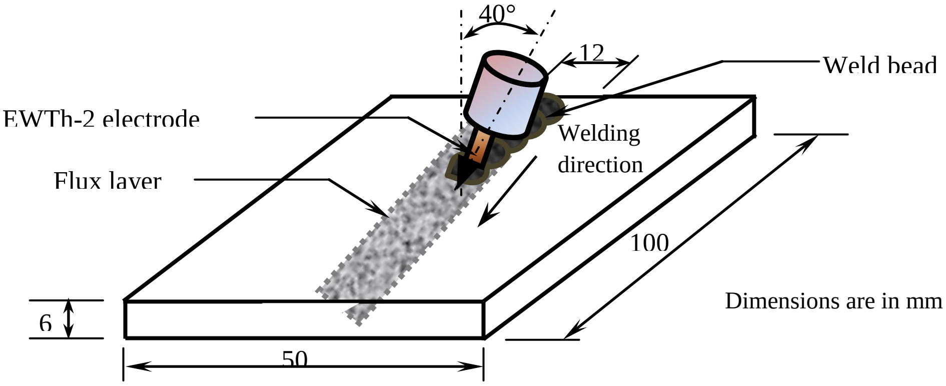

(a) Schematic arrangement of ATIG

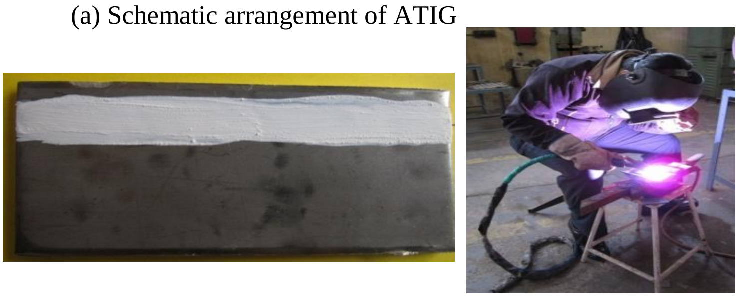

(b) Duplex 2205 plate with flux coating and welding operation

Figure3.6: (a) Schematic illustration of ATIG welding arrangement (b) welding operation

3.2.5 Metallurgical Preparation

After completion of welding beads, the samples are cut, ground and polished following the standard metallurgical sample preparation technique. The welded samples are cut from approximate centre of the workpiece for metallurgical examination and to check weld morphology and then surface grinding is carried out on the precision surface grinder as sown in Fig.3.7 to make the surface flat & smooth. Afterward the workpieces are polished on polishing machine, as shown in Fig. 3.8 by using the various numbers of emery papers. Polished samples are etched and then the depth and width of penetration are measured using a measuring microscope (make: Carl Zeiss, model: AxioScope A1) having 0.001 mm of measuring accuracy. In the present study two types of etchant, Carpenter SS etchant ($FeCl_3$ + $CuCl_3$ + Ethanol + HCl + HNO_3) for AISI 304, AISI 316 and Duplex 2205 etched with Killing's No. 2 etchant ($CuCl_2$ + HCl + Ethanol) are used after polishing of workpieces.

Figure 3.7: Precision surface grinder

Figure 3.8: Polishing machine for metallurgical sample preparation

3.3 Effect of TiO_2 Activated Flux on Depth of Penetration

Figure 3.9 shows the comparison of measured depth of penetration with and without TiO_2 flux for different steels at 140 A and 170 A current and with Ar as shielding gas. It can be seen that the depth of penetration increases for all the materials in ATIG when flux is used. The maximum increase of more than 100% in penetration is measured for Duplex 2205 steel at 140 A current when flux is used as compared to welding without using flux. Much higher increase in penetration is observed at 170 A, when flux is used (Figure 3.9 (b)).

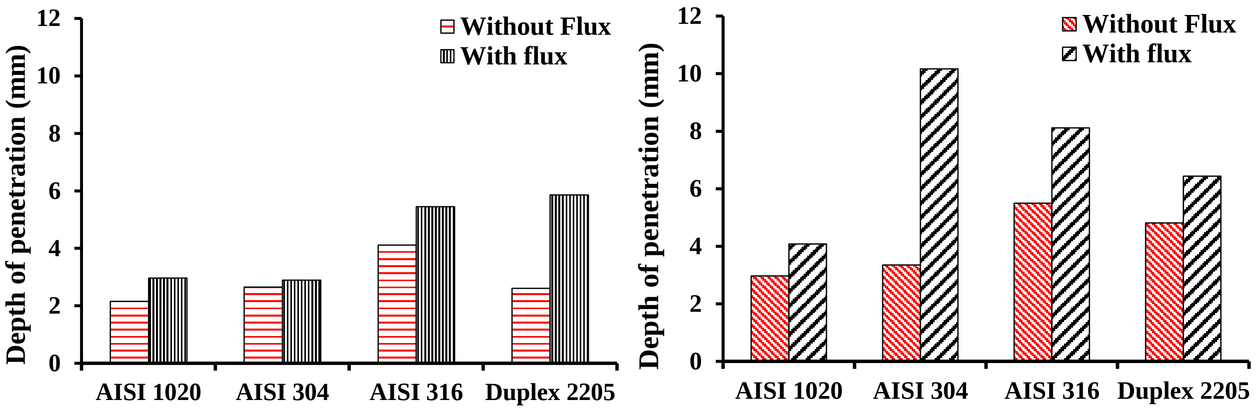

(a) At 140 A current (b) At 170 A current

Figure 3.9: Comparison between depth of penetration with and without use of flux for different steels using Ar as shielding gas with flow rate of 10 L/min.

The depth of penetration increases when TiO_2 flux is used and such narrowing behaviour of arc column increase the energy density within the arc column region and hence, increase the penetration depth as well as decrease the width of the weld bead. In ATIG process, arc constriction results in reduction in anode root area and constriction of plasma column diameter. This effect increases the anode current density and the arc force acting on the welding pool. Moreover, this also results in more temperature rise due to focused arc and heat flux increases the penetration. Towards the central region of arc, temperature of plasma column is much higher and electron attachment occurs near the peripheral region of the arc column with lower temperature. Oxygen ions of TiO_2 flux interacts with arc electrons and redistributes charger carriers that cause constriction of plasma column by capturing electrons. This phenomenon increases energy density, arc temperature and in turn, the electromagnetic Lorentz force promotes a downward flow in the liquid metal and higher depth of penetration. Also, oxygen acts as surface active-element for the stainless steel Workpieces and determines the temperature coefficient of surface tension of weld metal pool surface.

Macrographs showing the depth of penetration for AISI 304 and Duplex 2205 stainless steel at different condition with and without TiO2 flux coating are shown in Fig. 3.10.

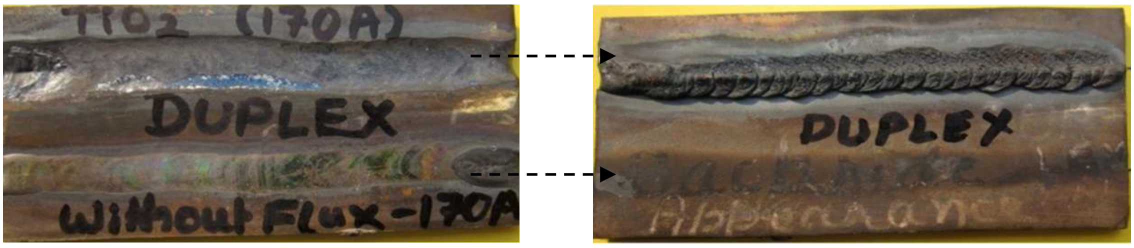

DUPLEX 2205,170 A, Ar (Top View) DUPLEX 2205,170 A, Ar (Back Side)

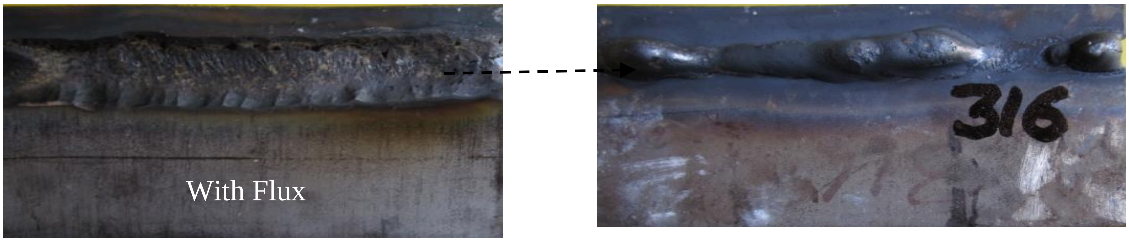

AISI 316,170 A, Ar+5 % H_2 (Top View) AISI 316,170 A, Ar+5 % H_2 (Back Side)

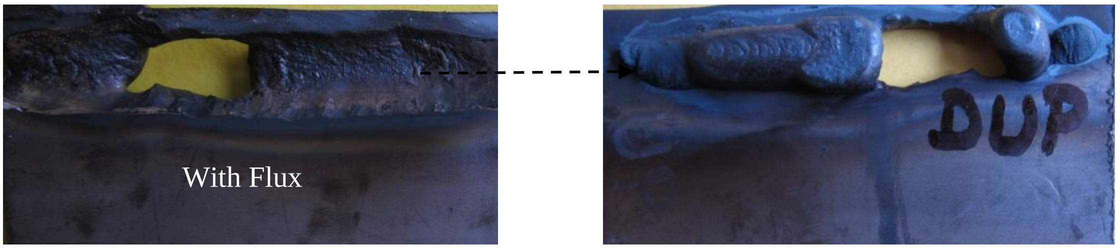

DUPLEX2205,170 A, Ar+5 %H_2 (Top View) DUPLEX 2205,170 A, Ar+5 %H_2 (Back Side)

Figure 3.10: Macrographs showing the bead appearance for AISI 304 and Duplex 2205 stainless steel at different condition with and without TiO2 flux coating.

Due to the presence of oxygen, the surface tension induced Marangoni convection (*i.e.*, heat flow) changes from outward (centrifugal) to inward (centripetal) direction and increases the penetration depth. Negative or positive slope of surface tension curve with temperature ($d\sigma/dT$ where σ = surface tension, T = temperature) decides the outward or inward direction of Marangoni convection respectively and values of slopes determine the strength of the Marangoni convection. It may be noted that the direction and magnitude of the Marangoni convection principally decides the depth of penetration. The surface tension induced shear stress, expressed as the product of temperature coefficient of surface tension (slope $d\sigma/dT$) and temperature gradient on the pool surface.

3.3.1 Effect of Current on Depth of Penetration

Figure 3.11 (a) and (b)) show the influence of welding current on depth of penetration during TIG and ATIG, respectively. It can be well observed that the influence of current on penetration becomes more significant for all kinds of steel and substantial increase in penetration is achieved for AISI 316 and Duplex 2205 material when flux is used. Although, the exact reaction and behaviour of liquid metal pool under the flux activated welding is not well known, the inward fluid flow and constriction of arc are the two prime reasons for the increase in depth of penetration in ATIG process**.**

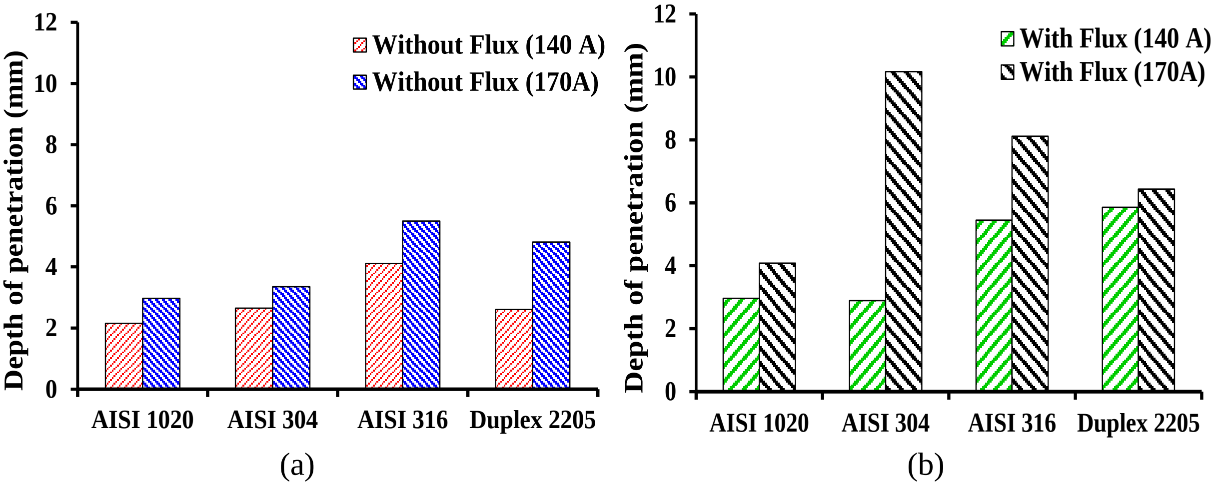

Figure 3.11: Influence of welding current on depth of penetration during TIG and A-TIG with flux and without flux.

It is clear that when we current icreases then heat input also increases which result into deep penetration. However, welding bead are performed on AISI -1020 steel (mild steel) at 140 A and 170 A with TiO_2 or without flux coating. No significant difference is found in the inrease of depth of penetration but a small increse in the depth of penetration is found, due to the increase in welding current. After that welding beads are performed on three different types of steel (AISI-304,AISI-316 and Duplex-2205) at 140 A current with or without flux/compound, which is shown in fig. 3.12.

Workpiece	No flux	With TiO_2 flux
AISI 304		
AISI316		
Duplex		

Figure 3.12: Macrographs showing the bead appearance for AISI 304 , AISI 316 and Duplex 2205 stainless steel at 140 A with and without flux using Ar shielding with flow rate of 10 L/min.

After this welding beads are perfomed at 170 A current on these three different steels while keep in mind that the workpiece should be cool before welding. These welding beads are also performed with or without flux, under Ar shielding which is shown in fig. 3.13.

Workpiece	No flux	With TiO_2 flux
AISI 304		
AISI316	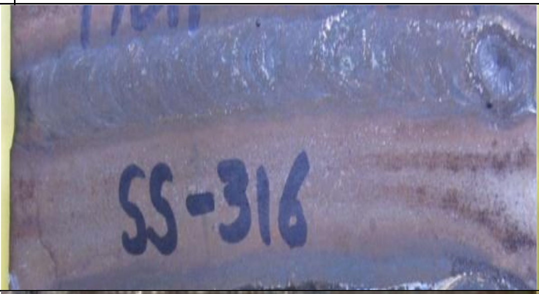	
Duplex 2205	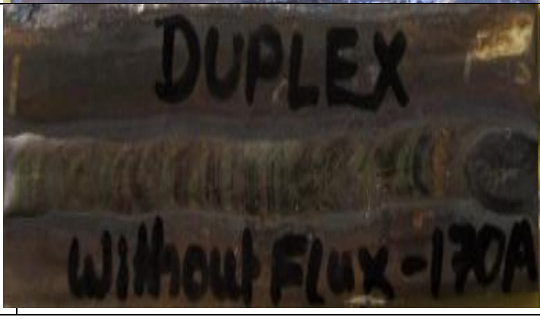	

Figure 3.13: Macrographs showing the bead appearance for AISI 304 , AISI 316 and Duplex 2205 stainless steel at 170 A with and without flux using Ar shielding with flow rate of 10 L/min.

It can be seen from Fig. 3.13 that when 170 A current is used then a concave type cavity is formed on the surface of weld bead due to inward flow of liquid molten metal hence makes the Marangoni statement true.

Constriction of arc column under the presence of activated flux (that contains oxygen) is shown in Figure 3.14. Such narrowing behaviour of arc column increases the energy density within the arc column region and hence, increases the penetration depth as well as decreases the width of the weld bead. In ATIG process, the constriction of arc behaviour is clearly visible during welding to the operator. The ions at the edge of the arc are assumed to have lower mobility than in the centre of the arc, leading to an increased current density at the centre of the arc, so when current density increases then heat increases causing deeper penetration.

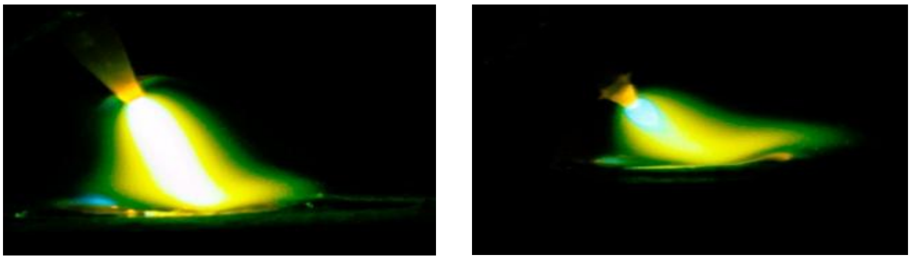

AISI 1020, No flux, 140 A

AISI 1020, No flux, 170 A

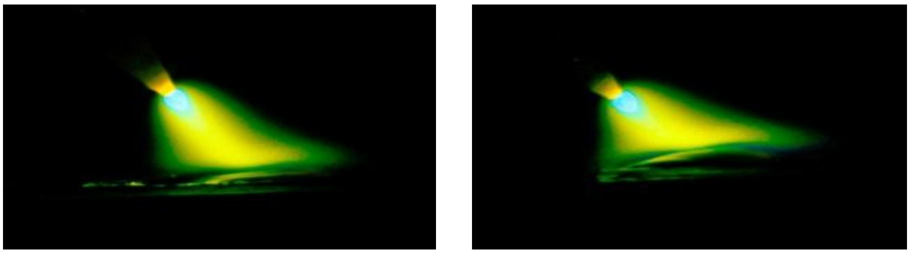

AISI 1020, TiO_2 flux, 140 A

AISI 1020, TiO_2 flux, 170 A

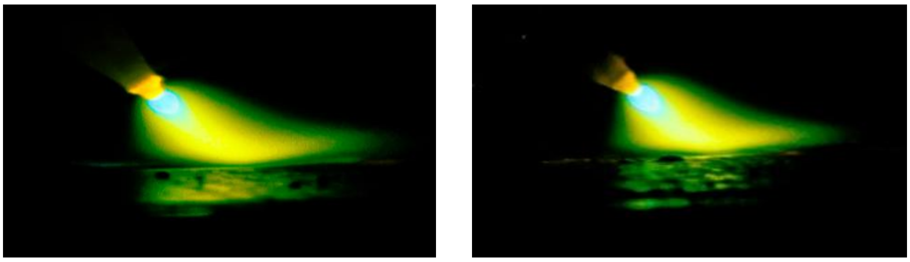

AISI 304, TiO_2 flux, 140 A

AISI 304, TiO_2 flux, 170 A

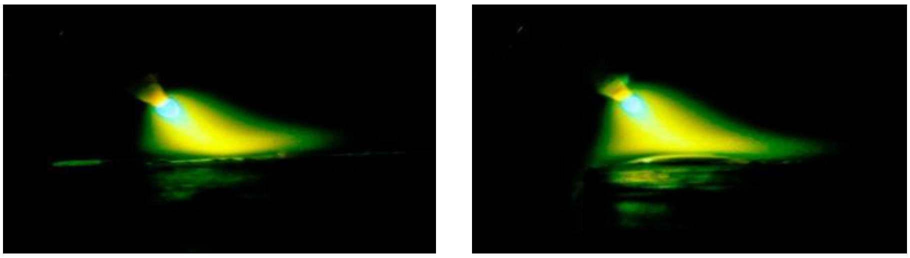

AISI 316, TiO_2 flux, 140 A

AISI 316, TiO_2 flux, 170 A

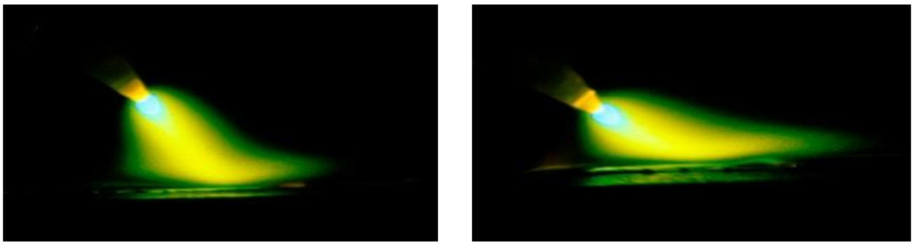

Duplex 2205, TiO_2 flux, 140 A

Duplex 2205, TiO_2 flux, 170 A

Figure 3.14: Arc constriction behaviour during flux activated TIG of different materials (Ar shielding gas, flow rate 10 L/min)

Figure 3.15 shows the macrographs of penetration for all specimens after the beads are cut, polished and etched. Macrographs of the samples clearly indicate the increase in penetration depth due to the use of activated flux for all materials. Another cause of increase in the penetration is the current value, when it is increase from 140 A to 170 A.

	
AISI 304, Ar, 140 A, No flux	AISI 304, Ar, 140 A, TiO_2 flux
	
AISI 304, Ar, 170 A, No flux	AISI 304, Ar, 170 A, TiO_2 flux
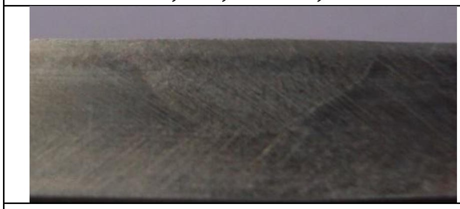	
AISI 316, Ar, 140 A, No flux	AISI 316, Ar, 140 A, TiO_2 flux
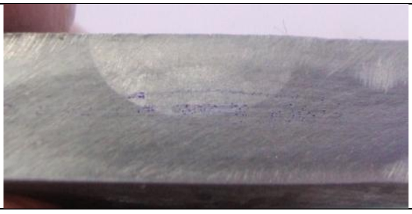	
AISI 316, Ar, 170 A, No flux	AISI 316, Ar, 170 A, TiO_2 flux
	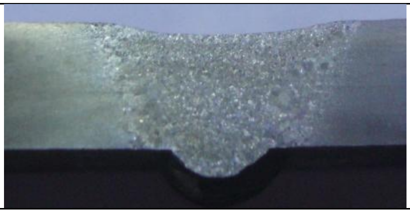
Duplex 2205, Ar, 140 A, No flux	Duplex 2205, Ar, 140 A, TiO_2 flux
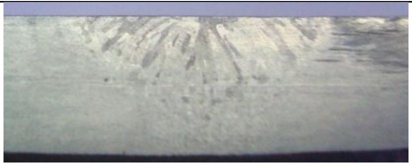	
Duplex 2205, Ar, 170 A, No flux	Duplex 2205, Ar, 170 A, TiO_2 flux

Figure 3.15 Effect of activated flux on penetration (weld morphology) for different materials at different welding currents and shielding gas environments.

3.3.2 Effect of H_2 in Shielding Gas During A-TIG

Figures 3.16 show the appearance of the welding bead for different steels for TIG and A-TIG (with and without TiO_2 coating) when Ar+5%H_2 is used as shielding gas at 170 A current. In this figure it is clear that whole the metal sag due to inward Marangoni convection and due to the constriction of the arc, which result in high heat generation on the workpiece surface.

Workpiece material	No flux	With TiO_2 flux
AISI 304		
AISI316		
Duplex		

Figure 3.16: Macrographs showing the bead appearance for AISI 304 , AISI 316 and Duplex 2205 stainless steel at 170 A with and without flux/compound (with Ar + 5% H_2).

Influence of shielding gas composition on depth of penetration is studied using Ar and Ar + 5% H_2 both used at a flow rate of 10 L/min) as shielding gas for different graded stainless steel workpieces. Figure 3.17(a) shows the comparison of depth of penetration between Ar and Ar +5 % H_2 shielded welding at170 A current and using TiO_2 flux assisted ATIG. It is seen from the Figure 3.17 (a) that addition of hydrogen in Ar as shielding gas increases the depth of penetration under similar process conditions as compared to pure Ar shielding for all stainless steel workpieces and more prominent effect is observed for Duplex 2205stainless steel. Addition of hydrogen in shielding gas makes the arc more conductive as compared to the pure argon shielding. This also helps to conduct more heat during welding and in turn increases the melting efficiency. Addition of hydrogen in shielding gas also reduces oxides and increases metal penetration and flow of the melt. Therefore, addition of hydrogen helps to achieve higher speed of welding, increased metal penetration and less oxidation of surfaces. Figure 3.17 (b) shows a significant decrease in WP ratio in ATIG as compared to simple TIG. This is mainly due to significant increase in depth of penetration due to more inward flow in ATIG as compared to TIG.

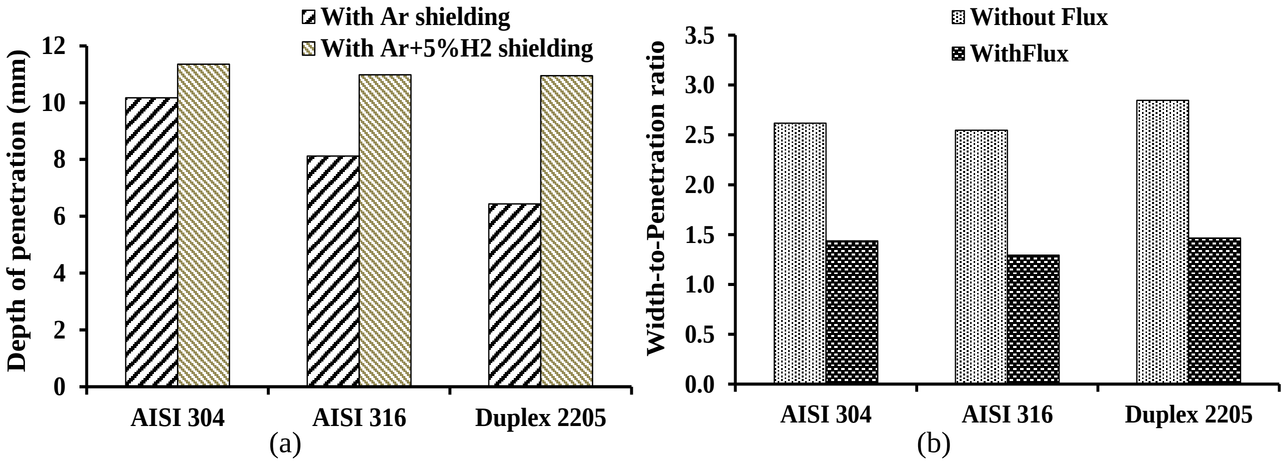

Figure 3.17: (a) Effect of shielding gas composition on depth of penetration (170 A, with TiO_2 flux), and (b) comparison of depth-to-width ratio between TIG and ATIG (170 A, Ar + 5% H_2 shielding gas)

Figure 3.18 shows the macrographs of penetration for all specimens after the beads are cut, polished and etched. Macrographs of the samples clearly indicate the increase in penetration depth due to the use of activated flux for all materials. This can also be noted from Fig. 3.17 and 3.18 that the addition of hydrogen in shielding gas further improves the melting and sometimes penetration beyond the plate thickness is observed.

AISI 304, Ar+5% H2, 170 A No flux AISI 304, Ar+5% H2, 170 A, TiO_2 flux

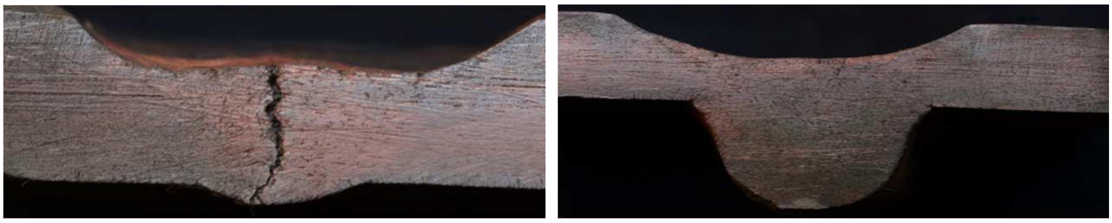

AISI 316, Ar+5% H2, 170 A, No flux AISI 316, Ar+5% H2, 170 A, TiO_2 flux

Dup. 2205, Ar+5% H2, 170 A, No flux Dup.2205, Ar+5%H2, 170 A, TiO_2flux

Figure 3.18: Effect of activated flux on penetration (weld morphology) for different materials at 140 A & 170 A welding currents and Ar + H_2 shielding gas environments

3.3.3 Metallurgical Observation

Figure 3.19 shows the microstructures at different zoom/magnification levels of weld regions of AISI 316 and AISI 304 austenitic stainless steel with and without using flux. After welding at 170 A current using Ar shielding gas, the samples are cut and is grinded with surface grinder, polished and etched, using (Carpenter SS etchant; FeCl3 + CuCl3 + Ethanol + HCl + HNO3) for microstructure study. In given below figure the fusion zone, heat affected zone (HAZ) and unaffected base metal are clearly visible, captured and the same is zoomed at three magnification level. In AISI 316 and 304 workpiece mostly austenite phases are visible. This signifies that the amount of heat input and laminar flow of shielding gas control the heat loss and cooling rate are sufficient to complete the transformation of austenite from ferrite and the solidification rate is sufficient. In AISI 304, not much significant difference is observed in microstructure when flux is used. In both cases, somewhat larger grains are formed when activated flux is used. In both cases typical austenite and δ-ferrite veins are observed.

	100X	200X	500X
AISI 316 (current = 170 A, shielding gas = Ar, gas flow rate = 10 L/min)			
Without flux (TIG)	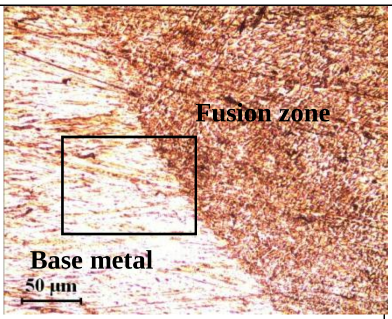	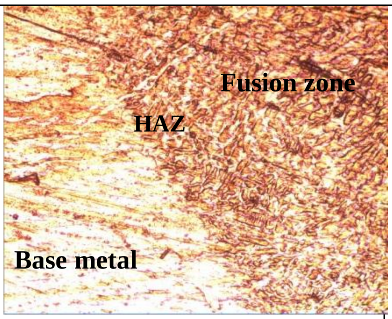	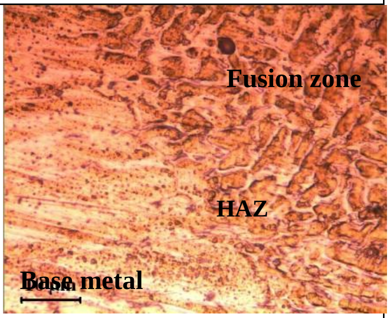
With flux (ATIG)	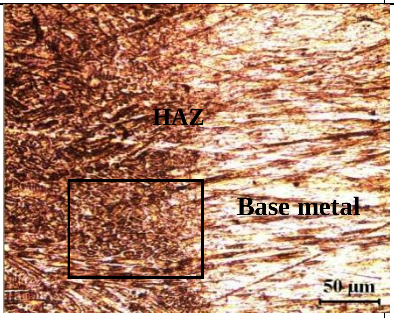	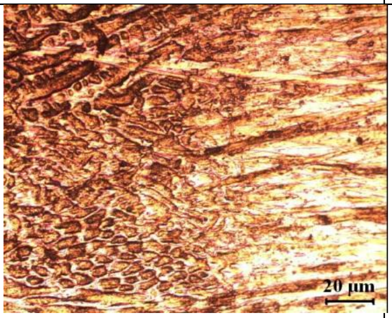	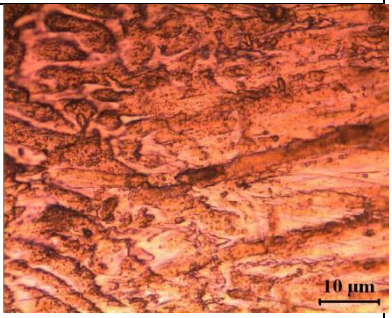
AISI 304 (170 A, Ar, 10 L/min)			
Without flux (TIG)	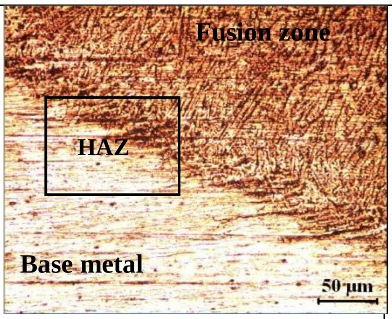	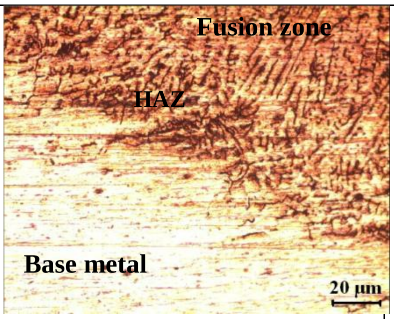	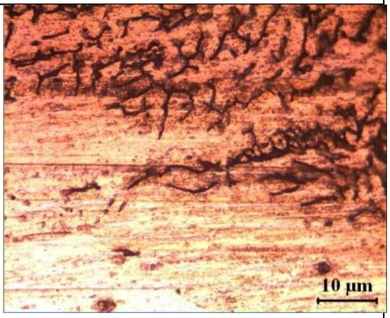
With flux (ATIG)	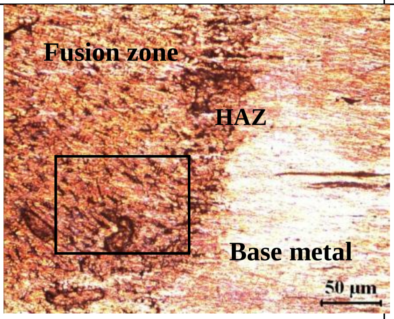	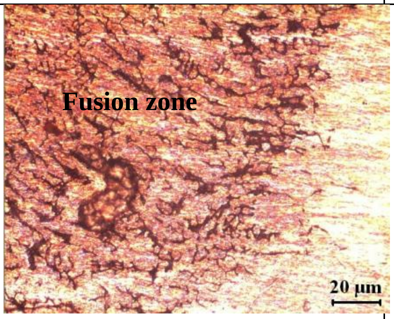	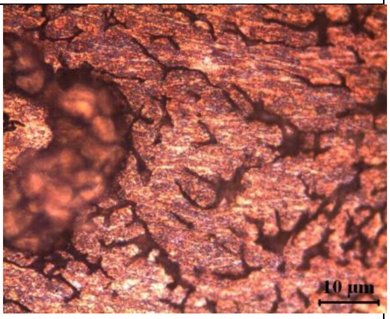

Figure 3.19: Microstructure after TIG and ATIG of AISI 316 and AISI 304 stainless steel at 170 A current and Ar shielding gas with flow of rate 10 L/min.

Figure 3.20 shows the microstructure (etched with Killing's no. 2 etchant; CuCl2 + HCl + Ethanol) for Duplex 2205 steel after welding using TiO2 flux at 170 A current with Ar and Ar + 5% H2 shielding gas. After welding at 170 A current, the samples are cut and grinded with surface grinder, polished and etched. Microstructure shows the dark grey phase of ferrite and nearly white austenite phase. After melting, the weld pool solidifies from liquid state to complete ferritic phase due to the presence of high chromium and molybdenum (ferrite stabilizers). However, as the material cools down to room temperature almost half the ferrite transforms to austenite and appears as islands or primary and secondary austenite grows on the edges of ferrite grains due to nickel and nitrogen; that acts as austenite stabilizers. For austenite transformation, diffusion becomes necessary and Cr, Ni, Mo diffuse slowly as they are substitutional elements and cannot separate between ferrite and austenite. The small amount of nitrogen present in the Duplex steel diffuse rapidly (interstitial element) and has the ability to partition austenite. The presence of nitrogen in the present case improves the austenite formation and it is clearly visible in given below figure that austenite is scattered throughout the large ferrite grains, rather than limited to ferrite grain boundaries.

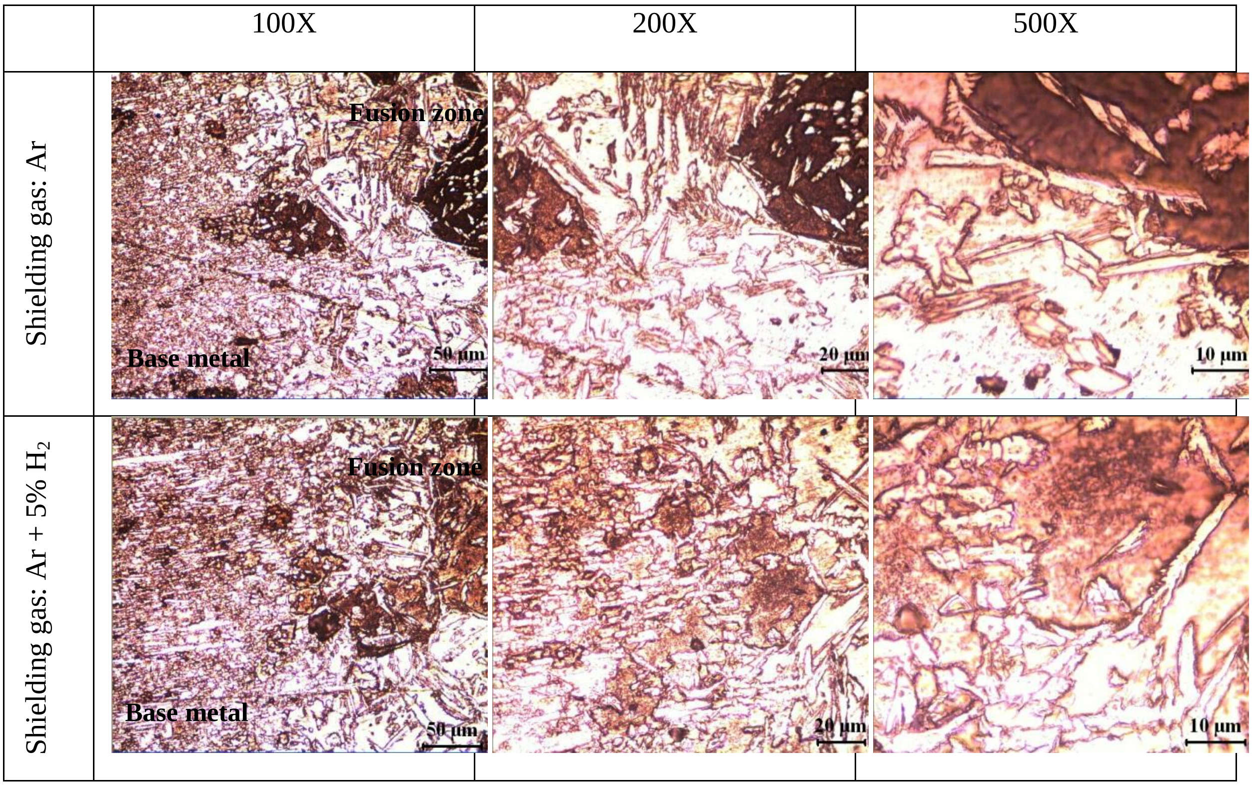

Figure 3.20: – Microstructure after ATIG of Duplex 2205 steels at 170 A current with different shielding gas environment.

Figure 3.21 shows the microhardness variation in and around the fusion zone after TIG and ATIG of the three stainless steel workpieces. The microhardness is taken at below 1 mm of the workpiece surface. The ratio of measured microhardness at different locations from the weld centreline to the microhardness of the base metal is considered to compare in the same scale. Hence, the dotted line passing through unity (Fig.3.22) represents the base metal. It is clear from the figure that no significant variation in microhardness takes place after ATIG. Also, relatively higher microhardness is obtained for austenitic stainless steel (316 or 304) when no flux is used. This could be due to the fact that when no flux is used, the rate of cooling is more and hence, the time required for the transformation from δ-ferrite to austenite phase is not available and δ-ferrite with BCC structure has more mechanical strength than austenite with FCC crystal structure. Lesser depth of penetration *i.e.*, lesser volume of molten pool gets cooled very rapidly due to high temperature gradient with the remaining body and environment. But with flux when molten pool is more due to high penetration, hence large time is taken by the molten pool.

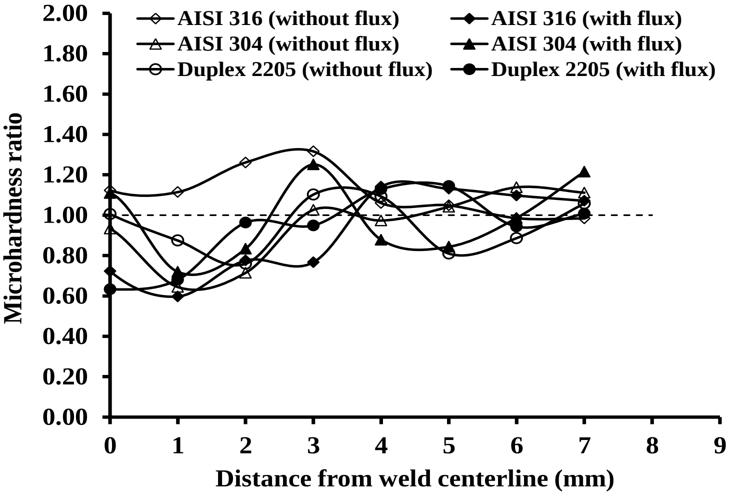

Figure 3.21: Variation of micro hardness after TIG and ATIG of different steel workpieces (current 170 A, Ar as shielding gas and flow rate of 10 L/min)

3.4 Effect of Different Fluxes on Depth of Penetration:

3.4.1Effect of Different Fluxes

The previous study had revealed that the depth of penetration increased whenTiO_2 flux is used and such narrowing behaviour of arc column increase the energy density within the arc column region and hence, increase the penetration depth as well as decrease the width of the weld bead. In traditional TIG welding without activating flux, the temperature coefficient of surface tension on the molten pool generally exhibited a negative value. In A-TIG process, arc constriction results in reduction in anode root area and constriction of plasma column diameter. This effect increases the anode current density and the arc force acting on the welding pool. So, to find out the influence of different oxide, chloride and fluoride based fluxes are evaluated on DOP, width-to-penetration ratio during flux-activated TIG (ATIG) welding of low alloy steel (AISI 4340), austenitic (AISI 304 and AISI 316) and duplex (DUPLEX 2205) stainless steels. Effect of welding current and three different shielding gas compositions are also studied during A-TIG for these workpieces. Arc and weld metal pool behaviours are captured in order to study the physical behaviour of the process. To find other/different fluxes and their effect on the base metal this study is carried out on four different graded steels (AISI 304, AISI 316, DUPLEX 2205 and AISI 4340). There is a noteworthy enhancement in penetration because of addition of H_2 in shielding gas. Addition of helium also helps to increase depth of penetration. Arc behaviour reveals the constriction of arc column during activated TIG welding and positive surface tension induced flow in centripetal (inward) direction is observed. The thickness of workpiece used is 5 mm.

3.4.2 Materials and Methods

Activated TIG welding are carried out by depositing bead layers on austenitic stainless steels AISI 304, AISI 316, duplex stainless steel DUPLEX 2205 and low alloy steel AISI 4340. The plates of each material are 5 mm thick and of size 100 mm × 50 mm. Chemical compositions of all workpiece materials are checked by spectroscopy (Foundry Master optical emission spectroscopy, Germany) and are provided in Table 3.2

Table 3.2- Compositions of different workpieces/ materials

Material	% Composition										
	C	Mn	Si	Cr	Ni	S	P	Mo	Cu	N	Fe
AISI 304	0.05	0.978	0.33	20.2	8.26	0.008	0.049	0.169	0.382	-	Balance
AISI 316	0.072	1.781	0.582	17.4	11.729	0.021	0.041	1.214	-	-	Balance
Duplex 2205	0.1	1.46	0.327	23.1	4.92	0.005	0.020	3.26	0.198	0.16	Balance
AISI 4340	0.35	1.55	0.918	0.199	0.277	0.150	0.182	0.500	0.152	-	Balance

For A-TIG, first fourteen different fluxes namely TiO_2, SiO_2, MoS_2, MoO_3, MnO_2, ZnO, NiO, CrO_3, $Al2O_3$, $CaCO_3$, CaF_2, NaF, KBr and KCl are used to carry out welding on all four workpiece materials. Same technique, for applying flux and cutting of samples metallurgical inspection is used in this case, which is used for single component flux (TiO_2). Torch inclination angle of 45° is maintained for all welding operations. Electrode tip shape and size with dimensions are shown in Fig. 3.22. For all welding, constant voltage = 22 V and speed of welding = 2.2 mm/s is maintained. Using fourteen individual fluxes, welding are carried out on each four workpieces at 125 A current and using pure argon shielding gas with 10 L/min flow rate.

Depth of penetration achieved after ATIG welding with fourteen different fluxes for four workpieces are measured and influence of individual fluxes are studied. Based on these results, five fluxes out of fourteen that most significantly enhances the DOP are selected for further study. The effect of different shielding gases on depth of penetration during A-TIG with these five significant fluxes is further studied using three different shielding gas compositions i.e.argon, argon + 5% hydrogen and 70% argon + 30% helium. The effect of shielding gas on DOP is investigated for all four workpieces using five fluxes and keeping other parameters like welding current (125 A), voltage (22 V), welding speed (2.2 mm/sec), torch inclination (45°) and gas flow rate (10 L/min). Next, influence of welding current in A-TIG on DOP under shielding gas environment of 70% Ar + 30% He is studied for AISI 304 and 316 workpiece at two different levels of current i.e. 100 A and 125 A and results are compared. Previous study showed that there is no significant change in microhardness of the samples in ATIG as compared to TIG welding in fusion as well as heat affected zone. Additionally, the arc and weld pool region during ATIG is captured using Sony-α77 camera (SLT/TMT with Exmoor™ APS HD CMOS sensor, 50 mm F1.4 prime Lens, 12 fps continuous shooting, make: Japan) to study the welding behaviour during ATIG.

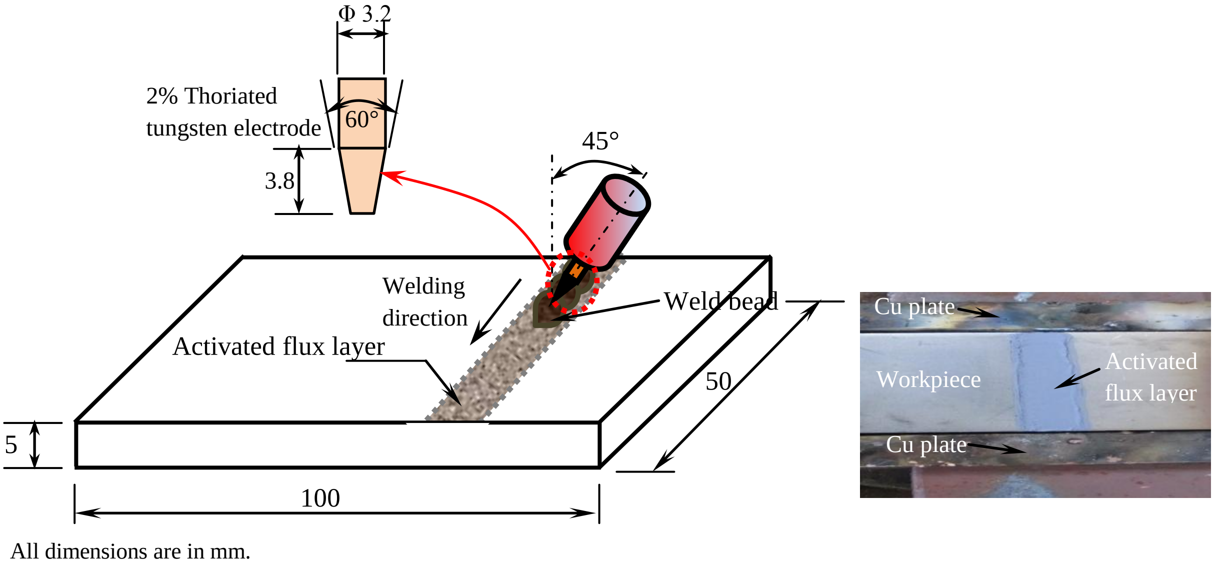

Figure 3.22: Schematic diagram to illustrate ATIG welding arrangement

The input parameter which is used in this study are tabulated below:

Table 3.3: Welding parameters

1. Current	125 A
2. Gas	Argon
3. Flow Rate	10 L/min
4. Material	AISI 4340, AISI 304, AISI 316 and Duplex 2205 steel (5mm)
5. Vertex angle of electrode	60°
6. Electrode	Thoriated Tungsten (EWTh-2) diameter (d) 3.2 mm
7. Conical length of electrode	3.8 mm
8. Welding Speed	3.3 mm/s
9. Fluxes (14 +1 no flux)	TiO_2, SiO_2, MoS_2, MoO_3, ZnO, NiO,AL_2O_3, $CaCO_3$, CaF2, NaF, KCl, KBr, MnO_2, CrO_3

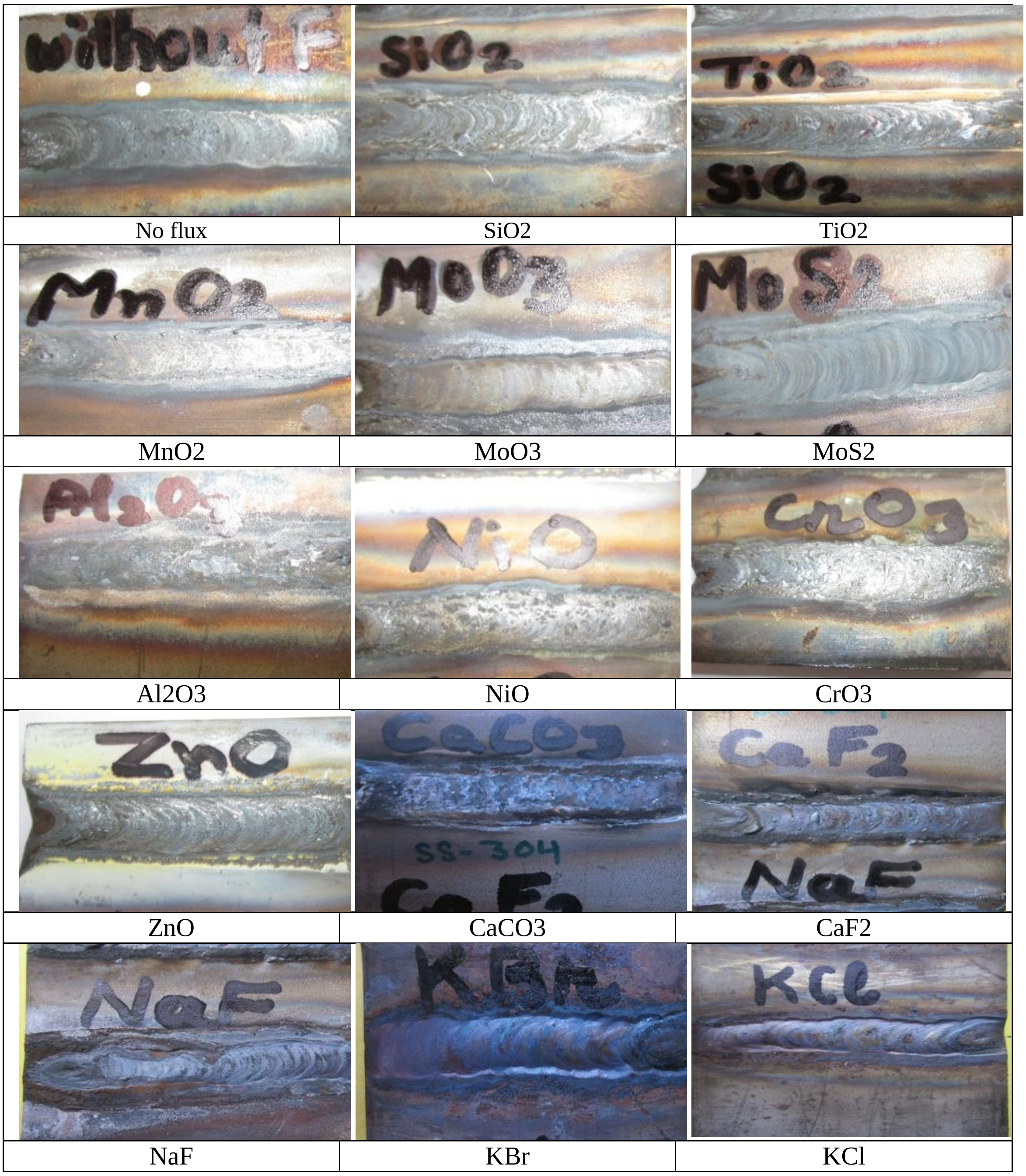

No flux | SiO2 | TiO2

MnO2 | MoO3 | MoS2

Al2O3 | NiO | CrO3

ZnO | CaCO3 | CaF2

NaF | KBr | KCl

Figure 3.23: Macrographs shows the bead appearance for AISI 304 steel at 125 A with and without flux/compound.

Due to the presence of oxygen, the surface tension induced Marangoni convection (*i.e.*, heat flow) changes from outward (centrifugal) to inward (centripetal) direction and increases the penetration. Figure 3.23 shows that the use of $CaCO_3$ flux created excessive residual slag and small spatters. Welding bead with flux of MnO_2, MoS_2, and MoO_3 shows a satisfactory surface appearance for the grade AISI 304. The weld bead appearance of ZnO flux shows litter residual slag and large spatters. Figure 3.24 represents the depth of penetration achieved without flux and with different types of fluxes at 125 A current and with argon shielding gas for AISI 304 workpiece. It can be easily observed from Fig. 3.24 that higher DOP is achieved with majority of the fluxes as compared to no flux condition. Maximum DOP (4.37 mm) is obtained with SiO_2 flux whereas other fluxes like MoS_2, MnO_2, NaF, $CaCO_3$, CrO_3, NiO, in order of significance, are also found to increase DOP considerably. It may be also observed that some of the fluxes likeCaF_2, KCl and KBr are found insignificant as far as increase in depth of penetration is considered and even a depth of penetration lesser than that of without flux is observed. Arc constriction may play a major role in determining the joint penetration. Although it's exact mechanism remains unclear.

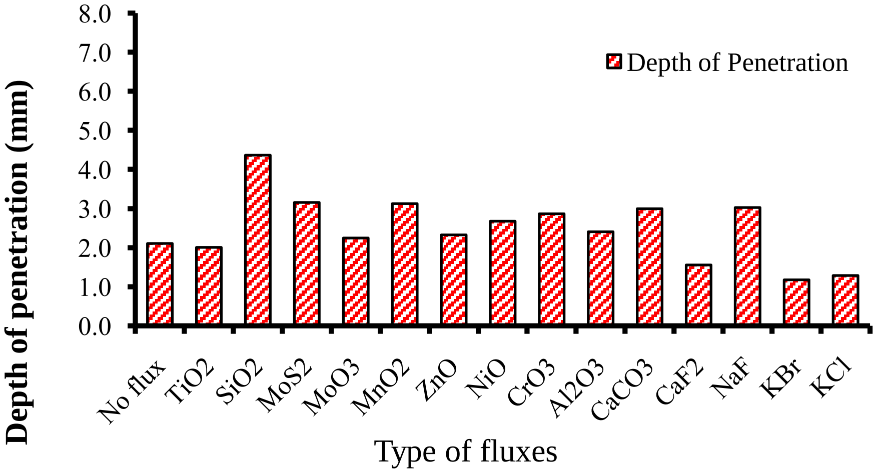

Figure 3.24: Comparison of penetration for AISI 304, with and without use of flux at 125 A, Ar, 10L/min

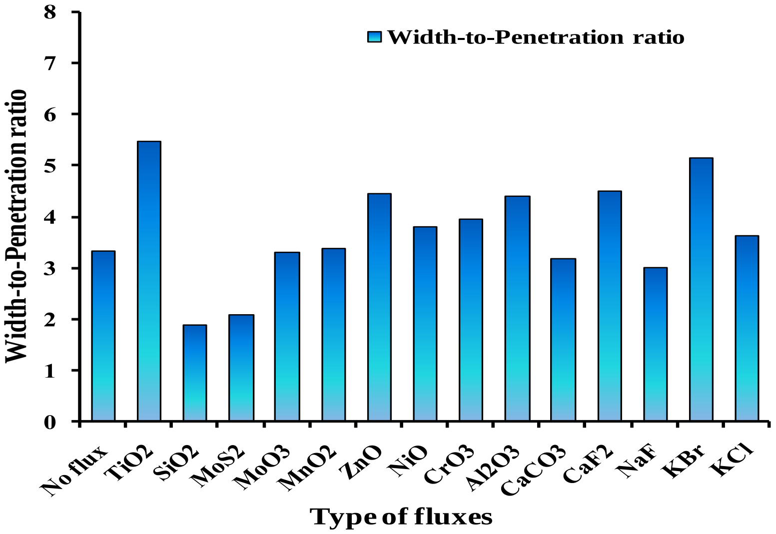

Figure 3.25 Comparison between width to penetration with and without use of flux for AISI 304 using Ar as shielding gas with flow rate of 10 L/min.

The maximum width to penetration which shows in Figure 3.25 is found with TiO_2 flux with comparison to other fluxes and the minimum width to penetration is found with SiO_2 flux at 125 A current.

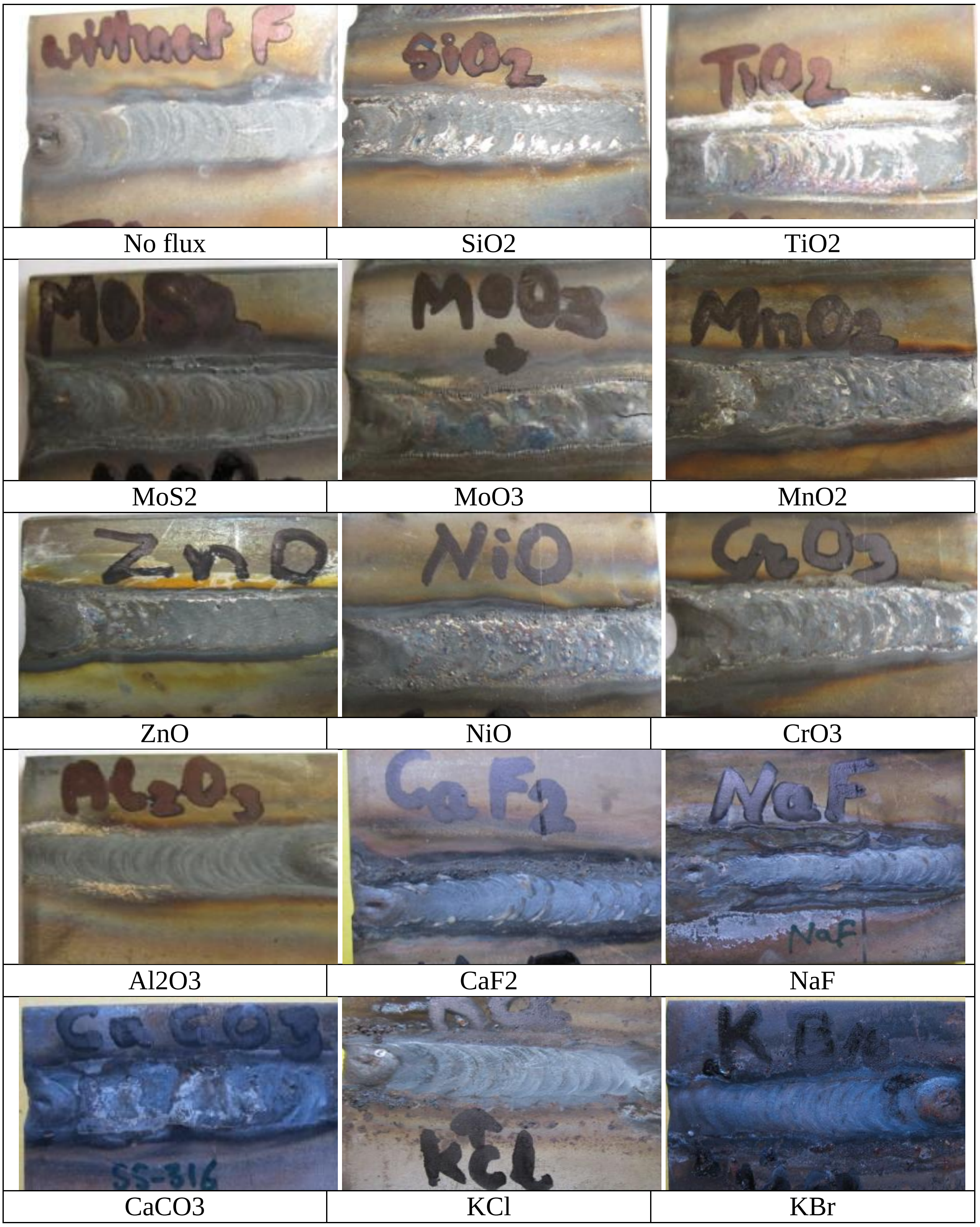

No flux	SiO2	TiO2
MoS2	MoO3	MnO2
ZnO	NiO	CrO3
Al2O3	CaF2	NaF
CaCO3	KCl	KBr

Figure 3.26: Macrographs shows the bead appearance for AISI 316 steel at 125 A with and without flux/compound.

Due to the surface tension induced Marangoni convection (*i.e.*, heat flow) changes from outward (centrifugal) to inward (centripetal) direction and increases the penetration. Figure

3.26 shows that the use of $CaCO_3$ flux and NaF flux created excessive residual slag and small spatters. Welding bead with flux of AL_2O_3, MoS2, TiO_2 and KCl shows a satisfactory surface appearance for the grade AISI 304. The weld bead appearance of $CaCO_3$ flux shows litter residual slag and large spatters. Arc constriction may play a major role in determining the joint penetration. Although it's exact mechanism remains unclear.

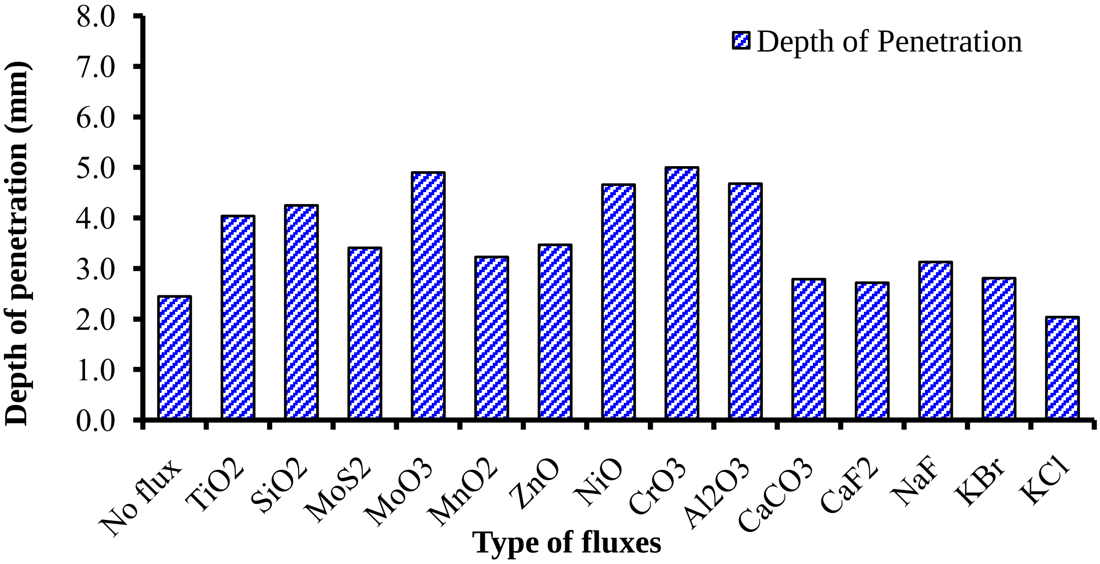

Figure 3.27: Comparison of depth of penetration for AISI 316, with and without use of flux steel at 125 A, Ar, 10L/min

Similarly for AISI 316 workpiece, increased DOPis observed with all fluxes except KCl (Fig. 3.27). With CrO_3 activated flux, maximum penetration (of 5 mm) is achieved which is in the order of plate thickness and more than the double depth of penetration as achieved without using flux. In order of their significance, fluxes like MoO_3, Al_2O_3, NiO SiO_2, TiO_2 greatly increases penetration depth.

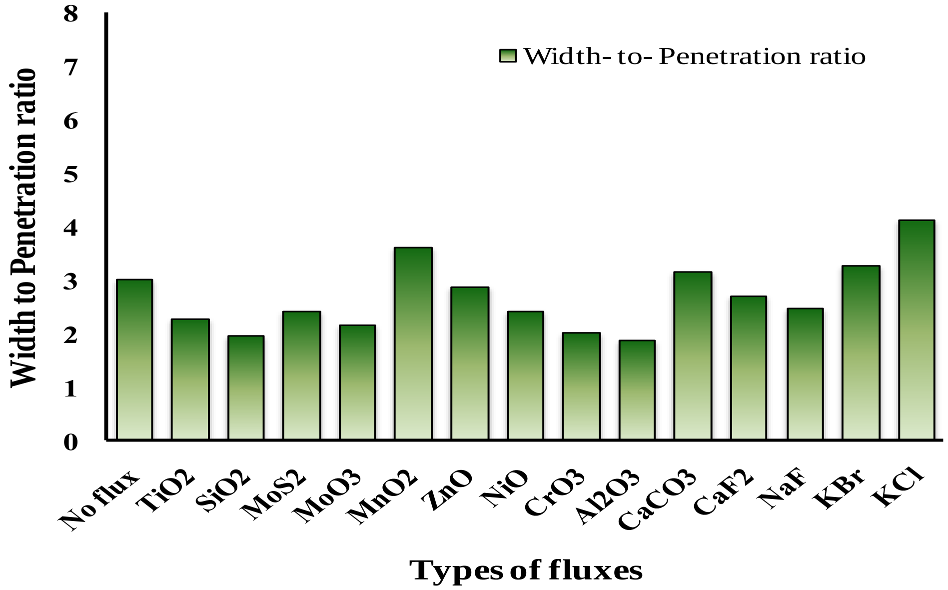

Figure 3.28: Comparison between width to penetration with and without use of flux for AISI 316 using Ar as shielding gas with flow rate of 10 L/min.

The maximum width to penetration which shows in Figure 3.28 is found with KCl flux with comparison to other fluxes and the minimum width to penetration is found with AL_2O_3 and SiO_2 flux at 125 A current with Ar shielding. It can be well observed from Fig. 3.28 that minimum width-to-penetration ratio is achieved for those fluxes for which the significant increase in penetration are observed.

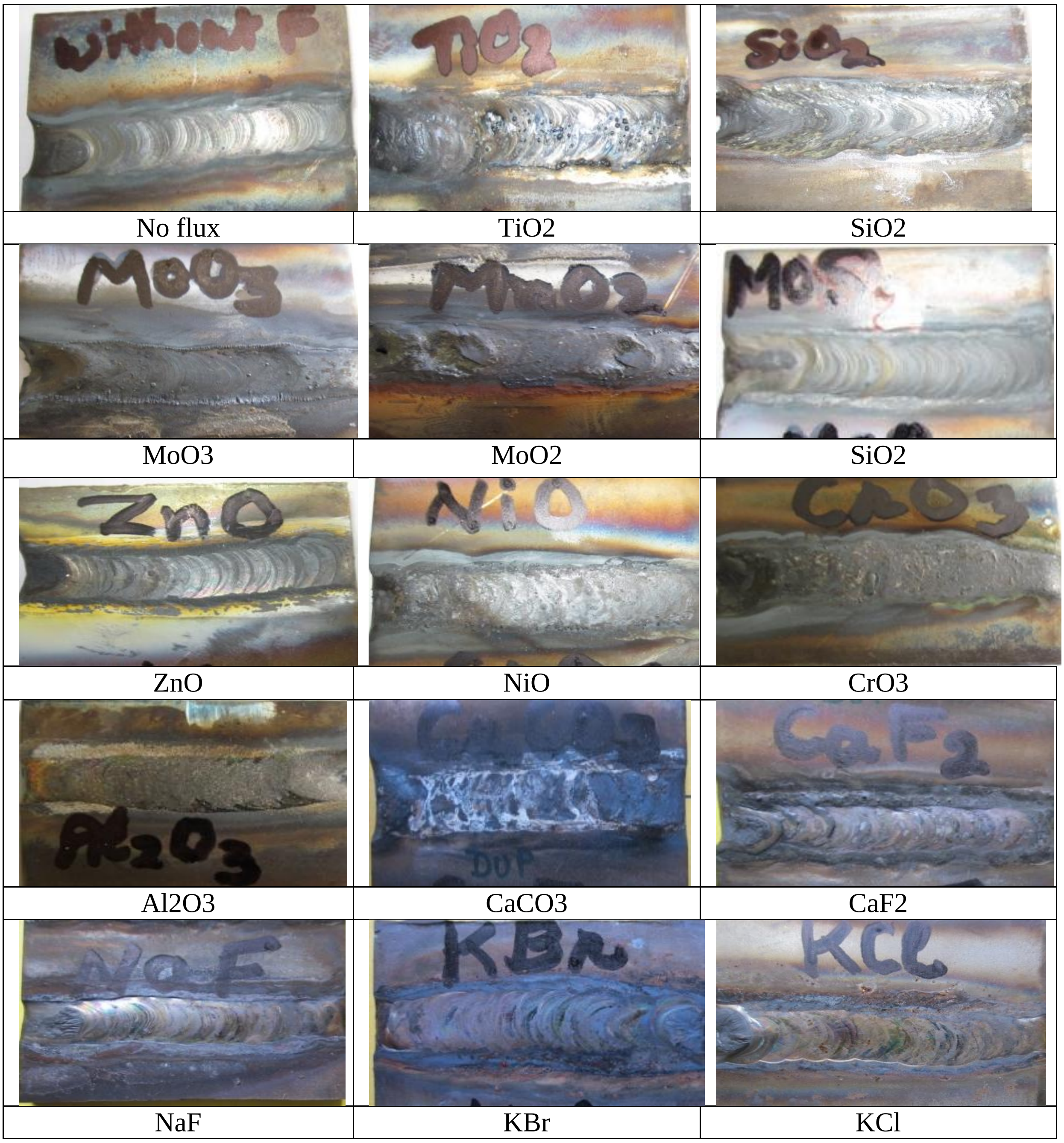

No flux | TiO2 | SiO2

MoO3 | MoO2 | SiO2

ZnO | NiO | CrO3

Al2O3 | CaCO3 | CaF2

NaF | KBr | KCl

Figure 3.29: Macrographs shows bead appearance for DUPLEX 2205 steel at 125 A with and without flux/compound

Similarly the weld samples with all the five fluxes for Duplex 2205 workpiece are shown in Fig. 3.29 where the excessive penetration and flowing of liquid metal beyond plate thickness can be seen. Figure 3.29 shows that the use of $CaCO_3$ flux and MnO_2 flux created excessive residual slag and small spatters. Welding bead with flux of AL_2O_3, MoS2, ZnO and KCl shows a satisfactory surface appearance for the grade AISI 304., depending on the flux. Arc constriction may play a major role in determining the joint penetration. Although it’s exact mechanism remains unclear.

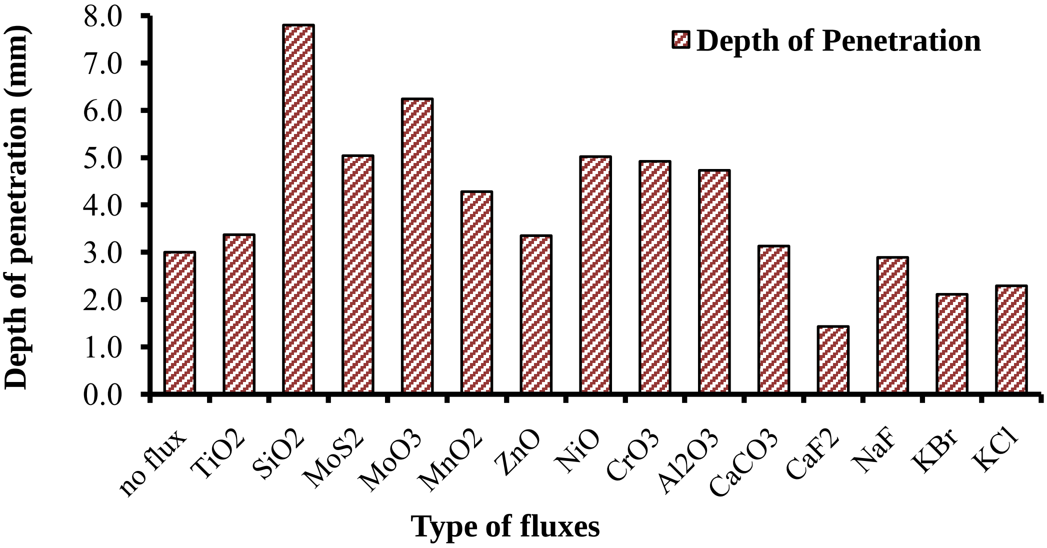

Figure 3.30: Comparison of depth of penetration for DUPLEX 2205, with and without use of flux steel at 125 A, Ar, 10L/min

Comparison of measured depth of penetration with and without flux is shown in Figure 3.30. It can be seen that the depth of penetration increases for all the materials in A-TIG when flux is used. For Duplex 2205 workpiece, more than 100% increase of penetration depth is noted when SiO_2, MoO_3, MoS_2, NiO fluxes are used as compared to conventional TIG when no flux is used and maximum penetration (7.8 mm) is obtained using SiO_2 flux (refer Fig. 3.30). Penetration for an amount higher than plate thickness in all such cases resulted due to excessive melting in such a way that liquid pool flows beyond thickness of the plate. Use of fluxes like NaF, KCl, KBr and CaF_2 has no effect on increase in penetration rather a lower penetration than without using flux is observed. During this study same constraints are taken, which are taken in the previous study of TiO_2 flux.

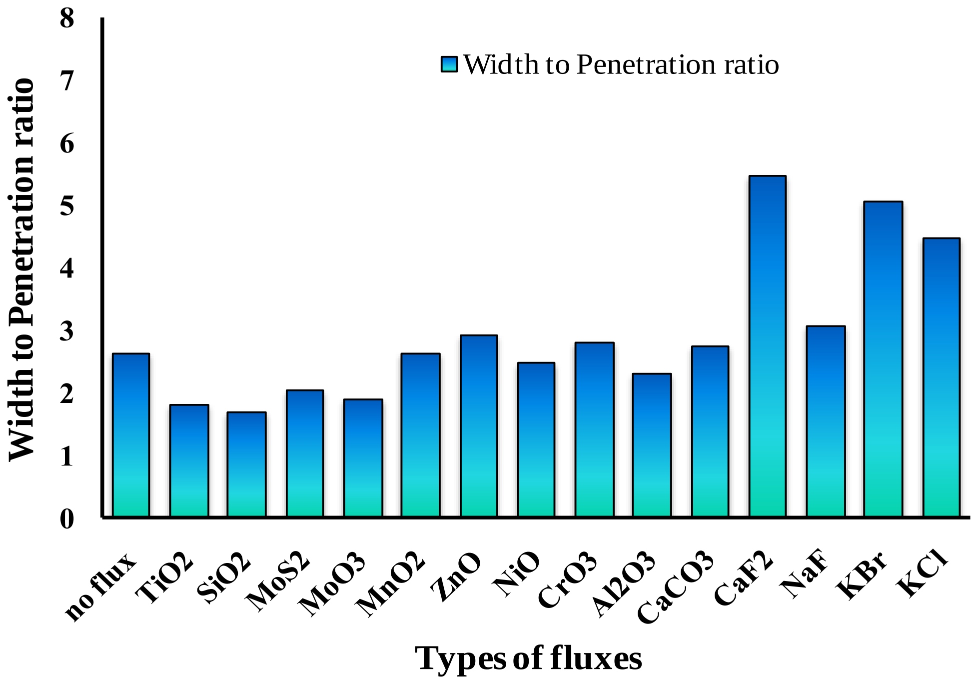

Figure 3.31: Comparison between width to penetration with and without use of flux for DUPLEX 2205 using Ar as shielding gas with flow rate of 10 L/min.

The maximum width to penetration which shows in figure 3.31 is found with CaF_2 flux with comparison to other fluxes and the minimum width to penetration is found with SiO_2 flux at 125 A current with Ar shielding.

No flux	TiO2	SiO2

MoS2	MoO3	MnO

ZnO	NiO	CrO3

NaF	KBr	KCl

Figure 3.32: Macrographs shows the bead appearance for AISI 4340 steel at 125 A with and without flux/compound

Surface tension induced Marangoni convection (*i.e.*, heat flow) changes from outward (centrifugal) to inward (centripetal) direction and increases the penetration. Figure 3.32

shows that the use of KCl flux creates excessive residual slag and poor weld bead appearance. Welding bead with flux of AL_2O_3, NiO_2 shows a satisfactory surface appearance for the grade AISI 304. Arc constriction may play a major role in determining the joint penetration. Although it's exact mechanism remains unclear. Also hot crack is found with without flux, TiO_2, MoS_2 and ZnO. Some porosity is also found with $CaCO_3$ and with NaF fluxes. Weld appearance of SiO_2, MoO_3, CrO_3 and KCl fluxes is also not good.

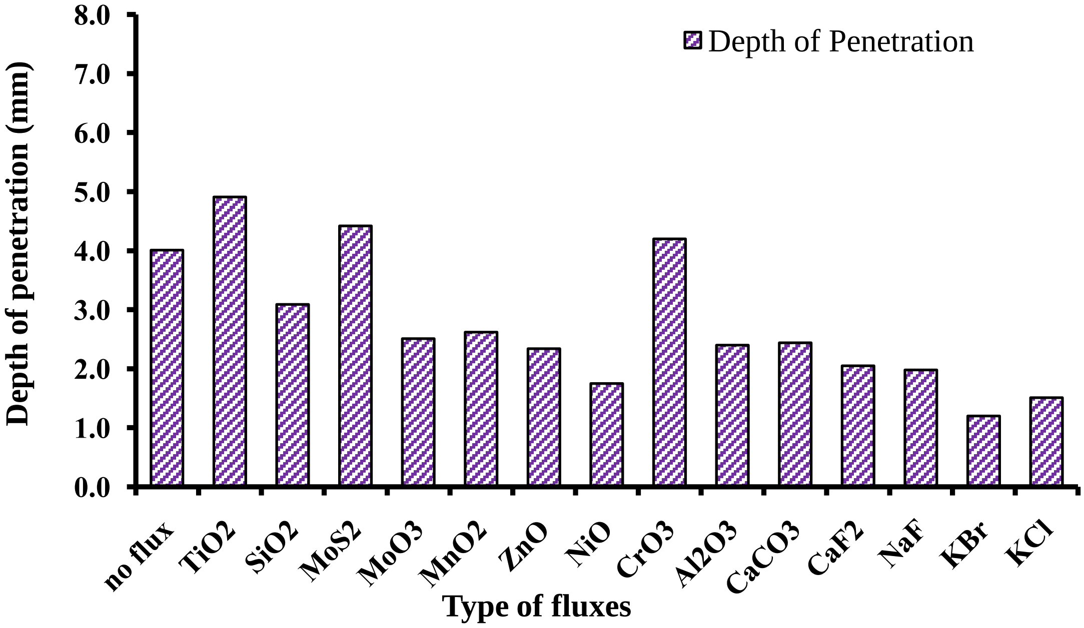

Figure 3.33: Comparison between depth of penetration with and without use of flux for AISI 4340 using Ar as shielding gas with flow rate of 10 L/min.

Comparison of measured depth of penetration with and without flux is shown in Figure 3.33. It can be seen that the depth of penetration increases for all the materials in ATIG when flux is used. The maximum increase of penetration is measured with TiO_2 flux at 125 A current. During this study same constraints are taken, which are taken in the previous study of TiO_2 flux. Other fluxes like MoS_2, CrO_3 and SiO_2 also significantly enhances the maximum achievable depth of penetration in single pass. It is also clear from the chart that minimum depth of penetration is with KBr. It is also found that the maximum depth of penetration of TiO_2 flux is approximately equal to the thickness of the workpiece.

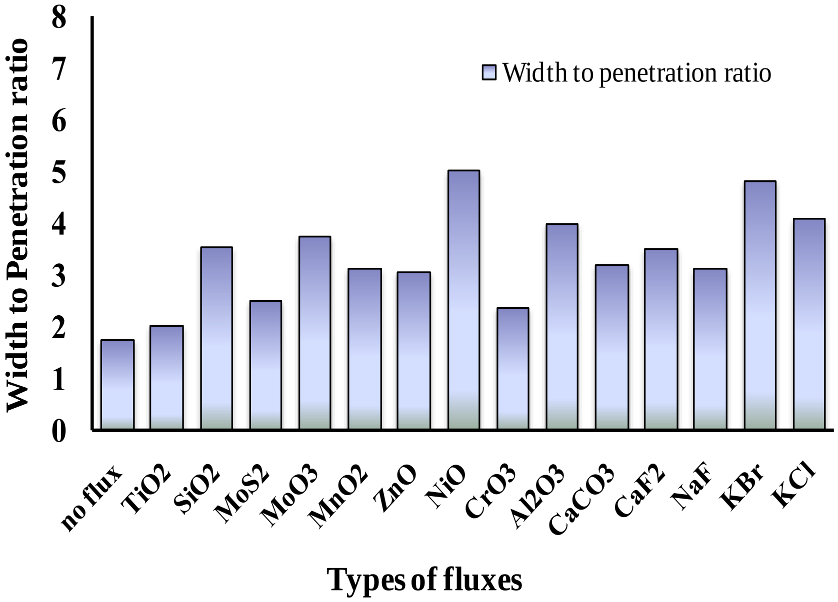

Figure 3.34: Comparison between width to penetration with and without use of flux for AISI 4340 using Ar as shielding gas with flow rate of 10 L/min.

The maximum width to penetration which shows in figure 3.34 is found with NiO flux with comparison to other fluxes and the minimum width to penetration ratio is found with no flux is used. Figure 3.34 also shows that the increase in the weld depth-to-width ratio with oxide fluxes is either weak or strong, depending on the flux.

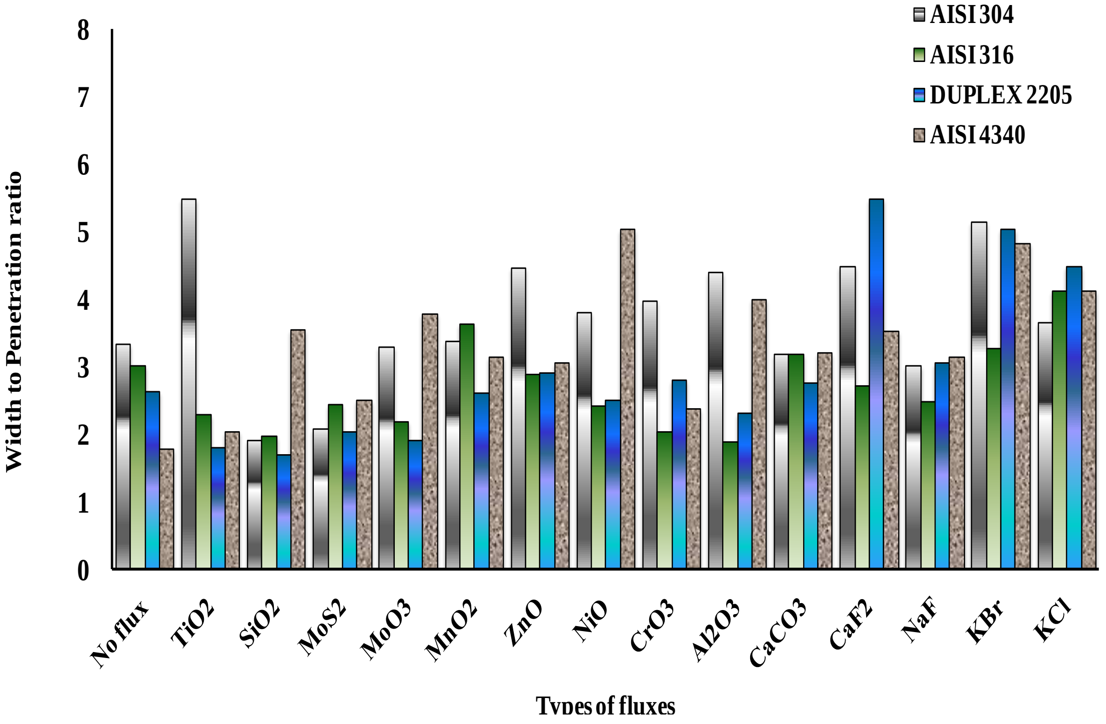

Figure 3.35: Comparison between depth of penetration with and without use of flux for different graded steels using Ar as shielding gas with flow rate of 10 L/min.

Some of the fluxes like CaF_2, NaF, NiO, KCl, KBr are found ineffective in ATIG welding to enhance penetration depth. Thus, the comprehensive investigation of influence of fourteen different fluxes for different steel reveals that the substantial enhancement in DOPis obtained using the activated fluxes that contain oxygen while the other fluxes that contain chlorine, fluorine or bromine (like CaF_2, NaF, KCl, KBr etc.) has insignificant effect in increasing penetration and most of the cases results in lower penetration even less than no flux condition. Also, the activated fluxes help to reduce the width-to-penetration ratio due to increase in DOPas well as significant reduction in fusion zone width.

Hence, from Fig. 3.35 it is concluded that the maximum depth of penetration is achieved with five fluxes. Based on these results, five fluxes out of fourteen that most significantly enhances the DOP are selected for further study. It is also concluded that the maximum penetration is achieved with AISI 304 steel, which is the base for further investigation.

In case of A-TIG welding when flux is used, constriction of arc column and reduction in anode root area takes place which increases the arc column energy density (due to narrow and concentrated arc) and has also been observed previously. Higher temperature rise because of focussed arc and increased heat flux enhances the DOP when fluxes are used. Constriction of plasma column and reduction in anode root area effectively raises current density as well as arc force on welding pool. Oxygen ions of fluxes interact with the electrons already present in the arc column, redistributes there by constricts plasma column and increases energy density of arc column. At the same time, a downward flow in the liquid metal is observed due to electromagnetic Lorentz force and higher DOP is obtained. Due to these effects, a crater type liquid pool just below to behind the arc region is observed (before the metal solidifies). This behavior for different workpiece material during A-TIG with SiO_2 and TiO_2 fluxes are shown in Fig. 3.36.

Material	With SiO_2 flux	With TiO_2 flux
AISI 304		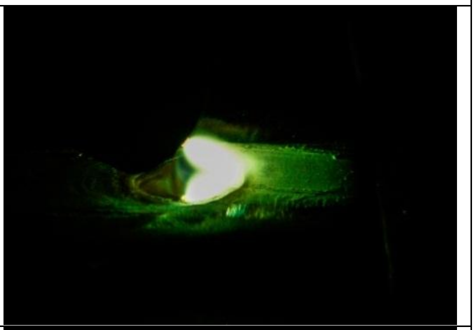
AISI 316	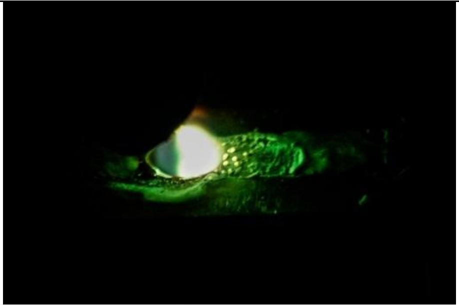	
Duplex 2205		

Figure 3.36: Arc constriction and weld pool shape during flux activated TIG (125 A, Ar at 10 L/min)

The downward force and flow of metal changes the direction of heat flow i.e. surface tension induced Marangoni convection from outward to inward (or centrifugal to centripetal) and helps in increasing DOP. This behavior is validated by observing the liquid weld pool just near the arc region as shown in Fig. 3.37. It can be also noted that arc constriction takes place in ATIG welding when activated fluxes (that contains oxygen) are used however, for same flux different DOP is achieved for different workpiece materials. This variation depends on the amount of constriction; high temperature reaction of flux with a particular workpiece material (depending upon composition) and slope of $d\sigma/dT$ curve (i.e. surface tension σ to temperature T) determine strength of the Marangoni convection and increase in penetration depth.

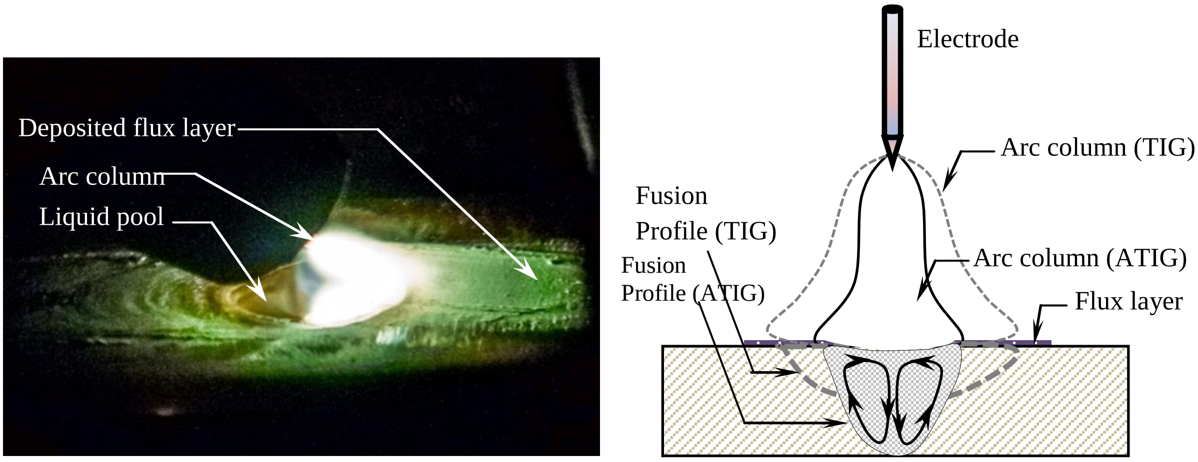

(a) (b)

Figure 3.37: (a) Weld pool shape and (b) schematic illustration of flow in ATIG

3.4.3 Effect of Shielding Gases during A-TIG:

From the last study of effect of different fluxes during Ar shielding, in which 14 different fluxes is used, it is found that only five fluxes plays the best role to achieve maximum depth of penetration. Hence, those fluxes (SiO_2, TiO_2, MoS_2, CrO_3, and MoO_3) are used in this study to find the effect of shielding gas (Ar + 5% H_2) on the depth of penetration and its microstructure.

Fig. 3.8 shows the bead appearance (top, bottom surface) and photographic view of the fusion zone after A-TIG with five different fluxes for AISI 304 workpiece (125 A, Ar + 5% H_2, flow rate 10 L/min).

Figure 3.38: Weld bead appearance (top, bottom surface) and photographic view of the fusion zone after A-TIG with five different fluxes for AISI 304 workpiece (125 A, Ar + 5% H_2, flow rate 10 L/min)

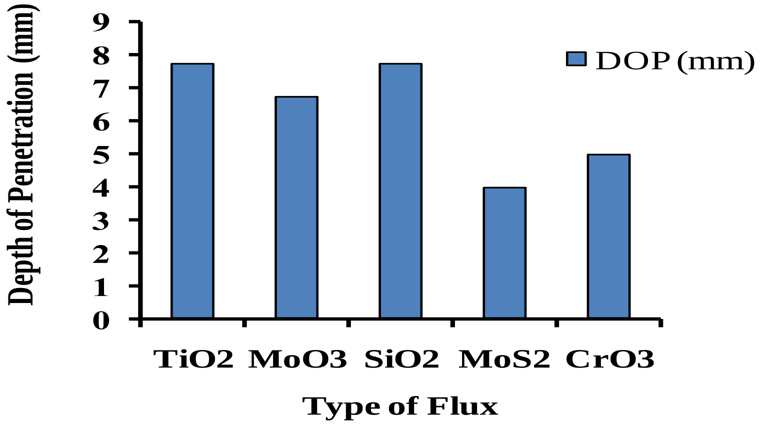

Figure 3.39: Comparison of depth of penetration for AISI 304 at 125 A with 5 different fluxes and with Ar + H_2 (5%) shielding at flow rate of 10 L/min.

From figure 3.39 it is clear that the maximum depth of penetration has come with the SiO_2 and TiO_2 flux and the minimum with the MoS_2 flux.

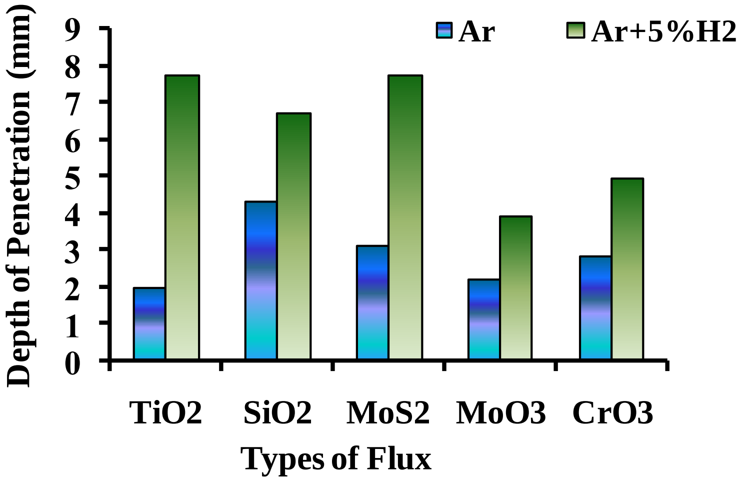

Figure 3.40: Comparison of depth of penetration for AISI 304 at 125 A with 5 different fluxes and with Ar and Ar + H_2 (5%) shielding at flow rate of 10 L/min.

From the above figure 3.40 it is clear that there is huge difference between the depths of penetration of different gases (Ar and Ar + 5% H_2). Maximum depth of penetration is found with Ar + H_2 mixture. It shows that addition of hydrogen in Ar as shielding gas increases the depth of penetration under similar process conditions as compared to pure Ar shielding. Addition of hydrogen in shielding gas makes the arc more conductive as compared to the pure argon shielding. This also helps to conduct more heat during welding and in turn increases the melting efficiency. Addition of hydrogen in shielding gas also reduces oxides and increases metal penetration and flow of the melt. Therefore, addition of hydrogen helps to achieve higher speed of welding, increased metal penetration and less oxidation of surfaces.

Figure 3.41: Macrographs shows the bead appearance for AISI 316 steel at 125 A with 5 different fluxes and with Ar+$H_2$5% shielding at flow rate of 10 L/min.

From Fig. 3.41 we can observed that due to excess heat of arc and fast solidification some hot crack are developed in case of AISI 316 steel specially with CrO3 which is another part of study.

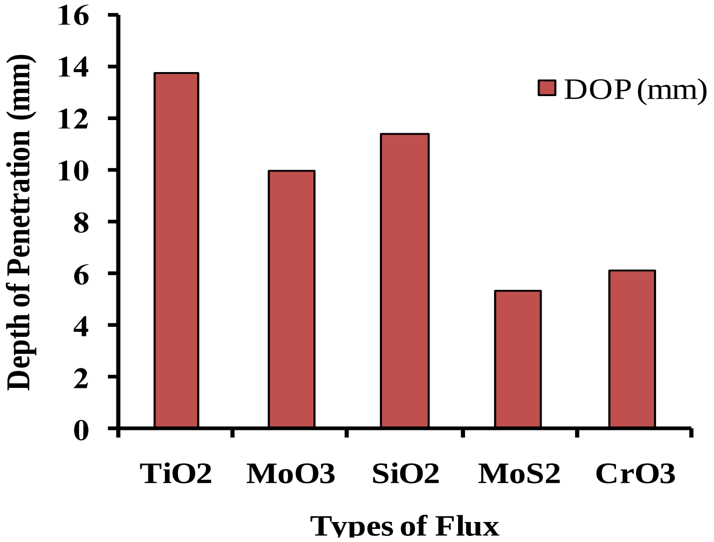

Figure 3.42: Comparison of depth of penetration for AISI 316 at 125 A with 5 different fluxes and with Ar + 5% H_2 shielding at flow rate of 10 L/min.

From figure 3.42 clear that the maximum depth of penetration has come with the TiO_2 flux and the minimum with the MoS_2 flux.

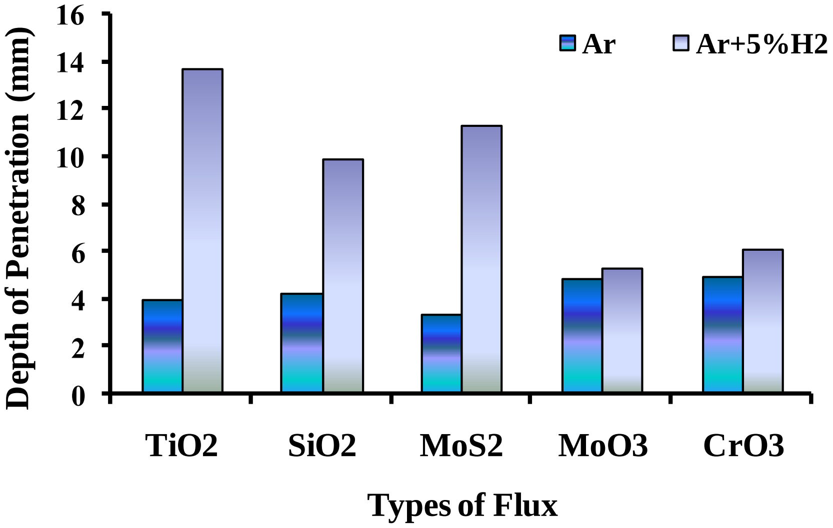

Figure 3.43: Comparison of depth of penetration for AISI 316 at 125 A with 5 different fluxes and with Ar and Ar +5% H_2 shielding at flow rate of 10 L/min.

From the above figure 3.43 it is clear that there is huge difference between the depths of penetration of different gases (Ar and Ar + 5% H_2). Maximum depth of penetration is found with Ar + H_2 mixture. Influence of shielding gas composition on depth of penetration is studied using Ar and Ar + 5% H_2 (both used at a flow rate of 10 L/min) as shielding gas for different graded stainless steel workpieces. The maximum depth of penetration is found with TiO_2 flux which is shown in Figure 3.41.

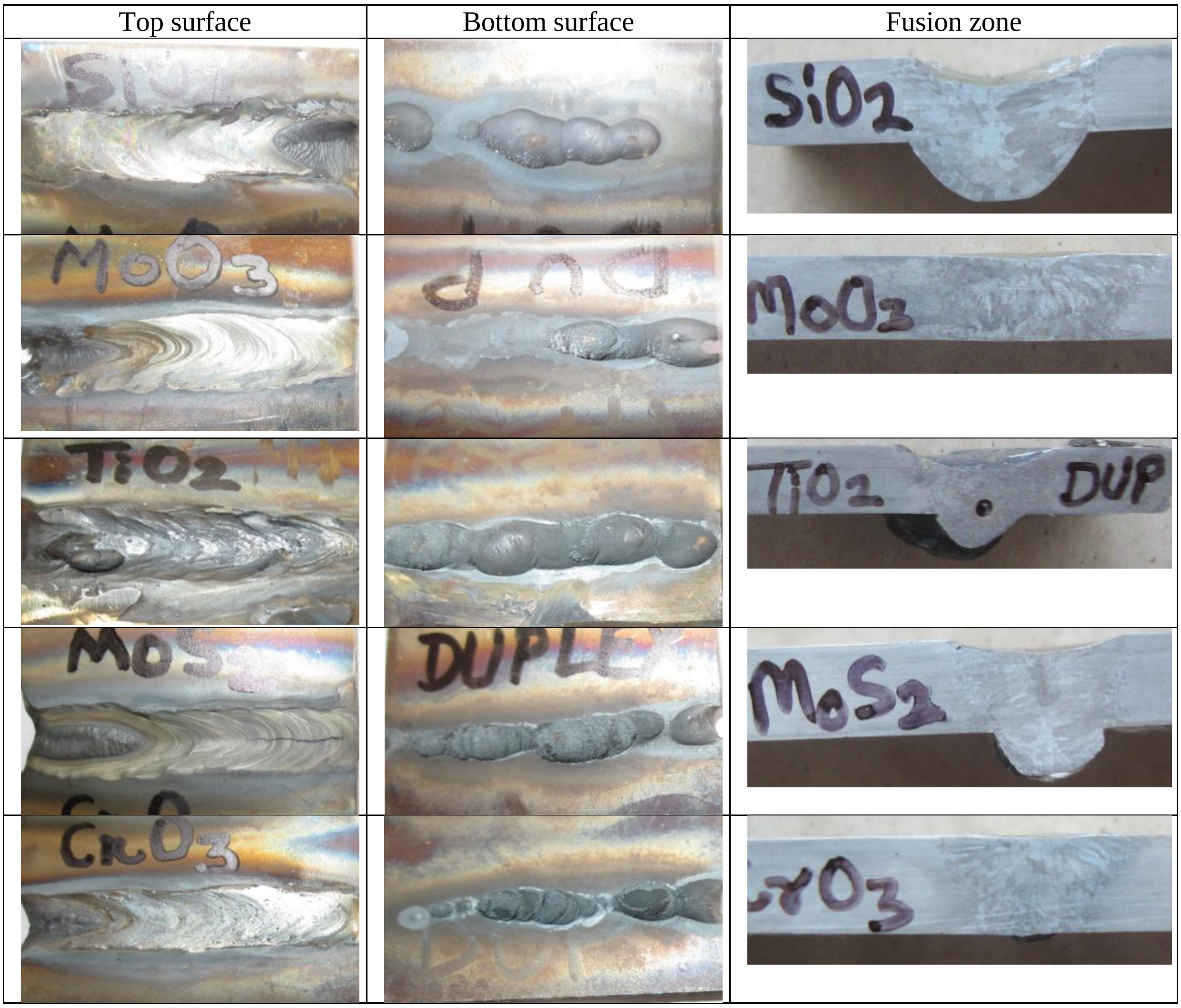

Figure 3.44: Weld bead appearance (top, bottom surface) and photographic view of the fusion zone after ATIG with five different fluxes for Duplex 2205 workpiece(125 A, Ar + 5% H_2, flow rate 10 L/min)

Similarly the weld samples with all the five fluxes for Duplex 2205 workpiece are shown in Fig. 3.44 where the excessive penetration and flowing of liquid metal beyond plate thickness can be seen. Fusion zone profiles of the cut samples after etching with Kalling’sNo. 2 etchant (HCl +$CuCl_2$ + ethanol) are also shown in Fig. 3.44.

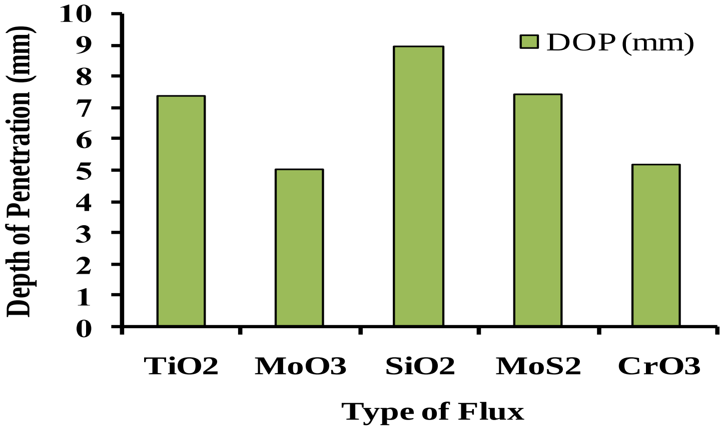

Figure 3.45: Comparison of depth of penetration for DUPLEX 2205 at 125 A with 5 different fluxes and with Ar+5% H_2 shielding at flow rate of 10 L/min.

From figure 3.45 it is clear that the maximum depth of penetration has come with the SiO_2 flux and the minimum with the MoO_3 flux.

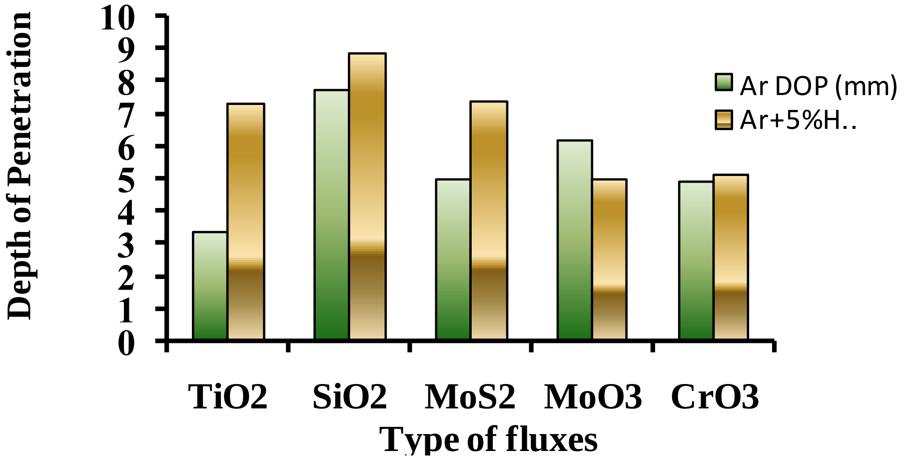

Figure 3.46: Comparison of depth of penetration for DUPLEX 2205 at 125 A with 5 different fluxes and with Ar and Ar+5% H_2 shielding at flow rate of 10 L/min.

From the figure 3.46 it is clear that there is huge difference between the depths of penetration of different gases (Ar and Ar + 5% H_2). Maximum depth of penetration is found with Ar + H_2 mixture. Influence of shielding gas composition on depth of penetration is studied using Ar and Ar + 5% H_2 (both used at a flow rate of 10 L/min) as shielding gas for different graded stainless steel workpieces. The maximum depth of penetration is found With MoS_2 flux.

Figure 3.47: Macrographs shows the bead appearance for AISI 4340 steel at 125 A with 5 different fluxes and with Ar+5% H_2 shielding at flow rate of 10 L/min.

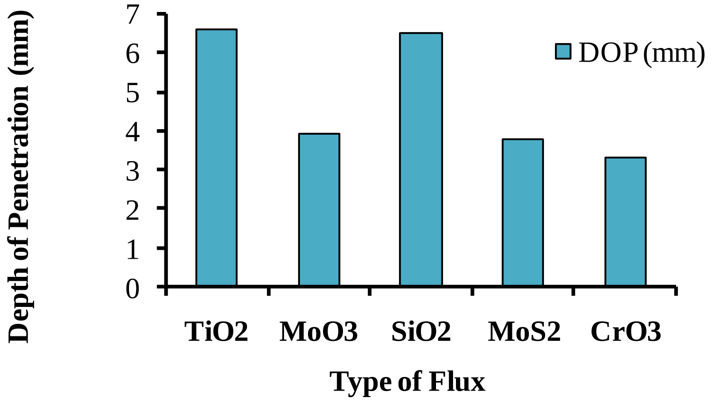

Figure 3.48: Comparison of depth of penetration for AISI 4340 at 125 A with 5 different fluxes and with Ar+5% H_2 shielding at flow rate of 10 L/min.

From figure 3.48 it is clear that the maximum depth of penetration has come with the SiO_2 and TiO_2 flux and the minimum with the CrO_3 flux.

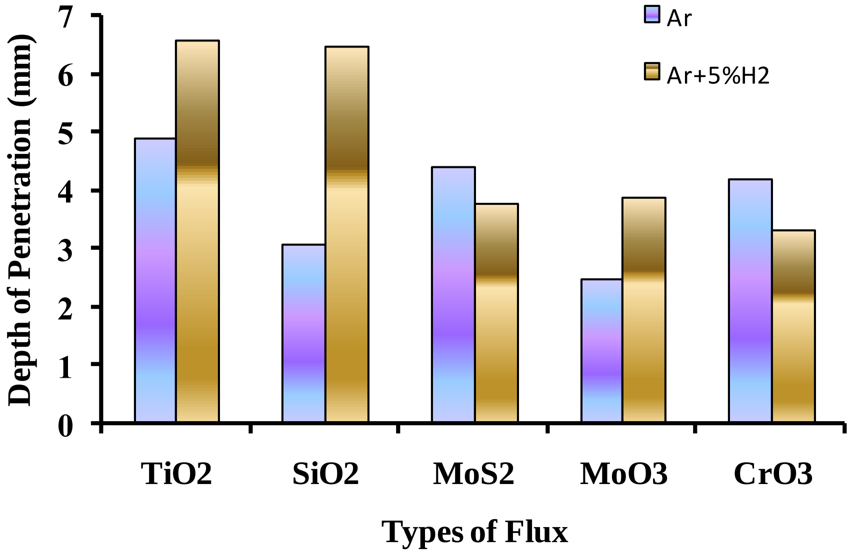

Figure 3.49: Comparison of depth of penetration for AISI 4340 at 125 A with 5 different fluxes and with Ar and Ar+5% H_2 shielding at flow rate of 10 L/min.

From the above figure 3.49 it is clear that there is huge difference between the depths of penetration of different gases (Ar and Ar + 5% H_2). Maximum depth of penetration is found with Ar + H_2 mixture. Influence of shielding gas composition on depth of penetration is studied using Ar and Ar + 5% H_2 (both used at a flow rate of 10 L/min) as shielding gas for different graded stainless steel workpieces. The maximum depth of penetration is found with MoS_2 and TiO_2 flux.

After this study Ar 70% + He 30% is used as a shielding gas, at two different parameters i.e. at 125 A and the other at 100 A to find the effect of this gas on the penetration and weld morphology. It is clear from Fig. 3.50 that metal penetrate in case of SiO_2 and MoS_2.

Figure 3.50: Weld bead appearance (top, bottom surface) of A-TIG with five different fluxes for AISI 304 workpiece (125 A, Ar 70 % + He 30 %, flow rate 10 L/min)

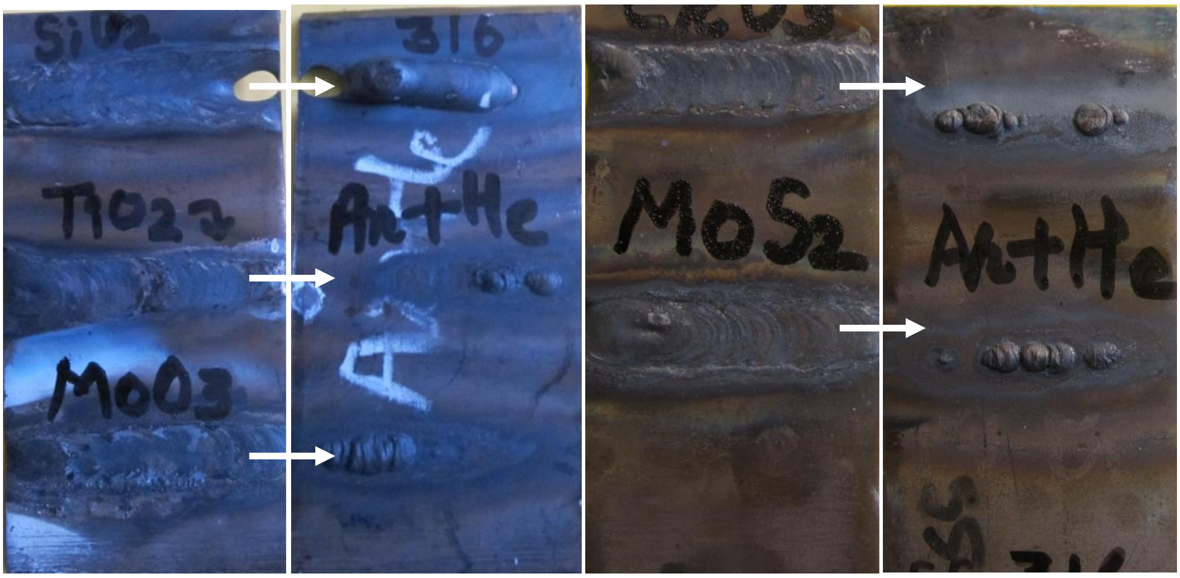

Figure 3.51: Weld bead appearance (top, bottom surface) of A-TIG with five different fluxes for AISI 316 workpiece (125 A, Ar 70% + He 30%, flow rate 10 L/min)

It is also observed that the maximum penetration achieved with SiO_2 (refer Fig. 3.51).

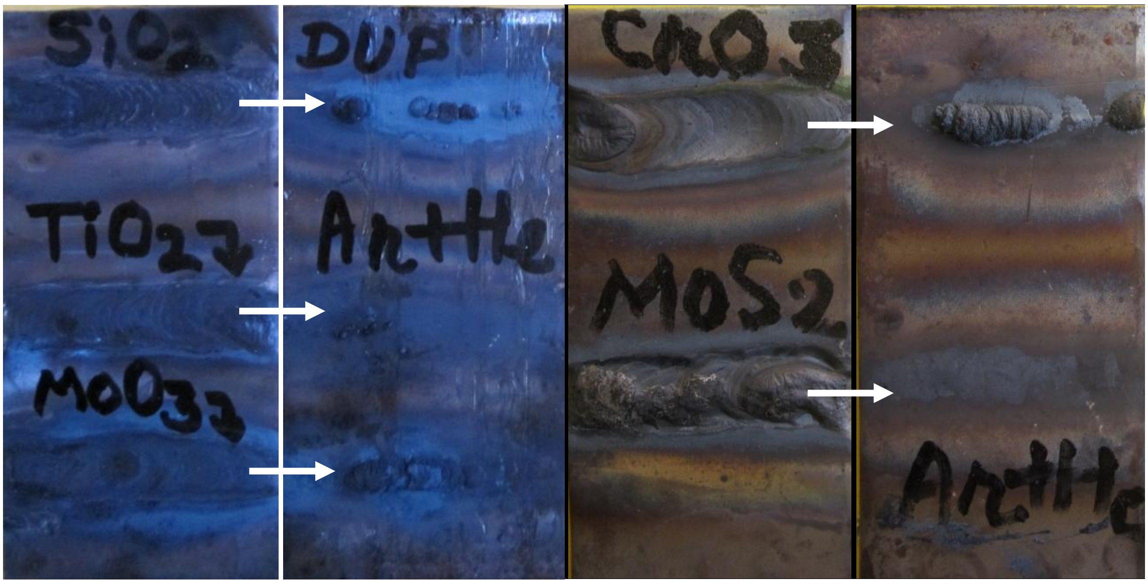

Figure 3.52: Weld bead appearance (top, bottom surface) of A-TIG with five different fluxes for DUPLEX 2205 workpiece (125 A, Ar 70% + He 30%, flow rate 10 L/min)

It is also observed that the maximum penetration achieved with SiO_2, CrO_3 (refer Fig. 3.52)

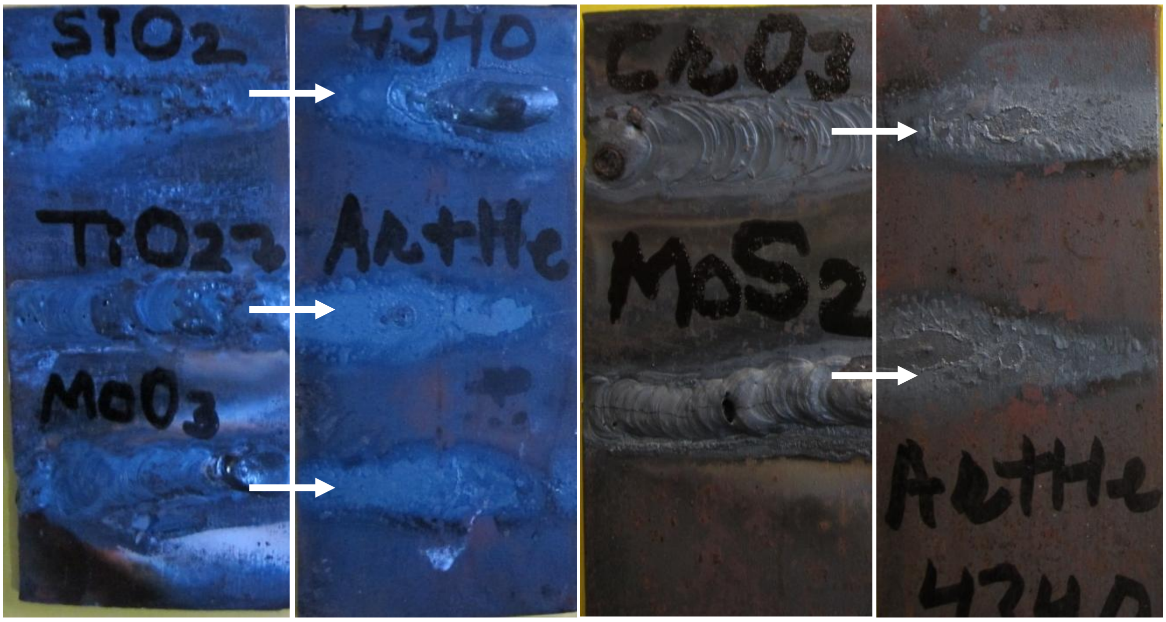

Figure 3.53: Weld bead appearance (top, bottom surface) of A-TIG with five different fluxes for AISI 4340 workpiece (125 A, Ar 70 % + He 30 %, flow rate 10 L/min)

Maximum penetration achieved with SiO_2, CrO_3 (refer Fig. 3.53) but they produced residual slag.

After this, same shielding gas is used for AISI 304 and AISI 316 steel with 100 A and macrographs shown in Fig. 3.54 and Fig. 3.55.

Figure 3.54: Weld bead appearance (top, bottom surface) of A-TIG with five different fluxes for AISI 304 workpiece (100 A, Ar 70 % + He 30 %, flow rate 10 L/min)

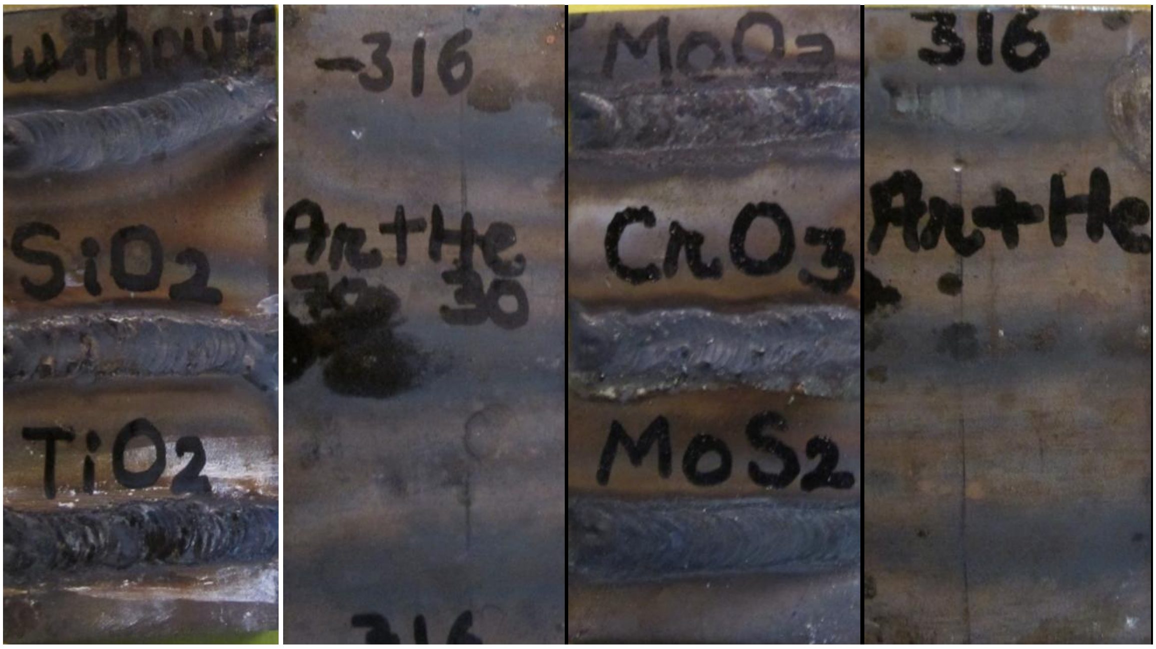

Figure 3.55: Weld bead appearance (top, bottom surface) of A-TIG with five different fluxes for AISI 316 workpiece (100 A, Ar 70 % + He 30 %, flow rate 10 L/min)

Figure 3.56 (a) to (d) represent the comparison of DOP under various shielding gas environment for four workpieces.

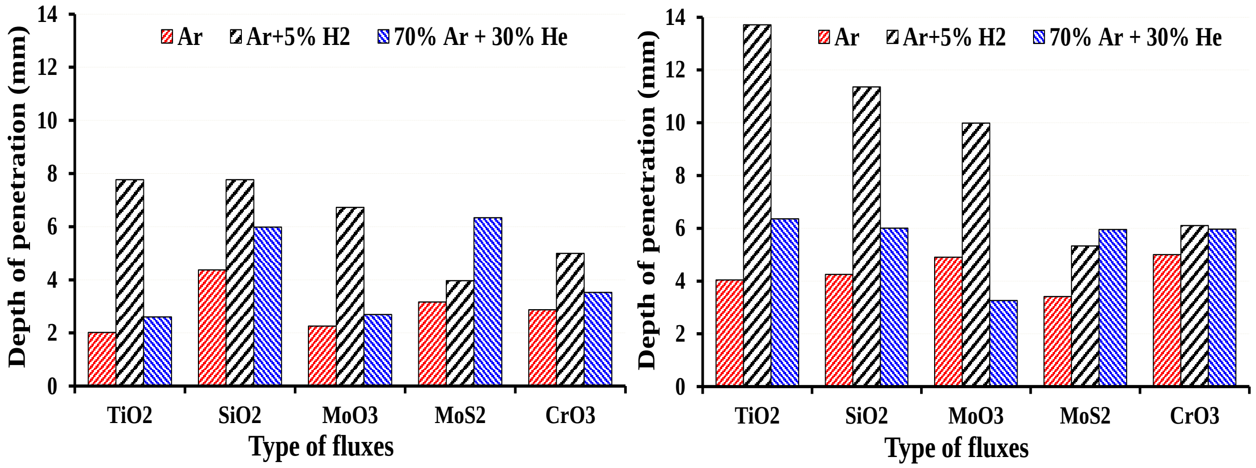

(a) AISI 304 workpiece

(b) AISI 316 workpiece

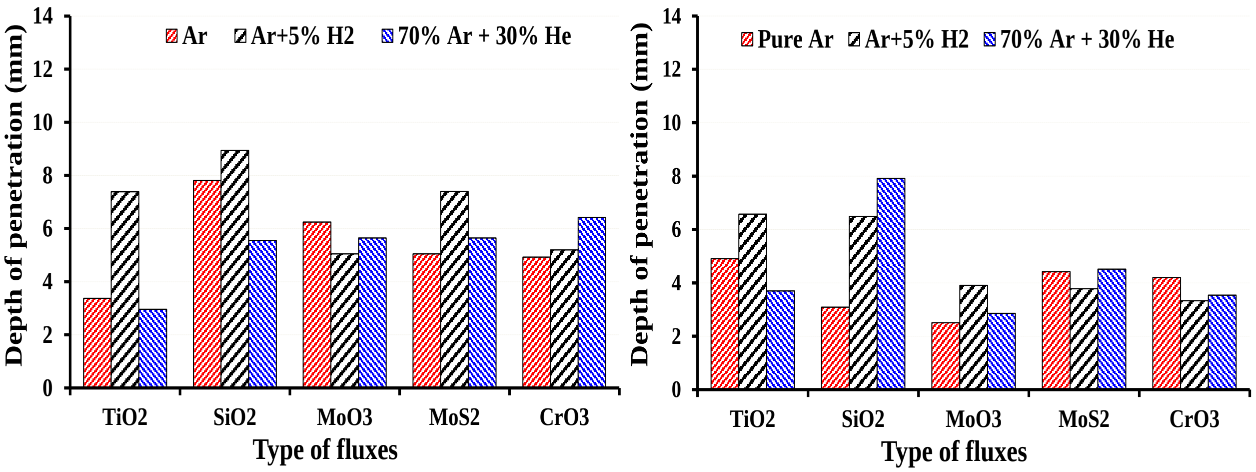

(c) Duplex 2205 workpiece

(d) AISI 4340 workpiece

Figure 3.56: Influence of shielding gas on penetration during ATIG welding with different fluxes for (a) AISI 304, (b) AISI 316, (c) Duplex 2205 and (d) AISI 4340 (125 A, flow rate 10 L/min)

Figure 3.56 indicates that presence of H_2 in shielding gas immensely enhances DOP and more than 200 – 300% increase in penetration is noted as compared to pure Ar when TiO_2, SiO_2 or MoO_3 fluxes are used. Hydrogen addition reduces oxides and significantly increases conductivity of the arc due to its higher thermal conductivity than argon (almost eight to ten times). Conduction of more heat and higher melting efficiency makes it possible to achieve higher depth of penetration. Similarly, addition of He also improves depth of penetration due to the same reason that He also has much higher conductivity than Ar, although He requires higher arc voltage than Ar. However, as helium is lighter than argon, use of helium only may influence the effectiveness of shielding and will require higher gas flow rate in order to provide good shielding. Thus, the results indicate that a higher DOP is possible to obtain by adding small amount of H_2 in shielding gas and a higher welding speed can be achieved to improve the productivity.

Chapter 4

Parametric Study during A-TIG for Mechanical and Metallurgical Study

4.1 Introduction

Mechanical and metallurgical study is concerned primarily with response of metals to forces and loads. The forces may arise from the use of from the use of metal as a member or part in a structure or machine, in which case it is necessary to know something about the limiting values which can be understood without failure. Mechanical and metallurgical study is a combination of many disciplines and approaches to the problem of understanding the response of materials to forces. In mechanical and metallurgical study emphasis is placed on the interpretation of tests and on the effects of metallurgical variables on the mechanical behavior. When mechanical behavior is understood in terms of metallurgical structure it is generally possible to improve the mechanical properties or at least control them.

Carbon steels and stainless steels are the most widely used materials for uncountable engineering applications and depth of penetration and speed of welding during TIG are low for such materials. Helium as shielding gas improves welding speed reasonably and increases bead penetration marginally in comparison to argon. A modification over the conventional TIG where a fine layer of activated flux (called activated TIG; ATIG) is used increases the penetration depth.

In second part of work, a parametric study is carried out during A-TIG welding of AISI 304 with five different fluxes/compounds such as TiO_2, SiO_2, MoS_2, MoO_3, and CrO3 along with no flux condition. Filler metal of E 304L is used at two different welding speed for two different shielding gases (Ar and $Ar+5\%H_2$) to find out the effect of fuxes, current, shielding gas flow rate, electrode tip angle and torch angle on the welding morphology and its mechanical properties.

4.2 Experimental Design

In any experimental study, if the experimental test procedure or method is time consuming to satisfy the desired objectives, so to gain most information from which valid conclusions may be drawn with the least number of experiments is an important requirement. Taguchi experimental technique provides well balanced and systematic approach with reduced “variance” for the experiments (based on Orthogonal Array) to determine optimum setting of control parameters for its performance. It involves lay down the experimental condition using specially constructed table kNown as “Orthogonal Arrays”. To overcome this situation orthogonal arras (OAs) technique is used. OAs is the special experimental designs which require a small number of experimental trials to help to find the main factor effects. The most favourable technique in Taguchi experimental technique is the design of experiment which lies in selection variable control factors. So, the number of factors which are not significant, included initially may be excluded at the selection stage of controlled parameters.

Calculation of DOF

DOF denotes the numbers that are free to vary [Howell, 1992] or the number of independent comparison that can be made in an experiment. Actually, the number of factors considered for experiments and their respective levels determine the total degree of freedom required for designing OAs.

Mathematically, *DOF = n-1,* where n is the level of each factor. Table 4.2 represents the number of factors and their DOF, which are taken in this study.

Table 4.1: Factors and degrees of freedom

S. No.	Factors	Degree of freedom
1.	Flux	5
2.	Current	2
3.	Gas flow rate	2
4.	Vertex angle of electrode	2
5.	Torch angle to the job	2

As it has been observed from result of chapter 3 that the use of $Ar+5\%H_2$ as a shielding gas in case of A-TIG welding increase the depth of penetration significantly, so it is decided to find out the most prominent speed of welding to justify the productivity of A-TIG welding in case of both Ar and $Ar+5\%H_2$ shielding environment. So, for the same a trial of A-TIG welding bead at different speed is done to check the effect of speed on the penetration.

Figure 4.1: Macrograph showing weld bead appearance of A-TIG welding on AISI 304 at 175 A, with Ar+5%H_2 as shielding at a flow rate of 10 L/min at welding speed of 3 mm/sec.

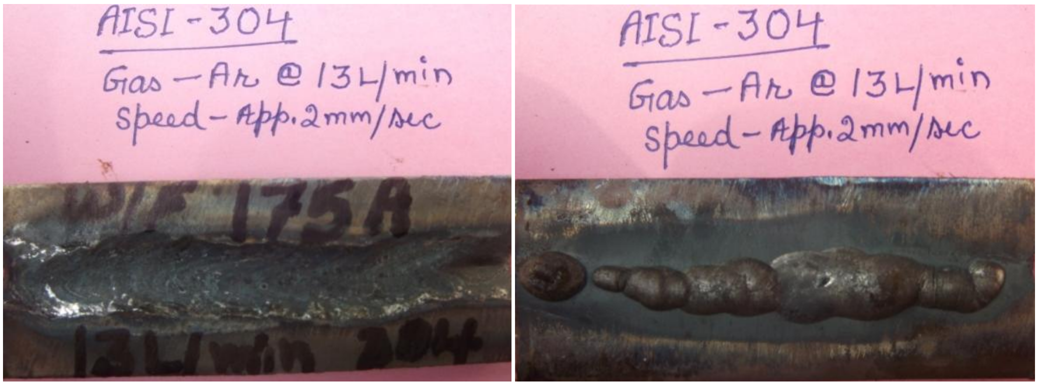

Figure 4.2: Macrograph showing weld bead appearance of A-TIG welding on AISI 304 at 175 A, with Ar as shielding at a flow rate of 113 L/min at welding speed of 2 mm/sec.

From Fig. 4.1 it is clear that metal penetrate beyond the thickness of the workpiece, but hot crack is found in the weld bead. This welding is done at 2 mm/s with Ar+5%H_2 shielding at 175 A current. Whereas the Fig. 4.2 represents the weld appearance with a gas flow rate of 13 L/min and it is found quite satisfactory. Hence, it is decided that the welding will be done at two different speeds for different gases. The main difference between these two studies will be of welding speed to justify the phenomenon of productivity. In case of Ar the speed of welding = 2 mm/s and in case of Ar+5%$H_{2,}$ the speed of welding = 3 mm/s will be maintained. Hence, after the study of single compound (TiO_2) and fourteen different compounds or fluxes which is previously done in chapter 3, so the vertex angle of electrode, type of flux, current, torch angle, gas flow rate and welding speed may be used as part of study and may also influence the result.

4.2.1 Orthogonal Array for A-TIG with Ar Shielding

After deciding the factors and their level the controlled parameters with various levels (shown in Table 4.2) are to be used for Ar shielding.

Table 4.2: Variable process parameters and levels for the welding of AISI 304 with Ar as shielding gas

S. No.	Parameters	Unit	Levels
1.	Flux	-	No flux, TiO_2, SiO_2, MoS_2, MoO_3, CrO_3
2.	Current	A	125, 150, 175
3.	Gas flow rate	L/min	10 , 13, 16
4.	Vertex angle of electrode	Degree	60, 75, 90
5.	Torch angle to the job	Degree	45, 65, 85

Finally, the influence of five different parameters with mixed level of factors, L18 is to be used for Ar study. The welding speed of 2 mm/s will be used for the orthogonal arrays of Table 4.3.

Table 4.3: Orthogonal array for A-TIG welding of AISI 304 under Ar shielding

Exp. No.	Flux	Current (A)	Gas flow rate (L/min.)	Tip angle (Degree)	Torch angle (Degree)
1	No	125	10	60	45
2	No	150	13	75	65
3	No	175	16	90	85
4	TiO_2	125	10	75	65
5	TiO2	150	13	90	85
6	TiO_2	175	16	60	45
7	SiO_2	125	13	60	85
8	SiO_2	150	16	75	45
9	SiO_2	175	10	90	65
10	MoO_3	125	16	90	65
11	MoO_3	150	10	60	85
12	MoO_3	175	13	75	45
13	CrO_3	125	13	90	45
14	CrO_3	150	16	60	65
15	CrO_3	175	10	75	85
16	MoS_2	125	16	75	85
17	MoS_2	150	10	90	45
18	MoS_2	175	13	60	65

4.2.2 Orthogonal Array for A-TIG with Ar+5 % H_2 Shielding

The same parameters will be used for Ar+5%H_2 study which are selected for Ar study is shown in Table 4.4.

Table 4.4: Variable process parameters and levels for the welding of AISI 304 with Ar+5%H_2 as shielding gas

S. No.	Parameters	Unit	Levels
1.	Flux	-	No flux, TiO_2, SiO_2, MoS_2, MoO_3, CrO_3
2.	Current	A	125, 150, 175
3.	Gas flow rate	L/min	10 , 13, 16
4.	Vertex angle of electrode	Degree	60, 75, 90
5.	Torch angle to the job	Degree	45, 65, 85

The main difference between these two studies is of welding speed. The welding speed of 3 mm/s will be used for the orthogonal arrays of Table 4.5.

Table 4.5: Orthogonal array for A-TIG welding of AISI 304 under Ar+5%H_2 shielding

Exp. No.	Flux	Current (A)	Gas flow rate (L/min.)	Tip angle (Degree)	Torch angle (Degree)
1	No	125	10	60	45
2	No	150	13	75	65
3	No	175	16	90	85
4	TiO_2	125	10	75	65
5	TiO2	150	13	90	85
6	TiO_2	175	16	60	45
7	SiO_2	125	13	60	85
8	SiO_2	150	16	75	45
9	SiO_2	175	10	90	65
10	MoO_3	125	16	90	65
11	MoO_3	150	10	60	85
12	MoO_3	175	13	75	45
13	CrO_3	125	13	90	45
14	CrO_3	150	16	60	65
15	CrO_3	175	10	75	85
16	MoS_2	125	16	75	85
17	MoS_2	150	10	90	45
18	MoS_2	175	13	60	65

4.2.3 Constant factors for experiments

The other following factors for the experiments will be to maintained constant for both types of study.

- Cu plate is used on both ends of the joint line for easy arc initiation and to avoid crater at the end.
- Filler diameter is same for both types of experiments.
- Filler material is of same composition (E 304 L).
- Flux is applied by same methods.
- For all welding, constant voltage = 22 volt is maintained.
- For A-TIG welding with Ar, speed of welding = 2 mm/s and in case of Ar+5%H_2 the speed of welding of 3 mm/s is maintained.

4.3 Experimental and Measurement Setup

4.3.1 Experimental Details

Activated TIG welding is carried out by making square butt joint (with no root gap) between two austenitic stainless steels (AISI 304) plates. The workpieces of 6 mm thickNess and of size 100 mm × 84 mm is used. Chemical compositions of workpiece material are checked by spectroscopy (Foundry Master optical emission spectroscopy, Germany) and the chemical compositions are provided in Table 4.6.

Table 4.6.—Chemical compositions of workpiece of AISI 304 workpiece

Material	Compositions in percentage											
	C	Cr	Ni	Mn	Si	S	P	Mo	Cu	V	Fe	Co
AISI 304	0.051	19.2	8.36	1.39	0.461	0.029	0.030	0.212	0.337	0.047	69.7	0.125

All workpieces are ground by a precision surface grinder and surfaces are cleaned by buffing operation and with acetone to remove surface impurities and contaminants. Workpiece materials after grinding and cleaning are shown in Fig. 4.3.

Figure 4.3: Cleaned workpiece (before welding)

Each of the selected individual flux is mixed with acetone at suitable proportion to prepare a paste. With the help of a brush, the paste is applied on joint surface (refer Fig. 4.4) and a coating of the flux for around 12 mm width is applied where the welding is to be carried out. ThickNess of flux coating layer could vary between 20–25 µm and welding is carried out after the acetone completely evaporates and flux layer dries out.

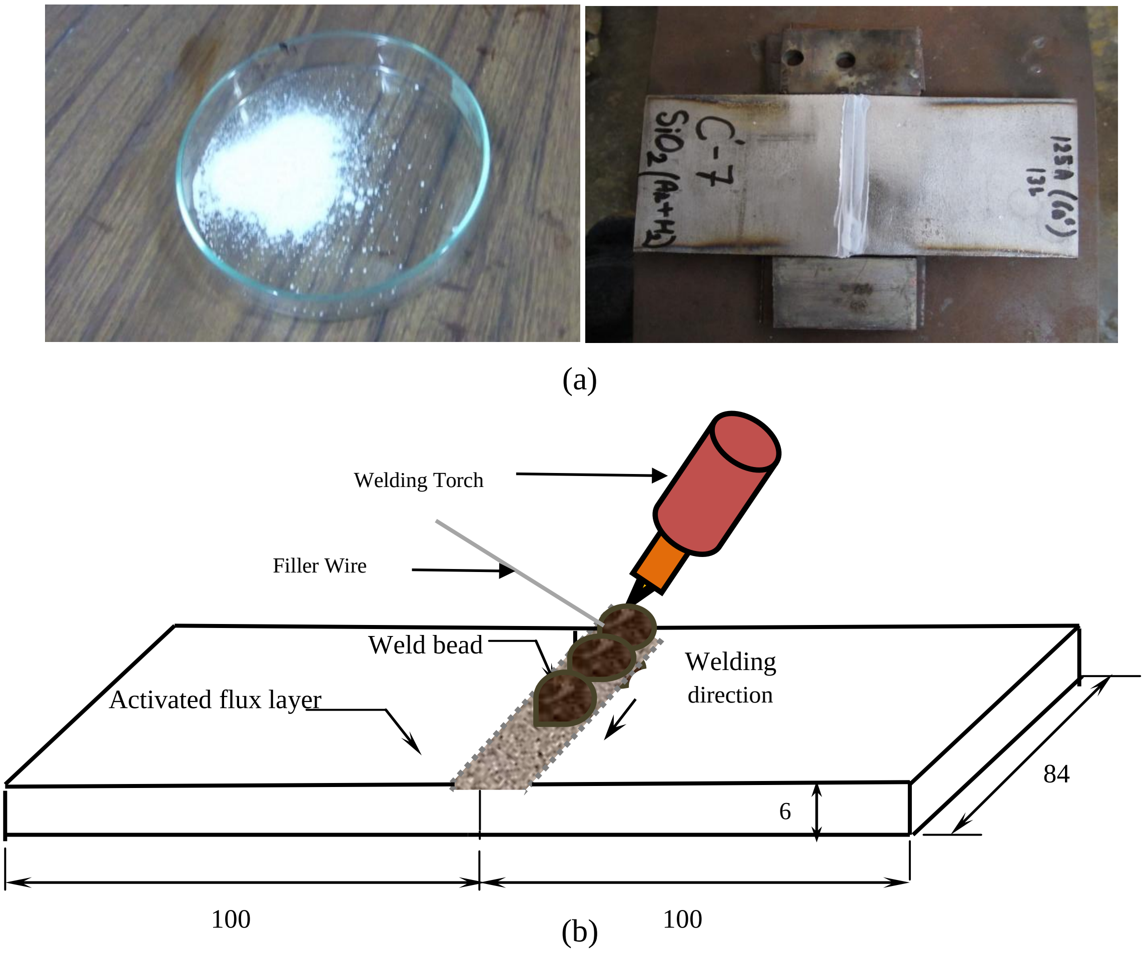

All dimensions are in mm.

Figure 4.4: Schematic diagram to illustrate ATIG welding arrangement

For all welding ER304L filler wire of 2.5 mm diameter is used (refer Fig. 4.5).

Figure 4.5: Filler wire (ER304L)

Electrodes EWTh-2 (2% thoriated tungsten) electrodes are used. Electrodes of three different tip angles i.e. 60°, 75° and 90° are used for welding. Figure 4.6 shows the tips of the electrodes. Each electrode tip is ground before each single welding during the experimental study.

Figure 4.6: Thoriated tungsten electrodes with different vertex angle

Two types of shielding gases Ar and Ar+5%H_2 are used in and their storage cylinders are shown in Fig. 4.7.

Figure 4.7: Cylinders containing Ar and Ar+5%H_2 used for A-TIG shielding gas

Five different fluxes such as TiO_2, SiO_2, MoS_2, MoO_3 and CrO_3 are used in this study and the loose powders are shown in Fig. 4.8(a). Each single flux is mixed with acetone to make a suitable paste and is applied on the plate top surface with the help of brush for about 12 mm width and thickNess around 20–25 µm (refer Fig. 4.8(b)). The flux is allowed to dry and it is ensured that acetone completely evaporates before the start of welding.

(a) (b)

Figure 4.8: (a) Different type of fluxes (b) Flux coated Sample

A special jig is fabricated for tacking of workpieces prior to welding for making butt joints. The jig is shown in Fig. 4.9. Tacking is done from back side at the two ends.

Figure 4.9 Tacked workpieces in jig

All the A-TIG welding of AISI 304 plates is completed by TIG welding setup (make: Techno Weld, India) which is available in central workshop, which has a capacity of 300 A at 60% duty cycle. In A-TIG welding 2% thoriated tungsten (EWTh-2) electrode of diameter 3.2 mm is used. The welding setup is shown in Fig. 4.10.

Figure 4.10: A-TIG welding setup

4.3.2 Measurement Setup

After selecting the variable parameters for A-TIG welding it is necessary to investigate the results from these parameters. To investigate the results from these selected parameters measurement setup are required. For measurement setup, universal testing machine (for face bend test), microhardness tester, toughness test machine (Charpy setup), SEM and dye penetrant test, Optical microscopy machine are used. Brief introduction of these measurement setup are as follows:

- Bend Test
- Indentation Microhardness Test
- Toughness test (Charpy)
- SEM analysis
- Optical Microscopy
- Dye Penetrant Test

Bend Test (Face Bend)

There are various types of bend tests which are used to evaluate the ductility and soundness of welded joint. Two types of bend test specimens are preferred for guided bend test. They are:

a) Face bend test (transverse)
a) Root bend test (transverse)

For the present work face bend test is done as per ASTM standards for testing of steels and the dimensions are shown in Fig. 4.11.

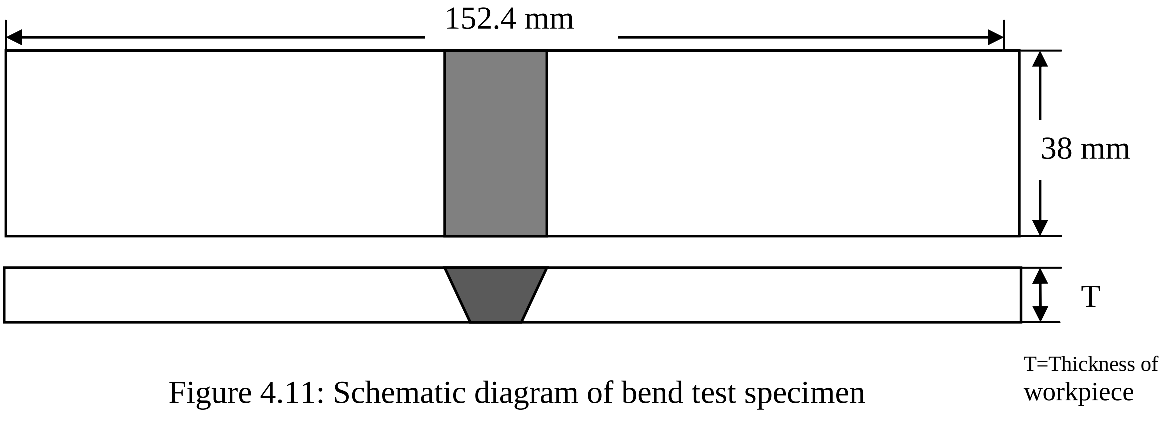

Figure 4.11: Schematic diagram of bend test specimen

A face bend test requires bending with the inside surface of the plate against the plunger. Face bend test is done on universal testing machine (Make: Fuel Instruments and Engineers Pvt. Ltd., capacity of 1000 KN) as sown in Fig. 4.12. Failure of the bend test depends upon the appearance of cracks in the area of the bend, of the nature and extent described in the product specifications.

Figure 4.12: Universal testing machine setup
(Courtesy: Venus Testing Services Pvt. Ltd, Patiala)

Indentation Microhardness Test

Microhardness test are used to determine the microhardness of substance is an important parameter to define the strength of its material. Actually it determines the hardness of a material to deformation. In micro indentation testing the hardness number is based on measurements made of the indent formed in the surface of the test piece, means the surface area of the indent. In the present work microhardness of the weld region (Fusion zone and HAZ) is measured by using the computer interfaced microhardness tester (Make: Omni Tech, Pune), as shown in Fig. 4.13. In this the diagonals of the indents formed by a pyramid shaped diamond indenter is measured with the help of Quantimet software at 40X magnification, which give a direct hardness Vickers number (HVN) for the measured microhardness. First the software needs to be calibrated. The load applied for the indenter is 300 gm for AISI 304 stainless steel with a dwell time of 20 seconds. The Samples for microhardness are first cut, ground, polished (by polishing machine) by using emery papers of 300, 600, 1000 and 2000 numbers and etched.

Figure 4.13: Microhardness test machine

Toughness test (Charpy) setup

The toughness of a material can be defined as, the ability of a material to absorb energy (per unit volume) without breaking or the resistance offered by the material against the sudden applied load. Charpy test is used to measure the toughness of the welded joint. The all specimens for Charpy test is made as per sketch given in Fig. 4.14.

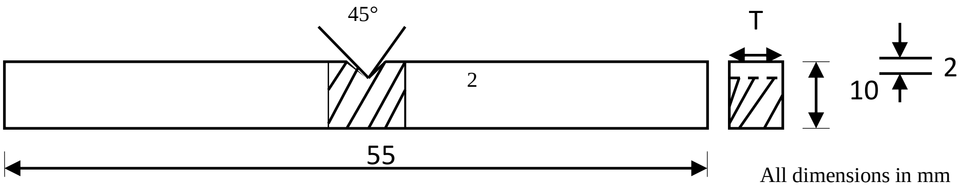

Figure 4.14: Detail dimension of Charpy test specimen

As plastic deformation capability of the test piece increases, the area under the curve also increases and absorbed energy and respectively toughness increase. For Charpy test, a notch is provided in the center of the test piece. Specimen is placed on supports or anvil so that the blow of hammer is opposite to the notch. The material is placed at simple supported position in Charpy test and it is place such that when hammer strikes the work piece, it will generate tensile force in it. For Charpy impact test, the standard size of specimen is 55 x 10 x 10 mm. An indicator is attached to the machine which shows the reading of toughness in Joule. There is a scale for impact reading and its one division equals to 2 Joule. First free energy is calculated without placing specimen and then all specimens are tested. The machine used for making notch and the machine used for toughness test (Charpy) is shown in Fig. 4.15 (a) and (b). The angle for striking hammer is maintained at 135° and the weight of hammer is 16.4 kg.


(a) (b)

Figure 4.15: (a) Shaper machine for making notch, (b) Charpy test machine
(Courtesy: (a) Central workshop, Thapar University, Patiala (b) Chandigarh University, Ghaduann)

Metallurgical study: For metallurgical study, different kinds of microscopes are used. The metallurgical and measuring microscopes are available in Mechanical Engineering department, Thapar University; Patiala (Refer Fig. 4.16). Metallurgical microscope can magnify the Samples at 10X, 20X, 50X and 100X. It is helpful in checking the different phases present in the structure and metallurgical effect of welded Samples. It has a camera attached to it which can take snapshots by enlarging the images. It is attached with computer which shows the different views in a proper manner. In this computer ‘LEICA’ software is used to watch the images in computer screen. With the help of this software annotation can be done on the images. The brightness of the image can also be adjusted. It can view the effect of different parameters of welding in fusion zone or in HAZ or the interface of these zone can be studied in this machine. It is helpful in predicting the behaviour of the surface.

Fig 4.16: Metallurgical Microscope

Scanning Electron Microscopy (SEM): The scanning electron microscopy (SEM) is used to produce images at different magnification level of the Sample surface by scanning over it with a focussed beam of electrons. Instead of light focussed electron beam is used in this method. When the specimen is irradiated with a fine electron beam (called an electron probe), secondary electrons are emitted from the specimen surface. Topography of the surface can be observed by the two-dimensional scanning of the electron probe over the surface and acquisition of an image from the detected secondary electrons (Web reference: www.jeol.com). This SEM (Make: JSM-6510LV, JEOL Ltd, Tokyo, Japan, Fig. 4.17) is used to observe the microstructure of selected A-TIG Samples under different gas shielding. SEM analysis is a “non-destructive” test.

Figure 4.17: Scanning electron microscope
(Courtesy: SAI Lab, Thapar University cAus, Patiala)

Dye Penetrant Test

Dye Penetrant Test (DPT) is used to detect the surface flaws and is performed on the welding region after buffing of welding Samples. For performing of this test three spray bottles of Penetrant ORION 115 P (red dye), Penetrant Remover ORION 115R, and developer ORION 115 D (Make: Oriental Chemical Works, Kolkata) is used as shown in Fig. 4.18. To perform this test minimum 15 min. are required for Penetrant to penetrate in the surface flaws.

Figure 4.18: Cleaner, penetrant and developer used for DPT

4.4 Result and Discussions

This chapter present the effect of selected variable parameters such as Flux, Current, Gas flow rate, Vertex angle of electrode, Torch angle to the job under different gas shielding (Ar and Ar+5% H_2) on the mechanical properties, weld morphology and microstructures of the joint by optical microscopy and SEM. Taguchi experimental technique is used to study the effect of above mentioned parameters. Except flux (5 fluxes + 1 no flux) all other parameters are varied at three levels. So, L_{18} orthogonal arrays having 18 experiments for mixed level design is used for two different gases (Ar and Ar+5% H_2). After conducting the experiments as per L_{18} OA's, various destructive and non destructive tests are performed and their result are analyse by using analysis of variance (ANOVA), main effect plot and response table are obtained to find the optimal design. In this chapter the effect of significant parameters and their behaviour, which are obtained from the mean effect plot are also discussed.

Figure 4.19 and 4.20 represents the macrographs of weld bead appearance for TIG and A-TIG welding under Ar and Ar+5%H_2 shielding environment.

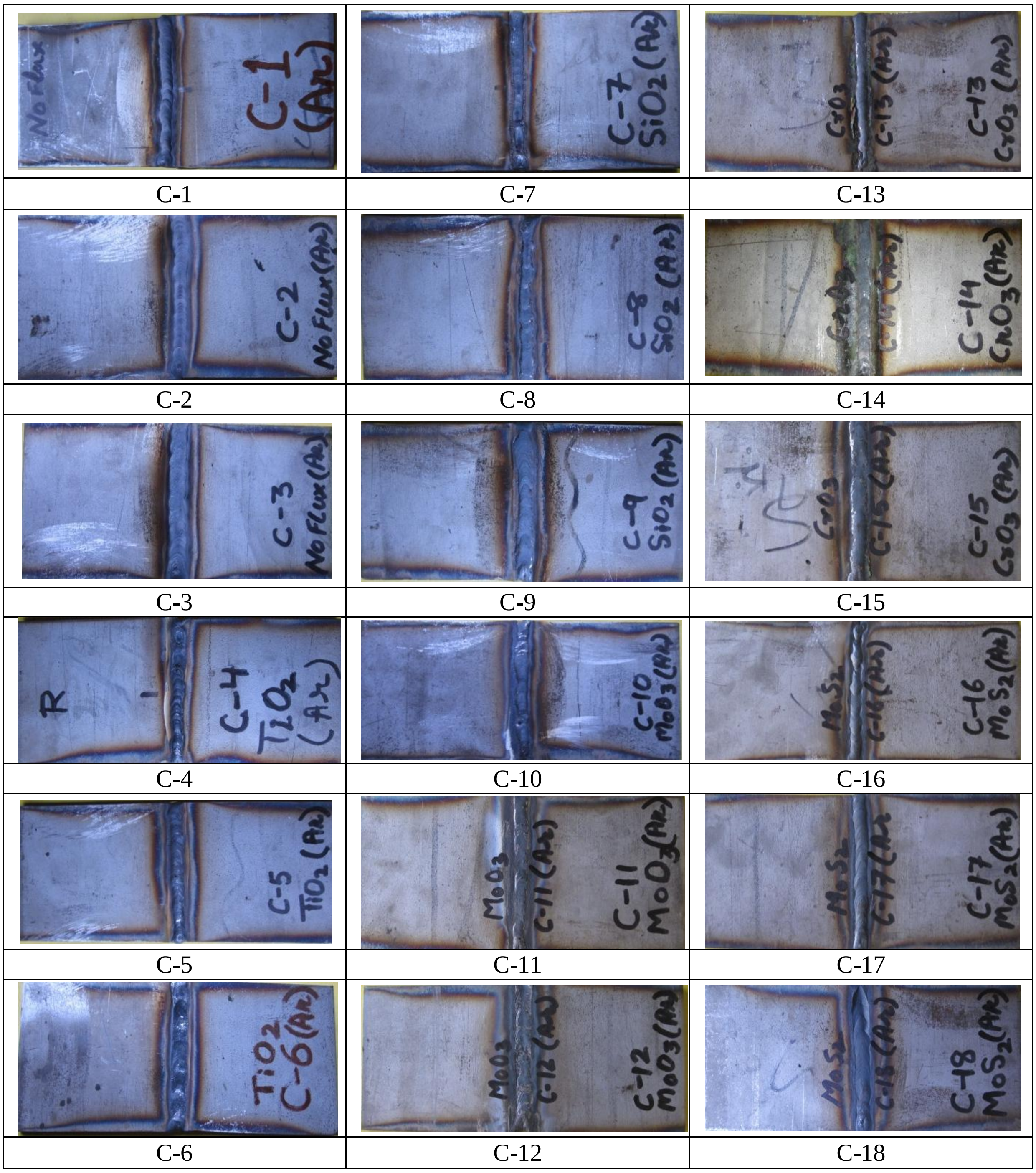

C-1 C-7 C-13

C-2 C-8 C-14

C-3 C-9 C-15

C-4 C-10 C-16

C-5 C-11 C-17

C-6 C-12 C-18

Figure 4.19: Macrograph showing the weld bead appearance of A-TIG welding of AISI 304 Under Ar shielding

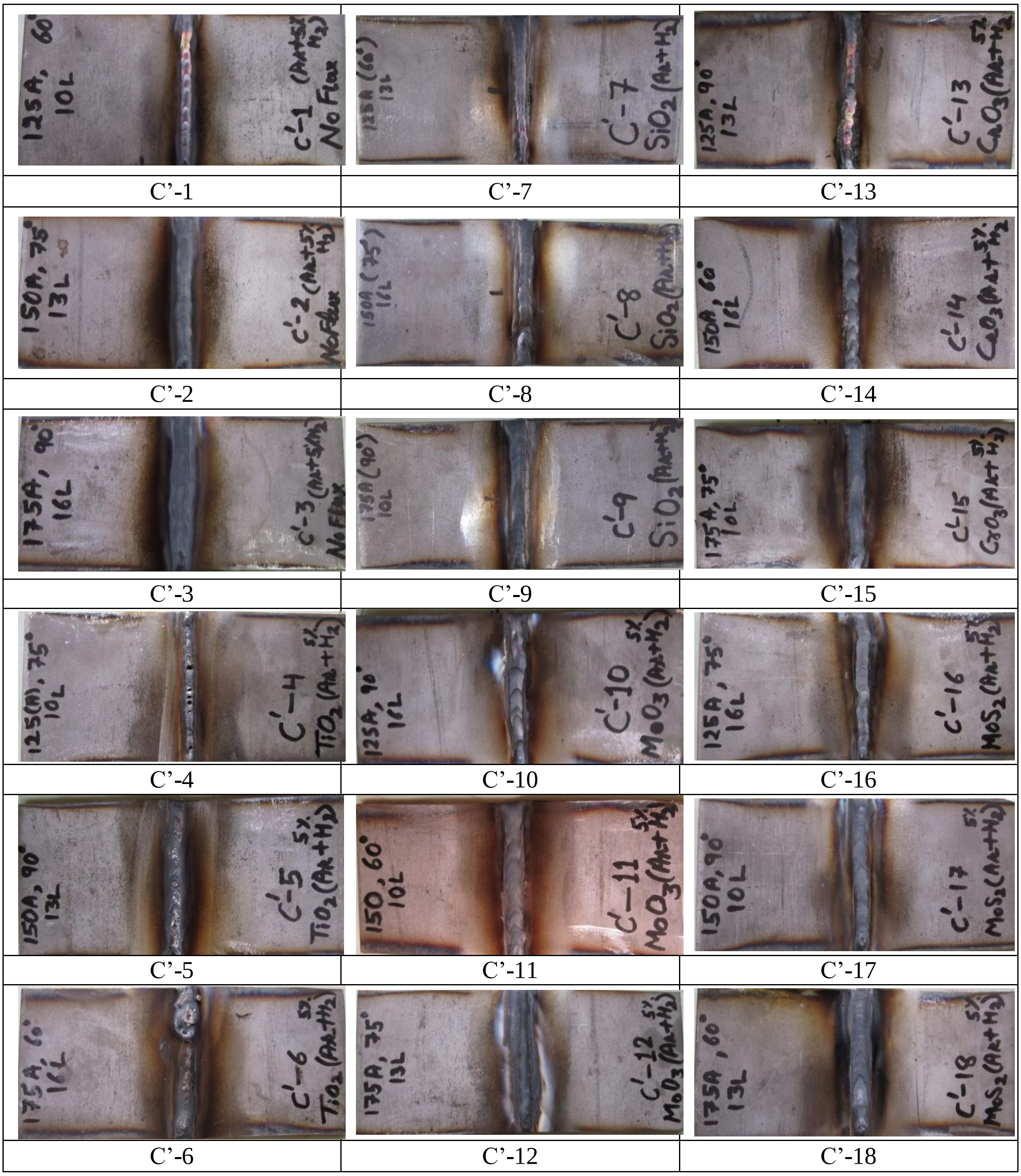

C'-1 C'-7 C'-13
C'-2 C'-8 C'-14
C'-3 C'-9 C'-15
C'-4 C'-10 C'-16
C'-5 C'-11 C'-17
C'-6 C'-12 C'-18

Figure 4.20: Macrograph showing the weld bead appearance of A-TIG welding of AISI 304 Under Ar+5% H_2

4.4.1 Face Bend Test of Samples Joint Using Ar Shielding Gas

According to ASTM standard E190 designate for guided bend test and is used here to find the ductility of the weld. So, transverse face bend test method is used in this study to investigate the ductility at maximum load absorbing capacity of the A-TIG welded joint. AISI 304 stainless steel is used to make square butt joint under two different shielding environments

(Ar and Ar+5% H_2). The specimens cut are approximately 1.5 in. (38 mm) wide; 8 in. (152 mm) in length with the weld at the centre and the load applied from bottom of weld (refer Fig. 4.11). The plunger size, to apply the load is selected as per ASTM standard (4t) and the gap between the supported rollers is also maintained (6t+1/8in.) distance. All face bend specimens of Ar study are shown in Fig. 4.21.

Figure 4.21: Face bend specimen of A-TIG welding of AISI 304 under Ar shielding

Face bend tests are performed on universal testing machine of 1000 KN load capacity and the results of maximum bending load are shown in Table 4.7.

Table: 4.7: Result of face bend test of AISI 304 under Ar shielding

Sample. No.	Sample Code No.	Flux	Current (A)	Gas flow Rate (L/min)	Tip/Vertex angle of electrode (°)	Torch angle (°)	Max. Bending Force (kN)
1	C-1	No	125	10	60	45	10.30
2	C-2	No	150	13	75	65	14.00
3	C-3	No	175	16	90	85	13.25
4	C-4	TiO_2	125	10	75	65	13.05
5	C-5	TiO_2	150	13	90	85	14.65
6	C-6	TiO_2	175	16	60	45	22.60
7	C-7	SiO_2	125	13	60	85	12.20
8	C-8	SiO_2	150	16	75	45	17.15
9	C-9	SiO_2	175	10	90	65	20.00
10	C-10	MoO_3	125	16	90	65	10.55
11	C-11	MoO_3	150	10	60	85	12.75
12	C-12	MoO_3	175	13	75	45	14.70
13	C-13	CrO_3	125	13	90	45	15.65
14	C-14	CrO_3	150	16	60	65	21.20
15	C-15	CrO_3	175	10	75	85	15.40
16	C-16	MoS_2	125	16	75	85	9.95
17	C-17	MoS_2	150	10	90	45	10.90
18	C-18	MoS_2	175	13	60	65	16.75

From Table 4.7 it is concluded that the maximum bending force is obtained from Sample- 6 (C-6) and the minimum bending force is obtained from Sample-16 (C-16).

Analysis of Variance for Face Bend Test

To find out the significance of various factors like flux, current, gas flow rate, tip/vertex angle of electrode and torch angle under Ar shielding on the maximum bending strength ANOVA is performed at obtained data with 90% confidence level. As F-test is normally used to find out the most significant factor correspond to each input parameter values and it is based on the principle that larger the F value, greater will be the effect of that parameter. The result obtained from ANOVA and response table for the maximum bending strength or maximum bending load for the A-TIG welding joint of AISI 304 are shown in Table 4.8 and Table 4.9. From Table 4.8 it is clear that the maximum percentage contribution is obtained from the factor flux and the least percentage contribution of factor gas flow rate.

Table 4.8: ANOVA for maximum bending force for the A-TIG welding joint of AISI 304 under Ar shielding

Source	Unit	DOF	SS	Variance	F-value	Percentage contribution
Flux	-	5	84.92	16.984	5.17	36.40
Current	A	2	81.41	40.703	12.39	34.90
Gas flow	L/min	2	12.65	6.324	1.93	5.42
Tip	°	2	13.92	6.961	2.12	5.97
Torch angle	°	2	27.26	13.630	4.15	11.68
Residual Error	-	4	13.14	3.284		5.63
Total	-	17	233.29			100

The response Table of various input parameters with their rank in term of significance is shown in Table 4.9 and from this table it is found that the current plays most significant factor with rank 1 but the least significant factor is tip angle of the electrode with rank 5.

Table 4.9: Response Table for maximum bending force the A-TIG welding joint of AISI 304 under Ar shielding

Level	Flux	Current (A)	Gas Flow (L/min)	Tip Angle (°)	Torch Angle (°)
1	12.52	11.95	13.73	15.97	15.22
2	16.77	15.11	14.66	14.04	15.93
3	16.45	17.12	15.78	14.17	13.03
4	12.67				
5	17.42				
6	12.53				
Delta	4.90	5.17	2.05	1.93	2.89
Rank	2	1	4	5	3

The main effect plot of the input parameters for the A-TIG welding of AISI 304 stainless steel under the shielding of Ar gas is shown in Fig. 4.22. The X-axis represents the process parameters and the Y-axis represents the bending load with the mean line. Fig. 4.22 shows that TiO_2, SiO_2 and CrO_3 are the most significant fluxes and when the current increases then the bending strength also increases significantly. It is also concluded that the 60° tip angle is best as compared with 75° and 90° tip angles. The bending force/load is also affected by the gas flow rate means when gas flow rate increases then bending load also increases with respect to the flow rate of the gas.

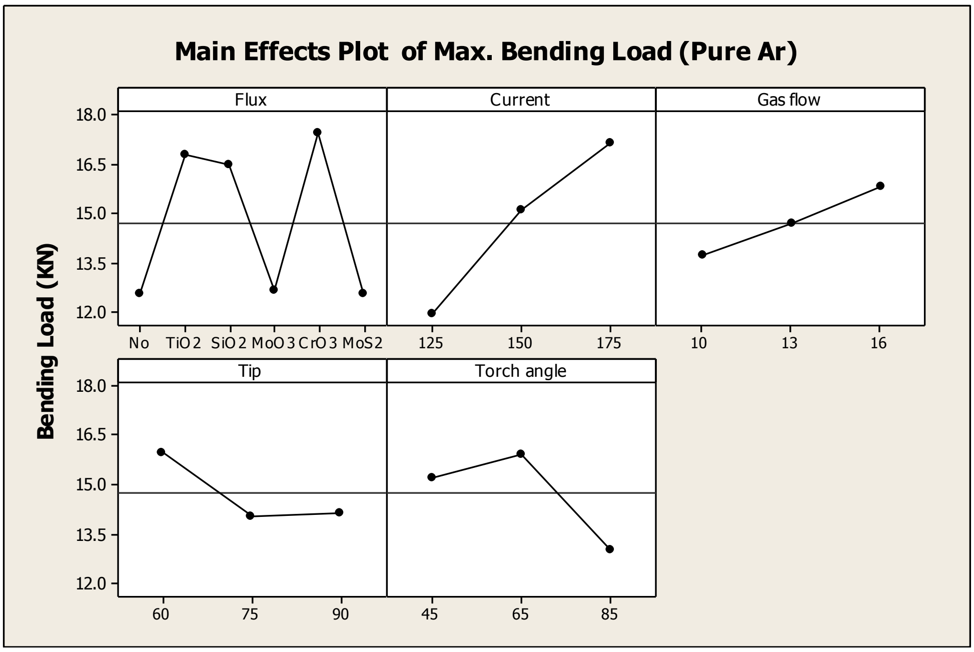

Figure 4.22: Main effect plot to show the influence of various input parameters on bending force of the joint of A-TIG welding of AISI 304 under Ar shielding

The 65° torch angle is the most prominent torch angle in case of A-TIG, whereas 85° torch angle shows that reverse effect because small weld puddle is created in case of 85°, which result into the small fusion zone, hence it took less bending force as compare to 65°.

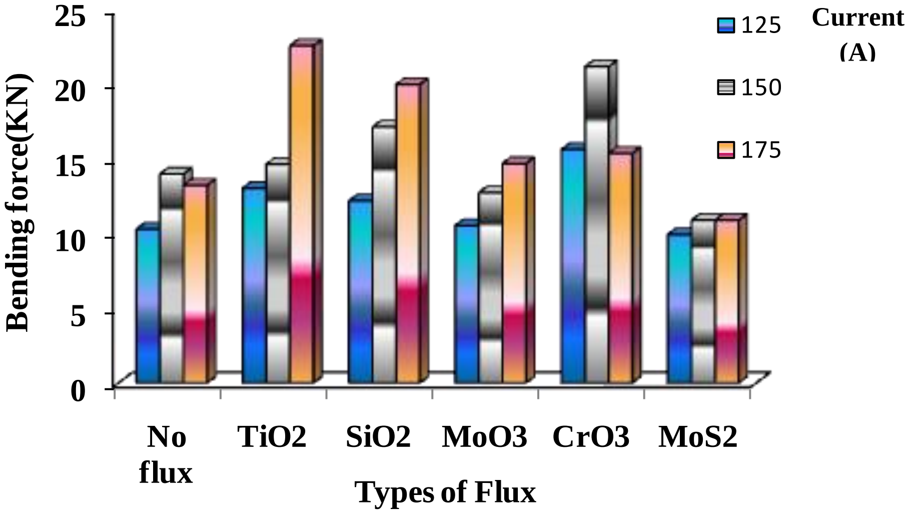

Figure 4.23: Effect of different fluxes on bending force at different current level during A-TIG welding of AISI 304 under Ar shielding

Figure 4.23 represent the effect of different fluxes on bending force at different current level during A-TIG welding of AISI 304 under Ar shielding. It can be easily observed from the bar graph that as the heat input increases with the increase of current then joints of A-TIG took maximum load, which shows joint have maximum strength. To achieve maximum strength flux like TiO_2, SiO_2 and CrO_3 plays an important role as already prove in chapter 3. The another thing to notice that in case of CrO_3 flux the maximum bending load is taken at 150 A current which is less than 175 A. This is due to the torch angle (refer Fig. 4.23).

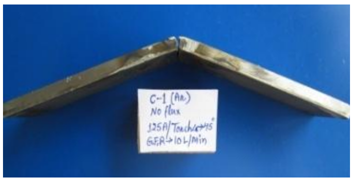		
C-1	C-7	C-13
		
C-2	C-8	C-14
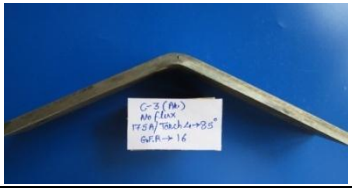		
C-3	C-9	C-15
		
C-4	C-10	C-16
		
C-5	C-11	C-17
		
C-6	C-12	C-18

Figure 4.24: Front view of bend test specimen of A-TIG welding of AISI 304 under Ar shielding

After bending it is clearly visible from Fig. 4.24 that the Samples C-6, C-8, C-9, C-12, C-15 and C-18 took "U" shape, which also justifies the results of bending force. The bead appearance of these Samples is shown in Fig. 4.25 and no flaws are present on these welds after complete bending.

	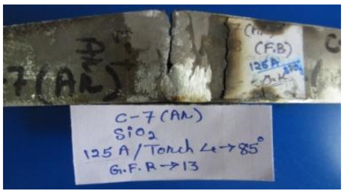	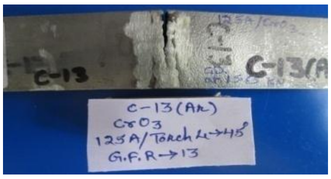
C-1	C-7	C-13
		
C-2	C-8	C-14
		
C-3	C-9	C-15
		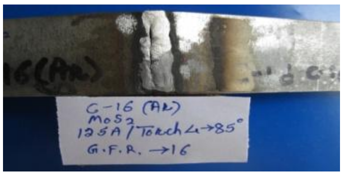
C-4	C-10	C-16
		
C-5	C-11	C-17
		
C-6	C-12	C-18

Figure 4.25: Top view of bend test specimen of A-TIG welding of AISI 304 under Ar shielding

4.4.2 Face Bend Test of Samples Joined Using Ar+5%H_2 Shielding Gas

Same method of study is applied to test A-TIG welded Samples of AISI 304 under Ar+H_2 shielding, which is used for Ar Samples. Fig. 4.26 shows the face bend specimen of Ar+5% H_2 study.

Figure 4.26: Face bend specimen of A-TIG welding of AISI 304 under Ar+5% H_2 shielding

Face bend tests are performed on universal testing machine of 1000 kN load capacity and the results of maximum bending load are shown in Table 4.10.

Table: 4.10: Result of face bend test of AISI 304 under Ar+5% H_2 shielding

Sample. No.	Sample Code No.	Flux	Current (A)	Gas flow Rate (L/min)	Tip/Vertex angle of electrode (°)	Torch angle (°)	Max. Bending Force (kN)
1	C’-1	No	125	10	60	45	12.95
2	C’-2	No	150	13	75	65	10.35
3	C’-3	No	175	16	90	85	12.20
4	C’-4	TiO_2	125	10	75	65	9.40
5	C’-5	TiO_2	150	13	90	85	9.85
6	C’-6	TiO_2	175	16	60	45	13.20
7	C’-7	SiO_2	125	13	60	85	12.05
8	C’-8	SiO_2	150	16	75	45	12.75
9	C’-9	SiO_2	175	10	90	65	10.20
10	C’-10	MoO_3	125	16	90	65	3.95
11	C’-11	MoO_3	150	10	60	85	15.80
12	C’-12	MoO_3	175	13	75	45	7.15
13	C’-13	CrO_3	125	13	90	45	9.05
14	C’-14	CrO_3	150	16	60	65	8.00
15	C’-15	CrO_3	175	10	75	85	8.20
16	C’-16	MoS_2	125	16	75	85	9.60
17	C’-17	MoS_2	150	10	90	45	8.30
18	C’-18	MoS_2	175	13	60	65	8.95

Analysis of Variance for Face Bend Test

To find out the significance of various parameters or the selected factors like flux, current, gas flow rate, tip/vertex angle of electrode and torch angle under Ar shielding on the maximum bending strength ANOVA is performed at obtained data with 90% confidence level. As F-test is normally used to find out the most significant factor correspond to each input parameter values and it is based on the principle that larger the F value, greater will be the effect of that parameter. The result obtained from ANOVA and response table for the maximum bending strength or maximum bending load for the A-TIG welding joint of AISI 304 under Ar+5% H_2 shielding are shown in Table 4.10 and Table 4.11. From Table 4.10 it is concluded that the maximum bending force is obtained from Sample-11 (C’-11) and the minimum bending force is obtained from Sample-10 (C’-10). The another thing to notice that the bending force of Sample 10 is also less than the bending force value of Sample -1 (C’-1) which is also weld at the same level of current. If it compares with the other parameters like torch angle, tip angle of the electrode, then its bending force value is also less than others (refer Table: 4.10). From Table 4.11 it is clear that the maximum percentage contribution is obtained from the factor flux and the least percentage contribution of factor gas flow rate which is same as in case of Ar study, but the values are different.

Table 4.11: ANOVA for maximum bending force the A-TIG welding joint of AISI 304 under Ar+5% H_2shielding

Source	Unit	DOF	SS	Variance	F-value	Percentage contribution
Flux	-	5	34.238	6.848	0.96	27.05
Current	A	2	5.541	2.770	0.39	4.37
Gas flow	L/min	2	4.851	2.425	0.34	3.83
Tip	°	2	27.790	13.895	1.95	21.97
Torch angle	°	2	25.551	12.775	1.79	20.20
Residual Error	-	4	28.571	7.143		22.58
Total	-	17	126.541			100

The response table of various input parameters with their rank in term of significance is shown in Table 4.12 and from this table it is found that the current plays most significant factor with rank 1 but the least significant factor is tip angle of the electrode with rank 5. Hence, the conclusion from the response table is same as in case of Ar study with different values.

Table 4.12: Response Table for maximum bending force the A-TIG welding joint of AISI 304 under Ar+5%H_2 shielding

Level	Flux	Current (A)	Gas Flow (L/min)	Tip Angle (°)	Torch Angle (°)
1	11.833	9.500	10.808	11.825	10.567
2	10.817	10.842	9.567	9.575	8.475
3	11.667	9.983	9.950	8.925	11.283
4	8.967				
5	8.417				
6	8.950				
Delta	3.417	1.342	1.242	2.900	2.808
Rank	1	4	5	2	3

The main effect plot of the input parameters for the A-TIG welding of AISI 304 stainless steel under the shielding of Ar+5%H_2 gas is shown in Fig. 4.27. The X-axis represents the process parameters and the Y-axis represents the bending load with the mean line. Fig. 4.27 shows that TiO_2, SiO_2 are the most significant fluxes. In this case the value of bending force increases when the current increase from 125 A to 150 A but when it exceed further then the bending force value decreases, because when further current increases then the heat input also increases but it creates porosity with the hydrogen content present in the shielding. It is also concluded that the 60° tip angle is best as compared with 75° and 90° tip angles.

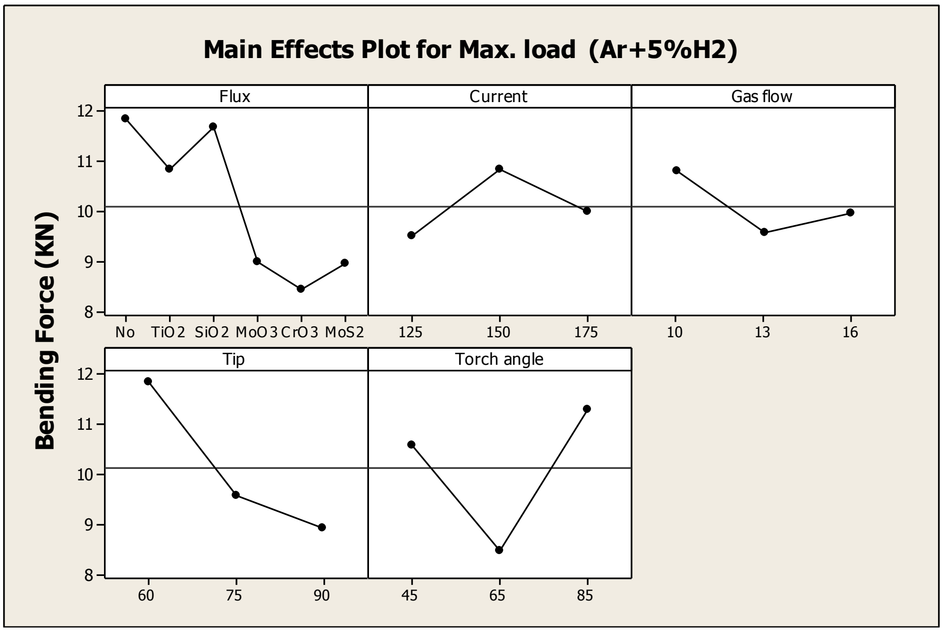

Figure 4.27: Main effect plot to show the influence of input parameters on bending force of the joint of A-TIG welding of AISI 304 under Ar+5%H_2 shielding

The bending force/load is also affected by the gas flow rate means it needs minimum gas flow rate, if more gas flows into the joint then more H_2 will be available to react with molten pool. The 85° and 45° torch angles are the most prominent torch angle in case of A-TIG, whereas 65° torch angle shows that reverse effect.

Figure 4.28 shows the Effect of different fluxes on bending force at different current level during A-TIG welding of AISI 304 under Ar+H_2 shielding. It shows the maximum bending force is taken by Sample-11, which is welded by using MoO_3 flux. The main conclusion from this graph is that, higher current did not work to get maximum bending force due to poor quality of weld produced at high current. As it is already discussed that at higher current and under the influence of flux, H_2 react with the molten metal and produce porous weld and due to hydrogen embrittlement it also produces hot crack.

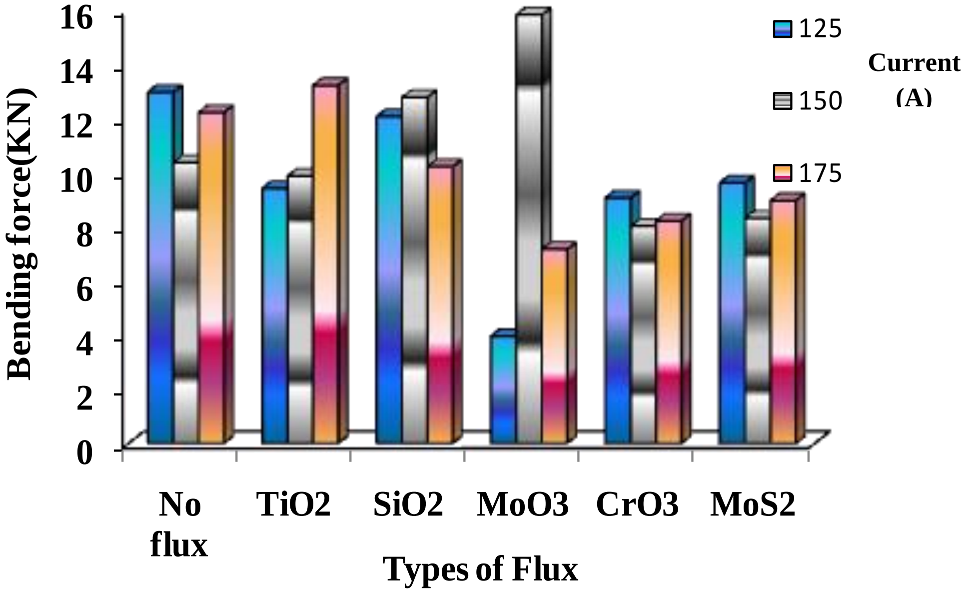

Figure 4.28: Effect of different fluxes on bending force at different current level during A-TIG welding of AISI 304 under Ar+H_2 shielding

The bend specimen of A-TIG welding of AISI 304 is which are welded under Ar+H_2 shielding is shown in Fig. 4.29 and the appearance of the weld bead after bending is also shown in Fig. 4.230. The appearance of Sample -11 (C’-11), no flaw is found on the weld surface after bending (refer Fig.4.28), where as Sample C’-3, C’-8 and C’-9 shows maximum bending and they gain “U” shape but they fail to show maximum bending force due to presence of defects.

		
C’-1	C’-7	C’-13
		
C’-2	C’-8	C’-14
		
C’-3	C’-9	C’-15
		
C’-4	C’-10	C’-16
		
C’-5	C’-11	C’-17
		
C’-6	C’-12	C’-18

Figure 4.29: Front view of bend test specimen of A-TIG welding of AISI 304 under Ar+H_2 shielding

		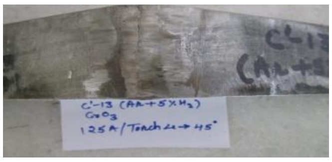
C’-1	C’-7	C’-13
		
C’-2	C’-8	C’-14
		
C’-3	C’-9	C’-15
		
C’-4	C’-10	C’-16
		
C’-5	C’-11	C’-17
		
C’-6	C’-12	C’-18

Figure 4.30: Top view of bend test specimen of A-TIG welding of AISI 304 under Ar+H_2 shielding

4.4.3 Impact Test of Samples Welded With Ar Shielding Gas

The impact strength of a material is a measure of energy (In joules), which a metal piece can absorb without breaking, at a particular temperature. According to ASTM standards E-23 designate for the impact testing of a material for a notched bar. Charpy V-notch impact test is used to check the impact strength of A-TIG welding joint of AISI 304 under Ar and Ar+5%H_2 shielding, in which notched specimen are broken by a single blow in a Charpy testing machine. The measured test values are the energy absorbed by these specimens. Hence toughness is opposite to brittleness. The toughness value of the parent metal is found, 70 Joules. Specimens for toughness test are shown in Fig. 4.31 and the broken specimen of Ar study is shown in Fig. 4.32.

Figure 4.31: Toughness specimens after toughness test of A-TIG welding joint of AISI 304 under Ar shielding

Figure 4.32: Broken specimens after toughness test of A-TIG welding joint of AISI 304 under Ar shielding

Table 4.13: Result of toughness for the joint of A-TIG welding of AISI 304 under Ar shielding

Sample No.	Sample Code No.	Flux	Current (A)	Gas flow (L/min)	Tip Angle (°)	Torch Angle (°)	Toughness (J)		
							Read.-1	Read.-2	Mean
1	C-1	No	125	10	60	45	40	26	33
2	C-2	No	150	13	75	65	34	34	34
3	C-3	No	175	16	90	85	20	30	25
4	C-4	TiO_2	125	10	75	65	18	22	20
5	C-5	TiO_2	150	13	90	85	66	66	66
6	C-6	TiO_2	175	16	60	45	40	122	81
7	C-7	SiO_2	125	13	60	85	16	24	20
8	C-8	SiO_2	150	16	75	45	60	134	97
9	C-9	SiO_2	175	10	90	65	72	40	56
10	C-10	MoO_3	125	16	90	65	10	4	7
11	C-11	MoO_3	150	10	60	85	48	30	39
12	C-12	MoO_3	175	13	75	45	116	80	98
13	C-13	CrO_3	125	13	90	45	28	16	22
14	C-14	CrO_3	150	16	60	65	20	46	33
15	C-15	CrO_3	175	10	75	85	84	118	101
16	C-16	MoS_2	125	16	75	85	12	8	10
17	C-17	MoS_2	150	10	90	45	18	18	18
18	C-18	MoS2	175	13	60	65	14	32	23

From the Table 4.13 it is clear that the maximum mean value of toughness is found for the Sample -15 (C-15) =101 J which is much greater than the value of parent metal toughness (70 J) and the minimum value of is found in case of Sample-10 (C-10).

Analysis of Variance for Toughness Test

To find out the significance of various factors like flux, current, gas flow rate, tip/vertex angle of electrode and torch angle under Ar shielding on the toughness strength ANOVA is applied at obtained data with 90% confidence level. As F-test is normally used to find out the most significant factor correspond to each input parameter values and it is based on the principle that larger the F value, greater will be the effect of that parameter. The result obtained from ANOVA and response table for toughness of the A-TIG welding joint of AISI 304 are shown in Table 4.14 and Table 4.15. From Table 4.14 it is clear that the maximum percentage contribution is obtained from the factor current and the least percentage contribution of factor gas flow rate.

Table 4.14: ANOVA for the toughness of A-TIG welding joint of AISI 304 under Ar shielding

Source	Unit	DOF	SS	Variance	F-value	Percentage contribution
Flux	-	5	3924.50	784.90	2.01	23.12
Current	A	2	6334.33	3167.17	8.11	37.32
Gas flow	L/min	2	17.33	8.67	0.02	0.11
Tip	°	2	2552.33	1276.17	3.27	15.04
Torch angle	°	2	2581.33	1290.67	3.30	15.20
Residual Error	-	4	1562.7	390.67		9.21
Total	-	17	16972.5			100

The response Table of various input parameters with their rank in term of significance is shown in Table 4.15 and from this table it is found that the current plays most significant factor with rank 1 but the least significant factor is gas flow rate with rank 5.

Table 4.15: Response Table for toughness of A-TIG welding joint of AISI 304 under Ar shielding

Level	Flux	Current (A)	Gas Flow (L/min)	Tip Angle (°)	Torch Angle (°)
1	30.67	18.67	44.50	38.17	58.17
2	55.67	47.83	43.83	60.00	28.83
3	57.67	64.00	42.17	32.33	43.50
4	48.00				
5	52.00				
6	17.00				
Delta	40.67	45.33	2.33	27.67	29.33
Rank	2	1	5	4	3

The main effect plot of the input parameters for the A-TIG welding of AISI 304 stainless steel under the shielding of Ar gas is shown in Fig. 4.33. The X-axis represents the process parameters and the Y-axis represents the toughness with the mean line. Fig. 4.33 shows that TiO_2, SiO_2, MoO_3 and CrO_3 are the most significant fluxes, whereas welding with no flux and MoS_2 could not help to improve the toughness. From main effect plot it is clear that the value of toughness increases, as heat input increases with the increase in current. It is also concluded that the 75° tip angle is best as compared with 60° and 90° tip angles. The toughness not affected by the gas flow rate. The 45° torch angle is the most prominent torch angle in this case, whereas 65° torch angle shows that reverse effect because small weld puddle is created in case of 65°, which result into the small fusion zone, hence less toughness achieved as compare to 45°.

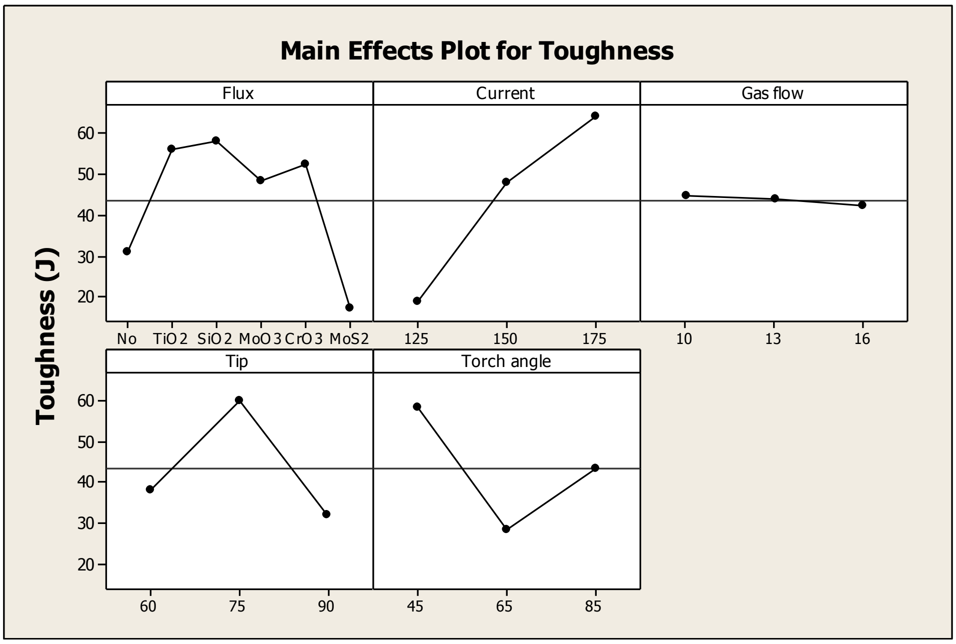

Figure 4.33: Main effect plot to show the influence various input parameters on toughness of the joint of A-TIG welding of AISI 304 under Ar shielding

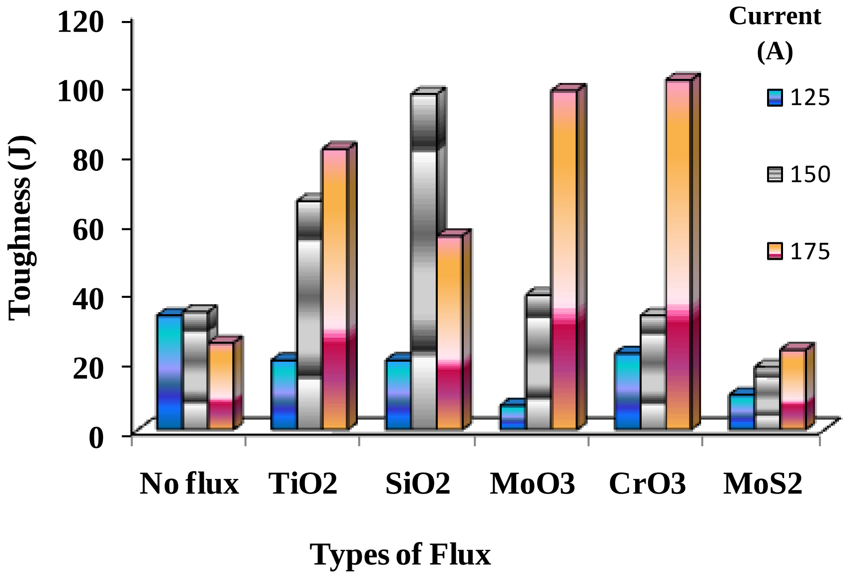

Figure 4.34: Effect of different fluxes on toughness at different current level during A-TIG welding of AISI 304 under Ar shielding

It can be observed from Fig. 4.34 that the toughness increases with the increase of current with TiO_2, SiO_2, MoO_3 and CrO_3 fluxes, but in case of SiO_2 the value of toughness increases at 150 A current, which is less than 175 A current due to the torch angle. In case of

CrO_3 more toughness is found due to more penetration with the help of CrO_3 flux as shown in Fig. 4.35.

Figure 4.35: Top and backside of Sample-15 (C-15) welded under Ar shielding with CrO_3

4.4.4 Impact Test of Samples Welded with Ar+5%H_2 Shielding Gas

According to ASTM standards E-23 designate for the impact testing of a material for a notched bar. Same Charpy impact test is used to check the impact strength of A-TIG welding joint of AISI 304 under Ar+5%H_2 shielding, in which notched specimen are broken by a single blow in a Charpy testing machine. Specimens for toughness test are shown in Fig. 4.36 and the broken specimen of Ar+5%H_2 study is shown in Fig. 4.37.

Figure 4.36: Toughness specimens after toughness test of A-TIG welding joint of AISI 304 under Ar+5%H_2 shielding

Figure 4.37: Broken specimens after toughness test of A-TIG welding joint of AISI 304 under Ar+5%H_2 shielding

Table 4.16: Result of toughness for the joint of A-TIG welding of AISI 304 under Ar+5%H_2 shielding

Sample. No.	Sample Code No.	Flux	Current (A)	Gas flow (L/min)	Tip Angle (°)	Torch Angle (°)	Toughness (J)		
							Read.-1	Read.-2	Mean
1	C’-1	No	125	10	60	45	14	22	18
2	C’-2	No	150	13	75	65	36	36	36
3	C’-3	No	175	16	90	85	62	60	61
4	C’-4	TiO_2	125	10	75	65	14	12	13
5	C’-5	TiO_2	150	13	90	85	44	46	45
6	C’-6	TiO_2	175	16	60	45	42	28	35
7	C’-7	SiO_2	125	13	60	85	12	12	12
8	C’-8	SiO_2	150	16	75	45	36	24	30
9	C’-9	SiO_2	175	10	90	65	92	74	83
10	C’-10	MoO_3	125	16	90	65	22	14	18
11	C’-11	MoO_3	150	10	60	85	22	28	25
12	C’-12	MoO_3	175	13	75	45	58	20	39
13	C’-13	CrO_3	125	13	90	45	8	14	11
14	C’-14	CrO_3	150	16	60	65	48	40	44
15	C’-15	CrO_3	175	10	75	85	60	90	75
16	C’-16	MoS_2	125	16	75	85	10	10	10
17	C’-17	MoS_2	150	10	90	45	16	16	16
18	C’-18	MoS2	175	13	60	65	38	38	38

From the Table 4.16 it is clear that the maximum mean value of toughness is found for the Sample -9 (C’-9) =83 J which is greater than the value of parent metal toughness (70 J) and the minimum value of is found in case of Sample-16 (C’-16).

Analysis of Variance for Toughness Test

To find out the significance of various factors like flux, current, gas flow rate, tip/vertex angle of electrode and torch angle under Ar shielding on the toughness strength ANOVA is applied at obtained data with 90% confidence level. As F-test is normally used to find out the most significant factor correspond to each input parameter values and it is based on the principle that larger the F value, greater will be the effect of that parameter. The result obtained from ANOVA and response table for toughness of the A-TIG welding joint of AISI 304 are shown in Table 4.17 and Table 4.18. From Table 4.17 it is clear that the maximum percentage contribution is obtained from the factor current and the least percentage contribution of factor gas flow rate.

Table 4.17: ANOVA for the toughness of A-TIG welding joint of AISI 304 under Ar+5%H_2 shielding

Source	Unit	DOF	SS	Variance	F-value	Percentage contribution
Flux	-	5	1135.2	227.0	1.93	14.12
Current	A	2	5179.0	2589.5	22.07	64.42
Gas flow	L/min	2	206.3	103.2	0.88	2.56
Tip	°	2	320.3	160.2	1.37	3.98
Torch angle	°	2	730.3	365.2	3.11	9.08
Residual Error	-	4	469.3	117.3		5.84
Total	-	17	8040.5			100

The response Table of various input parameters with their rank in term of significance is shown in Table 4.18 and from this table it is found that the current plays most significant factor with rank 1 but the least significant factor is gas flow rate with rank 5.

Table 4.18: Response Table for toughness of A-TIG welding joint of AISI 304 under Ar+5%H_2 shielding

Level	Flux	Current (A)	Gas Flow (L/min)	Tip Angle (°)	Torch Angle (°)
1	38.33	13.67	38.33	28.67	24.83
2	31.00	32.67	30.17	33.83	38.67
3	41.67	55.17	33.00	39.00	38.00
4	27.33				
5	43.33				
6	21.33				
Delta	22.00	41.50	8.17	10.33	13.83
Rank	2	1	5	4	3

The main effect plot of the input parameters for the A-TIG welding of AISI 304 stainless steel under the shielding of Ar+5%H_2 gas is shown in Fig. 4.38. The X-axis represents the process parameters and the Y-axis represents the toughness with the mean line. Fig. 4.38 shows that, SiO_2, and CrO_3 are the most significant fluxes, whereas MoS_2, MoO_3 flux are the least significant. From main effect plot it is clear that the value of toughness increases, as heat input increases with the increase in current. It is also concluded that the 90° tip angle is best as compared with 60° and 75° tip angles. The toughness is not affected by the gas flow rate. The 65° and 85° torch angle are the most prominent torch angle in this case, whereas 45° torch angle shows that reverse effect because small weld puddle is created in case of 65°, which result into the small fusion zone, hence less toughness achieved as compare to 65° and 85°.

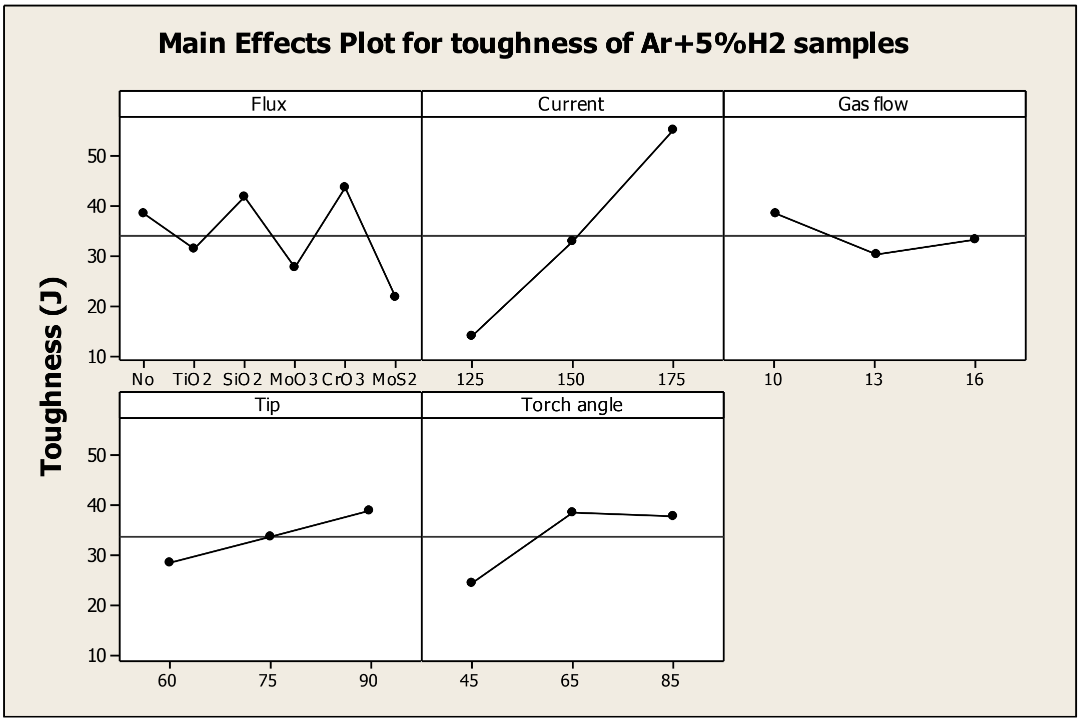

Figure 4.38: Main effect plot to show the influence various input parameters on toughness of the joint of A-TIG welding of AISI 304 under Ar+5%H_2 shielding

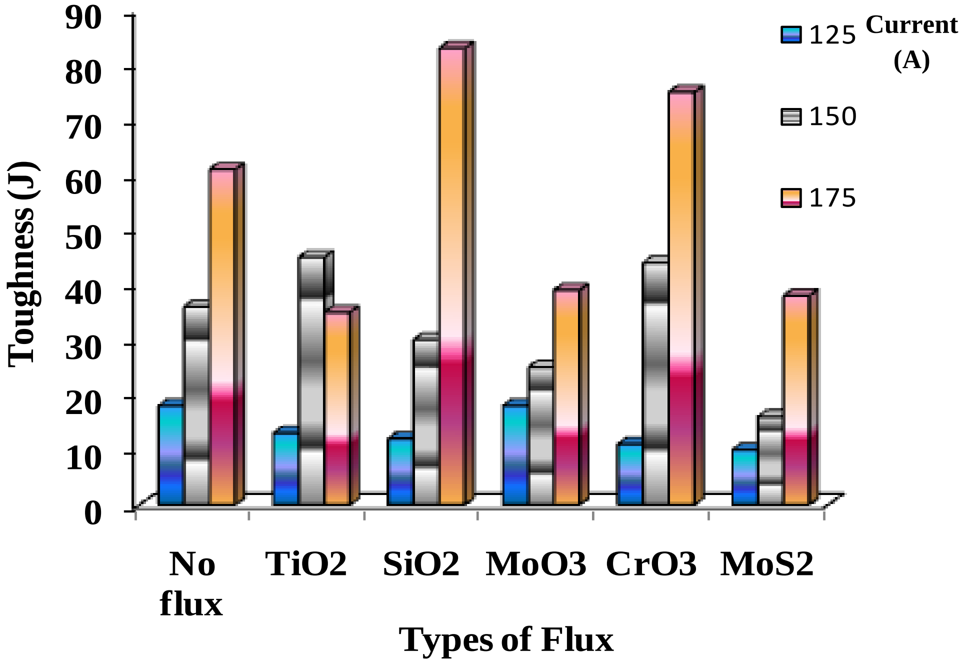

Figure 4.39: Effect of different fluxes on toughness at different current level during A-TIG welding of AISI 304 under Ar+5%H_2 shielding

It can be observed from Fig. 4.349 that the toughness increases with the increase of current with SiO_2, MoO_3 and CrO_3 fluxes, but in case of TiO_2 the value of toughness decreases due to presence of flaws in the weld bead (refer Fig. 4.40). Hence, in spite of full penetration it could not achieve high toughness value. In case of CrO_3 more toughness is found due to more penetration with the help of CrO_3 flux.

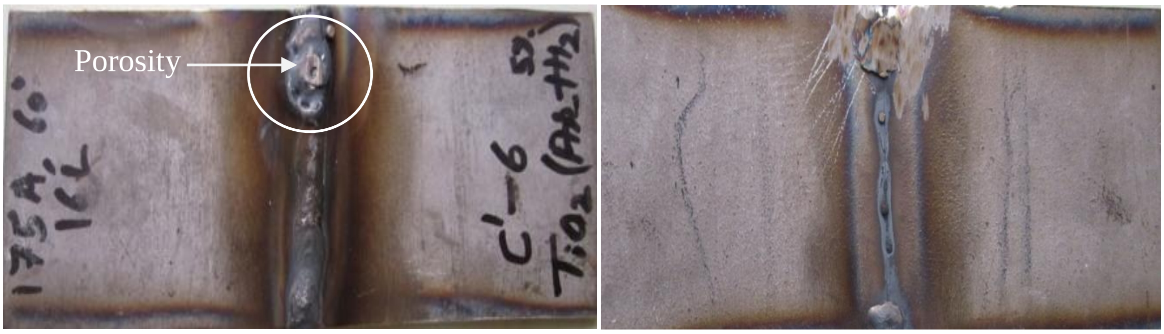

Figure 4.40: Weld bead appearance (top and bottom) of Sample-6 (C'-6) of A-TIG welding of AISI 304 under Ar+5%H_2 shielding

4.4.5 Microhardness Test

4.4.5.1 Microhardness Test of Fusion Zone (Ar Shielding)

Micro Hardness Testing of metals, composites and ceramics are employed at a selected area or selected phase of structure at micro level by applying a minimal load to check the hardness of that area. In this method by measurement of indent, which is of pyramid shape is done by the software itself is done to give a Vickers Hardness Number (VHN). In this study, microhardness is measured for two types of A-TIG welding joint of AISI 304 stainless steel, one is by using Ar gas and the other is completed by shielding with Ar+5%H_2 mixture. A dwell time of 20 seconds with a load of 300 gm is used to measure the microhardness. The microhardness is measured at the interface boundary means in the fusion zone (FZ and HAZ) at three points. The microhardness of parent metal (AISI 304) is found to be = 370 (HVN). The result of microhardness of A-TIG welding joint of AISI 304 (fusion zone) under Ar shielding is shown in Table 4.19.

Table 4.19: Result of microhardness for the joint of A-TIG welding of AISI 304 (Fusion zone) under Ar shielding

S. No.	Sample Code No.	Flux	Current (A)	Gas flow (L/min)	Tip Angle (°)	Torch angle (°)	Microhardness (HVN)			
							FZ-1	FZ-2	FZ-3	Mean
1	C-1	No	125	10	60	45	391.00	420.00	387.00	399.333
2	C-2	No	150	13	75	65	374.01	360.82	372.51	369.113
3	C-3	No	175	16	90	85	261.69	261.69	252.63	258.670
4	C-4	TiO2	125	10	75	65	268.81	281.34	276.23	275.460
5	C-5	TiO2	150	13	90	85	220.25	230.00	231.00	227.083
6	C-6	TiO2	175	16	60	45	208.62	200.58	196.22	201.807
7	C-7	SiO2	125	13	60	85	452.08	435.43	450.93	446.147
8	C-8	SiO2	150	16	75	45	259.72	264.42	246.35	256.830
9	C-9	SiO2	175	10	90	65	224.37	213.61	217.11	218.363
10	C-10	MoO3	125	16	90	65	232.01	238.00	250.69	240.233
11	C-11	MoO3	150	10	60	85	250.69	250.69	244.22	248.533
12	C-12	MoO3	175	13	75	45	339.23	335.80	328.56	334.530
13	C-13	CrO3	125	13	90	45	257.42	246.35	250.69	251.487
14	C-14	CrO3	150	16	60	65	253.90	266.82	262.06	260.927
15	C-15	CrO3	175	10	75	85	257.42	244.12	250.69	250.743
16	C-16	MoS2	125	16	75	85	402.22	394.43	380.77	392.473
17	C-17	MoS2	150	10	90	45	372.01	393.41	393.43	386.283
18	C-18	MoS2	175	13	60	65	390.14	402.73	402.22	398.363

From the Table 4.19 it is clear that the maximum mean value of microhardness is found for the Sample-7 (C-7)=446.147 which is greater than the value of parent metal (370) microhardness and the minimum value of is found in case of Sample-6 (C-6)=201.807.

Analysis of Variance for Microhardness Test (FZ)

To find out the significance of various factors like flux, current, gas flow rate, tip/vertex angle of electrode and torch angle under Ar shielding on the toughness strength ANOVA is applied at obtained data with 90% confidence level. As F-test is normally used to find out the most significant factor correspond to each input parameter values and it is based on the principle that larger the F value, greater will be the effect of that parameter. The result obtained from ANOVA and response table for toughness of the A-TIG welding joint of AISI 304 are shown in Table 4.20 and Table 4.21. From Table 4.20 it is clear that the maximum percentage contribution is obtained from the factor flux and the least percentage contribution of factor torch angle.

Table 4.20: ANOVA for the microhardness of A-TIG welding joint of AISI 304 under Ar shielding (in FZ)

Source	Unit	DOF	SS	Variance	F-value	Percentage contribution
Flux	-	5	52084	10416.9	3.97	51.48
Current	A	2	10588	5294.0	2.02	10.46
Gas flow	L/min	2	14585	7292.6	2.78	14.42
Tip	°	2	12951	6475.5	2.47	12.80
Torch angle	°	2	466	233.0	0.09	0.46
Residual Error	-	4	10502	2625.5		10.38
Total	-	17	101176			100

The response Table of various input parameters with their rank in term of significance is shown in Table 4.21 and from this table it is found that the flux plays most significant factor with rank 1 but the least significant factor is torch angle with rank 5.

Table 4.21: Response Table for microhardness of A-TIG welding joint of AISI 304 under Ar shielding (FZ)

Level	Flux	Current (A)	Gas Flow (L/min)	Tip Angle (°)	Torch Angle (°)
1	342.4	334.2	296.5	325.9	305.0
2	234.8	291.5	337.8	313.2	293.7
3	307.1	277.1	268.5	263.7	303.9
4	274.4				
5	254.4				
6	392.4				
Delta	157.6	57.1	69.3	62.2	11.3
Rank	1	4	2	3	5

The main effect plot of the input parameters for the A-TIG welding of AISI 304 stainless steel under the shielding of Ar gas is shown in Fig. 4.41. The X-axis represents the process parameters and the Y-axis represents the toughness with the mean line. Fig. 4.41 shows that TiO_2, MoO_3 and CrO_3 are the least significant fluxes, whereas welding with no flux and MoS_2 flux improves the microhardness. From main effect plot it is clear that the value of microhardness increases, as current decreases. The main reason of this is due to fast cooling rate at low heat input. It is also concluded that the 60° tip angle is best as compared with 75° and 90° tip angles. The toughness is also affected by the gas flow rate. It is found that 13 L/min produce maximum hardness. The torch angle did not play any significant role to achieve maximum hardness.

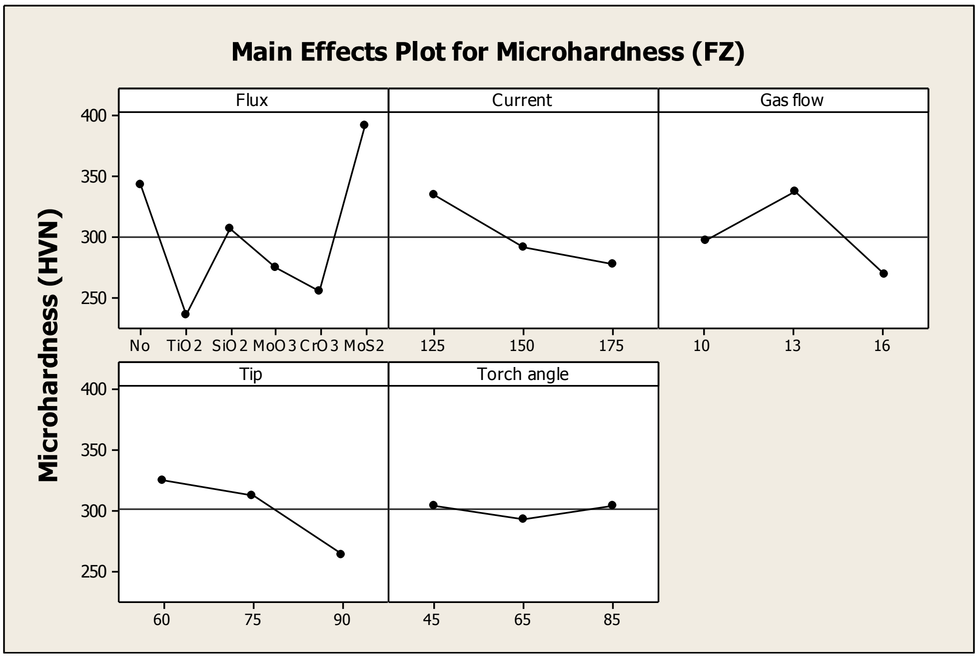

Figure 4.41: Main effect plot to show the influence various input parameters on microhardness of the joint (FZ) of A-TIG welding of AISI 304 under Ar shielding

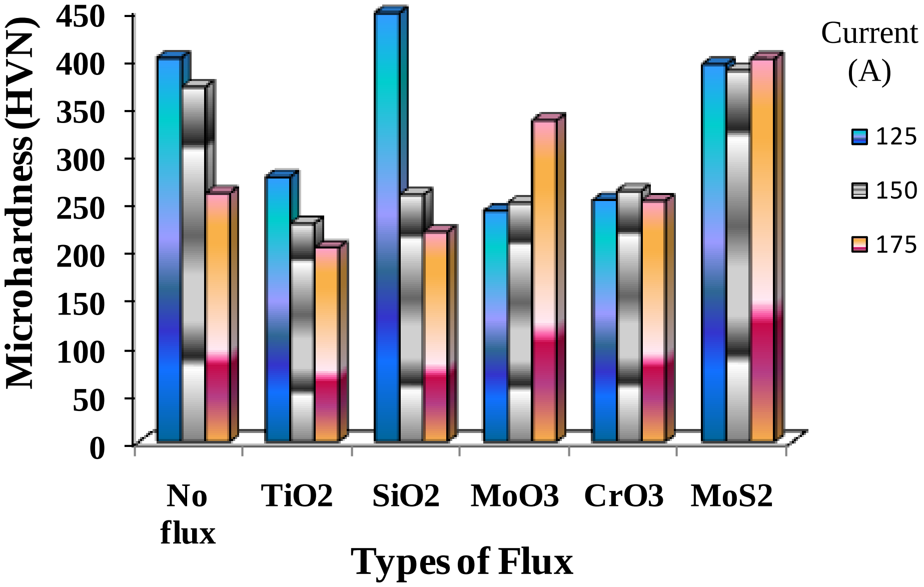

Figure 4.42: Effect of different fluxes on microhardness (FZ) at different current level during A-TIG welding of AISI 304 under Ar shielding

It can observed from the graph that the values of microhardness are high at low heat input rate, means at low current the metal solidification is fast and due to this the martensite formation is completed with carbide precipitation, which have high microhardness. It is also clear from the Fig. 4.42, that SiO2 flux produced maximum microhardness at lower current.

4.4.5.2 Microhardness Test of HAZ (Ar Shielding)

Same technique and same method is used to measure microhardness of HAZ of A-TIG welding joint of AISI 304 (Ar shielded). The microhardness of HAZ is measured at three different points which is adjacent to fusion zone. A dwell time of 20 seconds with a load of 300 gm is used for indentation purpose. The result of microhardness of A-TIG welding joint of AISI 304 (HAZ) under Ar shielding is shown in Table 4.22.

Table 4.22: Result of microhardness (HAZ) for the joint of A-TIG welding of AISI 304 Under Ar shielding

S. No.	Sample Code No.	Flux	Current (A)	Gas flow (L/min)	Tip Angle (°)	Torch angle (°)	HAZ H-1	HAZ H-2	HAZ H-3	Mean HAZ Hardness
1	C-1	No	125	10	60	45	399.00	400.00	420.00	406.333
2	C-2	No	150	13	75	65	352.35	342.56	360.63	351.847
3	C-3	No	175	16	90	85	244.03	244.03	254.85	247.637
4	C-4	TiO2	125	10	75	65	261.69	261.70	250.44	257.943
5	C-5	TiO2	150	13	90	85	233.88	228.10	233.88	231.953
6	C-6	TiO2	175	16	60	45	184.45	175.18	180.07	179.900
7	C-7	SiO2	125	13	60	85	376.69	364.83	380.77	374.097
8	C-8	SiO2	150	16	75	45	252.90	242.12	240.05	245.023
9	C-9	SiO2	175	10	90	65	205.21	198.27	220.52	208.000
10	C-10	MoO3	125	16	90	65	230.07	228.14	232.01	230.073
11	C-11	MoO3	150	10	60	85	226.25	230.07	238.00	231.440
12	C-12	MoO3	175	13	75	45	332.41	332.40	319.38	328.063
13	C-13	CrO3	125	13	90	45	242.12	248.51	252.42	247.683
14	C-14	CrO3	150	16	60	65	250.69	248.51	244.12	247.773
15	C-15	CrO3	175	10	75	85	255.15	252.90	248.51	252.187
16	C-16	MoS2	125	16	75	85	378.76	358.51	352.86	363.377
17	C-17	MoS2	150	10	90	45	357.23	357.22	367.69	360.713
18	C-18	MoS2	175	13	60	65	353.51	357.23	353.51	354.750

From the Table 4.22 it is clear that the maximum mean value of microhardness is found for the Sample-1 (C-1) = 406.333 which is greater than the value of parent metal (370) microhardness and the minimum value of is found in case of Sample-6 (C-6).

Analysis of Variance for Microhardness Test (HAZ)

To find out the significance of various factors like flux, current, gas flow rate, tip/vertex angle of electrode and torch angle under Ar shielding on the toughness strength ANOVA is applied at obtained data with 90% confidence level. As F-test is normally used to find out the most significant factor correspond to each input parameter values and it is based on the principle that larger the F value, greater will be the effect of that parameter. The result obtained from ANOVA and response table for toughness of the A-TIG welding joint of AISI 304 are shown in Table 4.23 and Table 4.24. From Table 4.23 it is clear that the maximum percentage contribution is obtained from the factor flux and the least percentage contribution of factor torch angle.

Table 4.23: ANOVA for the microhardness (HAZ) of A-TIG welding joint of AISI 304 Under Ar shielding

Source	Unit	DOF	SS	Variance	F-value	Percentage contribution
Flux	-	5	41237	8247.5	3.91	52.22
Current	A	2	8307	4153.5	1.97	10.52
Gas flow	L/min	2	11721	5860.6	2.78	14.84
Tip	°	2	8120	4059.9	1.93	10.28
Torch angle	°	2	1155	577.5	0.27	01.46
Residual Error	-	4	8432	2108.0		10.68
Total	-	17	78972			100

The response Table of various input parameters with their rank in term of significance is shown in Table 4.21 and from this table it is found that the flux plays most significant factor with rank 1 but the least significant factor is torch angle with rank 5.

Table 4.24: Response Table for microhardness (HAZ) of A-TIG welding joint of AISI 304 under Ar shielding

Level	Flux	Current (A)	Gas Flow (L/min)	Tip Angle (°)	Torch Angle (°)
1	342.4	334.2	296.5	325.9	305.0
2	234.8	291.5	337.8	313.2	293.7
3	307.1	277.1	268.5	263.7	303.9
4	274.4				
5	254.4				
6	392.4				
Delta	157.6	57.1	69.3	62.2	11.3
Rank	1	4	2	3	5

The main effect plot of the input parameters for the A-TIG welding of AISI 304 stainless steel under the shielding of Ar gas is shown in Fig. 4.43. The X-axis represents the process parameters and the Y-axis represents the toughness with the mean line. Fig. 4.43 shows that TiO_2, MoO_3 and CrO_3 are the least significant fluxes, whereas welding with no flux and MoS_2 flux improves the microhardness. From main effect plot it is clear that the value of microhardness increases, as current decreases. The main reason of this is due to fast cooling rate at low heat input. It is also concluded that the 60° and 75° tip angles produced higher microhardness as compared to 90° tip angle. The microhardness also affected by the gas flow rate. It is found that 13 L/min produce maximum hardness. The torch angle did not play any significant role to achieve maximum hardness.

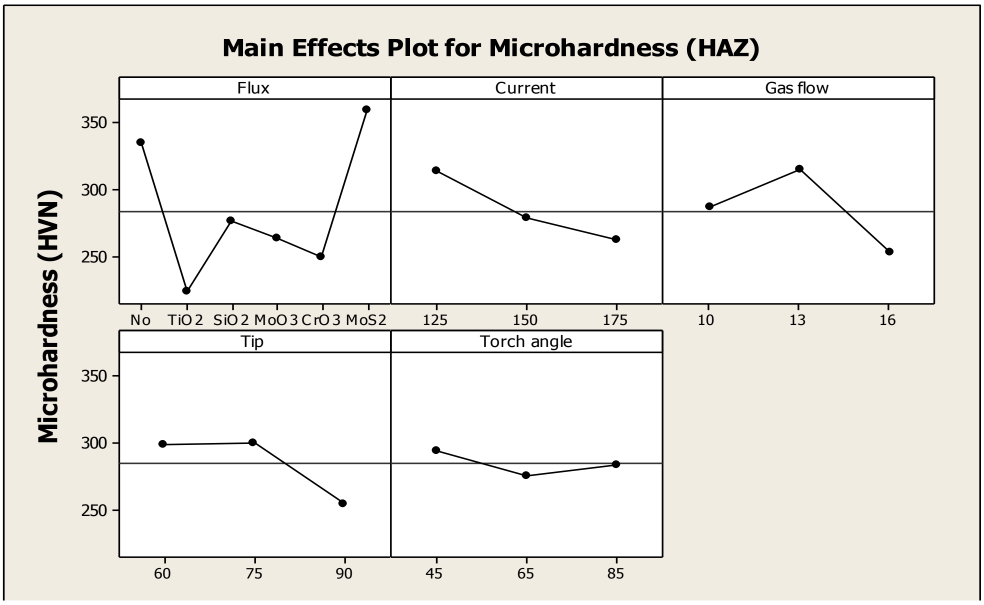

Figure 4.43: Main effect plot to show the influence various input parameters on microhardness of the joint (HAZ) of A-TIG welding joint of AISI 304 (Ar shielded)

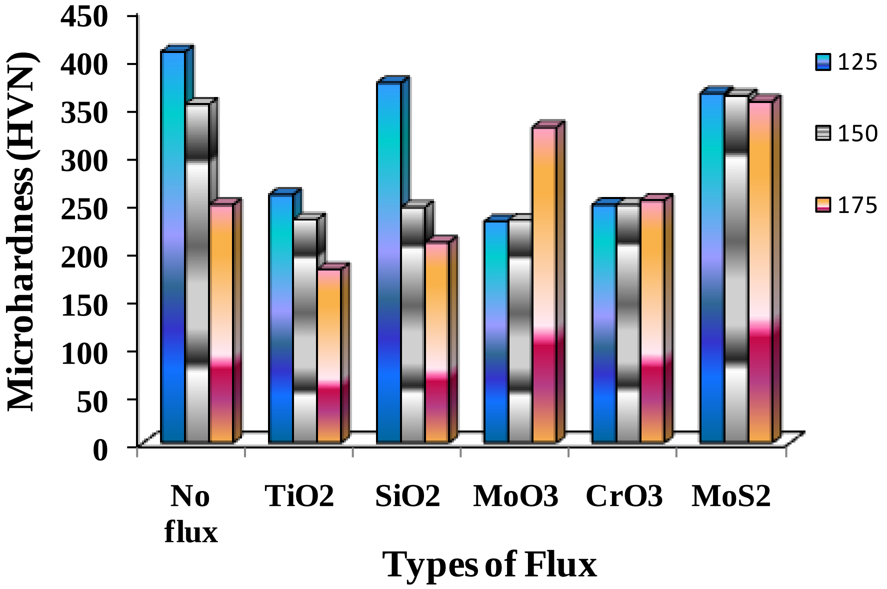

Figure 4.44: Effect of different fluxes on microhardness (HAZ) at different current level during A-TIG welding of AISI 304 under Ar shielding

It can observed from the Fig. 4.44 graph that the values of microhardness is found high in case of no flux at low current means at low heat input rate. It is also found in this study that, when hardness value is more than 450 then there is a chance of presence of martensite in the microstructure of HAZ. Hence, due to presence of precipitated carbide the microhardness increases at low level of current either without flux or with flux. If we look at the bending result (Table 4.7), then we find that the Samples which are weld at 125 A current took minimum bending force, which proves they have poor ductility.

Figure 4.45: Appearance of crack in the weld bead (Sample-1 of Ar shielding) after bending shows poor ductility

4.4.5.3 Microhardness Test of Fusion Zone (Ar+5%H_2 Shielding)

Same technique and same machine is used for testing microhardness of fusion zone of A-TIG welding joint of AISI 304 (Ar+5%H_2 shielded). The result of microhardness of A-TIG welding joint of AISI 304 (fusion zone) under Ar shielding is shown in Table 4.25.

Table 4.25: Result of microhardness for the joint of A-TIG welding of AISI 304 (Fusion zone) under Ar+5%H_2 shielding

S. No.	Sample Code No.	Flux	Current (A)	Gas flow (L/min)	Tip Angle (°)	Torch angle (°)	F.Z. H-1	F.Z. H-2	F.Z. H-3	MEAN F.Z.H
1	C’-1	No	125	10	60	45	438.34	442.51	438.33	439.727
2	C’-2	No	150	13	75	65	388.82	391.60	391.24	390.553
3	C’-3	No	175	16	90	85	423.35	418.79	415.33	419.157
4	C’-4	TiO2	125	10	75	65	400.54	391.24	395.60	395.793
5	C’-5	TiO2	150	13	90	85	400.74	400.03	406.12	402.297
6	C’-6	TiO2	175	16	60	45	266.74	264.82	269.38	266.980
7	C’-7	SiO2	125	13	60	85	396.60	396.50	404.14	399.080
8	C’-8	SiO2	150	16	75	45	407.39	413.48	408.90	409.923
9	C’-9	SiO2	175	10	90	65	361.00	357.23	353.51	357.247
10	C’-10	MoO3	125	16	90	65	357.37	348.26	357.23	354.287
11	C’-11	MoO3	150	10	60	85	338.41	346.26	349.86	344.843
12	C’-12	MoO3	175	13	75	45	266.82	274.22	273.72	271.587
13	C’-13	CrO3	125	13	90	45	440.58	451.07	442.66	444.770
14	C’-14	CrO3	150	16	60	65	327.92	327.92	324.68	326.840
15	C’-15	CrO3	175	10	75	85	292.01	302.22	294.77	296.333
16	C’-16	MoS2	125	16	75	85	322.56	326.26	329.08	325.967
17	C’-17	MoS2	150	10	90	45	260.72	259.72	266.25	262.230
18	C’-18	MoS2	175	13	60	65	390.14	384.92	393.43	389.497

From the Table 4.25 it is clear that the maximum mean value of microhardness is found for the Sample-13 (C'-13) = 444.770which is greater than the value of parent metal (370) microhardness and the minimum value of is found in case of Sample-6 (C'-6)= 266.980.

Analysis of Variance for Microhardness Test (FZ) For Ar+5%H_2 Shielding

Same way to find out the significance of various factors on microstructure of fusion zone, ANOVA is applied at obtained data with 90% confidence level. The result obtained from ANOVA and response table for microhardness of the A-TIG welding joint of AISI 304 are shown in Table 4.26 and Table 4.27. From Table 4.26 it is clear that the maximum percentage contribution is obtained from the residual error and the least percentage contribution of factor torch angle.

Table 4.26: ANOVA for the microhardness (FZ) of A-TIG welding joint of AISI 304 under Ar+5%H_2 Shielding

Source	Unit	DOF	SS	Variance	F-value	Percentage contribution
Flux	-	5	19626	3925.1	0.77	33.53
Current	A	2	10940	5470.0	1.07	18.70
Gas flow	L/min	2	4365	2182.7	0.43	07.46
Tip	°	2	1871	935.6	0.18	03.20
Torch angle	°	2	1301	650.4	0.13	02.22
Residual Error	-	4	20426	5106.5		34.89
Total	-	17	58529			100

The response Table of various input parameters with their rank in term of significance is shown in Table 4.27 and from this table it is found that the flux plays most significant factor with rank 1 but the least significant factor is torch angle with rank 5.

Table 4.27: Response Table for microhardness (HAZ) of A-TIG welding joint of AISI 304 under Ar+5%H_2 shielding

Level	Flux	Current (A)	Gas Flow (L/min)	Tip Angle (°)	Torch Angle (°)
1	416.5	393.3	349.4	361.2	349.2
2	355.0	356.1	383.0	348.4	369.0
3	388.8	333.5	350.5	373.3	364.6
4	323.6				
5	356.0				
6	325.9				
Delta	92.9	59.8	33.6	25.0	19.8
Rank	1	2	3	4	5

The main effect plot of the input parameters for the A-TIG welding of AISI 304 stainless steel under the shielding of Ar+5%H_2 mixture gas is shown in Fig. 4.46. The X-axis represents the process parameters and the Y-axis represents the toughness with the mean line. Fig. 4.46 shows that MoO_3 and MoS_2 are the least significant fluxes, whereas welding with no flux and SiO_2 flux improves the microhardness. From main effect plot it is clear that the value of microhardness increases, as current decreases which justify the presence of martensite and precipitated carbide. The main reason of this is due to fast cooling rate at low heat input. The toughness is also affected by the gas flow rate. It is found that 13 L/min produce maximum hardness. The torch angle and tip angle did not play any significant role to achieve maximum hardness.

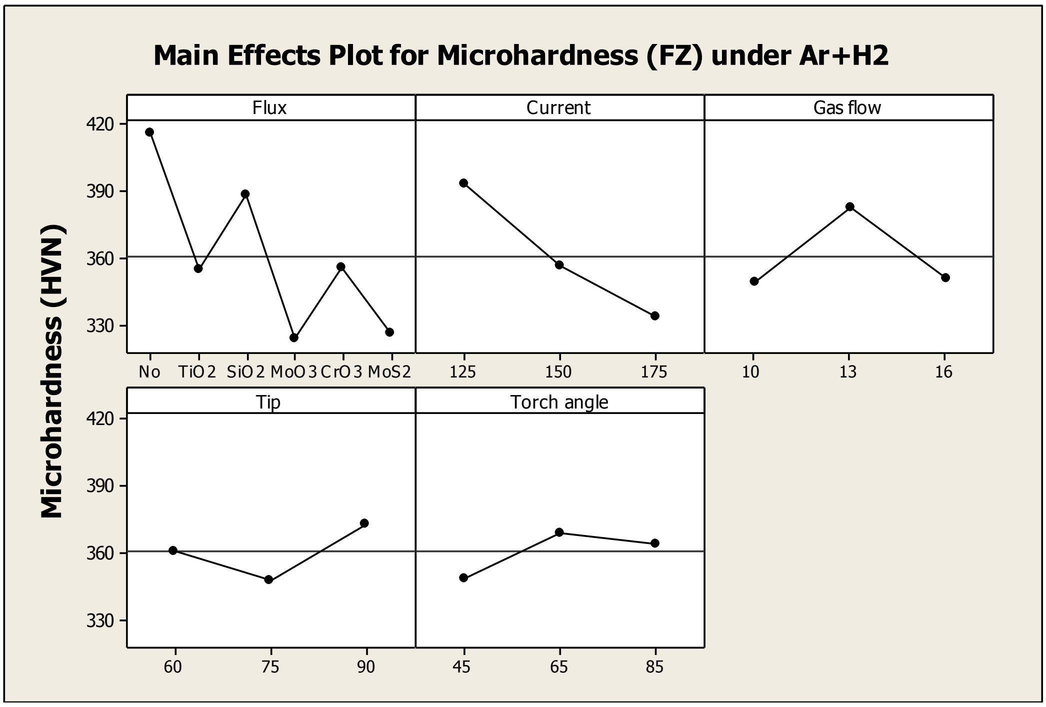

Figure 4.46: Main effect plot to show the influence various input parameters on microhardness of the joint (FZ) of A-TIG welding joint of AISI 304 (Ar+5%H_2 shielded)

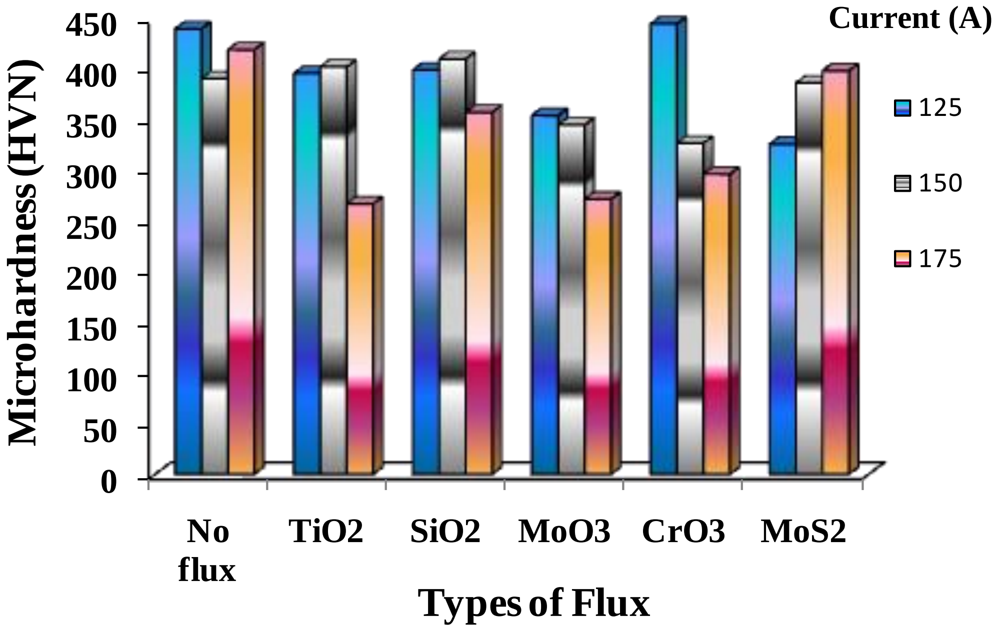

Figure 4.47: Effect of different fluxes on microhardness (FZ) at different current level during A-TIG welding of AISI 304 under Ar+5%H_2 shielding

It can be observed from Fig. 4.47 that the microhardness of fusion zone at 125 A current is high in most of the cases except the case of MoS_2 flux. Microhardness increases at minimum current due to fast solidification which converts into martensite and due to presence of carbide precipitation. In case of high current except the case of MoS_2 flux, the value of microhardness decreases.

4.4.5.4 Microhardness Test of Heat Affected Zone (Ar+5%H_2 Shielding)

Same method is used here for testing microhardness of HAZ of A-TIG welding joint of AISI 304 (Ar+5%H_2 shielded), which is used for Ar shielded. The result of microhardness of HAZ of A-TIG welding joint of AISI 304 under Ar+5%H_2 shielding is shown in Table 4.28.

Table 4.28: Result of microhardness of HAZ for the joint of A-TIG welding of AISI 304 Under Ar+5%H_2 shielding

S. No.	Sample Code No.	Flux	Current (A)	Gas flow (L/min)	Tip Angle (°)	Torch angle (°)	HAZ H-1	HAZ H-2	HAZ H-3	MEAN HAZ Hardness
1	C'-1	No	125	10	60	45	400.03	396.24	404.54	400.270
2	C'-2	No	150	13	75	65	382.74	370.49	365.82	373.017
3	C'-3	No	175	16	90	85	401.60	404.45	409.12	405.057
4	C'-4	TiO2	125	10	75	65	361.35	372.74	375.95	370.013
5	C'-5	TiO2	150	13	90	85	378.59	388.24	390.24	385.690
6	C'-6	TiO2	175	16	60	45	256.44	268.22	260.38	261.680
7	C'-7	SiO2	125	13	60	85	391.31	387.09	387.09	388.497
8	C'-8	SiO2	150	16	75	45	361.37	356.67	366.28	361.440
9	C'-9	SiO2	175	10	90	65	349.86	353.51	346.26	349.877
10	C'-10	MoO3	125	16	90	65	350.23	339.23	346.26	345.240
11	C'-11	MoO3	150	10	60	85	318.51	308.47	319.41	315.463
12	C'-12	MoO3	175	13	75	45	387.09	378.86	378.84	381.597
13	C'-13	CrO3	125	13	90	45	348.86	355.67	352.01	352.180
14	C'-14	CrO3	150	16	60	65	306.22	309.18	309.20	308.200
15	C'-15	CrO3	175	10	75	85	272.25	280.29	273.72	275.420
16	C'-16	MoS2	125	16	75	85	326.26	329.08	329.08	328.140
17	C'-17	MoS2	150	10	90	45	288.32	290.71	279.00	286.010
18	C'-18	MoS2	175	13	60	65	362.67	357.67	364.83	361.723

From the Table 4.28 it is clear that the maximum mean value of microhardness is found for the Sample-3 (C'-3) = 405.057 which is greater than the value of parent metal (370) microhardness and the minimum value of is found in case of Sample-6 (C'-6)= 261.680.

Analysis of Variance for Microhardness Test (HAZ) For Ar+5%H_2 Shielding

To find out the significance of various factors on microstructure of fusion zone, ANOVA is applied at obtained data with 90% confidence level. The result obtained from ANOVA and response table for microhardness of the A-TIG welding joint of AISI 304 are shown in Table 4.29 and Table 4.30.

Table 4.29: ANOVA for the microhardness (HAZ) of A-TIG welding joint of AISI 304 under Ar+5%H_2 Shielding

Source	Unit	DOF	SS	Variance	F-value	Percentage contribution
Flux	-	5	12729.4	2545.9	1.19	40.71
Current	A	2	2561.3	1280.7	0.60	8.19
Gas flow	L/min	2	6376.1	3188.0	1.49	20.38
Tip	°	2	659.0	329.5	0.15	2.11
Torch angle	°	2	407.9	203.9	0.10	1.31
Residual Error	-	4	8538.4	2134.6		27.30
Total	-	17	31272.1			100

From Table 4.29 it is clear that the maximum percentage contribution is obtained from the factor flux and the least percentage contribution of factor torch angle.

The response Table of various input parameters with their rank in term of significance is shown in Table 4.30 and from this table it is found that the flux plays most significant factor with rank 1 but the least significant factor is torch angle with rank 5.

Table 4.30: Response Table for microhardness (HAZ) of A-TIG welding joint of AISI 304 under Ar+5%H_2 shielding

Level	Flux	Current (A)	Gas Flow (L/min)	Tip Angle (°)	Torch Angle (°)
1	392.8	364.1	332.8	339.3	340.5
2	339.1	338.3	373.8	348.3	351.3
3	366.6	339.2	335.0	354.0	349.7
4	347.4				
5	311.9				
6	325.3				
Delta	80.8	25.8	40.9	14.7	10.8
Rank	1	3	2	4	5

The main effect plot of the input parameters for the A-TIG welding of AISI 304 stainless steel under the shielding of Ar+5%H_2 mixture gas is shown in Fig. 4.48. The X-axis represents the process parameters and the Y-axis represents the toughness with the mean line. Fig. 4.48 shows that CrO_3 and MoS_2 are the least significant fluxes, whereas welding with no flux and SiO_2 flux improves the microhardness. From main effect plot it is clear that the value of microhardness increased at low current which justify the presence of martensite. The main reason of this is due to fast cooling rate at low heat input. The toughness is also affected by the gas flow rate. It is found that 13 L/min produce maximum hardness. The torch angle and tip angle did not play any significant role to achieve maximum hardness.

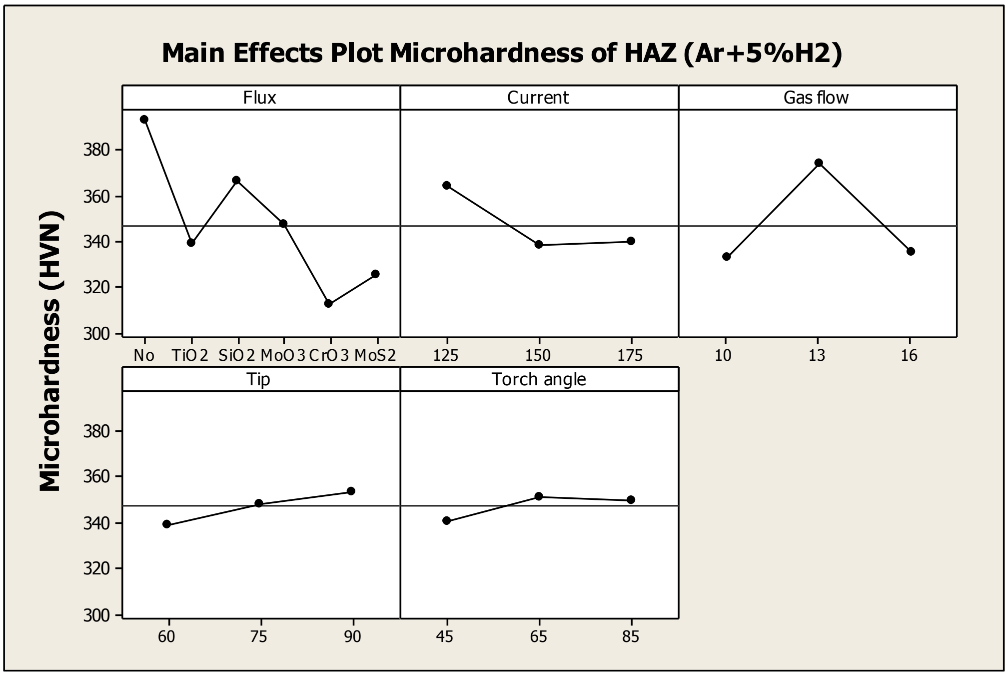

Figure 4.48: Main effect plot to show the influence various input parameters on microhardness of the joint (FZ) of A-TIG welding joint of AISI 304 (Ar+5%H_2 shielded)

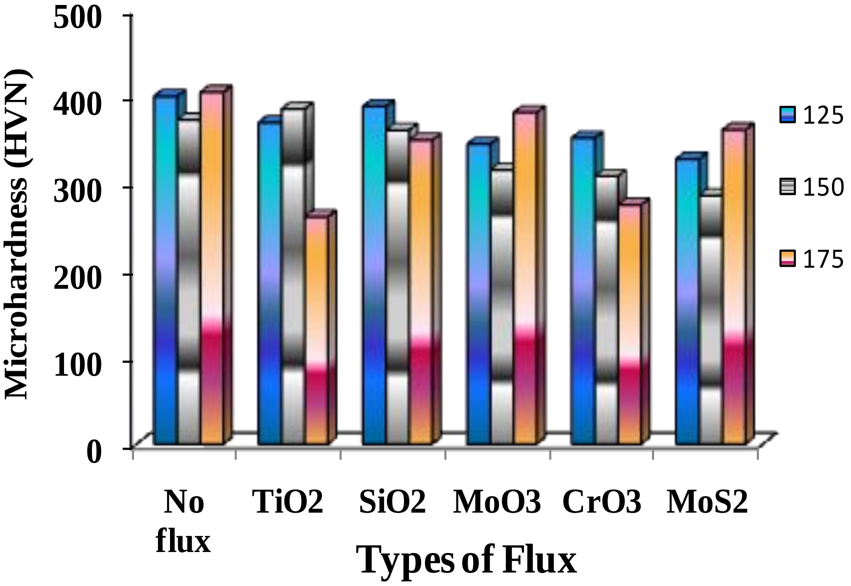

Figure 4.49: Effect of different fluxes on microhardness (HAZ) at different current level during A-TIG welding of AISI 304 under Ar+5%H_2 shielding

It can be observed from Fig. 4.49 that the microhardness of fusion zone at 125 A current is high in most of the cases due to fast cooling, so it attain fine grain structure which is also converted into martensite. At high current the microhardness does not increase significantly because martensite could not form. Hence, ferrite coverts into austenite at slow cooling rate, which has less hardness.

4.4.6 Metallurgical Analysis Using Optical Microscopy

Microstructure analysis is carried out for all TIG and A-TIG welded specimens of AISI 304 stainless steel welded joint using pure Ar shielding supply, by using metallurgical microscope at 10X, 20X, 50X magnification. Fig. 4.50 to Fig. 4.53 shows the microstructures at 10X, 20X, 50X magnification levels of weld regions of AISI 304 austenitic stainless steel which is welded as per orthogonal array design for Ar study. After welding the Samples are cut and is grounded with surface grinder, polished and etched, using (…….) for microstructure study.

4.4.6.1 Metallurgical Analysis of AISI 304 Welding Joint (Ar Shielded)

Figure 4.50 to Figure 4.53 the fusion zone, heat affected zone (HAZ) and unaffected base metal are clearly visible, captured and the same is zoomed at above mentioned magnification level. In Fig. 4.50, C-1 to C-3 depicts the microstrucural pictures of weld metal welded under pure Ar at 125 A, 150 A, 175 A, without flux. Rests of the pictures are the microstructural pictures of Samples C-4 to C-18 which are welded under Ar shielding with different welding parameters and by using different fluxes. The structure of weld metal is found totally different from the structure of the base metal.

From the results of bend test, toughness test and microhardness test, it is found that the Sample-6 (C-6) has maximum bending force, minimum microhardness values of both FZ and HAZ (i.e. 201.807 and 179.9), which justifies that the presence of skeletal type δ-ferrite in the FZ and HAZ with opposite orientation of coarse grains. As the heat input in case3 of Sample C-6 is high enough due to use of high current, so solidification occurs at slow rate which result into the formation of austenite in large quantity. Hence, the Sample C-6 has low value of microhardness and due to good ductility it has high value of bending force and good toughness value also.

Whereas the result of toughness test, bending test and microhardness test of Sample-7 (C-7) shows that it has maximum hardness value for FZ and HAZ (i.e. 446.147 and 374.097), but the value of HAZ is less than the value of C-1 Samples. It is clear from the hardness value and its microstructure that it has lathe type δ-ferrite and precipitation of carbide with martensite in its FZ and HAZ which result into maximum hardness. Sample C-7 also has a low value of toughness (20 J) which justifies that it has high hardness value. Similarly it takes a low bending force during bend test (i.e. 12.2 KN).

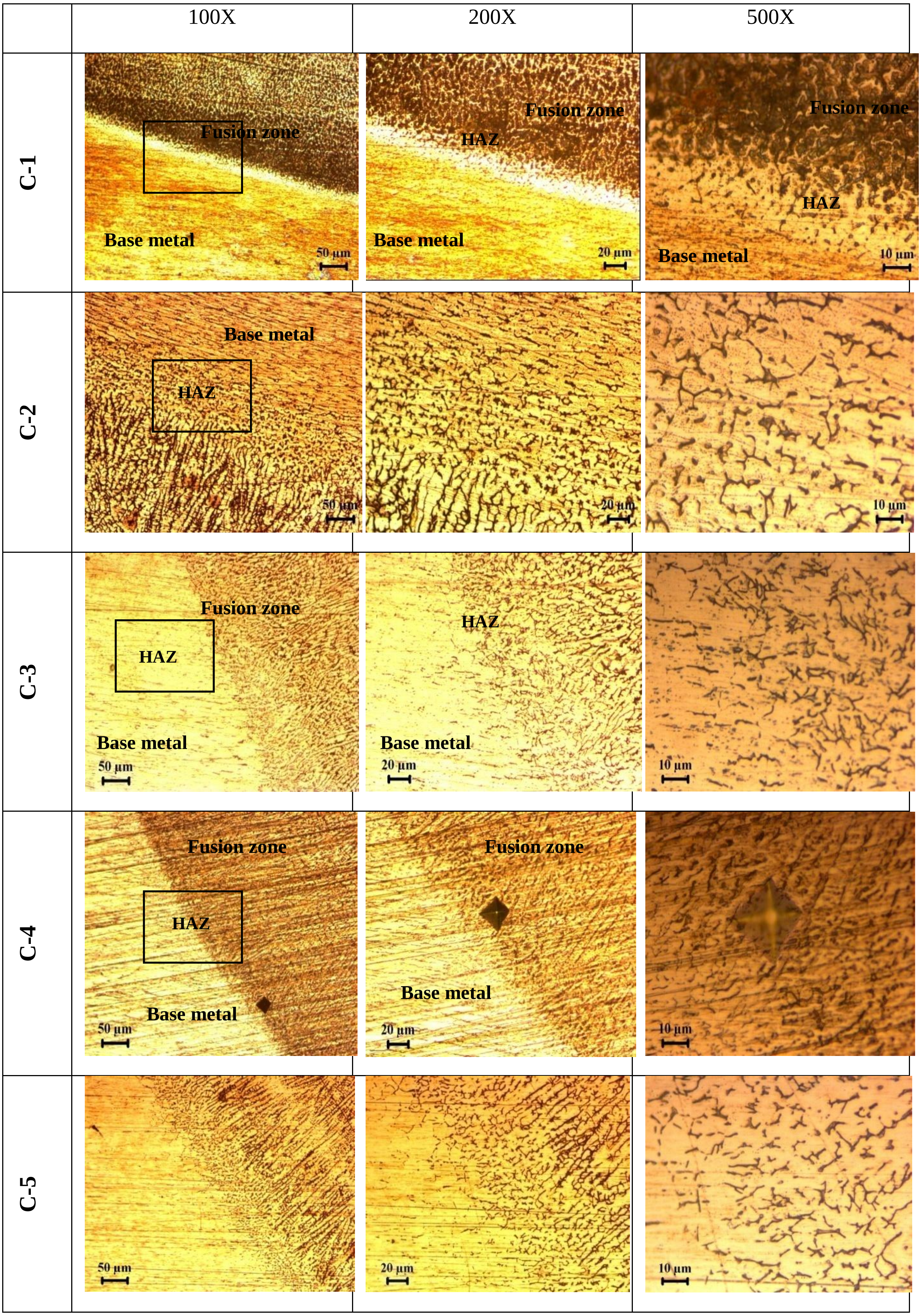

Figure 4.50: Microstructure after TIG and ATIG of AISI 304 stainless steel (Ar shielded) From Sample 1 to 5 (C-1 to C-5)

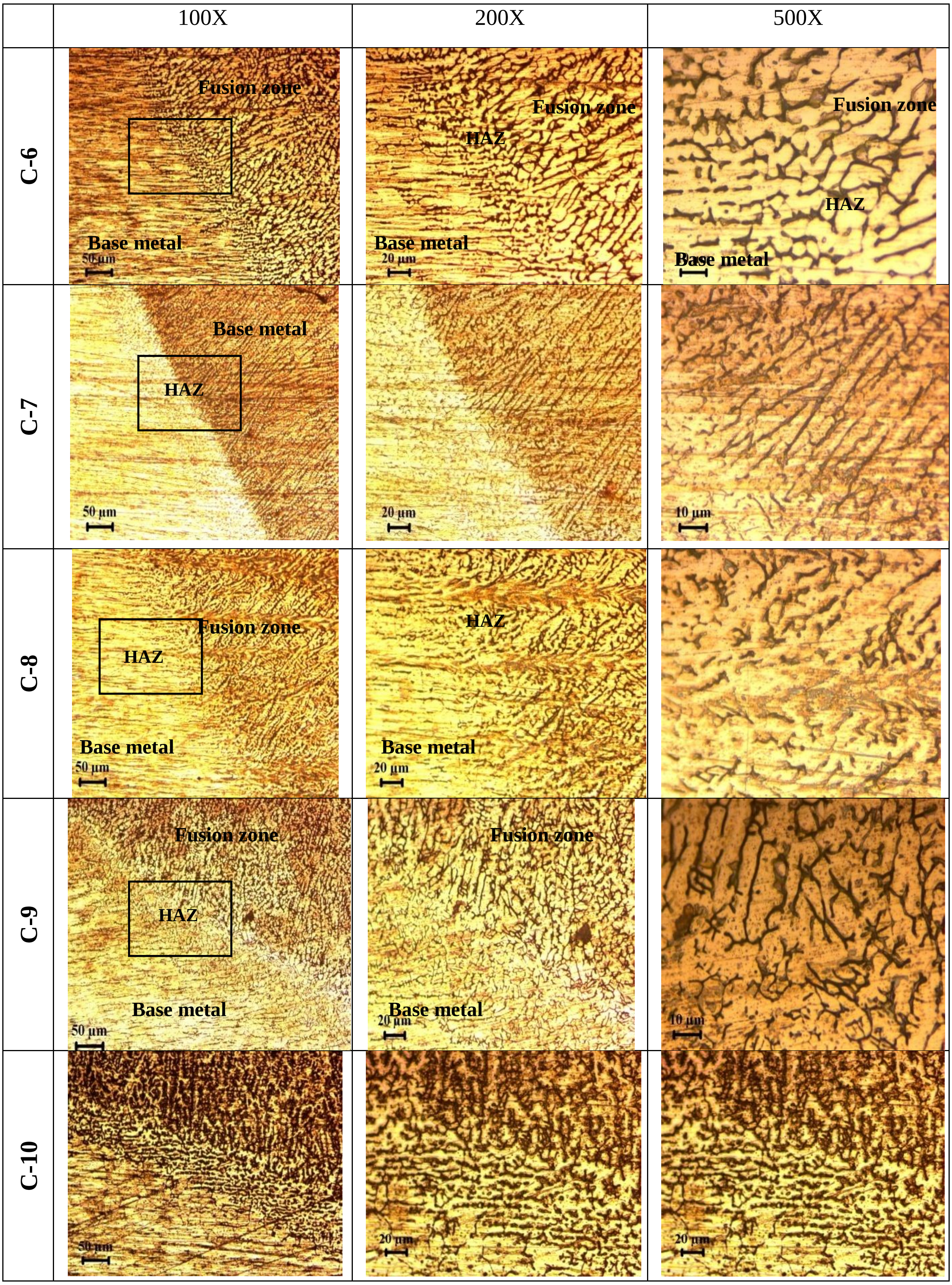

Figure 4.51: Microstructure after ATIG of AISI 304 stainless steel (Ar shielded) From Sample 6 to 10 (C-6 to C-10)

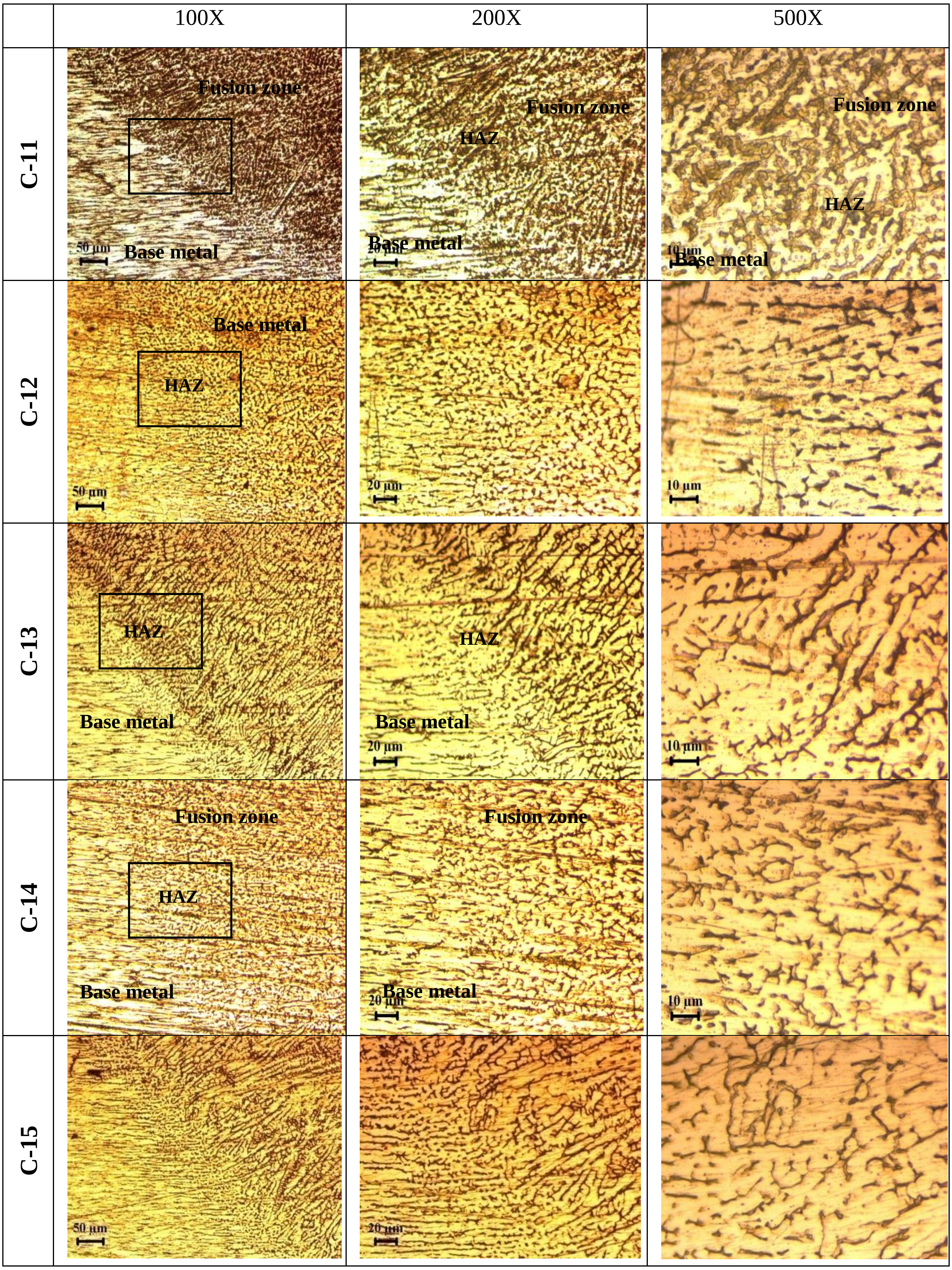

Figure 4.52: Microstructure after ATIG of AISI 304 stainless steel (Ar shielded) From Sample 11 to 15 (C-11 to C-15)

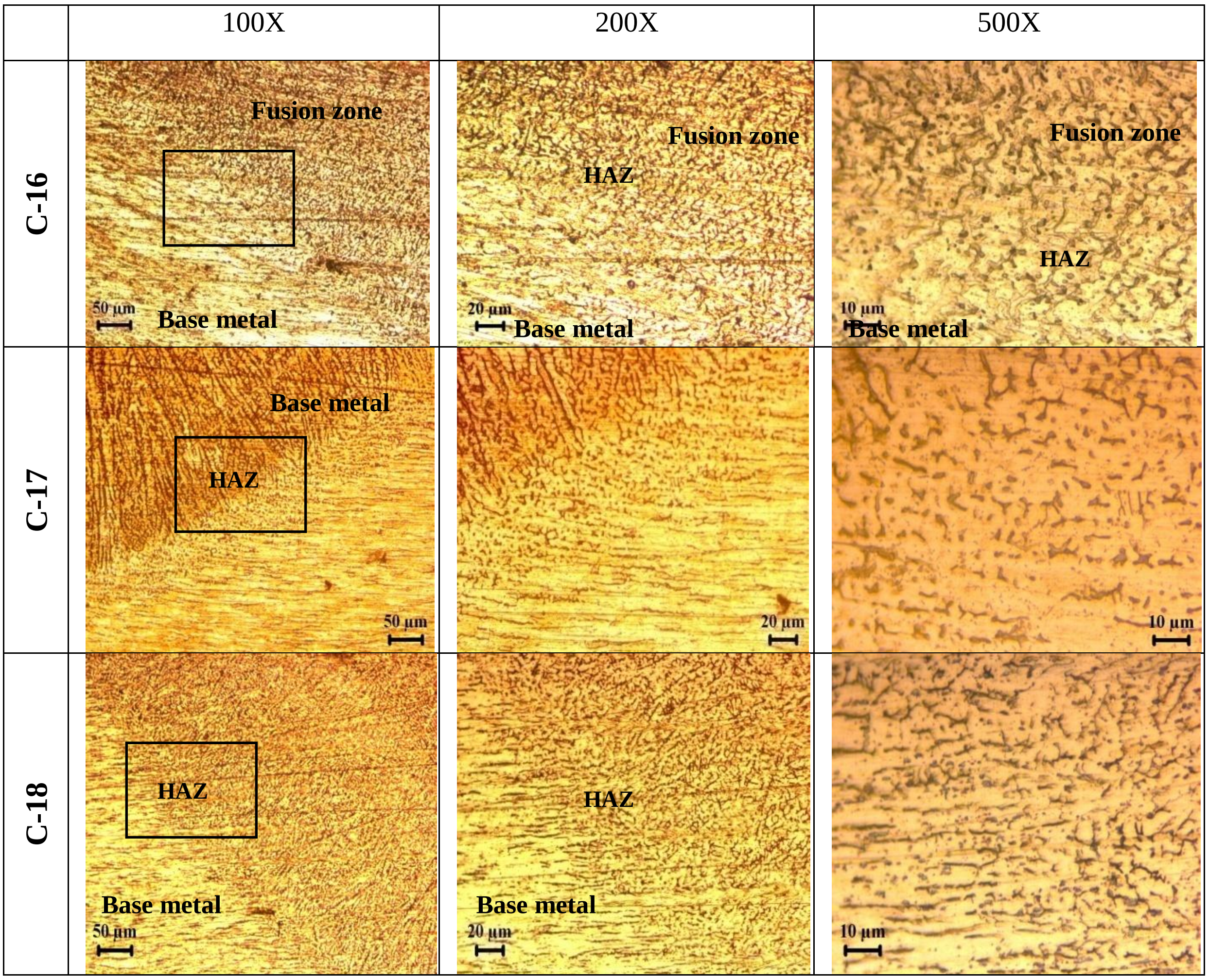

Figure 4.53: Microstructure after ATIG of AISI 304 stainless steel (Ar shielded)
From Sample 16 to 18 (C-16 to C-18)

Sample-1 (C-1) has a close pack of grains in its FZ and HAZ with carbide precipitation, due to fast cooling of weld metal as it was welded with leas current (125A). Hence due to fast cooling carbide and martensite appears between the grains of ferrite. It is also justified with low value of toughness (33 J), which is less than the toughness of parent metal toughness (i.e. 70 J). Similarly, it takes a low bending force (i.e. 10.3 KN) during bending.

Most of the workpieces have austenite phases, which are visible in their microstructures. This signifies that the amount of heat input and flow of shielding gas control the heat loss and cooling rate are sufficient to complete the transformation of austenite from ferrite and the solidification rate is sufficient. In AISI 304, not much significant difference is observed in microstructure when flux is used. In this case, somewhat larger grains are formed when activated flux is used.

4.4.6.2 Metallurgical Analysis of AISI 304 Welding Joint (Ar+5%H_2 Shielded)

Microstructure analysis is carried out for all TIG and A-TIG welded specimens of AISI 304 stainless steel under Ar+5%H_2 shielding gas supply, by using metallurgical microscope at 10X, 20X, 50X magnification. Fig. 4.54 to Fig. 4.57 shows the microstructures at 10X, 20X, 50X magnification levels of weld regions of AISI 304 austenitic stainless steel which is welded as per orthogonal array design for Ar+5%H_2 study. After welding the Samples are cut and is grounded with surface grinder, polished and etched, using (Ralph’s) for microstructure study. In Fig. 4.54 to Fig. 4.57 the fusion zone, heat affected zone (HAZ) and unaffected base metal are clearly visible, captured and the same is zoomed at above mentioned magnification level. In Fig. 4.54, Sample C’-1 to C’-3 depicts the microstrucural pictures of weld metal welded under Ar+5%H_2 at 125 A, 150 A, 175 A, without flux. Rests of the pictures are the microstructural pictures of Samples C’-4 to C’-18 which are welded under Ar+5%H_2 shielding with different welding parameters and by using different fluxes. The structure of weld metal is found totally different from the structure of the base metal.

Hydrogen is added in argon gas to achieve maximum penetration due to higher thermal conductivity of this mixture and higher welding speed can be achieved with this mixture, so for this reason it is used in this study at a welding speed of 3 mm/second.

From the results of bend test, toughness test and microhardness test, it is found that the Sample-13 (C’-13) has maximum microhardness values of both FZ and HAZ (i.e. 444.77 and 352.18), which justifies that the presence of precipitate carbide in the FZ and HAZ (shown in 4.53, C’-13). Sample C’-13 has also a low toughness value (i.e. 11 J), which is very low as compare to base metal microhardness (i.e. 70 J). Similarly this Sample has a low bending force (i.e. 9.05), which justify that it is brittle and hard.

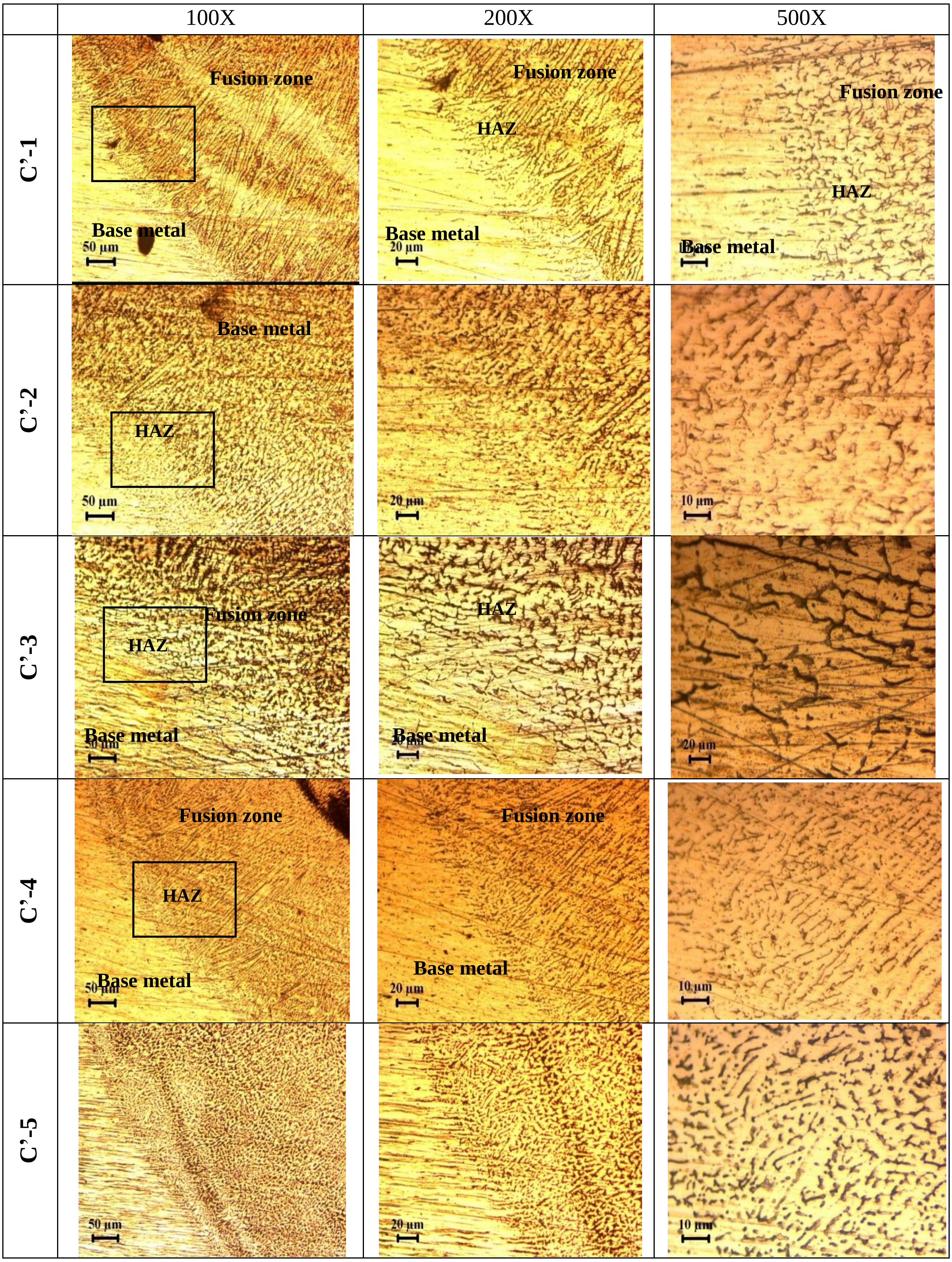

Figure 4.54: Microstructure after TIG and ATIG of AISI 304 stainless steel (Ar+5%H_2 shielded) From Sample 1 to 5 (C'-1 to C'-5)

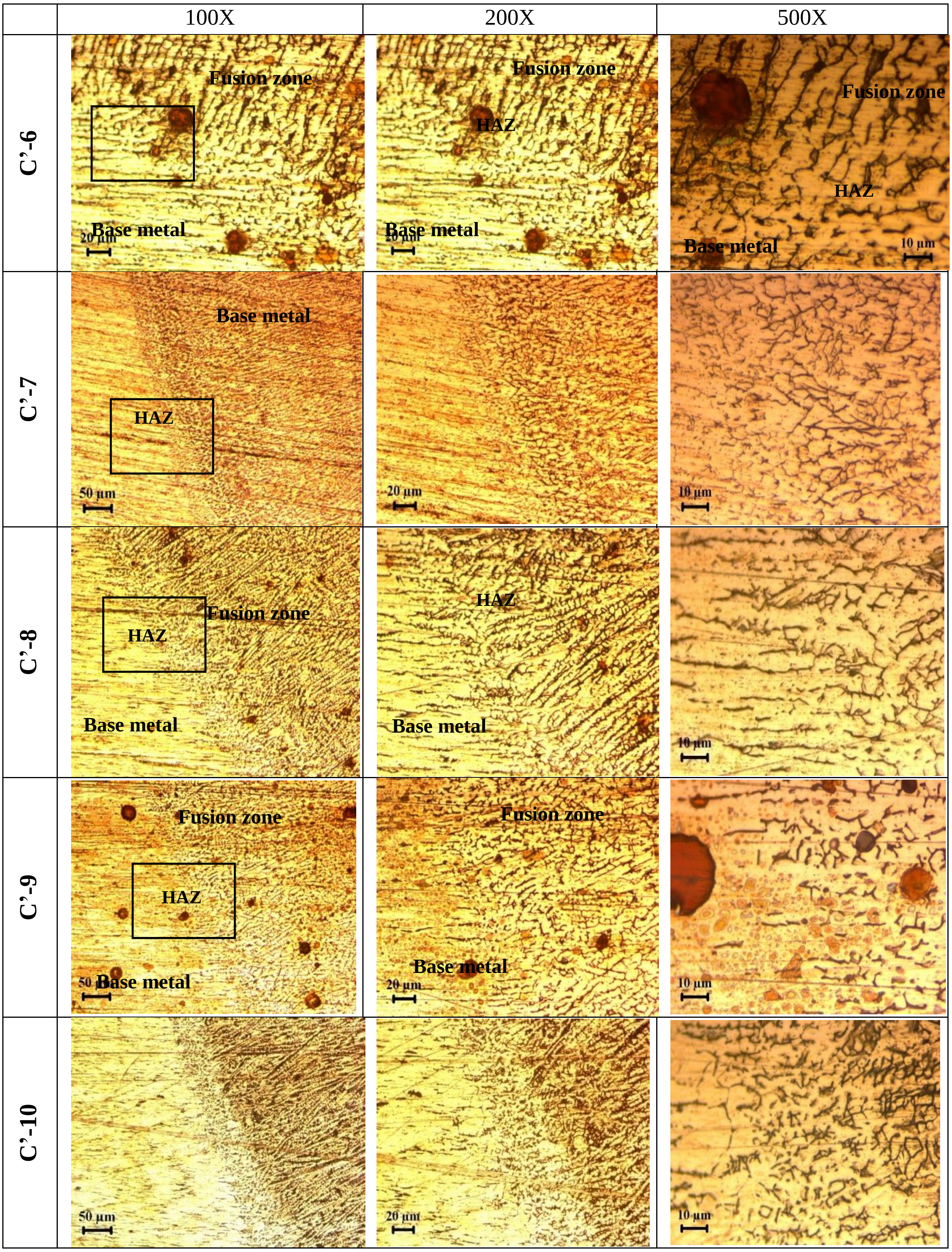

Figure 4.55: Microstructure after ATIG of AISI 304 stainless steel (Ar+5%H_2 shielded) From Sample 5 to 10 (C'-5 to C'-10)

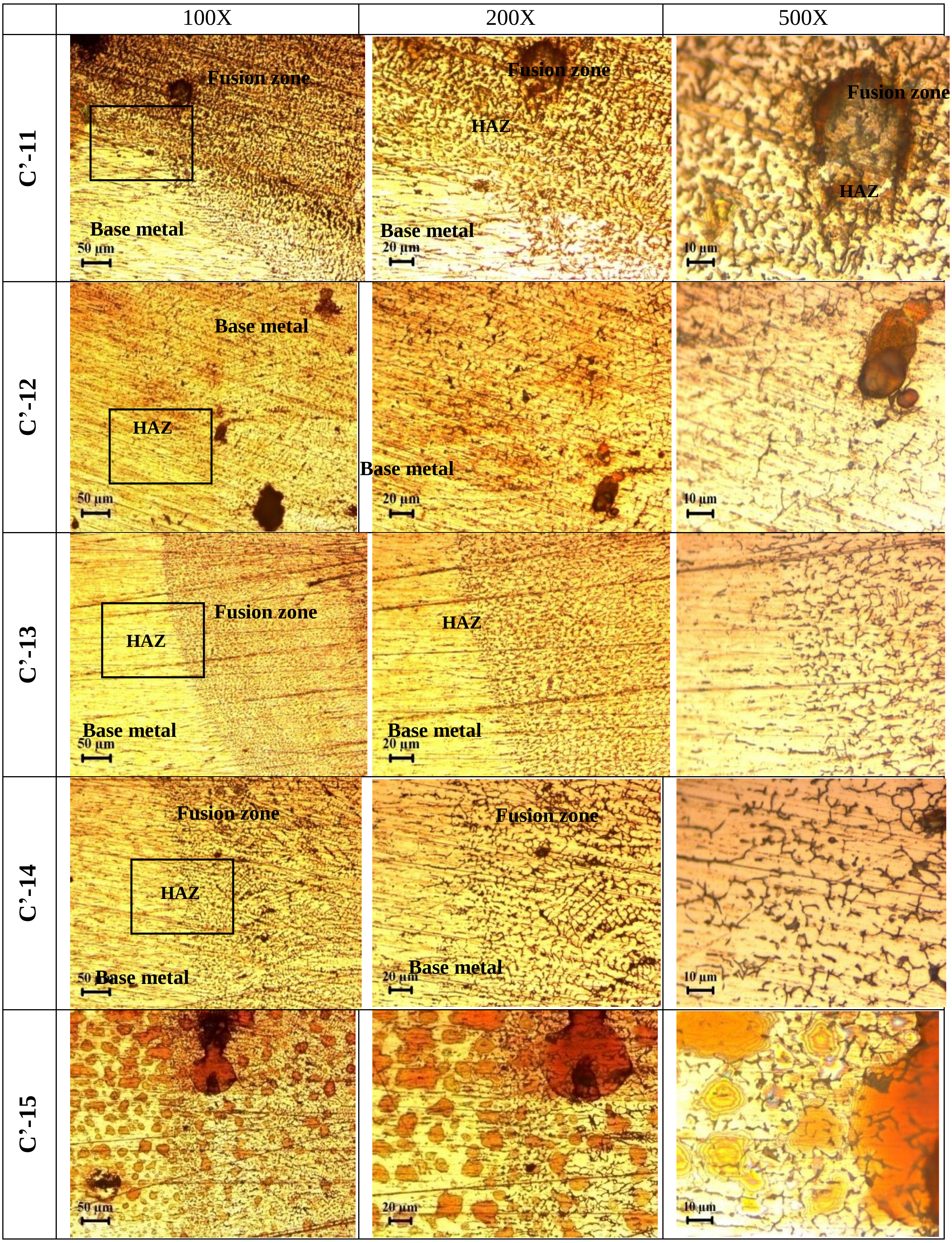

Figure 4.56: Microstructure after ATIG of AISI 304 stainless steel ($Ar+5\%H_2$ shielded) From Sample 10 to 15 (C'-10 to C'-15)

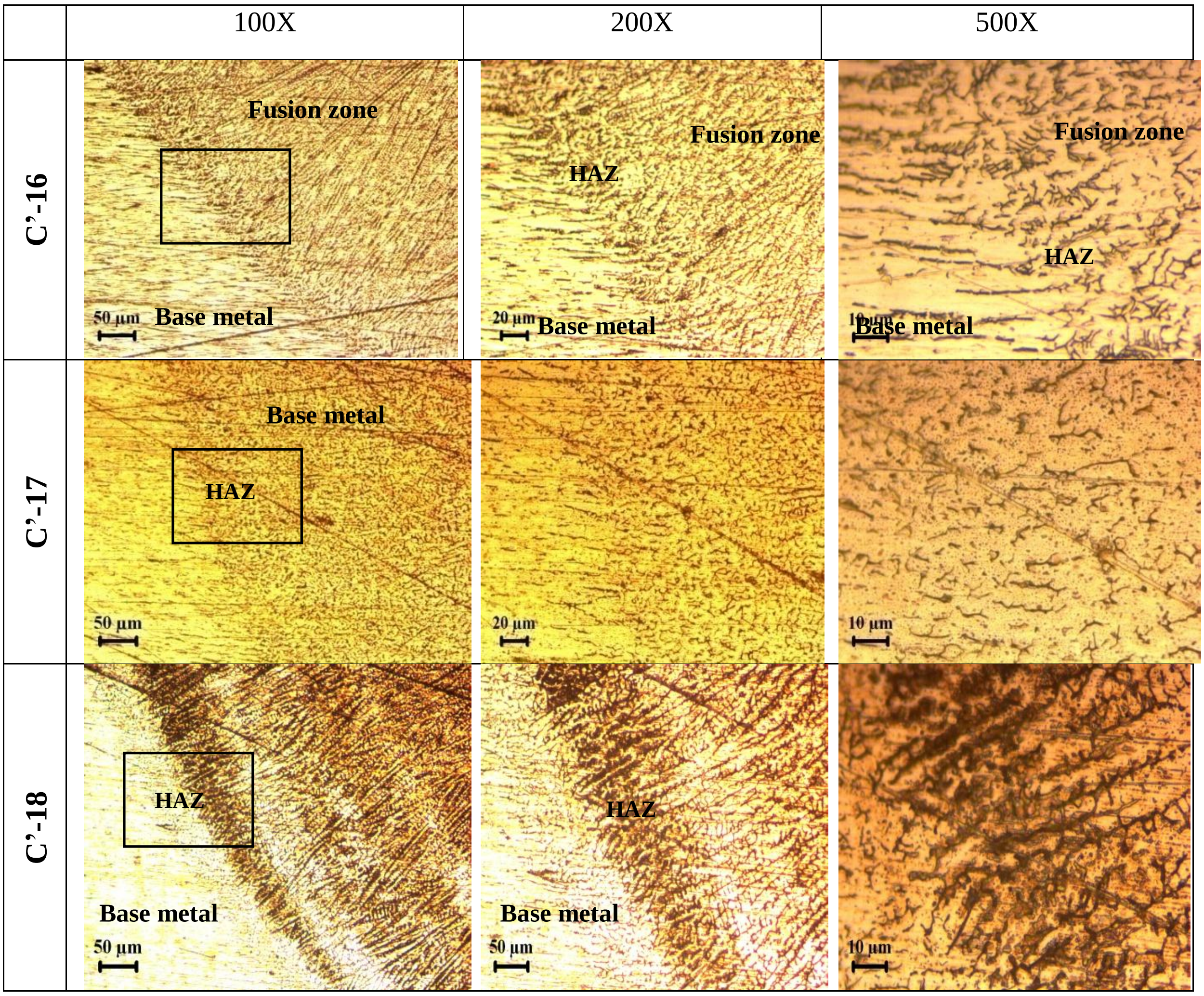

Figure 4.57: Microstructure after ATIG of AISI 304 stainless steel (Ar+5%H_2 shielded) From Sample 16 to 18 (C'-16 to C'-18)

4.4.7 Metallurgical Analysis Using Scanning Electron Microscope (SEM)

The microstructural analysis is carried out on the selected Samples, after seeing the result of bending, toughness and microhardness test. This test is done in SAI lab using scanning electron microscope machine (Model-JEOL JSM-6480LV) to investigate the change in microstructure of FZ and HAZ of TIG and A-TIG welded specimens under pure argon and Ar+5%H_2 shielded. Samples of SEM are prepared by polishing machine using emery papers of different grit size ranging from 600 to 2000 and further processed by etching. Before SEM the Samples are properly clean with acetone to remove any residual impurities. Finally SEM micrographs are taken at the interface of FZ and HAZ by covering the area into 50% and in the ratio of 25% and 75% at 500X and 1000X.

4.4.7.1 Metallurgical Analysis of joints of AISI 304 (Ar shielded) by SEM

Figure 4.58 to Figure 4.60 shows the microstructures of joints of AISI 304 of TIG and A-TIG welded under shielding of pure Ar gas supply. The Sample (C-10) welded with MoO_3 flux at 125 A current. The SEM photograph shows porous weld. The minimum value of toughness is found in this case due to low heat input and presence of porosity in the FZ and HAZ.

At high heat input (1925 J/mm) the Sample -6 (C-6) produce fine and close compact grains. This Sample was weld at 175 A with TiO_2 flux, so due to close compact grains it takes maximum bending force (22.6 KN) and proper U-shape is formed after bending. No tearing or crack was found on the surface of the bend specimen.

A fine grain structure is produced by Sample-12 (C-12) due to its fine grain structure it has a good toughness value (98 J), which is greater than the toughness of parent metal (i.e. 70J). This Sample is welded with MoO_3 flux at 175 A current.

The Sample-15 (C-15) is welded with CrO3 flux at 175A current. This Sample has maximum value of toughness (101 J) which is greater than other Samples which are welded under Ar shielding.

Sample No:	**Heat Input (J/mm)**	**500X**	**1000X**	**1000X**
C-2	1650	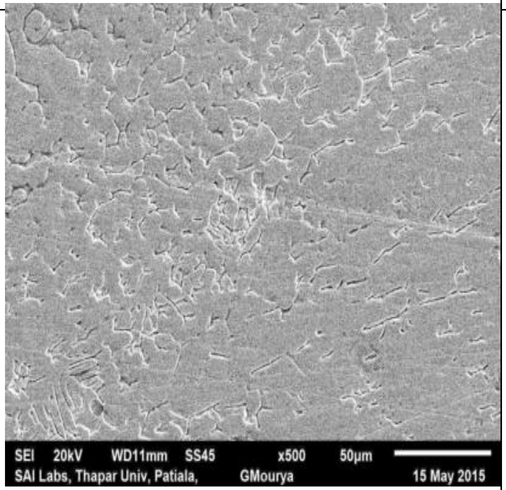	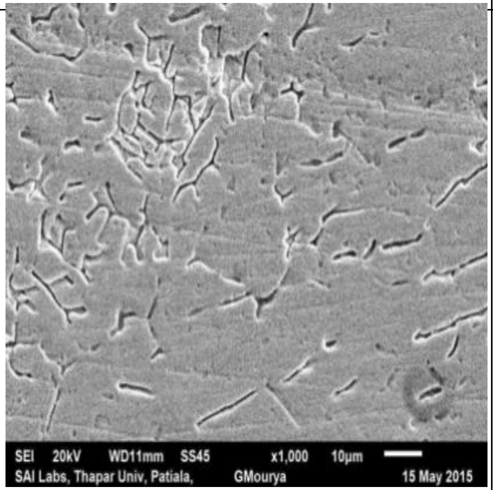	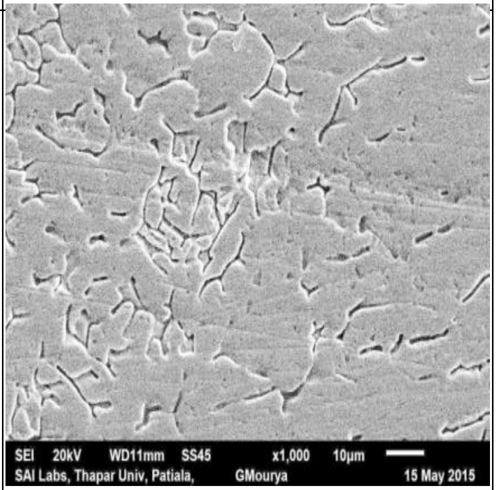
C-6	1925	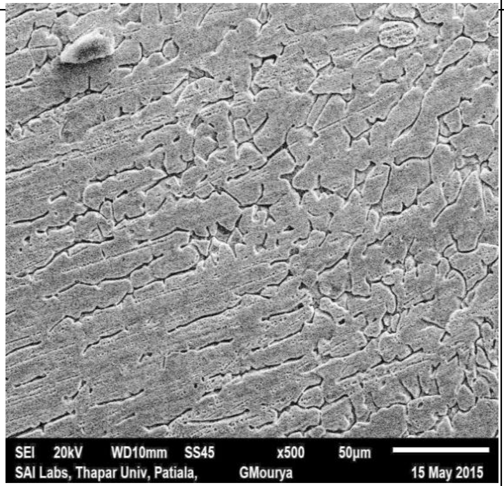	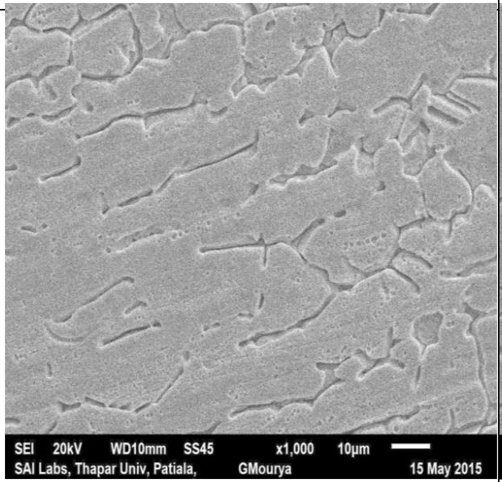	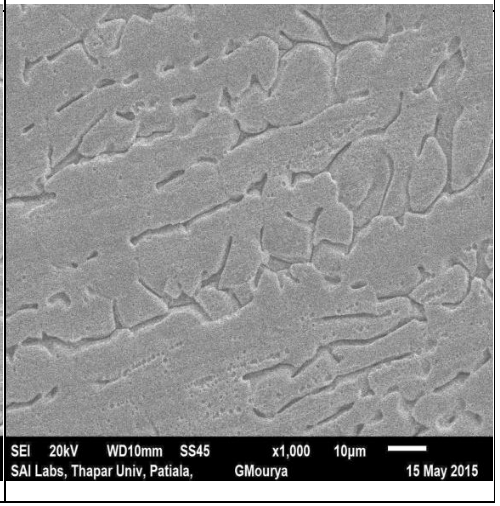

Figure 4.58: SEM pictures of Sample-2 and 6 of AISI 304 (Ar shielded)

Sample No:	Heat Input (J/mm)	500X	1000X	1000X
C-8	1650	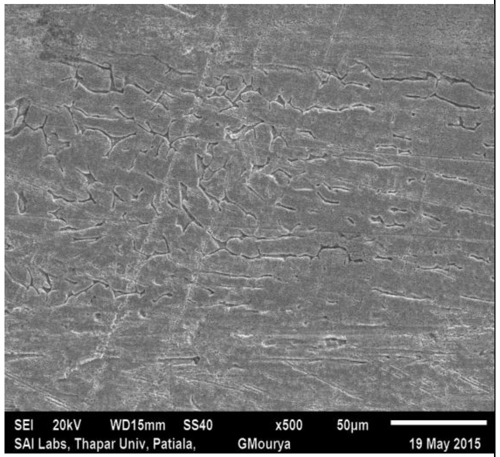	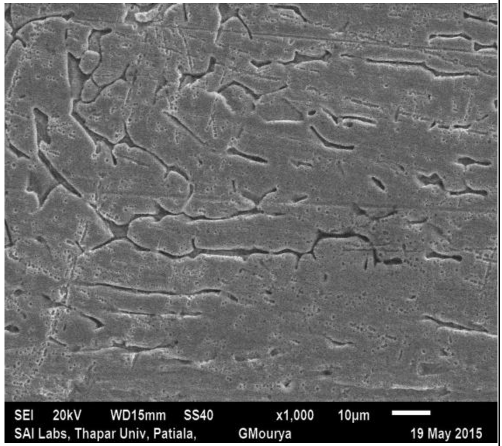	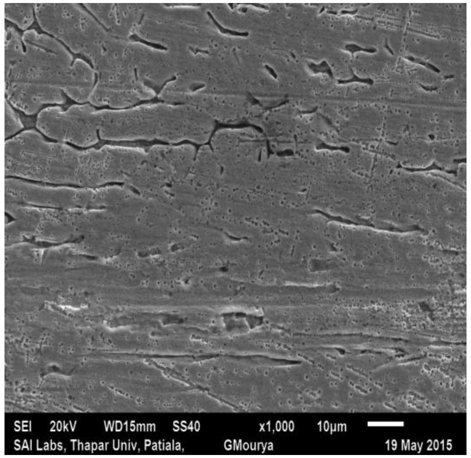
C-10	1375	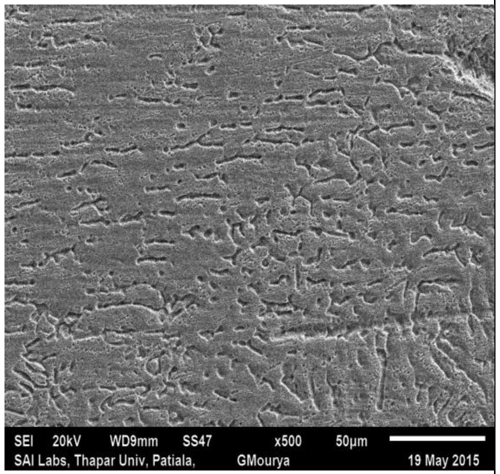	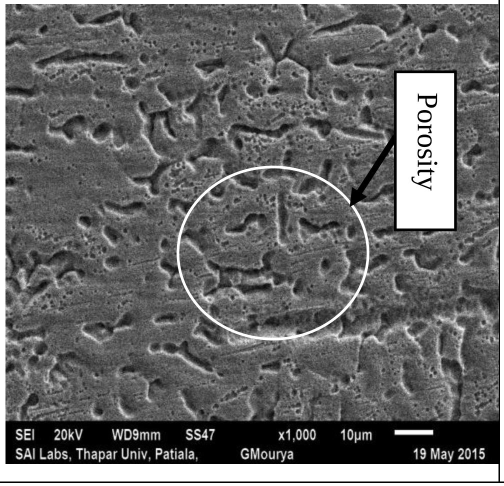	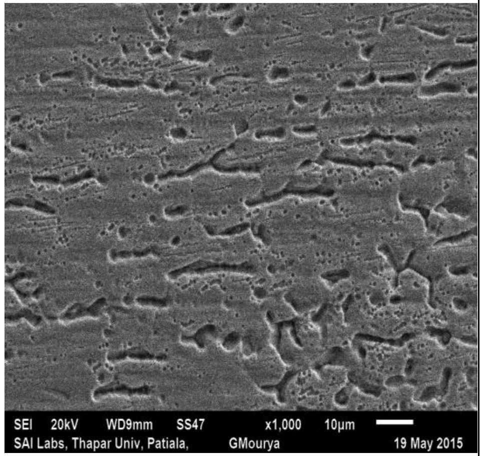

Figure 4.59: SEM pictures of Sample-8 and 10 of AISI 304 (Ar shielded)

Sample No:	**Heat Input (J/mm)**	**500X**	**1000X**	**1000X**
C-12	1925	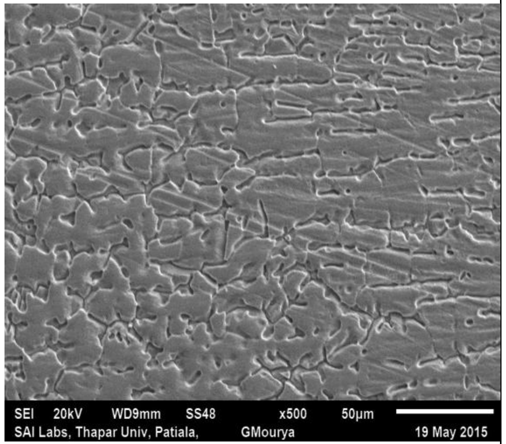	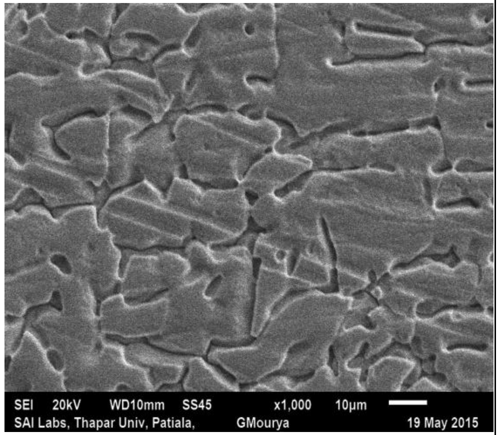	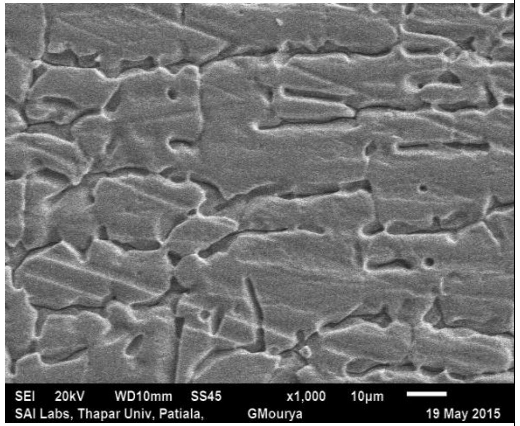
C-15	1925	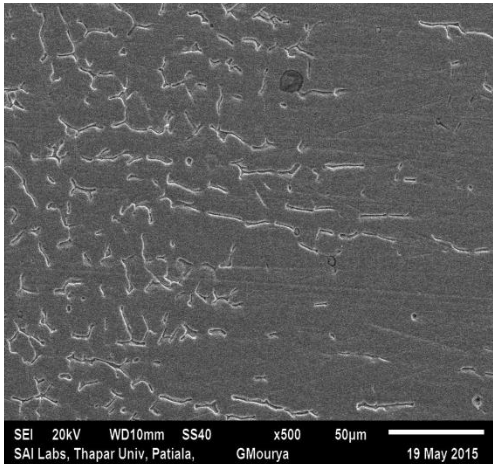	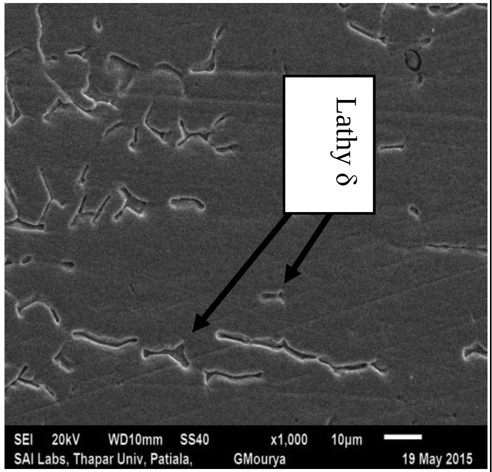	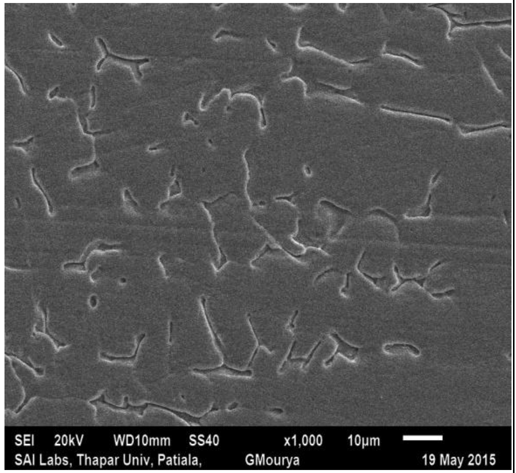

Figure 4.60: SEM pictures of Sample-12 and 15 of AISI 304 (Ar shielded)

4.4.7.2 Metallurgical Analysis of joints of AISI 304 (Ar+5%H_2 shielded) by SEM

Figure 4.61 to Figure 4.63 shows SEM pictures of joints of AISI 304 of TIG and A-TIG welded under shielding of pure Ar+5%H_2 gas supply. In case of AISI 304 austenitic stainless steel the value of δ-ferrite is found to increase from its normal value under the influence of flux and increase the mechanical properties of the joint consequently. From Fig. 4.61 (C'-9, 55X, welded with SiO_2 flux at 175 A) it is clear that a big cavity is formed in the FZ. In spite of a big cavity the Sample has good toughness value (83 J) which greater than the value of parent metal toughness (70 J) and its FZ and HAZ mean hardness are 357.247 and 349.877 which is little lower than parent metal microhardness (i.e. 370).

The lathy δ-ferrite is found in the FZ of Sample C'-11, whereas skeletal δ-ferrite is ound in Sample C'-9 and in Sample C'-15. The main difference between the Ar shielded and Ar+5% H_2 shielded SEM pictures is that both pictures are the result of different heat input and in case of Ar+5% H_2 Samples hydrogen entrap in the weld zone. As the heat input increases then the chances of hydrogen contamination is increases.

Sample No:	Heat Input (J/mm)	500X	1000X	1000X
C’-3	1283.33	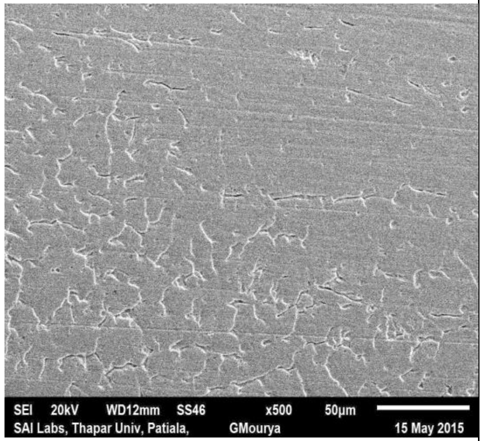	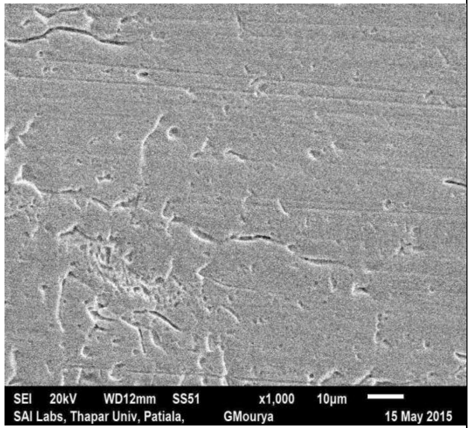	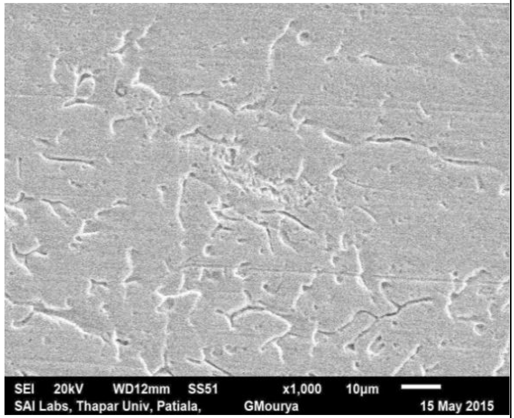
C’-5	1100.00	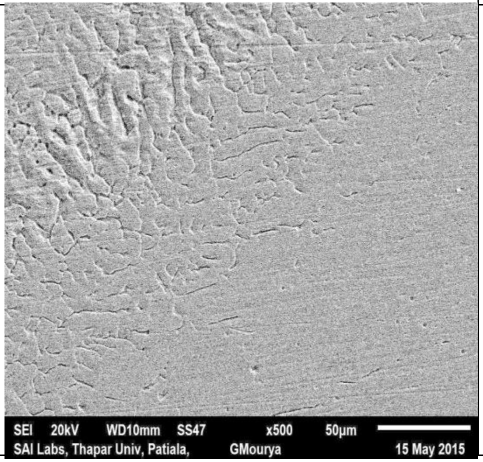	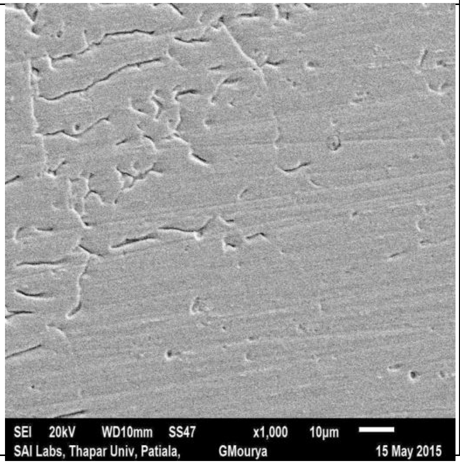	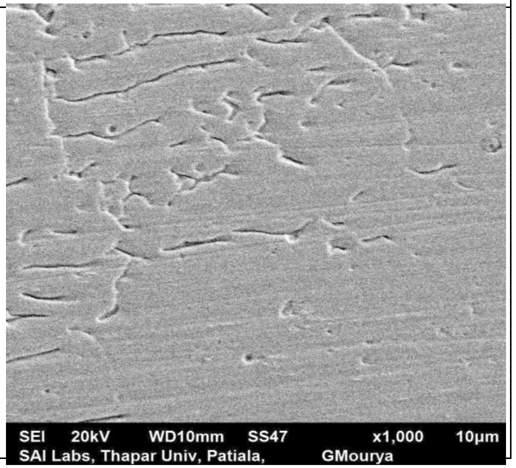

Figure 4.61: SEM pictures of Sample-C’-3 and C’-5 of AISI 304 (Ar+5%H_2 shielded)

Sample No:	**Heat Input (J/mm)**	**500X**	**1000X**	**1000X**
C’-9	1283.33	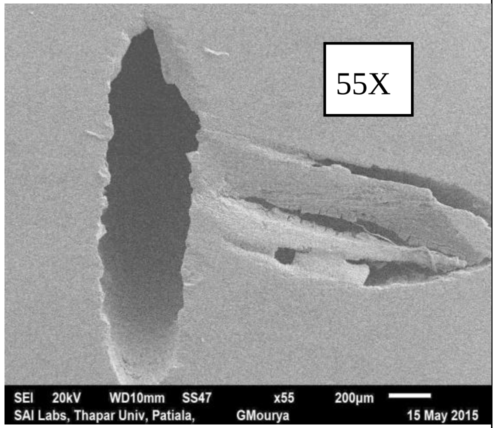	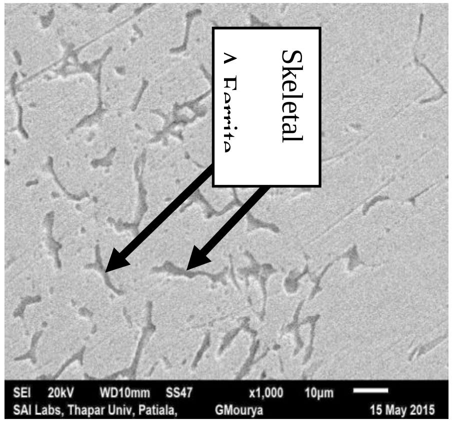	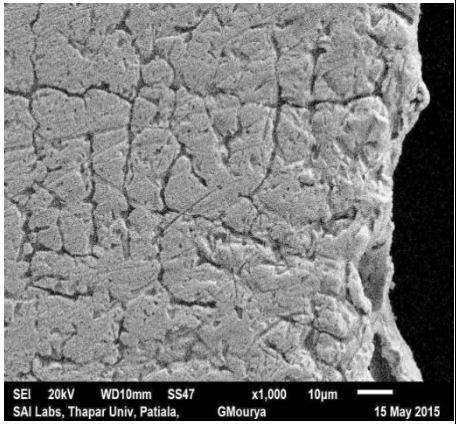
C’-11	1100.00	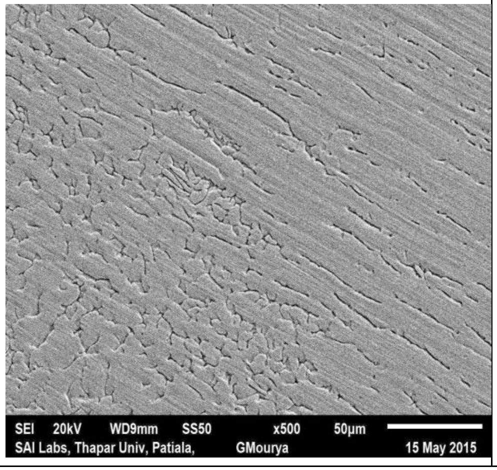	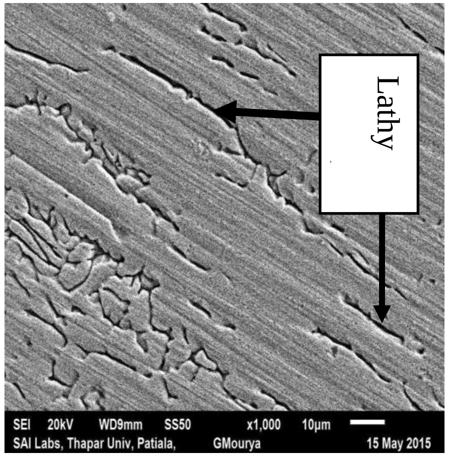	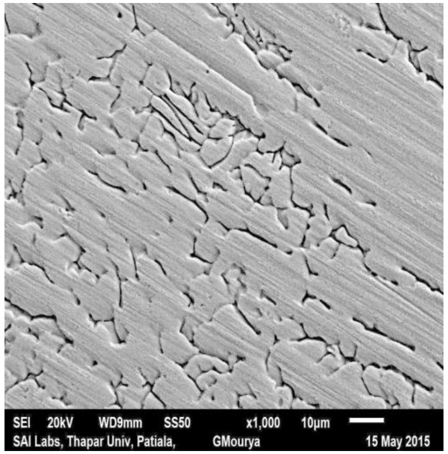

Figure 4.62: SEM pictures of Sample-C’-9 and C’-11of AISI 304 (Ar+5%H_2 shielded)

Sample No:	Heat Input (J/mm)	500X	1000X	1000X
C’-15	1283.33	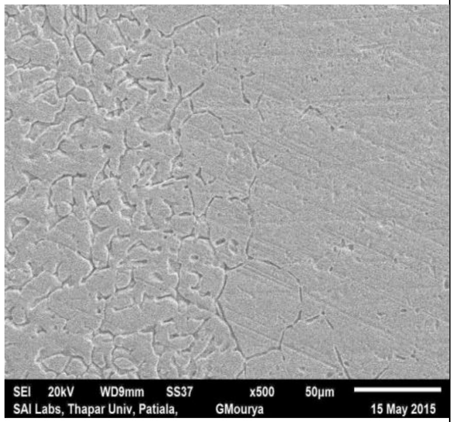	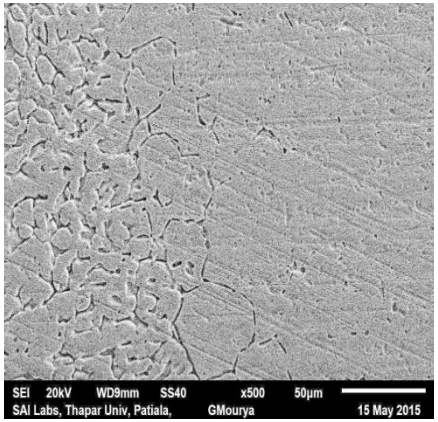	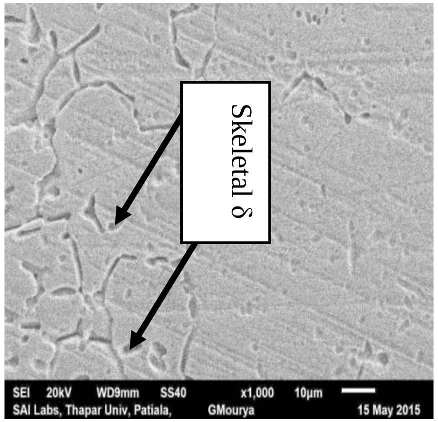
C’-18	1283.33	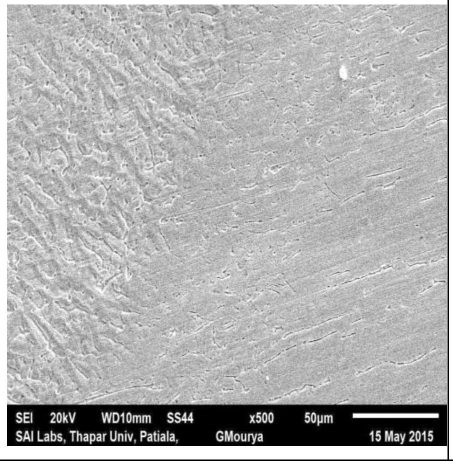	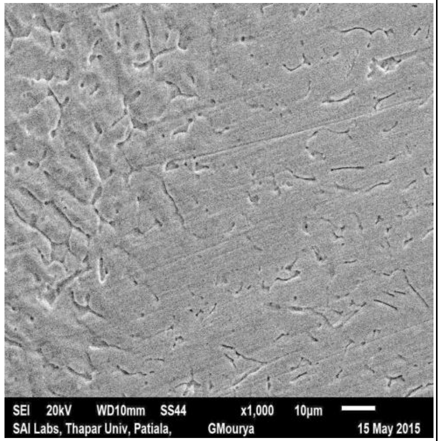	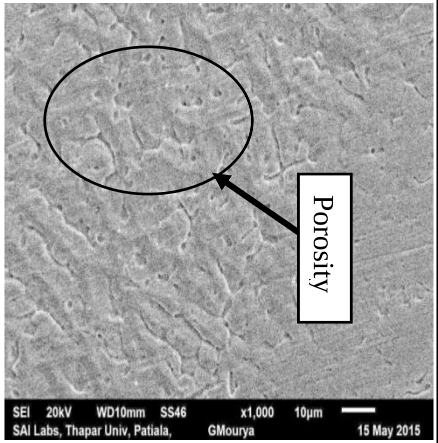

Figure 4.63: SEM pictures of Sample-C’-15 and C’-18 of AISI 304 (Ar+5%H_2 shielded)

Chapter 5

Conclusions and Scope for Future Work

5.1 Conclusions

The main aim of the present study is to investigate the influence of different types of activated flux on depth of penetration, depth-to-width ratio during flux activated TIG welding. Effect of fourteen different fluxes, at different levels of current and different shielding gases (pure Ar, Ar+5% H_2 and Ar+He) are studied. The investigation is carried out on different graded steels like low carbon steel (AISI 1020), austenitic stainless steels (AISI 304 and AISI 316), low alloy steel (AISI 4340) and duplex stainless steel (Duplex 2205) using conventional TIG and A-TIG welding.

After selecting five best fluxes from above study a parametric study is conducted to investigate the influence of different fluxes, current, gas flow rate, vertex angle of electrode, and torch angle on joint bending load, toughness, microhardness. This study is carried out at two different welding speeds and under the two different shielding environments (i.e. 2 mm/s for Ar and 3 mm/s for Ar+5% H_2). Microstructural analysis by optical microscope and SEM are also carried out. Based on the results obtained of the present work, the following conclusions are drawn.

- By using TiO2 flux, significant increase in depth of penetration and reduction in width-to-penetration is found in case of AISI 1020, AISI 304, AISI 316 and Duplex 2205 stainless steel.
- Due to constriction of arc and change in the surface tension gradient from negative to positive the molten metal fluid flow from outward direction to inward direction result into deep penetration and this phenomenon is called reverse Marangoni convection.
- It has been found that by increasing current the depth-of-penetration also increases and the use of flux make it more significant.
- Maximum of 37.8%, 44.3%, 47%, and 124% increase in depths of penetration is measured for AISI 1020, AISI 304, AISI 316, and Duplex 2205 steels with pure Ar, respectively, when activated flux is used. H2 in shielding gas immensely enhances DOP and more than 200–300% increase in penetration is noted as compared to pure Ar when TiO2, SiO2, or MoO3 fluxes are used.

- Addition of small percentage of hydrogen in argon gas helps to increase the conductivity of shielding gas. Hence the melting efficiency increases, which further melt oxide layer and increase the penetration depth.
- Microstructure observation shows that fluxes do not deteriorate the mechanical properties and sufficient austenite is found in the fusion zone from the transformation of austenite from ferrite especially in the case of duplex 2205 stainless steel.
- Five fluxes (TiO_2, SiO_2, MoO_3, MoS_2 and CrO_3) are found to be most significant in this study to increase the depth of penetration and to reduce width-to-penetration ratio.
- During ATIG welding with Ar shielding gas environment, maximum bending load is obtained when welding is carried out with TiO_2 flux, 175 A current. Higher level of current (175A), higher gas flow rate and 60° tip angle helps to obtain higher bending load of the welded joints. Use of CrO_3, TiO_2, SiO_2 fluxes can improve the bending load of the welded joints.
- During A-TIG welding with Ar+5% H_2 shielding gas environment, maximum bending load is obtained when welding is carried out with MoO_3 flux, 150 A current. Medium level of current (150A), lower gas flow rate, 60° tip angle and 85° torch angle helps to obtain higher bending load of the welded joints. Without flux and use of SiO_2 fluxes can improve the bending load of the welded joints.
- In case of A-TIG welding with Ar shielding gas environment, maximum toughness is achieved when welding is carried out with CrO_3 flux, 175 A current. Higher level of current (175A), 75° tip angle and 45° torch angle helps to obtain higher bending load of the welded joints. Use of CrO_3, TiO_2, SiO_2 fluxes can improve toughness of the welded joints.
- In case of A-TIG welding with Ar+5% H_2 shielding gas environment, maximum toughness is achieved when welding is carried out with SiO_2 flux, 175 A current. Higher level of current (175A) and use of SiO_2 and CrO_3 flux can improve toughness of the welded joints.
- Use of Ar+5% H_2 shielding gas can improve the penetration and can be used for higher speed welding as compared to pure Ar shielded welding. However, there could be probability of hydrogen induced porosity in the welded region which may further decrease the welded joint quality.

- Large amount of austenite is formed in case of A-TIG welding with Ar shielding environment with lathy ferrite content.
- Maximum value of microhardness (446.147 HVN) in the FZ is obtained in case of Ar shielding, with SiO2 flux at 125 A (low current) and in case of Ar+5% H2 shielding the maximum microhardness (444.77 HVN) is found with CrO3 flux at 125 A current.
- Lathy δ-ferrite and skeletal δ-ferrite is found in some samples.

5.2 Scope for Future Work

The present work also leaves ample scope for future investigators to explore in the field of A-TIG welding. Some of the future recommendations are:

- A-TIG welding has an ample scope in the stainless steel welding. So, it may use to join dissimilar metals.
- Distortion is the common problem in welding. It has also come in A-TIG welding at low heat input, means at low welding current. So, it may investigate for further study.
- Large percentages of H_2 in pure Ar gas also cause some porosity in the weld zone. So, it may try with varying the percentage of H_2 gas.
- Effect of post weld heat treatment (PWHT) may also be carried out to see the change in microstructure.
- XRD and TEM analysis may also be carried out to see the variation of alloying element at particular location and to see the formation of δ-ferrite in different phases of the weld zone.
- Mixture of fluxes in different proportion can be used to see the variation in the weld morphology.
- Tensile test and radiography test will be helpful to see the internal defects and to find the joint strength.

References

Arunkumar, V.; Vasudevan, M.; Maduraimuthu, V.; Mutupandi, V. (2012**)** Effect of activated flux on the microstructure and mechanical properties of 9cr-1mo steel weld joint. *Materials and Manufacturing Processes,* 27: 1171–1177.

Arivazhan. B and Vasudevan. M. (2015) Studies on A-TIG welding of 2.25Cr-1Mo (P22) steel. *Journal of Manufacturing Process*, 18: 55-59.

Brauser, S. and Kannengiesser, T. (2010) Hydrogen absorption of different welded duplex steels. *International Journal of Hydrogen Energy*, 35: 4368-4374.

Chern, T. S.; Tseng, K. H.; Tsai H. L. (2011) Study of the characteristics of duplex stainless steel activated tungsten inert gas welds**.** *Materials and Design,* 32: 255–263.

Durgutlu, A (2004) Experimental investigation of the effect of hydrogen in argon as a shielding gas on TIG welding of austenitic stainless steel. *Materials and Design*, 25: 19-23.

Dhandha, H. K.; Badheka. J. V. (2015) Effect of activating fluxes on weld bead morphology of P91 steel bead-on-plate welds by flux assisted tungsten inert gas welding process. *Journal of Manufacturing Process*, 17: 48-57.

Diaz, C. D. J. J.; Rodriguez M. P.; Nieto, G. J.P.; Fresno, C. D. (2010) Comparative analysis of TIG welding distortions between austenitic and duplex stainless steels by FEM. *Applied Thermal Engineering,* 30: 2448-2459.

Gulenc, B.; Develi, K.; kahraman, N.; Durgutlu, A. (2005) Experimental study of the effect of hydrogen in argon as a shielding gas in MIG welding of austenitic stainless steel. *International Journal of Hydrogen Energy*, 30: 1475-1481.

Lu, S., LI, D.; Fujii, H.; Nogi *K. (*2007) Time Dependant Weld Shape in Ar-O2 Shielded Stationary GTA Welding**,** *Journal of Material Science and Technology,* 23(5):650.

Lu, S.; Fujii, H.; Nogi K. (2010) Weld Shape Variation and Electrode Oxidation Behaviour under Ar-(Ar-CO2) Double Shielded GTA Welding, *Journal of Materials Science and Technology*, 26(2): 170-176.

Lin, H. L. & Wu, T. M. (2012) Effects of Activating Flux on Weld Bead Geometry of Inconel 718 Alloy TIG Welds**,** *Materials and Manufacturing Processes*, 27: 1457–1461.

Modenesi P. J.; Apolinario P. R.; Pereira I. M. (2000) TIG welding with single-component fluxes, *Journal of Materials Processing Technology*, 99:260-265.

Morisada, Y.; Fujii, H.; Inagaki, F.; Kamai, M. (2013) Development of high frequency tungsten inert gas welding method. *Materials and Design*, 44: 12-16.

Morisada, Y.; Fujii, H.; Xukun, N. (2014) Development of simplified active flux tungsten inert gas welding for deep penetration. *Materials and Design*, 54: 526-530.

Niagaj, J. (2013) Effect of A-TIG welding on deformation of austenitic steel components. *Welding International*, 27(11): 853–856.

Parshin, S.G. (2012) Using ultrafine particles of activating fluxes for increasing the productivity of MIGMAG welding of steels.*Welding International* , 26 (10): 800–804.

Ruckert, G.; Huneau, B.; Marya, S. (2007) Optimizing the design of silica coating for poductivity gains during the TIG welding of 304L stainless steel. *Materials and Design*, 28: 2387-2393.

Sandor, T.; Mekler, C.; Dobranszky, J.; Kaptay G. (2012) An Improved Theoretical Model for A-TIG Welding Based on Surface Phase Transition and Reversed Marangoni Flow**.** *The Minerals, Metals & Materials Society and ASM International, 44A: 351.*

Sakthivel, T.; Vasudevan, M.; Laha, K.; Parameswaran, P.; Chandravathi, S. K.; Mathew, D. M.; Bhaduri, K. A. (2011) Creep rupture strength of activated-TIG welded 316L(N) stainless steel. *Journal of Nuclear Materials,* 413: 36-40.

Tseng, K. H. & Hsu, C. Y. (2010) Performance of activated TIG process in austenitic stainless steel weld**.** *Journal of Materials Processing Technology*, 211: 503–512.

Tseng, K. H., & Chen K. L. (2012) Comparisons Between TiO_2 and SiO_2 Flux Assisted TIG Welding Processes. *Journal of Nanoscience and Nanotechnology,* 12: 6359–6367.

Tusek, J. and Suban, M. (2000) Experimental research of the effect of hydrogen in argon as a shielding gas in arc welding of high-alloy stainless steel. *International Journal of Hydrogen Energy*, 25: 369-376.

Tathgir, S. K.; Bhattacharya, A.; Bera, T. K. (2015) Influence of current and shielding gas in TiO2 flux activated TIG welding on different graded steels. *Materials and manufacturing Processes,* 30: 1115-1123.

Vasantharaja, P.; Vasudevan, M.; Palanichamy, P. (2014) Effect of welding processes on the residual stress and distortion in type 316LN stainless steel weld joints. *Journal of Manufacturing Process,* http://dx.doi.org/10.1016/j.jmapro.2014.09.004.

Xie, X.; Shen, J.; Cheng, C.; Li, Y.; Pu, Y. (2015) Effects of nano-particles strengthening activating flux on the microstructures and mechanical properties of TIG welded AZ31 magnesium alloy joints. *Materials and Design,* 81: 31-38.

Yuri, T.; Ogata, T.; Saito, M.; Hirayama, Y. (2000) Effect of welding structure and d-ferrite on fatigue properties for TIG welded austenitic stainless steels at cryogenic temperatures. *Cryogenics,* 40: 251-259.

Younes, M. C.; steele, M. A.; Nicholson, A. J.; Barnett, J. C. (2013) Influence of hydrogen content on the tensile properties and fracture of austenitic stainless steel welds. *International Journal of Hydrogen Energy*, 38: 4864-4876.

Zhang, G.; Xiong, J.; Gao, H.; Wu, L. (2012) Effect of process parameters on temperature distribution in twin-electrode TIG coupling arc. *Journal of Quantitative Spectroscopy & Radiative Transfer,* 113: 1938-1945.

Publications

1. Surinder Tathgir , Anirban Bhattacharya, Tarun kumar Bera, Influence of current and shielding gas in TiO2 flux activated TIG welding on different graded steels. *Materials and manufacturing Processes*, 30 (2015): 1115-1123. (**Published**)
2. Surinder Tathgir , Anirban Bhattacharya, Activated-TIG Welding of Different Steels: Influence of Various Flux and Shielding Gas. *Materials and manufacturing Processes,* DOI: 10.1080/10426914.2015.1037914 (**Available online**)

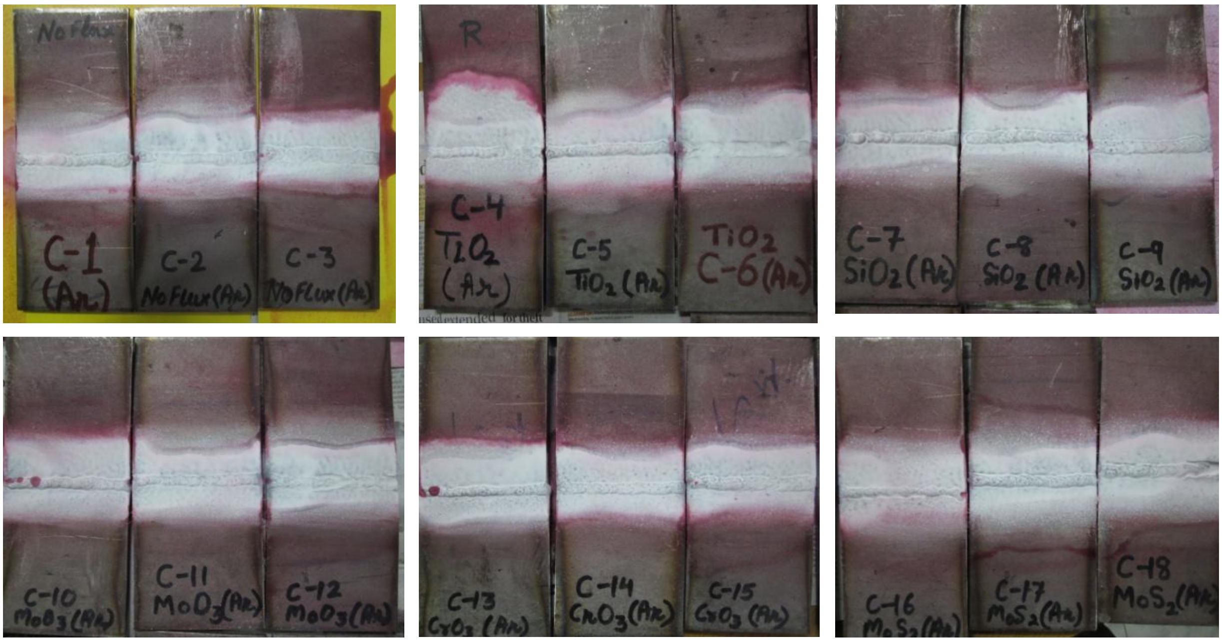

Figure Y: Photographs of samples after DPT, C-1 to C-18 of Ar shielding

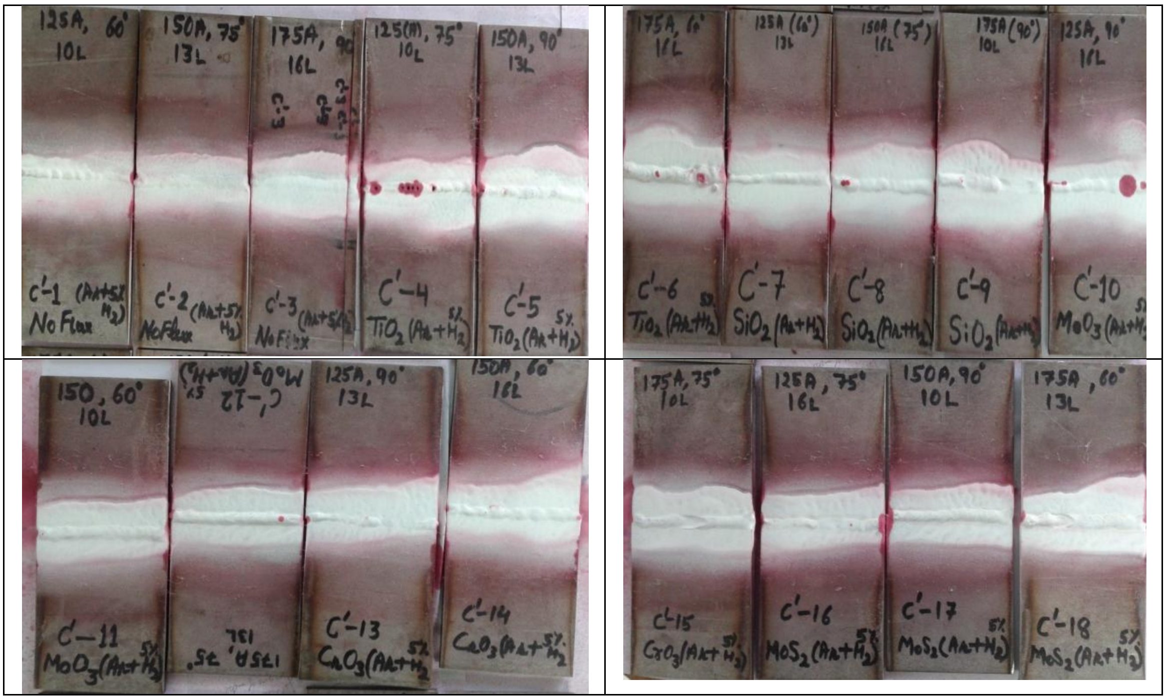

Figure Z: Photographs of samples after DPT, C'-1 to C'-18 of Ar+5%H_2 shielding

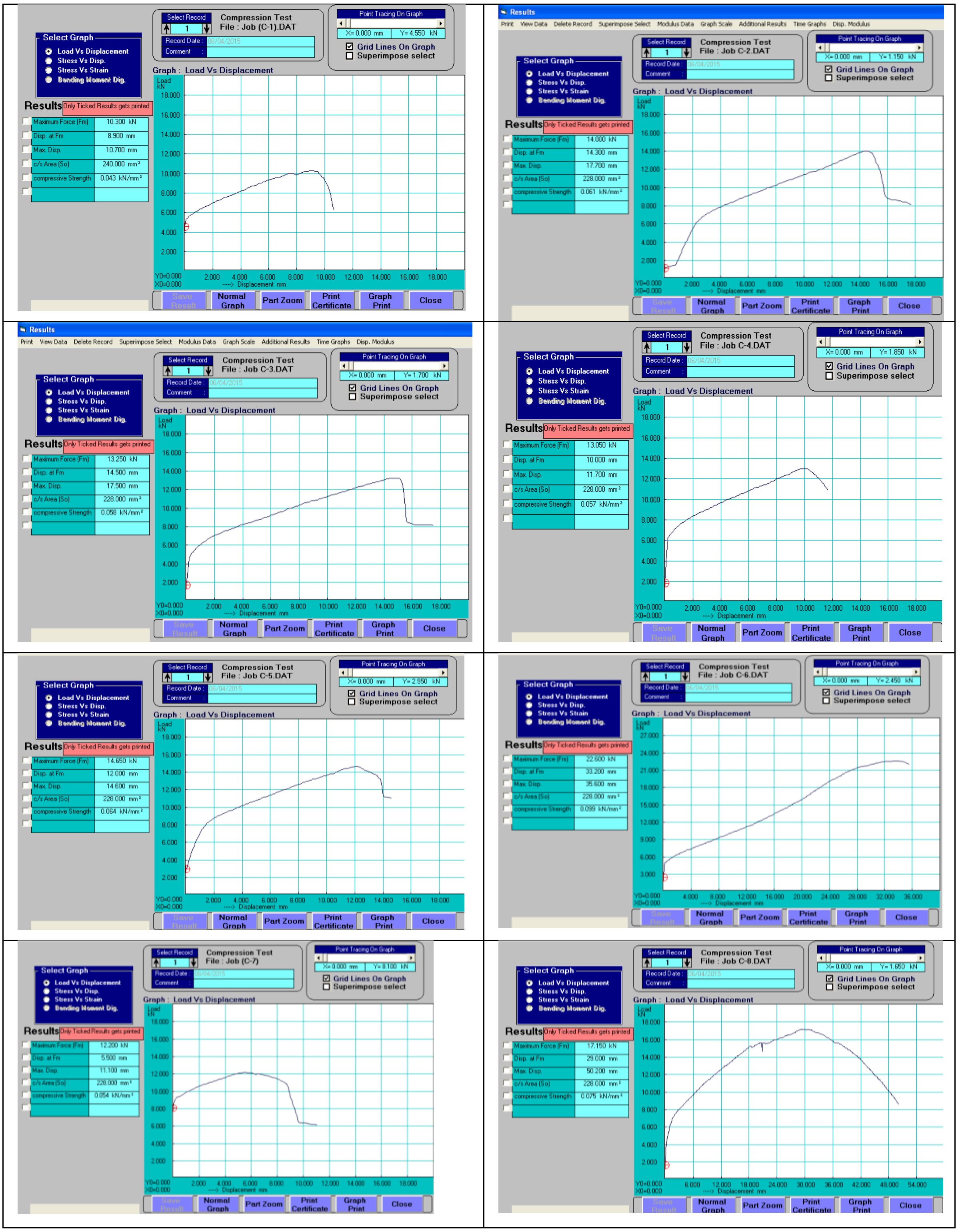

Compression Test
File : Job (C-1).DAT
Select Record: 1
Record Date : 06/04/2015
X= 0.000 mm Y= 4.550 kN
☑ Grid Lines On Graph
☐ Superimpose select

Results Only Ticked Results gets printed

☐	Maximum Force (Fm)	10.300 kN
☐	Disp. at Fm	8.900 mm
☐	Max. Disp.	10.700 mm
☐	c/s Area (So)	240.000 mm²
☐	compressive Strength	0.043 kN/mm²

Compression Test
File : Job C-2.DAT
Select Record: 1
Record Date : 06/04/2015
X= 0.000 mm Y= 1.150 kN
☑ Grid Lines On Graph
☐ Superimpose select

Results Only Ticked Results gets printed

☐	Maximum Force (Fm)	14.000 kN
☐	Disp. at Fm	14.300 mm
☐	Max. Disp.	17.700 mm
☐	c/s Area (So)	228.000 mm²
☐	compressive Strength	0.061 kN/mm²

Compression Test
File : Job C-3.DAT
Select Record: 1
Record Date : 06/04/2015
X= 0.000 mm Y= 1.700 kN
☑ Grid Lines On Graph
☐ Superimpose select

Results Only Ticked Results gets printed

☐	Maximum Force (Fm)	13.250 kN
☐	Disp. at Fm	14.500 mm
☐	Max. Disp.	17.500 mm
☐	c/s Area (So)	228.000 mm²
☐	compressive Strength	0.058 kN/mm²

Compression Test
File : Job C-4.DAT
Select Record: 1
Record Date : 06/04/2015
X= 0.000 mm Y= 1.850 kN
☑ Grid Lines On Graph
☐ Superimpose select

Results Only Ticked Results gets printed

☐	Maximum Force (Fm)	13.050 kN
☐	Disp. at Fm	10.000 mm
☐	Max. Disp.	11.700 mm
☐	c/s Area (So)	228.000 mm²
☐	compressive Strength	0.057 kN/mm²

Compression Test
File : Job C-5.DAT
Select Record: 1
Record Date : 06/04/2015
X= 0.000 mm Y= 2.950 kN
☑ Grid Lines On Graph
☐ Superimpose select

Results Only Ticked Results gets printed

☐	Maximum Force (Fm)	14.650 kN
☐	Disp. at Fm	12.000 mm
☐	Max. Disp.	14.600 mm
☐	c/s Area (So)	228.000 mm²
☐	compressive Strength	0.064 kN/mm²

Compression Test
File : Job C-6.DAT
Select Record: 1
Record Date : 06/04/2015
X= 0.000 mm Y= 2.450 kN
☑ Grid Lines On Graph
☐ Superimpose select

Results Only Ticked Results gets printed

☐	Maximum Force (Fm)	22.600 kN
☐	Disp. at Fm	33.200 mm
☐	Max. Disp.	35.600 mm
☐	c/s Area (So)	228.000 mm²
☐	compressive Strength	0.099 kN/mm²

Compression Test
File : Job (C-7)
Select Record: 1
Record Date : 06/04/2015
X= 0.000 mm Y= 8.100 kN
☑ Grid Lines On Graph
☐ Superimpose select

Results Only Ticked Results gets printed

☐	Maximum Force (Fm)	12.200 kN
☐	Disp. at Fm	5.500 mm
☐	Max. Disp.	11.100 mm
☐	c/s Area (So)	228.000 mm²
☐	compressive Strength	0.054 kN/mm²

Compression Test
File : Job C-8.DAT
Select Record: 1
Record Date : 06/04/2015
X= 0.000 mm Y= 1.650 kN
☑ Grid Lines On Graph
☐ Superimpose select

Results Only Ticked Results gets printed

☐	Maximum Force (Fm)	17.150 kN
☐	Disp. at Fm	29.000 mm
☐	Max. Disp.	50.200 mm
☐	c/s Area (So)	228.000 mm²
☐	compressive Strength	0.075 kN/mm²

Figure A: Load v/s displacements curve during face bend test of samples C-1 to C-8 (Ar shielding)

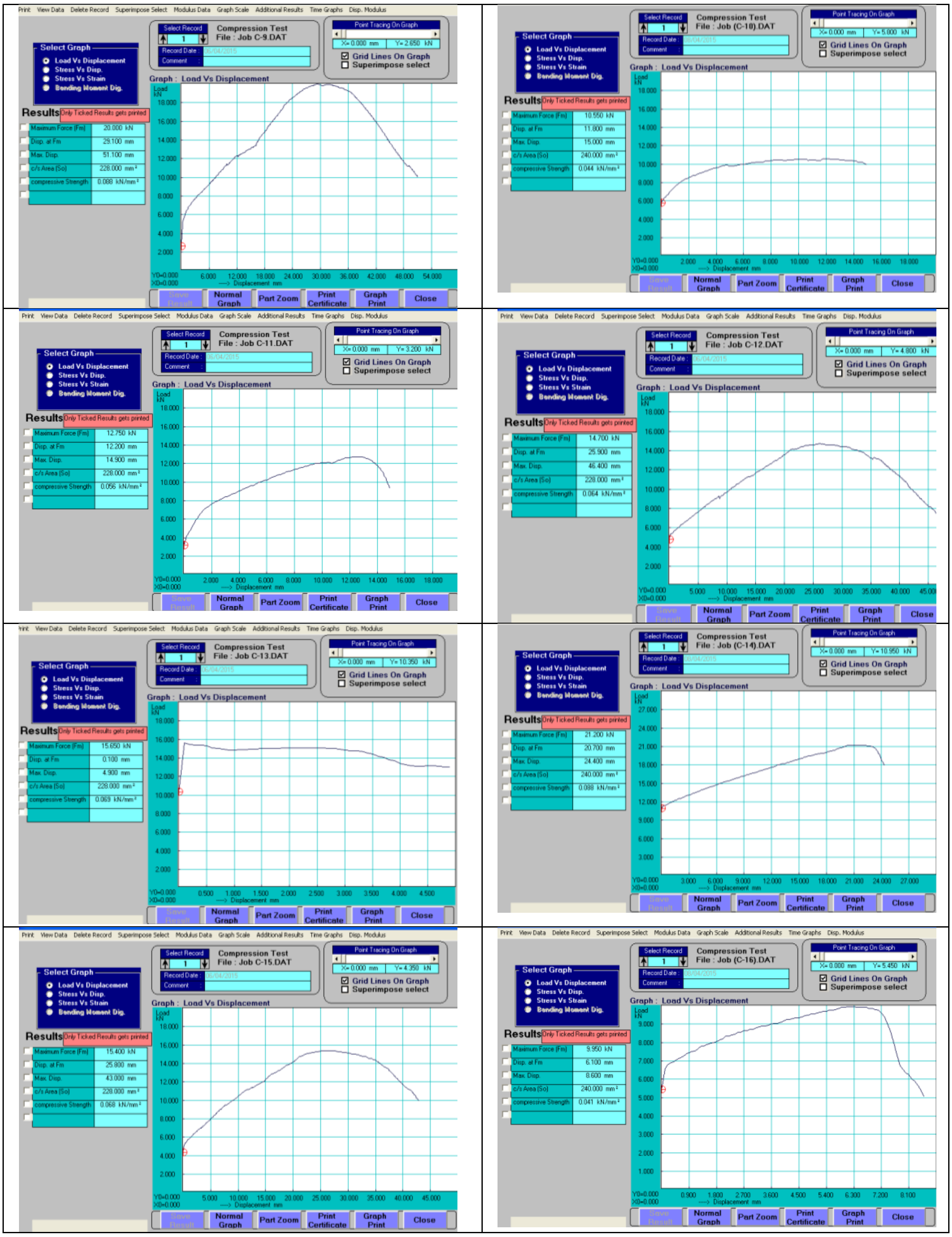

Compression Test
File : Job C-9.DAT
Select Record 1
Record Date : 06/04/2015
Comment :
X= 0.000 mm Y= 2.650 kN
☑ Grid Lines On Graph
☐ Superimpose select

Results Only Ticked Results gets printed

☐	Maximum Force (Fm)	20.000 kN
☐	Disp. at Fm	29.100 mm
☐	Max. Disp.	51.100 mm
☐	c/s Area (So)	228.000 mm^2
☐	compressive Strength	0.088 kN/mm^2
☐		

Compression Test
File : Job (C-10).DAT
Select Record 1
Record Date : 08/04/2015
Comment :
X= 0.000 mm Y= 5.800 kN
☑ Grid Lines On Graph
☐ Superimpose select

Results Only Ticked Results gets printed

☐	Maximum Force (Fm)	10.550 kN
☐	Disp. at Fm	11.800 mm
☐	Max. Disp.	15.000 mm
☐	c/s Area (So)	240.000 mm^2
☐	compressive Strength	0.044 kN/mm^2
☐		

Compression Test
File : Job C-11.DAT
Select Record 1
Record Date : 06/04/2015
Comment :
X= 0.000 mm Y= 3.200 kN
☑ Grid Lines On Graph
☐ Superimpose select

Results Only Ticked Results gets printed

☐	Maximum Force (Fm)	12.750 kN
☐	Disp. at Fm	12.200 mm
☐	Max. Disp.	14.900 mm
☐	c/s Area (So)	228.000 mm^2
☐	compressive Strength	0.056 kN/mm^2
☐		

Compression Test
File : Job C-12.DAT
Select Record 1
Record Date : 06/04/2015
Comment :
X= 0.000 mm Y= 4.800 kN
☑ Grid Lines On Graph
☐ Superimpose select

Results Only Ticked Results gets printed

☐	Maximum Force (Fm)	14.700 kN
☐	Disp. at Fm	25.900 mm
☐	Max. Disp.	46.400 mm
☐	c/s Area (So)	228.000 mm^2
☐	compressive Strength	0.064 kN/mm^2
☐		

Compression Test
File : Job C-13.DAT
Select Record 1
Record Date : 06/04/2015
Comment :
X= 0.000 mm Y= 10.350 kN
☑ Grid Lines On Graph
☐ Superimpose select

Results Only Ticked Results gets printed

☐	Maximum Force (Fm)	15.650 kN
☐	Disp. at Fm	0.100 mm
☐	Max. Disp.	4.900 mm
☐	c/s Area (So)	228.000 mm^2
☐	compressive Strength	0.069 kN/mm^2
☐		

Compression Test
File : Job (C-14).DAT
Select Record 1
Record Date : 08/04/2015
Comment :
X= 0.000 mm Y= 10.950 kN
☑ Grid Lines On Graph
☐ Superimpose select

Results Only Ticked Results gets printed

☐	Maximum Force (Fm)	21.200 kN
☐	Disp. at Fm	20.700 mm
☐	Max. Disp.	24.400 mm
☐	c/s Area (So)	240.000 mm^2
☐	compressive Strength	0.088 kN/mm^2
☐		

Compression Test
File : Job C-15.DAT
Select Record 1
Record Date : 06/04/2015
Comment :
X= 0.000 mm Y= 4.350 kN
☑ Grid Lines On Graph
☐ Superimpose select

Results Only Ticked Results gets printed

☐	Maximum Force (Fm)	15.400 kN
☐	Disp. at Fm	25.800 mm
☐	Max. Disp.	43.000 mm
☐	c/s Area (So)	228.000 mm^2
☐	compressive Strength	0.068 kN/mm^2
☐		

Compression Test
File : Job (C-16).DAT
Select Record 1
Record Date : 08/04/2015
Comment :
X= 0.000 mm Y= 5.450 kN
☑ Grid Lines On Graph
☐ Superimpose select

Results Only Ticked Results gets printed

☐	Maximum Force (Fm)	9.950 kN
☐	Disp. at Fm	6.100 mm
☐	Max. Disp.	8.600 mm
☐	c/s Area (So)	240.000 mm^2
☐	compressive Strength	0.041 kN/mm^2
☐		

Figure B: Load v/s displacements curve during face bend test of samples C-9 to C-16 (Ar shielding)

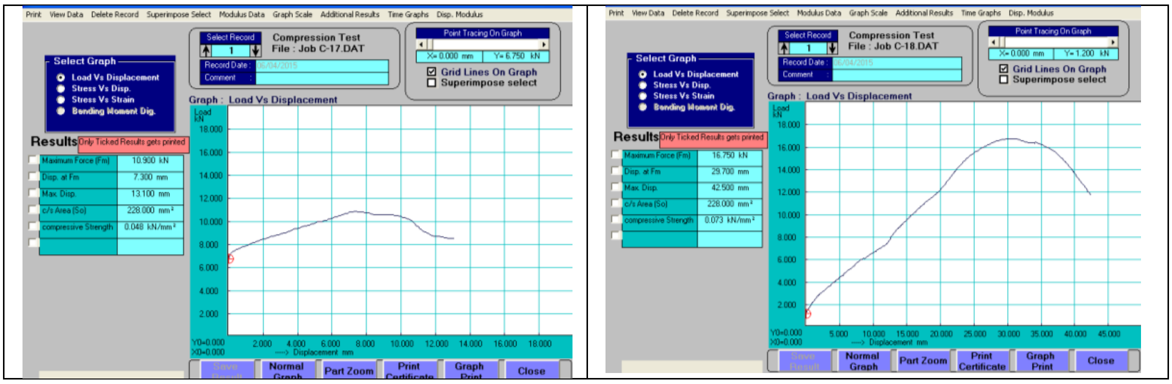

Compression Test
File : Job C-17.DAT
Select Record: 1
Record Date : 06/04/2015
Comment :
X= 0.000 mm Y= 6.750 kN

Results Only Ticked Results gets printed

☐ Maximum Force (Fm)	10.900 kN
☐ Disp. at Fm	7.300 mm
☐ Max. Disp.	13.100 mm
☐ c/s Area (So)	228.000 mm²
☐ compressive Strength	0.048 kN/mm²

Compression Test
File : Job C-18.DAT
Select Record: 1
Record Date : 06/04/2015
Comment :
X= 0.000 mm Y= 1.200 kN

Results Only Ticked Results gets printed

☐ Maximum Force (Fm)	16.750 kN
☐ Disp. at Fm	29.700 mm
☐ Max. Disp.	42.500 mm
☐ c/s Area (So)	228.000 mm²
☐ compressive Strength	0.073 kN/mm²

Figure C: Load v/s displacements curve during face bend test of samples C-17 and C-18 (Ar shielding)

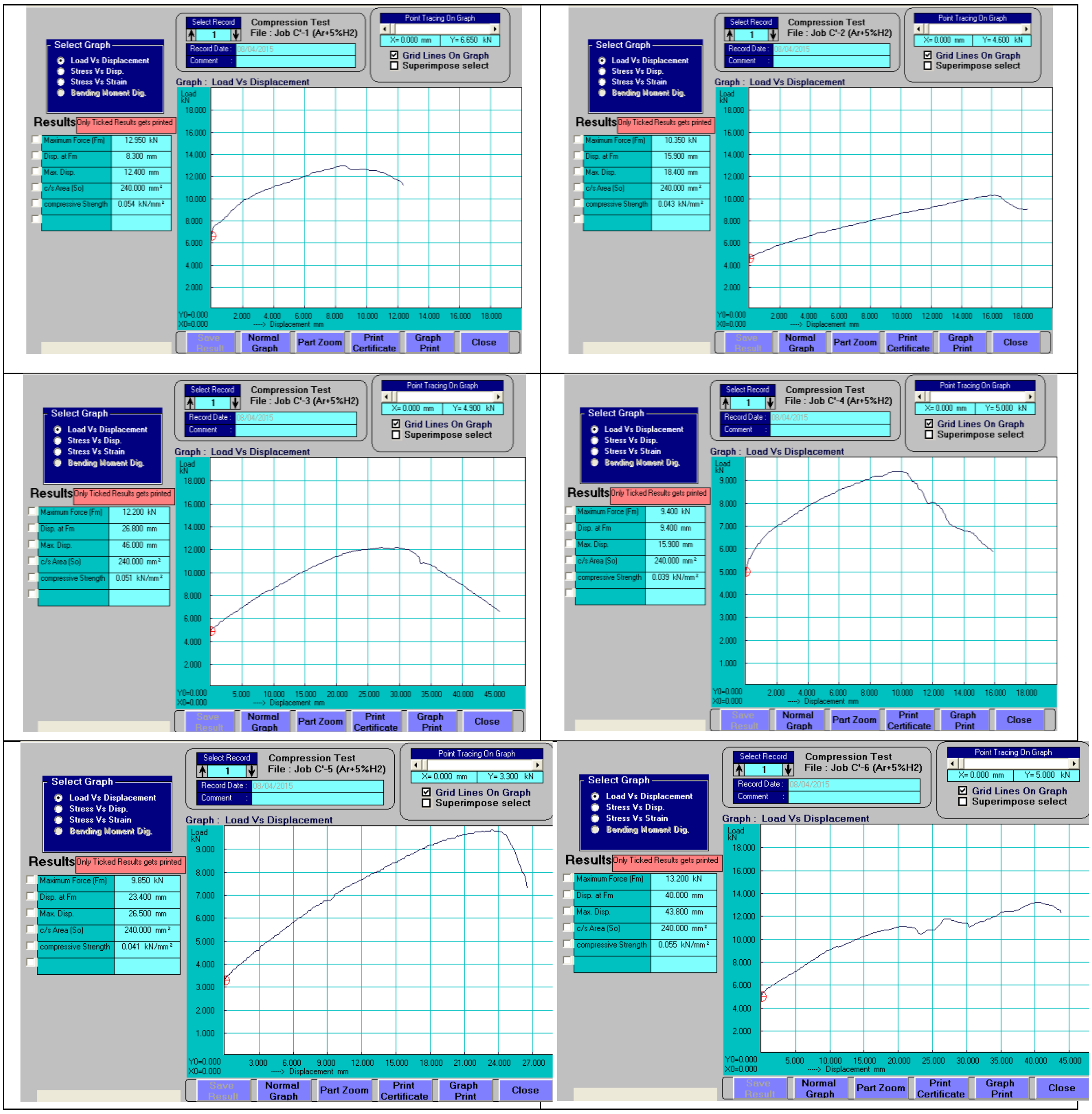

Compression Test
File : Job C'-1 (Ar+5%H2)
Select Record: 1
Record Date : 08/04/2015
Comment :
X= 0.000 mm Y= 6.650 kN

Results Only Ticked Results gets printed

☐ Maximum Force (Fm)	12.950 kN
☐ Disp. at Fm	8.300 mm
☐ Max. Disp.	12.400 mm
☐ c/s Area (So)	240.000 mm²
☐ compressive Strength	0.054 kN/mm²

Compression Test
File : Job C'-2 (Ar+5%H2)
Select Record: 1
Record Date : 08/04/2015
Comment :
X= 0.000 mm Y= 4.600 kN

Results Only Ticked Results gets printed

☐ Maximum Force (Fm)	10.350 kN
☐ Disp. at Fm	15.900 mm
☐ Max. Disp.	18.400 mm
☐ c/s Area (So)	240.000 mm²
☐ compressive Strength	0.043 kN/mm²

Compression Test
File : Job C'-3 (Ar+5%H2)
Select Record: 1
Record Date : 08/04/2015
Comment :
X= 0.000 mm Y= 4.900 kN

Results Only Ticked Results gets printed

☐ Maximum Force (Fm)	12.200 kN
☐ Disp. at Fm	26.800 mm
☐ Max. Disp.	46.000 mm
☐ c/s Area (So)	240.000 mm²
☐ compressive Strength	0.051 kN/mm²

Compression Test
File : Job C'-4 (Ar+5%H2)
Select Record: 1
Record Date : 08/04/2015
Comment :
X= 0.000 mm Y= 5.000 kN

Results Only Ticked Results gets printed

☐ Maximum Force (Fm)	9.400 kN
☐ Disp. at Fm	9.400 mm
☐ Max. Disp.	15.900 mm
☐ c/s Area (So)	240.000 mm²
☐ compressive Strength	0.039 kN/mm²

Compression Test
File : Job C'-5 (Ar+5%H2)
Select Record: 1
Record Date : 08/04/2015
Comment :
X= 0.000 mm Y= 3.300 kN

Results Only Ticked Results gets printed

☐ Maximum Force (Fm)	9.850 kN
☐ Disp. at Fm	23.400 mm
☐ Max. Disp.	26.500 mm
☐ c/s Area (So)	240.000 mm²
☐ compressive Strength	0.041 kN/mm²

Compression Test
File : Job C'-6 (Ar+5%H2)
Select Record: 1
Record Date : 08/04/2015
Comment :
X= 0.000 mm Y= 5.000 kN

Results Only Ticked Results gets printed

☐ Maximum Force (Fm)	13.200 kN
☐ Disp. at Fm	40.000 mm
☐ Max. Disp.	43.800 mm
☐ c/s Area (So)	240.000 mm²
☐ compressive Strength	0.055 kN/mm²

Figure D: Load v/s displacements curve during face bend test of samples C'-1 and C'-6 (Ar+5% H_2 shielding)

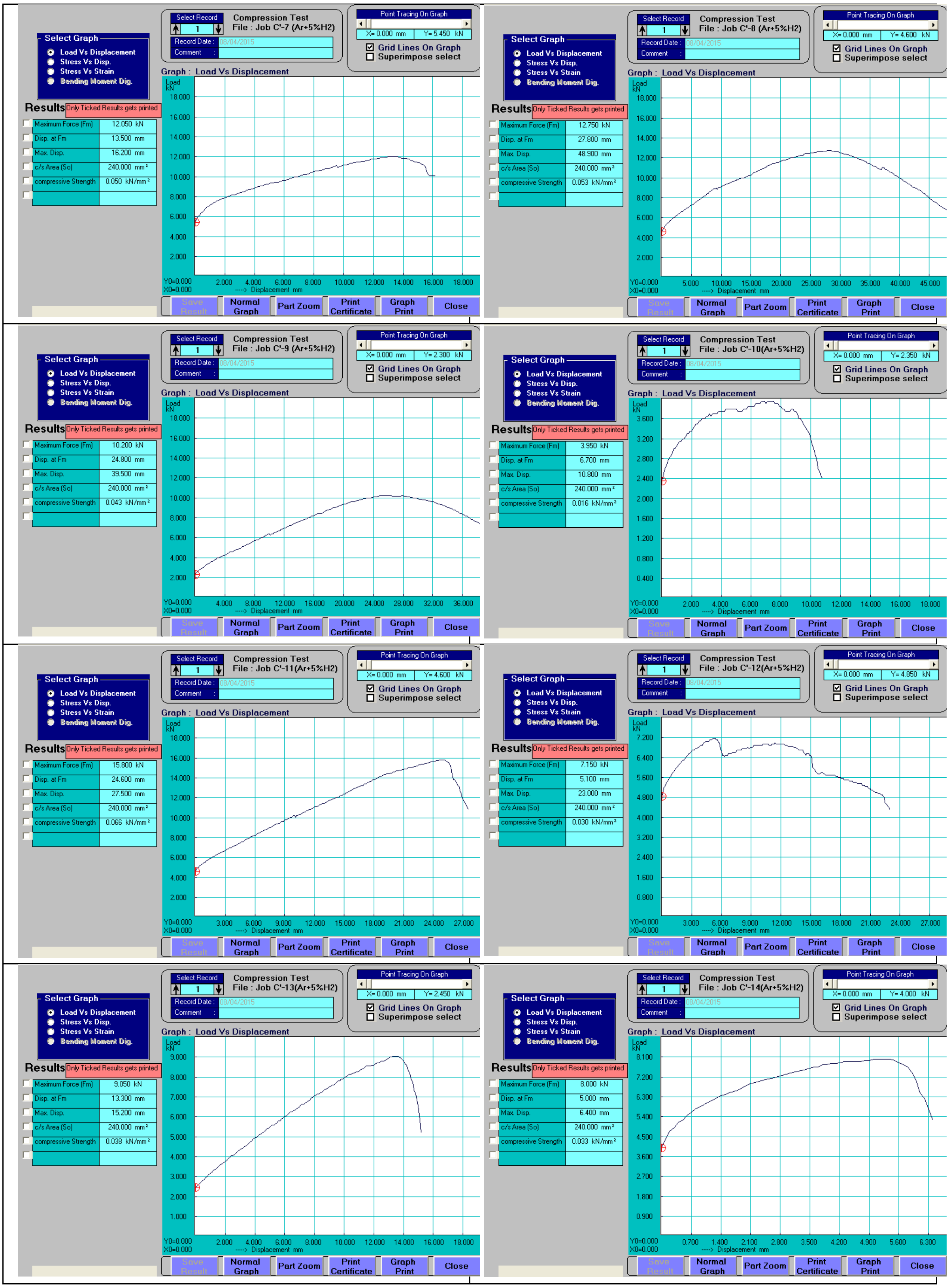

Compression Test
File : Job C'-7 (Ar+5%H2)
Select Record: 1
Record Date : 08/04/2015
Comment :
X= 0.000 mm Y= 5.450 kN
☑ Grid Lines On Graph
☐ Superimpose select
Graph : Load Vs Displacement
Y0=0.000
X0=0.000

☐ Maximum Force (Fm)	12.050 kN
☐ Disp. at Fm	13.500 mm
☐ Max. Disp.	16.200 mm
☐ c/s Area (So)	240.000 mm²
☐ compressive Strength	0.050 kN/mm²
☐	

Compression Test
File : Job C'-8 (Ar+5%H2)
Select Record: 1
Record Date : 08/04/2015
Comment :
X= 0.000 mm Y= 4.600 kN
☑ Grid Lines On Graph
☐ Superimpose select
Graph : Load Vs Displacement
Y0=0.000
X0=0.000

☐ Maximum Force (Fm)	12.750 kN
☐ Disp. at Fm	27.800 mm
☐ Max. Disp.	48.900 mm
☐ c/s Area (So)	240.000 mm²
☐ compressive Strength	0.053 kN/mm²
☐	

Compression Test
File : Job C'-9 (Ar+5%H2)
Select Record: 1
Record Date : 08/04/2015
Comment :
X= 0.000 mm Y= 2.300 kN
☑ Grid Lines On Graph
☐ Superimpose select
Graph : Load Vs Displacement
Y0=0.000
X0=0.000

☐ Maximum Force (Fm)	10.200 kN
☐ Disp. at Fm	24.800 mm
☐ Max. Disp.	39.500 mm
☐ c/s Area (So)	240.000 mm²
☐ compressive Strength	0.043 kN/mm²
☐	

Compression Test
File : Job C'-10(Ar+5%H2)
Select Record: 1
Record Date : 08/04/2015
Comment :
X= 0.000 mm Y= 2.350 kN
☑ Grid Lines On Graph
☐ Superimpose select
Graph : Load Vs Displacement
Y0=0.000
X0=0.000

☐ Maximum Force (Fm)	3.950 kN
☐ Disp. at Fm	6.700 mm
☐ Max. Disp.	10.800 mm
☐ c/s Area (So)	240.000 mm²
☐ compressive Strength	0.016 kN/mm²
☐	

Compression Test
File : Job C'-11(Ar+5%H2)
Select Record: 1
Record Date : 08/04/2015
Comment :
X= 0.000 mm Y= 4.600 kN
☑ Grid Lines On Graph
☐ Superimpose select
Graph : Load Vs Displacement
Y0=0.000
X0=0.000

☐ Maximum Force (Fm)	15.800 kN
☐ Disp. at Fm	24.600 mm
☐ Max. Disp.	27.500 mm
☐ c/s Area (So)	240.000 mm²
☐ compressive Strength	0.066 kN/mm²
☐	

Compression Test
File : Job C'-12(Ar+5%H2)
Select Record: 1
Record Date : 08/04/2015
Comment :
X= 0.000 mm Y= 4.850 kN
☑ Grid Lines On Graph
☐ Superimpose select
Graph : Load Vs Displacement
Y0=0.000
X0=0.000

☐ Maximum Force (Fm)	7.150 kN
☐ Disp. at Fm	5.100 mm
☐ Max. Disp.	23.000 mm
☐ c/s Area (So)	240.000 mm²
☐ compressive Strength	0.030 kN/mm²
☐	

Compression Test
File : Job C'-13(Ar+5%H2)
Select Record: 1
Record Date : 08/04/2015
Comment :
X= 0.000 mm Y= 2.450 kN
☑ Grid Lines On Graph
☐ Superimpose select
Graph : Load Vs Displacement
Y0=0.000
X0=0.000

☐ Maximum Force (Fm)	9.050 kN
☐ Disp. at Fm	13.300 mm
☐ Max. Disp.	15.200 mm
☐ c/s Area (So)	240.000 mm²
☐ compressive Strength	0.038 kN/mm²
☐	

Compression Test
File : Job C'-14(Ar+5%H2)
Select Record: 1
Record Date : 08/04/2015
Comment :
X= 0.000 mm Y= 4.000 kN
☑ Grid Lines On Graph
☐ Superimpose select
Graph : Load Vs Displacement
Y0=0.000
X0=0.000

☐ Maximum Force (Fm)	8.000 kN
☐ Disp. at Fm	5.000 mm
☐ Max. Disp.	6.400 mm
☐ c/s Area (So)	240.000 mm²
☐ compressive Strength	0.033 kN/mm²
☐	

Figure E: Load v/s displacements curve during face bend test of samples C'-7 and C'-14 (Ar+5% H_2 shielding)

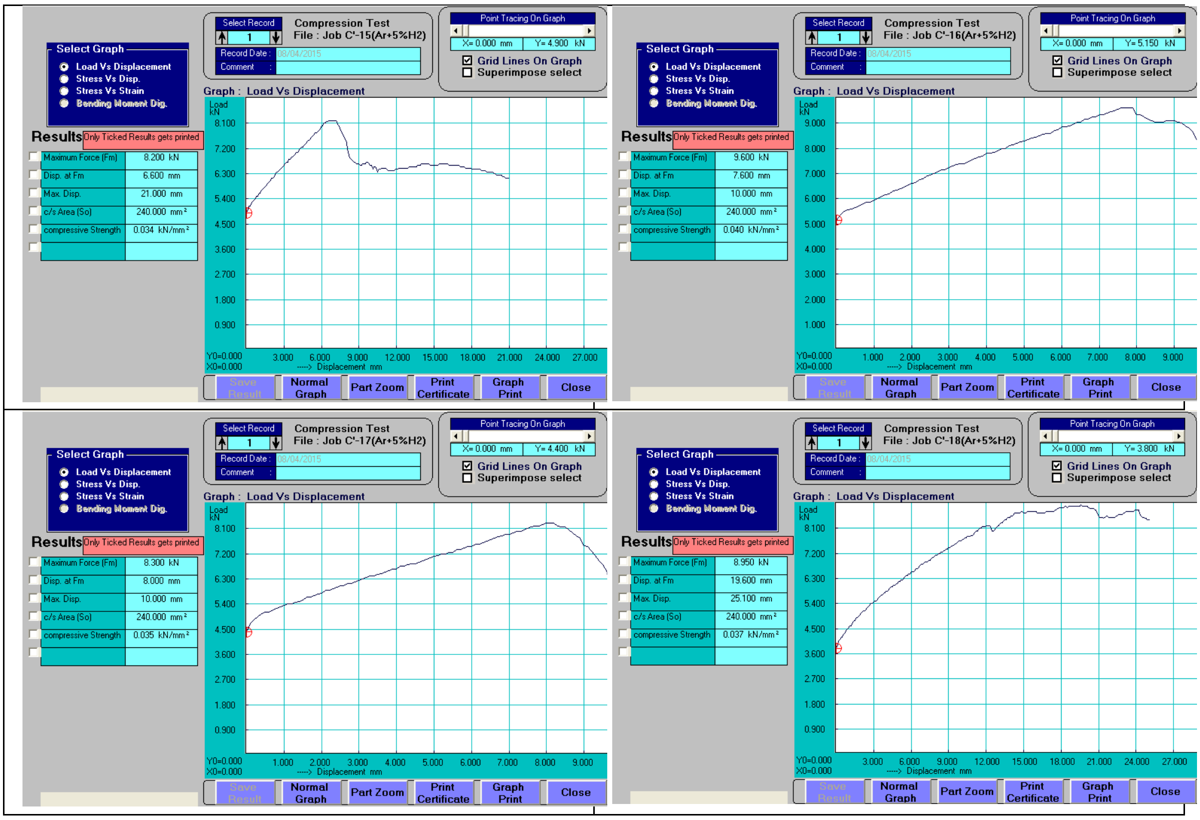

Compression Test
File : Job C'-15(Ar+5%H2)
Select Record: 1
Record Date : 08/04/2015
Comment :
X= 0.000 mm Y= 4.900 kN
☑ Grid Lines On Graph
☐ Superimpose select

☐ Maximum Force (Fm)	8.200 kN
☐ Disp. at Fm	6.600 mm
☐ Max. Disp.	21.000 mm
☐ c/s Area (So)	240.000 mm²
☐ compressive Strength	0.034 kN/mm²
☐	

Compression Test
File : Job C'-16(Ar+5%H2)
Select Record: 1
Record Date : 08/04/2015
Comment :
X= 0.000 mm Y= 5.150 kN
☑ Grid Lines On Graph
☐ Superimpose select

☐ Maximum Force (Fm)	9.600 kN
☐ Disp. at Fm	7.600 mm
☐ Max. Disp.	10.000 mm
☐ c/s Area (So)	240.000 mm²
☐ compressive Strength	0.040 kN/mm²
☐	

Compression Test
File : Job C'-17(Ar+5%H2)
Select Record: 1
Record Date : 08/04/2015
Comment :
X= 0.000 mm Y= 4.400 kN
☑ Grid Lines On Graph
☐ Superimpose select

☐ Maximum Force (Fm)	8.300 kN
☐ Disp. at Fm	8.000 mm
☐ Max. Disp.	10.000 mm
☐ c/s Area (So)	240.000 mm²
☐ compressive Strength	0.035 kN/mm²
☐	

Compression Test
File : Job C'-18(Ar+5%H2)
Select Record: 1
Record Date : 08/04/2015
Comment :
X= 0.000 mm Y= 3.800 kN
☑ Grid Lines On Graph
☐ Superimpose select

☐ Maximum Force (Fm)	8.950 kN
☐ Disp. at Fm	19.600 mm
☐ Max. Disp.	25.100 mm
☐ c/s Area (So)	240.000 mm²
☐ compressive Strength	0.037 kN/mm²
☐	

Figure F: Load v/s displacements curve during face bend test of samples C’-15 to C’-18 (Ar+5% H_2 shielding)